Structure and magnetism of transition-metal implanted dilute magnetic semiconductors

Lino Miguel da Costa Pereira

Examination committee:
Prof. dr. André Vantomme,[1] promotor
Prof. dr. Kristiaan Temst,[1] promotor
Dr. Ulrich Wahl,[2] co-promotor
Prof. dr. João Pedro Esteves Araújo,[3] co-promotor
Prof. dr. Wilfried Vandervorst[1,5]
Prof. dr. Margriet Van Bael[4]
Prof. dr. Chris Van Haesendonck[4]
Dr. Kay Potzger [6]

Dissertation presented in partial fulfillment of the requirements for the degree of Doctor in Science

[1] Instituut voor Kern- en Stralingsfysica, K.U.Leuven, Celestijnenlaan 200D, B-3001 Leuven, Belgium
[2] Instituto Tecnológico e Nuclear, UFA, 2686-953 Sacavém, Portugal
[3] IFIMUP and IN-Institute of Nanoscience and Nanotechnology, Faculty of Sciences of the University of Porto, 4169-007 Porto, Portugal
[4] Laboratorium voor Vaste-Stoffysica en Magnetisme, K.U.Leuven, Celestijnenlaan 200D, B-3001 Leuven, Belgium
[5] Imec, Kapeldreef 75, B-3001 Leuven, Belgium
[6] Helmholtz-Zentrum Dresden-Rossendorf, 01328 Dresden, Germany

December 2011

ISBN 978-90-8649-482-8
D/2011/10.705/99

Acknowledgements

A PhD is not 'just' research and science. Mine, at least, was also about reinventing my life and myself in a new country, a new culture, with new challenges. And I can say that these four years were some of the most wonderful years of my life. Sure there were many tough moments. But that's a small price to pay for the truly meaningful ones. And these I owe entirely to the people I acknowledge here.

I must start by thanking my supervisors. André and Kristiaan, my supervisors in Leuven. Thank you for welcoming me to your group which, thanks to you, has probably the best work environment I've seen. Honestly, I still didn't figure out how you managed to read and correct, within those tight schedules, all the pages I wrote during these four years. Always constructive, and always with a good suggestion, you did more than supervising, you helped me build a scientific attitude. João Pedro, my first mentor, in Porto. Today I am an experimentalist mostly because of you, and that was probably one of the best decisions I ever made. You also showed me that one person (and a young one) can really make a difference. So thanks for making such a good one in my life. Uli, in addition to mentor and supervisor, you were a colleague in the true meaning of the word, a fellow worker, even far away in Lisbon. People usually say that a PhD is a very lonely and unpredictable process. But thanks to your precise, continuous, hands-on work, and your unique expertise, you made my PhD a confident and much smoother trip.

I am also deeply indebted to those who, while not official supervisors, were far more than collaborators. Thank you Guilherme for all your support at CERN and your friendship. You are an example of passion and dedication, and of care for the people who work with you. Thank you Margriet for welcoming me in your lab, and for sharing with me some of the

endless mysteries of SQUID magnetometers. Thank you Tapobrata; a lot of what I learned during your three-month visit at IKS was extremely useful throughout the rest of my PhD.

I would also like to thank the members of the jury, Prof. Wilfried Vandervorst, Prof. Chris Van Haesendonk and Dr. Kay Potzger, for taking the time to read this thesis, and for the valuable corrections and suggestions.

None of this would have been possible without the help of many wonderful people. A big thanks to all the people from IFIMUP in Porto, my first group. Thank you Célia, João Ventura, André, Ju, Arlete, Mariana, Diana, Tânia, João Amaral, Zé Miguel, and many others. You will always be 'my group'. Thank you Stefan, Ligia and Daniel, my buddies at the emission channeling runs at ISOLDE. A special word of thanks to Stefan, for helping out since the very beginning, and for the many interesting discussions and ideas. Thank you Jelle, Shilpa and Dries, my office buddies when I arrived at IKS. Great times! Jelle, I wanted to make references to some of the best memories I have of sharing an office with you. Unfortunately, none of them are appropriate to bring up here. Thank you Annelore, you've been putting up with me all by yourself, after Shilpa and Jelle left. Not an easy job, I know... A special thanks for your help in key (read: overly stressful) moments at the finish line of this PhD. Thanks everyone else from IKS: Martine, Isabelle, Sally, Joost, Claudia, Maarten, Sebastien, Nandan, Kristof, Enric, Daniel, Huan, Tomas, Manuel, Pieter, Dieter, Zhou, Annemie, Bas, Luc, Bert, Willy, Dries and many others. You helped me in so many different ways, from giving me a hand in the lab, to helping me with paperwork, sharing a lunch break, or just playing a ping-pong match when I needed to blow off some steam. A special thanks to Maarten for the heavy foot on the gas pedal between Grenoble and Lyon, when I really couldn't miss that flight.

A big thanks to all my other friends in Leuven. Eric and Kamila, my first good friends in Belgium. Feeling like home has nothing to do with geography, it's all about being surrounded by the right people. Thank you Steve, Olalla, Serge, Melina, Sophie, Gabe, Molly, Roelof, Matthias and many others, for all those BBQs, beers at the Oude Markt, birthday parties, PhD defenses and afterparties, poker nights, Thanksgiving dinners, Super Bowl Sundays... You guys are great!

Acima de tudo, obrigado à minha famlia, pai, mãe, Zé e Daniel. As vossas vidas mostraram-me que nenhum desafio é demasiado grande, e que qualquer objectivo pode ser alcançado através de trabalho, persistência e respeito por aqueles à nossa volta. Foram voçês quem tornou este doutoramento possível. E um grande obrigado Cátia, por tudo que tens feito ao longo deste ano difícil para a nossa família.

Above all, I thank my father, my mother, and my brothers. Your lives have shown me that no challenge is too big, and that any goal can be achieved with hard work, persistence and respect for those around us. You are the ones who ultimately made this PhD possible.

Finally, thank you Charlotte. Many good things happened because of this PhD, but you were by far the best of all of them. I promise I'll make up for everything we missed doing together, while I was too busy with the PhD. People say life is a rocky road. But we don't notice it if we share that life with someone who makes us float above the rocks.

Lino
December 2011

Abstract (EN)

The discovery of a dilute magnetic semiconductor (DMS) in which ferromagnetism is carrier-mediated and persists above room temperature is a critical step towards the development of semiconductor-based spintronics. Among the many types of DMS materials which have been investigated, the current research interest can be narrowed down to two main classes of materials: (1) *narrow-gap* III-V semiconductors, mostly GaAs and InAs, doped with Mn; (2) *wide-gap* oxides and nitrides doped with $3d$ transition metals, mostly Mn- and Co-doped ZnO and Mn-doped GaN. With a number of interesting functionalities deriving from the carrier-mediated ferromagnetism and demonstrated in various proof-of-concept devices, Mn-doped GaAs has become, among DMS materials, one of the best candidates for technological application. However, despite major developments over the last 15 years, the maximum Curie temperature (185 K) remains well below room temperature. On the other hand, wide-gap DMS materials appear to exhibit ferromagnetic behavior at and above room temperature, but there is no consensus regarding the origin (intrinsic or not) of such ferromagnetism. The major challenges facing the DMS field can thus be summarized as: (i) in narrow-gap DMS, to increase the Curie temperature above the current record values; (ii) in wide-gap DMS, to understand the origin of the often observed high-temperature ferromagnetism and identify the conditions under which it can be reproduced.

In Mn-doped GaAs, the narrow-gap DMS with the highest Curie temperature reported so far (T_C = 185 K), a further increase in T_C depends on a better understanding and control over the balance between substitutional and interstitial Mn impurities. Here, we studied the lattice location of Mn in GaAs, and to what extent thermal annealing can be used as a means to remove the detrimental interstitial fraction. We determined that the interstitial Mn fraction occupies tetrahedral interstitial sites with As nearest neighbors, where it is stable up to 400°C, with an activation energy for diffusion of 1.7–2.3 eV. Substitutional Mn (in Ga sites) becomes mobile at higher temperatures (∼700°C) with an activation energy of ∼3 eV. Being difficult to reconcile with the general belief that interstitial Mn is the donor defect that out-diffuses at ∼200°C, these findings motivate a careful reassessment of the structural effects of low temperature annealing. First, placing the diffusion of interstitial Mn well above 200°C reopens the problem of identifying the donor defect that diffuses at low temperatures. Second, and more importantly, it suggests new strategies and prospects

for achieving pure substitutional doping and higher Curie temperatures in Mn-doped GaAs.

In transition-metal doped ZnO and GaN, the emerging picture of defect-related ferromagnetism indicates that high-temperature magnetic order may be associated with structural disorder, i.e. lattice defects. Here, we searched for room-temperature ferromagnetism in ZnO and GaN implanted with $3d$ transition-metals (Cr, Mn, Fe, Co) for a varying degree of lattice disorder, by varying the implantation and thermal annealing conditions. However, none of the prepared wide-gap DMS systems showed measurable room-temperature ferromagnetism. Among these systems, we focused on selected impurity-host combinations, performing detailed studies of their structural and magnetic properties, in terms of the lattice location and the magnetic interactions between transition-metal impurities, as well as their interplay with other lattice defects. We determined that, in addition to the majority substituting for the host cations (Zn in ZnO and Ga in GaN), significant fractions of the Mn and Co impurities ($\sim$ 20 – 30%) occupy substitutional anion sites (O in ZnO and N in GaN), which are virtually unaffected by thermal annealing up to 900°C. Although anion site fractions have never been identified before in ZnO and only for Mn in GaN, a number of arguments can be put forward which suggest that anion-site Co and Mn defects may indeed have low formation energies, particularly under a high concentration of anion vacancies (or equivalently, under O or N deficient conditions). Regarding the magnetism of the wide-gap DMS, we focused on two representative impurity-host combinations: Cr-implanted GaN and Fe-implanted ZnO. With Cr-implanted GaN, we aimed at studying the magnetic interactions between Cr moments, by varying the Cr atomic concentrations from the very dilute regime to well above the percolation threshold. With Fe-implanted ZnO, we aimed at a comprehensive description of the material's structure in terms of phase pureness and lattice location of the Fe impurities, as well as a detailed modeling of the paramagnetism observed with a varying density of lattice defects created by ion implantation. For both systems, we have shown that the magnetic interactions between the transition-metal moments are antiferromagnetic. Our findings support the view of a growing fraction of the DMS community that in general *the transition-metal impurities in wide-gap semiconductors do not order ferromagnetically at high temperatures*. The often observed high-temperature ferromagnetism can, alternatively, be attributed to non-intrinsic sources, such as a non-uniform distribution of the magnetic impurities, magnetic contamination or setup-related artifacts.

Abstract (NL)

De ontdekking van verdunde magnetische halfgeleiders (DMS), waarin ferromagnetisme door ladingsdragers gemedieerd wordt en aanwezig blijft boven kamertemperatuur, is een cruciale stap voor de ontwikkeling van halfgeleider-gebaseerde spintronica. Terwijl reeds heel wat DMS-materialen bestudeerd werden, kan het huidige wetenschappelijk onderzoek gereduceerd worden tot twee belangrijke klassen van materialen: (1) III-V halfgeleiders met een kleine energiekloof, zoals GaAs en InAs, gedopeerd met Mn; (2) oxides en nitrides met een grote energiekloof, gedopeerd met $3d$-transitiemetalen, met als voornaamste voorbeelden Mn- en Co-gedopeerd ZnO en Mn-gedopeerd GaN. Omwille van zijn interessante eigenschappen die voortvloeien uit het ladingsdrager-gemedieerde ferromagnetisme, is Mn-gedopeerd GaAs uitgegroeid tot één van de beste kandidaten om gebruikt te worden voor technologische toepassingen. Echter, ondanks belangrijke ontwikkelingen tijdens de afgelopen 15 jaar, blijft de maximale Curie-temperatuur (185 K) ruim onder kamertemperatuur. Anderzijds lijken de DMS-materialen met grote energiekloof ferromagnetisch gedrag te vertonen bij en zelfs boven kamertemperatuur, zonder dat de oorsprong (al dan niet *intrinsiek*) van dergelijk ferromagnetisme begrepen wordt. De belangrijkste uitdagingen voor het DMS-onderzoeksgebied kunnen dus als volgt samengevat worden: (i) de Curie-temperatuur verhogen boven de huidige maximale waarden voor DMS-materialen met kleine energiekloof; (ii) het begrijpen van de aard van het ferromagnetisch gedrag bij hoge temperatuur, en het bepalen van de voorwaarden waarbij dit gedrag kan worden gereproduceerd.

Bij Mn-gedopeerd GaAs, de kleine-energiekloof-DMS met de totnogtoe hoogste gerapporteerde Curie-temperatuur (T_C = 185 K), hangt een verdere verhoging van de T_C af van een beter begrip van de ingenomen roosterplaats (*substitutioneel* versus *interstitieel*) van de onzuiverheden. In dit werk werd de roosterplaats van Mn in GaAs bestudeerd, en meer bepaald in welke mate thermische uitgloeiing kan worden gebruikt om de interstitiële fractie te reduceren. We hebben vastgesteld dat de interstitiële Mn-onzuiverheden een tetrahedrale interstitiële positie innemen, omringd door As dichtste buren, en dat deze roosterplaats thermisch stabiel is tot 400°C, met een activatie-energie voor diffusie van 1.7-2.3 eV. Substitutioneel Mn (op de Ga roosterplaats) wordt pas mobiel bij hogere temperaturen (∼700°C), hetgeen resulteert in een activatie-energie van ∼3 eV. Aangezien deze bevindingen niet overeenkomen met de algemene overtui-

ging dat interstitieel Mn het donordefect is dat uitdiffundeert bij 200°C, is het noodzakelijk om de structurele eigenschappen van dit materiaal na uitgloeiing bij lage temperatuur beter te begrijpen. In de eerste plaats is er de waargenomen thermische stabiliteit van interstitieel Mn tot ver boven 200°C, waardoor de identificatie van het donordefect dat diffundeert bij lage uitgloeitemperatuur herzien moet worden. Nog belangrijker is dat er door deze resultaten nieuwe strategieën en perspectieven ontstaan voor het realiseren van pure substitutionele dopering en hogere Curie-temperaturen bij Mn-gedopeerd GaAs.

Het waargenomen ferromagnetisch gedrag bij hoge temperaturen in ZnO en GaN, gedopeerd met transitiemetalen, is volgens velen te wijten aan roosterdefecten. In deze studie werd er gezocht naar ferromagnetisme bij kamertemperatuur in ZnO en GaN geïmplanteerd met 3*d* transitiemetalen (Cr, Mn, Fe, Co). Echter, bij geen enkele van de onderzochte DMS-materialen met brede energiekloof werd er ferromagnetisch gedrag geobserveerd bij kamertemperatuur. In dit onderzoek, dat werd uitgevoerd bij welgekozen combinaties van onzuiverheden en DMS-materiaal, werden de magnetische en structurele eigenschappen in detail in kaart gebracht, meer bepaald door de roosterplaats te bestuderen, evenals de magnetische interactie tussen de transitiemetalen en de invloed van de roosterschade op deze magnetische eigenschappen. We hebben waargenomen dat, terwijl de meerderheid van de onzuiverheden de kationroosterplaats innemen (Zn in ZnO en Ga in GaN), er zich ook een significante hoeveelheid (∼20-30%) Mn- en Co-onzuiverheden op de substitutionele anionpositie (O in ZnO en N in GaN) bevinden, hetgeen thermisch stabiel is tot 900°C. Alhoewel tot dusver nog geen onzuiverheden op de anionpositie werden waargenomen in ZnO en enkel voor Mn onzuiverheden in GaN, zijn er argumenten die aantonen dat Co en Mn op anionposities een lagere vormingsenergie kunnen hebben. Wat betreft het magnetisch gedrag van de DMS-materialen met grote energiekloof, werd de focus gelegd op twee representatieve onzuiverheid-gastrooster combinaties: Cr-geïmplanteerd GaN en Fe-geïmplanteerd ZnO. Voor beide systemen werd er aangetoond dat de magnetische interacties tussen de momenten van de transitiemetalen antiferromagnetisch zijn. Onze bevindingen ondersteunen de mening van een groeiend deel van de DMS-gemeenschap dat, in het algemeen, de transitiemetalen in halfgeleiders met grote energiekloof niet ferromagnetisch oplijnen bij hoge temperatuur. Het vaak waargenomen ferromagnetisme bij hoge temperaturen kan worden toegeschreven aan niet-intrinsieke bronnen.

Preface

This thesis is the result of experimental research performed at the Instituut voor Kern- en Stralingsfysica of the Katholieke Universiteit Leuven, at the Institute of Nanoscience and Nanotechnology (IFIMUP unit) of the Unversity of Porto, Portugal, at the Organisation Européenne pour la Recherche Nucléaire (CERN) in Geneva, Switzerland. The first four chapters of this thesis introduce the field of dilute magnetic semiconductors, and outline the research performed in the framework of this PhD. All results are presented in chapter 5, based on articles which have been published, submitted or in preparation for submission. At the end of the thesis, a general conclusion summarizes the results and discusses their implications on the future of the field.

This thesis is based on the following publications:

I **Practical limits for detection of ferromagnetism using highly sensitive magnetometry techniques**
L. M. C. Pereira, J. P. Araújo, M. J. Van Bael, K. Temst, A. Vantomme
Journal of Physics D: Applied Physics **44**, 215001 (2011)

II **Direct identification of interstitial Mn in heavily p-type doped GaAs and evidence of its high thermal stability**
L. M. C. Pereira, U. Wahl, S. Decoster, J. G. Correia, M. R. da Silva, A. Vantomme, J. P. Araújo
Applied Physics Letters **98**, 201905 (2011)

III **Stability and diffusion of interstitital and substitutional Mn in GaAs of different doping types**
L. M. C. Pereira, U. Wahl, S. Decoster, J. G. Correia, L. M. Amorim, M. R. da Silva, J. P. Araújo, A. Vantomme
In preparation for *Physical Review B*

IV **Mixed Zn and O substitution of Co and Mn in ZnO**
L. M. C. Pereira, U. Wahl, S. Decoster, J. G. Correia, L. M. Amorim, M. R. da Silva, J. P. Araújo, A. Vantomme
Physical Review B **84**, 125204 (2011)

V **Evidence of N substitution by Mn in wurtzite GaN**
L. M. C. Pereira, U. Wahl, S. Decoster, J. G. Correia, L. M. Amorim, M. R. da Silva, A. Vantomme, J. P. Araújo
In preparation for *Physical Review Letters*

VI **Cation versus anion substitution of transition metals in GaN and ZnO**
L. M. C. Pereira, U. Wahl, S. Decoster, J. G. Correia, L. M. Amorim, M. R. da Silva, A. Vantomme, J. P. Araújo
In preparation for *Physical Review B*

VII **Searching for room temperature ferromagnetism in transition metal implanted ZnO and GaN**
L. M. C. Pereira, J. P. Araújo, U. Wahl, M. J. Van Bael, K. Temst, A. Vantomme
In preparation for *Journal of Applied Physics*

VIII **Paramagnetism and antiferromagnetic interactions in Cr-doped GaN**
L. M. C. Pereira, T. Som, J. Demeulemeester, M. J. Van Bael, K. Temst, A. Vantomme
Journal of Physics-Condensed Matter **23**, 346004 (2011)

IX **Paramagnetism and antiferromagnetic interactions in phase-pure Fe-implanted ZnO**
L. M. C. Pereira, L. M. C. Pereira, U. Wahl, J. G. Correia, M. Van Bael, S. Decoster, A. Vantomme, J. P. Araujo
In preparation for *Physical Review B*

Contents

Acronyms and abbreviations

AFGM	alternating field gradient magnetometer
Al_2O_3	aluminum oxide
BCA	binary collision approximation
BMP	bound magnetic polaron
BOM	bond-orbital model
CBM	conduction band minimum
CTF	charge-transfer ferromagnetism
CVD	chemical vapor deposition
DFT	density functional theory
DMS	dilute magnetic semiconductor

EPR	electron paramagnetic resonance
EXAFS	extended X-ray absorption fine structure
FC-ZFC	field-cooled zero-field-cooled
FET	field-effect transistor
GaAs	gallium arsenide
GaN	gallium nitride
GMR	giant magnetoresistance
hcp	hexagonal close-packed
HDD	hard-disk drive
HFS	hydrogen forward scattering spectrometry
IC	integrated circuit
InAs	indium arsenide
LBE	lattice binding energy
LED	light emitting diode
LT-MBE	low-temperature molecular beam epitaxy
MBE	molecular beam epitaxy
MOVPE	metalorganic vapor phase epitaxy
MTJ	magnetic tunnel junction
NRA	nuclear reaction analysis
PAC	perturbed angular correlation
PIXE	particle-induced X-ray emission
PLD	pulsed laser deposition
RBS	Rutherford backscattering spectrometry
RBS/C	Rutherford backscattering and channeling spectrometry
RKKY	Rudderman Kittel Kasuya and Yosida

SAXS	small-angle X-ray scattering
SIB	spin-split impurity band
SQUID	superconducting quantum interference device
SRIM	stopping and range of ions in matter
T_C	Curie temperature
TDE	threshold displacement energy
TiO_2	titanium dioxide
TM	transition metal
TMR	tunnel magnetoresistance
T_N	Néel temperature
TRIM	transport of ions in matter
VBM	valence band maximum
VSM	vibrating sample magnetometer
XAFS	x-ray absorption fine structure
XLD	x-ray linear dichroism
XRD	x-ray diffraction
ZnO	zinc oxide

Introduction

> *"One shouldn't work on semiconductors, that is a filthy mess; who knows whether any semiconductors exist?"*
>
> Wolfgang Pauli [1]

Despite Pauli's advice more than 70 years ago, today our lives revolve around a technology which is *based* on semiconductors: electronics. Ironically, I probably would have never even known of Pauli's pessimism if it wasn't for those same semiconductors functioning with perfection in my computer and the network of servers that brought the information to it. From computers and cell phones to medical and engineering equipment, electronics have shaped the modern society. In fact, with the exception of smell and taste, the senses of the average inhabitant of a developed country are likely more experienced with the digital than they are with the rest of the (some would call it the "real") world.

Why magnetic semiconductors? Transistors, packed by millions in integrated circuits (or chips), are the building block of virtually every electronic device. Processing speed and integration density of silicon chips have been increasing following "Moore's law", which postulates that transistor density on integrated circuits doubles about every eighteen months. However, as this packing endures, the materials which are currently used are reaching their functional limits.

> *"Moore's Law is dead. It can't continue forever. (...) We have another 10 to 20 years before we reach a fundamental limit."*
>
> Gordon E. Moore [2]

In other words, conventional electronics based on the electron *charge* and its transport, the same basic principle of the first transistor made more than fifty years ago, is reaching a dead end.

A solution: spintronics. Either by upgrading electronics with the additional degree of freedom of the electron *spin* or by using the spin alone, *spintronics* promises a new generation of devices with the advantages of non-volatility and higher processing speed, integration densities and power efficiency [3]. The concept emerged from the discovery of giant magnetoresistance (GMR) by Albert Fert and Peter Grünberg [4, 5], which earned them the Nobel Prize in Physics in 2007. Spin-valves based on the GMR effect quickly made their way to our daily lives in the form of read heads of hard disks, revolutionizing data storage technology. However, in this first form of spintronics (known as magnetoelectronics), data are stored in *metal-based* magnetic devices, and processed in *semiconductor-based* electronic devices. Exchanging data between the two costs both time and energy, which could be saved if storage and processing could be integrated in a single device. This essentially translates to evolving from *metal-based* to *semiconductor-based* spintronics. Doing so requires a material which displays electrically tunable ferromagnetism at temperatures well above room temperature and which can be incorporated into complex integrated circuits [3, 6]. However, even though ferromagnetic and semiconducting behaviors do coexist in some materials, such as europium chalcogenides and chromium spinels, their ordering temperatures (Curie temperatures) are well below room temperature (< 100 K), limiting their use in practical applications.

An alternative: dilute magnetic semiconductors. In a similar approach to electrical doping (which makes insulating or nearly insulating materials conducting by substituting host atoms by donor or acceptor impurities), magnetic ions can be incorporated in nonmagnetic semiconductors to make them ferromagnetic. Such materials are known as *dilute magnetic semiconductors* (DMS). The history of DMS is a long (almost 30 years) and exciting one. Generation after generation of DMS materials, with an always increasing Curie temperature, have captured the attention of the semiconductor and the magnetism communities. With many promising but also puzzling developments, and hundreds of publications every year, the DMS field is considered by some "the most controversial research topic in materials science and condensed-matter physics today" [8]. Among the many types of DMS materials which are currently investigated, the research interest can be narrowed down to two main classes of materials: (1) *narrow-gap* III-V semiconductors, mostly GaAs and InAs, doped with Mn; (2) *wide-gap* oxides (mostly ZnO) and nitrides (mostly GaN) doped with $3d$ transition metals.

In narrow-gap semiconductors such as GaAs and InAs, Mn impurities

behave as both electrical and magnetic dopants. Substituting for Ga, the Mn ions act as acceptors, and the itinerant holes which they introduce mediate the ferromagnetic coupling between the localized Mn magnetic moments. This carrier-mediated ferromagnetism has offered the opportunity to study new spin-related phenomena in semiconductors, such as spin-polarized light emission [9] and electrical and optical control over the magnetization [10, 11]. In addition, InAs and GaAs are well-established semiconductors with wide application in the electronics and optoelectronics industries. With such a strong technological background and a number of interesting functionalities deriving from the carrier-mediated ferromagnetism and demonstrated in various proof-of-concept devices [12], this class of materials became the most promising candidate for the technological implementation of DMS materials. However, despite major development over the last 15 years, maximum Curie temperatures remain below room-temperature (185 K in GaAs [13, 14] and 90 K in InAs [15]).

For the wide-gap oxides and nitrides, the situation is far more unclear. Although the large majority of the reports claim the existence of ferromagnetic order at and above room temperature, there is no consensus regarding the origin of such ferromagnetism [8, 16]. The persistent irreproducibility between and within laboratories, and the fact that the ferromagnetic behavior appears to be unstable over time, earned it the label of "phantom" or "fickle" ferromagnetism [16]. Since the very first reports of high-temperature ferromagnetism, the magnetism community has been divided between optimists and skeptics. The optimists believe that irrefutable evidence of intrinsic ferromagnetism will eventually emerge, once a wide-gap DMS "fruitfly" is discovered - a system which is easy to prepare and reproduce [16]. Others, more skeptical, are convinced that the observed high-temperature ferromagnetism is a consequence of either experimental artifacts or a non-random distribution of the magnetic ions [8]. In this work, we address the challenges facing these two classes of DMS materials. In Mn-doped GaAs, the narrow-gap DMS with the highest Curie temperature (T_C) reported so far, further increase in T_C depends on a better understanding and control of the balance between substitutional and interstitial Mn impurities. Here, we study the lattice location of Mn in GaAs, and to what extent thermal annealing can be used as a means to remove the detrimental interstitial fraction. In transition-metal doped ZnO and GaN the challenges are twofold: to find the wide-gap DMS "fruitfly" and to understand the origin of the often observed (but "fickle") high-temperature ferromagnetism. Here, we search for room-temperature ferromagnetism in ZnO and GaN doped with transition-metals (Cr, Mn, Fe, Co), using ion implantation as doping technique. In line with the emerging picture of

defect-related ferromagnetism [16], the goal is to search for intrinsic ferromagnetism under a varying degree of beam-induced disorder, by surveying a wide range of impurity-host combinations and implantation and thermal annealing conditions. In addition, we focus on representative DMS systems aiming at a detailed description of their structural and magnetic properties, i.e. in terms of the lattice location and the magnetic interactions between transition-metal impurities, as well as their interplay with other lattice defects.

Chapter 1 introduces the field of dilute magnetic semiconductors. Following a short overview of the field, motivating the choice to study (narrow-gap) Mn-doped GaAs and (wide-gap) transition-metal doped ZnO and GaN, the current understanding of the structural and magnetic properties of these materials are reviewed. **Chapter 2** then explains the overall objectives and outline of this work, addressing the field's major challenges summarized at the end of chapter 1. **Chapter 3** describes the experimental techniques which were used. Sample preparation consisted of doping single-crystals and epitaxial thin films by ion implantation. Sample characterization was based on electron emission channeling to study the lattice location of the implanted impurities, Rutherford backscattering and channeling spectrometry (RBS/C) to study the damage formation and recovery, and superconducting quantum interference device (SQUID) magnetometry for magnetic characterization. The results are presented in **chapter 4** (following the same structure as the research objectives in **chapter 2)**, based on the articles which have been published and the manuscripts that have been prepared for publication. Finally, the last chapter concludes the thesis by summarizing the main results and discussing their implications on the current goals and future of the field.

References

[1] L. Hoddeson, E. Braun, J. Teichmann, and S. Weart, eds., *Out of the Crystal Maze: Chapters from the History of Solid-State Physics*. Oxford Univ. Press, Oxford, 1992.

[2] M. Dubash, "Operating systems and servers news," *Techworld*, 13 April 2005.

[3] H. Ohno, "Making nonmagnetic semiconductors ferromagnetic," *Science*, vol. 281, p. 951, 1998.

[4] M. N. Baibich, J. M. Broto, A. Fert, F. N. Vandau, F. Petroff, P. Eitenne, G. Creuzet, A. Friederich, and J. Chazelas, "Giant magnetoresistance of (001)Fe/(001)Cr magnetic superlattices," *Phys. Rev. Lett.*, vol. 61, p. 2472, 1988.

[5] G. Binasch, P. Grunberg, F. Saurenbach, and W. Zinn, "Enhanced magnetoresistance in layered magnetic-structures with antiferromagnetic interlayer exchange ," *Phys. Rev. B*, vol. 39, p. 4828, 1989.

[6] A. H. Macdonald, P. Schiffer, and N. Samarth, "Ferromagnetic semiconductors: moving beyond (Ga,Mn)As," *Nat. Mater.*, vol. 4, p. 195, 2005.

[7] I. Zutic, J. Fabian, and S. Das Sarma, "Spintronics: Fundamentals and applications," *Rev. Mod. Phys.*, vol. 76, p. 323, 2004.

[8] T. Dietl, "A ten-year perspective on dilute magnetic semiconductors and oxides," *Nat. Mater.*, vol. 9, p. 965, 2010.

[9] S. Ghosh and P. Bhattacharya, "Surface-emitting spin-polarized $In_{0.4}Ga_{0.6}As$/GaAs quantum-dot light-emitting diode," *Appl. Phys. Lett.*, vol. 80, p. 658, 2002.

[10] D. Chiba, F. Matsukura, and H. Ohno, "Electric-field control of ferromagnetism in (Ga,Mn)As," *Appl. Phys. Lett.*, vol. 89, p. 162505, 2006.

[11] K. C. Hall, J. P. Zahn, A. Gamouras, S. March, J. L. Robb, X. Liu, and J. K. Furdyna, "Ultrafast optical control of coercivity in GaMnAs," *Appl. Phys. Lett.*, vol. 93, p. 032504, 2008.

[12] T. Dietl, D. D. Awschalom, M. Kaminska, and O. H, *Semiconductors and Semimetals*. Elsevier, 2008.

[13] M. Wang, R. P. Campion, A. W. Rushforth, K. W. Edmonds, C. T. Foxon, and B. L. Gallagher, "Achieving high Curie temperature in (Ga,Mn)As," *Appl. Phys. Lett.*, vol. 93, p. 132103, 2008.

[14] V. Novak, K. Olejnik, J. Wunderlich, M. Cukr, K. Vyborny, A. W. Rushforth, K. W. Edmonds, R. P. Campion, B. L. Gallagher, J. Sinova, and T. Jungwirth, "Curie point singularity in the temperature derivative of resistivity in (Ga,Mn)As," *Phys. Rev. Lett.*, vol. 101, p. 077201, 2008.

[15] T. Schallenberg and H. Munekata, "Preparation of ferromagnetic (In,Mn)As with a high Curie temperature of 90 K," *Appl. Phys. Lett.*, vol. 89, p. 042507, 2006.

[16] J. M. D. Coey in *Handbook of Spin Transport and Magnetism* (E. I. Tsymbal and I. Zutic, eds.), ch. Magnetism of Dilute Oxides, Chapman and Hall/CRC, 2011.

Chapter 1

Dilute magnetic semiconductors

This chapter introduces the field of dilute magnetic semiconductors. It starts by giving a short motivation and definition of the field (section 1.1), followed by an overview of the history of DMS research which motivates the choice to study Mn-doped GaAs and transition-metal doped ZnO and GaN in this work (section 1.2). Sections 1.3 and 1.4 then focus in these materials, describing the current understanding of their structural and magnetic properties relevant in the DMS context. The chapter ends by summarizing the major challenges and open questions in the DMS field related to Mn-doped GaAs and transition-metal doped ZnO and GaN.

1.1 Motivation and definition

Spin electronics or *spintronics* can be defined as the technology which simultaneously exploits the two fundamental properties of the electron: charge and spin. With its operation based on the manipulation, transport, and detection of spin-polarized carriers, spintronics is expected to improve upon traditional electronic and photonic devices in terms of reduced power consumption, faster device operation, and new forms of information computation [1]. Possible spintronic devices include, for example, spin-polarized LEDs, spin-field effect transistors (FETs), and spin-based qubits for quantum computation. Multifunctionality is also expected to improve overall device performance, for example by integrating magnetic (spin-related) and electronic (charge-related) operations on the same chip. Since the electron

spin is fundamentally a "binary" quantity (spin-up or spin-down), spintronic materials may also be used in fast rewritable memory which is non-volatile.

Spintronics is already present in current technology, playing an important role in metal-based magnetic-storage devices. This initial form of spintronics, known as magnetoelectronics, emerged with the discovery of the giant magnetoresistance (GMR) effect in spin-valve structures in 1988. Used in the read-heads of computer hard-disks (HDD), it allowed for a significant decrease in bit size and consequently an increase in integration density, revolutionizing data storage technology. The GMR-based spin-valves (multilayers of ferromagnetic-nonferromagnetic metals) were soon replaced in the read-heads of HDDs by magnetic tunnel junctions (MTJs), based on the tunnel magnetoresistance (TMR). The principle of operation of MTJs and spin-valves is very similar, the main difference being that the metallic nonferromagnetic spacer of the spin-valve structure is replaced by a thin insulator layer in an MTJ.

However, while revolutionizing data storage technology, this first generation of spintronic (magnetoelectronic) devices has also created a bottleneck in the way current devices handle information: data is stored in *metal-based* magnetic devices, while data processing is carried out in *semiconductor-based* electronic devices. Integrating both functionalities in one system would necessarily increase the speed, energy efficiency and packing densities of electronic devices. However, the semiconductors currently used in integrated circuits, transistors and lasers, such as silicon (Si), gallium arsenide (GaAs) and gallium nitride (GaN) are not magnetic. On the other hand, ferromagnetic materials used in digital storage devices, such as iron (Fe), cobalt (Co), nickel (Ni) and their alloys are not semiconductors. In addition, the crystal structures of magnetic materials are usually quite different from that of the semiconductors used in electronics, making it difficult to combine the two in functional heterostructures [1]. Also, the conductivity mismatch between metals and semiconductors limits the efficiency of spin-injection [2]. The alternative is then to use materials which combine ferromagnetic and semiconducting behavior [3].

Ferromagnetism and semiconducting behavior indeed coexist in some materials. Semiconducting behavior in ferromagnetic materials was first observed in europium chalcogenides (EuO) and chromium spinels ($CdCr_2S_4$, $CdCr_2Se_4$). These can be considered true *ferromagnetic semiconductors* in the sense that they contain magnetic elements in their chemical formula and the ferromagnetic order is established in the magnetic (periodic) sub-

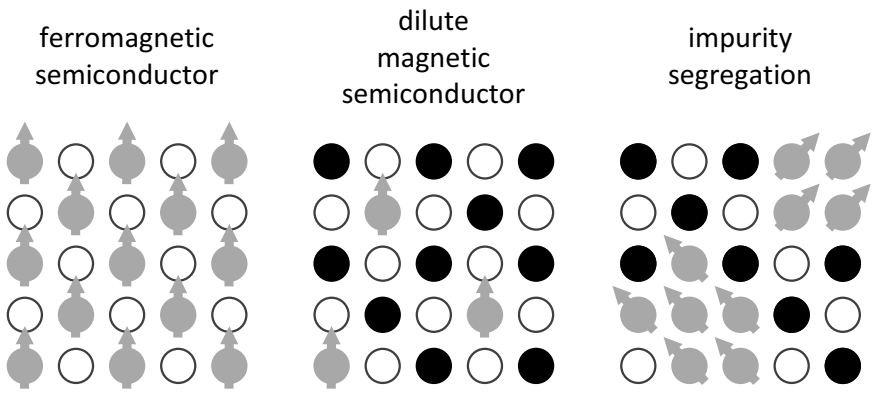

Figure 1.1: Representation of three types of distribution of magnetic atoms in a semiconductor matrix: periodic in the sublattice of the material; random substitution as an impurity in a dilute magnetic semiconductor; segregated (i.e. non-uniformly distributed) impurities.

lattice [Fig. 1.1 (a)]. In these ferromagnetic semiconductors, which were extensively studied from late 1960s to early 1970s, exchange interactions between the electrons in the semiconductor bands and the localized magnetic moments are manifested in various interesting properties, such as the red-shift of the bandgap upon the onset of ferromagnetic order. However, the interest in these materials was limited to academic research. Their crystal structures are incompatible with conventional semiconductors, like Si and GaAs, making their integration with current electronics difficult. In addition, the synthesis of these materials is rather cumbersome and difficult to reproduce. Most importantly, low Curie temperatures ($T_C < 100$ K) make them of little use in practical applications, which require that the ferromagnetic behavior is retained up to typical device operation temperatures (room temperature and above).

Fortunately, this is not the end of the story. In a similar approach to electrical doping, which makes insulating (or nearly insulating) materials conducting by incorporating donor and acceptor impurities, one may introduce magnetic atoms into nonmagnetic semiconductors to make them ferromagnetic. In these materials, known as *diluted magnetic semiconductors*, magnetic impurities randomly substitute a few percent of the atoms in the host matrix of the nonmagnetic semiconductor [Fig. 1.1 (b)]. A *magnetic impurity* is, in this context, an atom or ion of an element which is not only

different from the host's constituents, but which also carries a nonvanishing magnetic moment. These magnetic moments may originate, for example, in unfilled $3d$ or $4f$ shells of transition metals or rare earths, respectively. The usefulness of a DMS material system depends on two conditions: (1) by some long-range mechanism, the localized magnetic moments must order ferromagnetically and the ferromagnetic state must be attained up to typical junction operation temperatures (room temperature and above); (2) the charge carriers in the semiconductor must be spin-polarized, in order to allow, for example, the control of magnetization by an electric field or the use of these semiconductors as efficient spin-injectors. Condition (2) indirectly poses a third condition on the distribution and structure of the magnetic impurities in the host semiconductor. Efficient spin-polarization of the carriers requires that these must be involved in the order mechanism, which is the case for carrier-mediated ferromagnetism. This excludes materials where the ferromagnetic order and the semiconductor bands involved in the conduction are independent of each other, which is the case, for example, for materials composed of small ferromagnetic precipitates embedded in a semiconductor matrix [Fig. 1.1 (c)]. Even though such a material may show both semiconducting and ferromagnetic behavior, and even some degree of correlation may exist between the two, an efficient spin-polarization of the carriers is extremely unlikely. This distinction between randomly substituted DMS materials (commonly referred to as *intrinsic* DMS) from those where the ferromagnetism originates from secondary phases embedded in the semiconductor matrix, is of fundamental importance. When synthesizing DMS materials, it may happen that the impurities are not randomly incorporated, but instead segregate into impurity-rich regions or even in secondary phases. These non-DMS regions or phases may themselves be ferromagnetic, and this ferromagnetism is commonly referred to as *non-intrinsic*.

1.2 History of dilute magnetic semiconductors

The first generation of DMS materials emerged in the early 1980s, consisting of Mn-doped II-VI alloys of the form $A_{1-x}Mn_xB$, e.g. $Cd_{1-x}Mn_xTe$, $Hg_{1-x}Mn_xTe$. These compounds were attractive for various reasons. For example, their lattice and band parameters can easily be tuned by varying the alloy composition [4], making them suitable for heterostructure devices. In addition, the very efficient Mn-related electroluminescence makes them attractive for optoelectronic applications. The exchange interactions be-

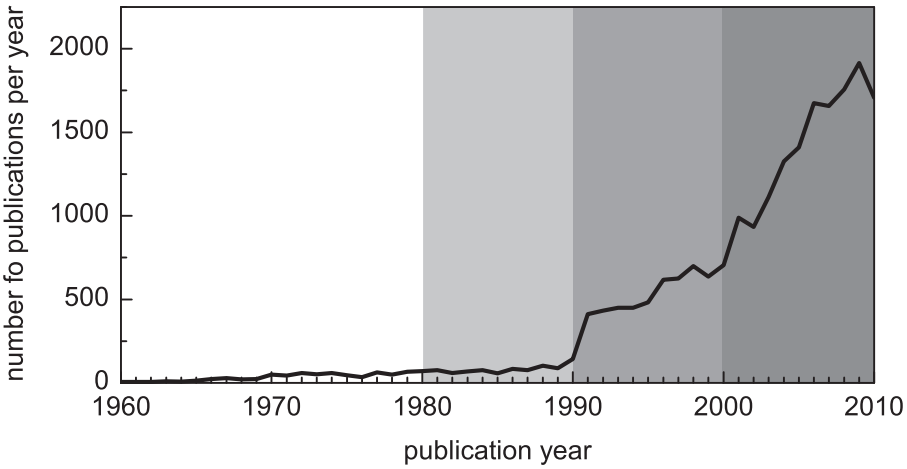

Figure 1.2: Number of publications per year, obtained from "Web of Science" using the keywords "magnetic" and "semiconductors" in the search field *Topic*. The white region corresponds to the period before the emergence of dilute magnetic semiconductors (DMS). The gray regions indicate the three generations of DMS materials described in the text.

tween localized Mn moments and the *sp*-band electrons have a dramatic effect on the optical and electrical properties of the material, such as giant Faraday rotation and bound magnetic polaron formation [4]. However, dominated by antiferromagnetic superexchange, the magnetic order in these materials is either antiferromagnetic or spin-glass [5]. Ferromagnetism in this type of materials, driven by hole-mediated exchange, was only reported more recently, in $Cd_{1-x}Mn_xTe$ [6] and $Zn_{1-x}Mn_xTe$ [7]. Their low Curie temperatures ($T_C \sim 2$ K) and the fact that II-VI based DMSs are difficult to dope both *n*- and *p*-type (bipolar doping) make them of limited use in practical applications [8].

The first boom in the field (c.f. Fig. 1.2) coincides with the emergence of the second generation of DMS materials, in the early 1990s. Overcoming the low solubility of transition metal impurities in III-V semiconductors by developing nonequilibrium epitaxial growth using low-temperature molecular beam epitaxy (LT-MBE), Ohno *et al.* discovered ferromagnetism up to 35 K in Mn-doped InAs ($In_{1-x}Mn_xAs$) [9]. Eventually, the success of LT-MBE growth of $In_{1-x}Mn_xAs$ led to the development of Mn-doped GaAs ($Ga_{1-x}Mn_xAs$), with even higher Curie temperatures [10]. InAs and GaAs

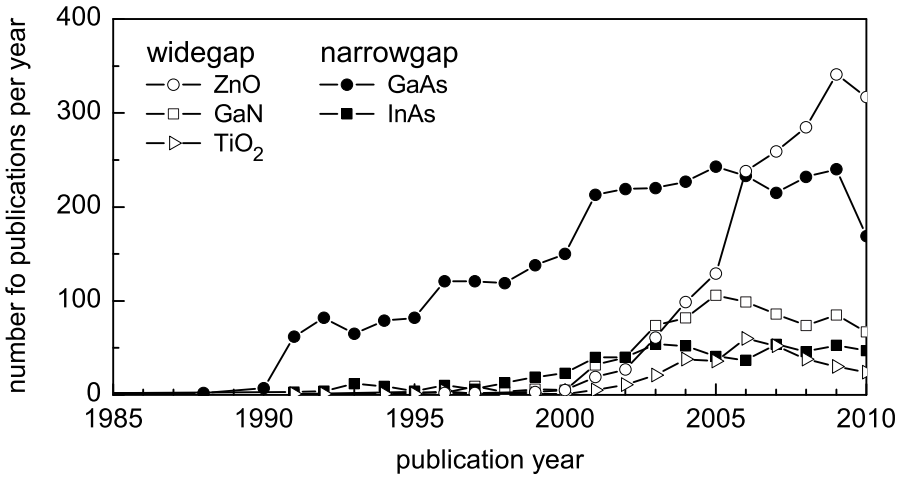

Figure 1.3: Number of publications per year, obtained from "Web of Science" using the keywords "magnetic" and "semiconductors" each the host semiconductors ("ZnO", "GaN", "TiO2", "GaAs", "InAs") in the search field *Topic*.

are well-established III-V semiconductors, with wide application in the electronics and optoelectronics industries, which makes them particularly attractive for applications. Because Mn acts as an acceptor when substituting for the group III elements, high Mn concentrations (up to $x \approx 0.10$) result in a high concentration of free holes, which, as described in section 1.3, mediate the ferromagnetic interaction between the localized Mn moments. This carrier-mediated ferromagnetism in $In_{1-x}Mn_xAs$ and $Ga_{1-x}Mn_xAs$ offered the opportunity to study new spin-based phenomena in semiconductor devices, such as spin-polarized light emission [11] and electrical and optical control of the magnetization [12, 13]. $Ga_{1-x}Mn_xAs$ became one of the best candidates for the technological implementation of DMS materials thanks to a number of factors: strong technological background of GaAs; the higher Curie temperature in $Ga_{1-x}Mn_xAs$ (185 K) [14,15] compared to $In_{1-x}Mn_xAs$ (90 K) [16]; various interesting functionalities deriving from its carrier-mediated ferromagnetism and demonstrated in various proof-of-concept devices [17]. However, despite major development over the last 15 years, further increase in Curie temperature faces difficult technical challenges [14, 18].

The major boom in the field began around the year 2000 (Fig. 1.2). While *narrow-gap* materials such as Mn-doped GaAs and InAs continued

being intensively studied throughout the 1990s until today, a third generation of DMS materials emerged in the last ten years (c.f. Fig. 1.3). This new class of DMS materials consisted mainly of wide-gap oxides (e.g. ZnO and TiO_2) and nitrides (e.g. GaN) doped with $3d$ transition metals, mostly Mn, Fe and Co. The main characteristic that distinguishes this generation of DMS materials from the previous is the bandgap of the semiconductor host: InAs and GaAs are *narrow-gap* whereas ZnO and GaN are *wide-gap* semiconductors. Following the first report of high temperature ferromagnetism in Co-doped TiO_2 by Matsumoto *et al.* [19] and the prediction by Dietl *et al.* [20] that highly p-type Mn-doped ZnO and GaN could attain a T_C above room temperature, ferromagnetism at and above room temperature was reported in a rapidly growing number of wide-gap DMS materials (cf. for example the reviews [21–24]). Although virtually any of the attempted impurity-host DMS combinations was sooner or later reported to display room temperature ferromagnetism, materials like Co- and Mn-doped ZnO and Mn- and Fe-doped GaN received particular attention. This "natural selection" can be attributed to various factors, the most important of which probably being the early predictions of room temperature ferromagnetism in ZnO and GaN, by Dietl *et al.* [20] in p-type materials and by Sato *et al.* [25, 26] even in the absence of additional carrier doping. In addition, ZnO and GaN based DMS materials are particularly attractive due to their compatibility with existing semiconductor heterostructure technology. Research in the ensuing years followed two main directions, i.e., the search (i) for new DMS materials displaying signatures of high-temperature ferromagnetic order (e.g. Gd-doped GaN [27], C-doped ZnO [28], and undoped HfO_2 [29]) and (ii) for the origin and control of the ferromagnetism in the most intensively studied materials. However, as the understanding of the magnetism in these materials increased, issues of irreproducibility and instability became increasingly evident. As the origin of the observed ferromagnetism became increasingly debated, a number of non-intrinsic sources of ferromagnetism were identified and became well documented: magnetic contamination [30–32], measurement artifacts [31,32], and formation of ferromagnetic precipitates (e.g. [33–35]). On the other hand, several comprehensive studies on carefully characterized materials with respect to phase purity found only paramagnetism (e.g. [36, 37]), antiferromagnetic interactions (e.g. [38–41]), or at best, ferromagnetic order with very low T_C (e.g. $T_C < 10$ K in Mn-doped GaN [42]).

The current status of DMS research can be divided between narrow- and wide-gap materials. *Narrow-gap* DMS materials such as $In_{1-x}Mn_xAs$

and $Ga_{1-x}Mn_xAs$ are widely accepted to exhibit intrinsic carrier-mediated ferromagnetism, but their Curie temperatures remain well below room temperature. *Wide-gap* DMS materials appear to exhibit ferromagnetic behavior at and above room temperature, but there is no consensus regarding the origin and the usefulness of such ferromagnetism. It follows that the major challenges facing the field can be summarized as: (1) in narrow-gap DMS, to increase the Curie temperature above the current record values (185 K in $Ga_{1-x}Mn_xAs$); (2) in wide-gap DMS, to understand the origin of the often observed high-temperature ferromagnetism and identify the conditions under which it can be easily reproduced.

1.3 Structure and magnetism of Mn-doped GaAs

High quality, high T_C, epitaxial $Ga_{1-x}Mn_xAs$ (zinblende structure) is typically grown using nonequilibrium low-temperature molecular beam epitaxy (LT-MBE). Thanks to developments in LT-MBE growth, the amount of Mn that can be incorporated in high quality $Ga_{1-x}Mn_xAs$ has been increased throughout the years up to $x \approx 0.12$ [10, 18]. This section reviews the current understanding of the structure and magnetism of $Ga_{1-x}Mn_xAs$, focusing on the aspects of interest for further increase in T_C.

1.3.1 Ferromagnetic order in $Ga_{1-x}Mn_xAs$

It has been demonstrated by photoemission [43] and optical studies [44] that Mn impurities in Ga sites provide both localized magnetic moments and itinerant holes, which are mutually coupled by a *p-d* exchange interaction. A model of exchange interaction between band carriers and localized moments was first proposed by Zener [45]. Dietl *et al.* proposed in 2000 a model of *p-d* Zener exchange in dilute magnetic semiconductors, in which the localized Mn $3d^5$ moments are ferromagnetically coupled via the $2p$ holes [20]. This long-range hole-mediated ferromagnetic interaction is counteracted by short-range antiferromagnetic superexchange, and T_C is determined by the competition between the two. This approach was shown to adequately describe the magnitudes of T_C and the strain-induced magnetic anisotropy [20].

1.3.2 Compensation by interstitial Mn

In agreement with the *p-d* Zener model, it has been experimentally established that the T_C of $Ga_{1-x}Mn_xAs$ increases with increasing Mn concen-

tration and hole concentration p [18]. More precisely, T_C increases with effective Mn concentration, which takes into account the balance between the fractions of Mn substituting for Ga (Mn_{Ga}) and on interstitial sites (Mn_I). While Mn_{Ga} provides both the localized magnetic moment and the itinerant hole that mediates the magnetic coupling, Mn_I has a two-fold compensating effect: magnetic, as Mn_I-Mn_{Ga} pairs couple antiferromagnetically, and electrical, since double donor Mn_I compensates Mn_{Ga} acceptors [18]. This implies that the effective Mn concentration is not the nominal Mn concentration x but roughly $x_{\text{eff}} = (x - x_I - x_{\text{pair}})$ where x_I is the concentration of interstitial Mn and x_{pair} corresponds to the fraction of those which form antiferromagneticaly coupled pairs with substitutional Mn (thus rendering them magnetically inactive). This also implies that the concentration of holes p is not equal to the nominal concentration x of Mn. Assuming that the double-donor level of Mn_I is ionized and that no other compensating defects are present, i.e. that each Mn_I donor compensates two Mn_{Ga} acceptors, the hole concentration is then $p = x - 2x_I$. As a consequence of this self-compensation, p and T_C do not monotonously follow the increase in nominal Mn concentration x, particularly in the high x regime ($x > 0.05$) [18].

The highest T_C and p values achieved in $Ga_{1-x}Mn_xAs$ are obtained after annealing around ∼200°C [46]. However, a significant fraction of the initially introduced Mn atoms still remains inactive [18, 46], i.e. $x_{\text{FM}} < x$ and $p < x$ after annealing, where x_{FM} is the concentration of Mn atoms contributing to the ferromagnetic component of the magnetization. Based on transport measurements, this partial activation by annealing was demonstrated to result from the out-diffusion of a compensating defect with low thermal stability, with an activation energy (E_a) of 0.7 eV [47]. Based on *ab initio* calculations yielding a similar activation energy for Mn_I [47], it became generally accepted that the low temperature diffuser was indeed interstitial Mn. This established the belief that pure substitutional Mn doping can be achieved by low-temperature (∼200°C) thermal annealing. Since then, attempts to increase T_C above room temperature have focused on increasing the Mn concentration that can be incorporated in $Ga_{1-x}Mn_xAs$. However, film growth development beyond $x \approx 0.10$ and of $T_C = 185$ K faces difficult technical challenges [14, 18].

In contrast to the relatively well established scenario of low thermal stability, there are reports in the literature which indicate that interstitial Mn is *not* removed by low temperature annealing. Although ion channeling measurements qualitatively detected a decrease of the Mn_I fraction after

annealing at 282 °C [48], they show that at least a significant fraction actually persisted, i.e, almost 100 °C above the temperature at which Mn_I would become mobile if it was the low temperature diffuser. Moreover, using secondary ion-mass spectrometry (SIMS), the out-diffusion of Mn in $Ga_{1-x}Mn_xAs$ was found to be almost negligible below 400°C [49], with a diffusion coefficient at 200°C that is at least four orders of magnitude smaller than the one derived for the out-diffusion of the donor defect in [47].

Knowing whether interstitial Mn in $Ga_{1-x}Mn_xAs$ out-diffuses or not upon low temperature (∼200°C) annealing is of extreme importance for the development of $Ga_{1-x}Mn_xAs$. If the interstitial Mn fraction actually remains in the matrix after annealing, it may still be possible to convert it to substitutional (thus achieving full activation of the nominal Mn concentration x) via an alternative post-processing method. Since it is believed that a T_C of 300 K can be achieved with $x \approx 0.10$ of purely substitutional Mn [18], such post-growth processing would allow for the realization of room temperature ferromagnetism in $Ga_{1-x}Mn_xAs$ without further film growth development.

1.3.3 Lattice site of interstitial Mn

Understanding the thermal stability and diffusion behavior of interstitial Mn starts with identifying which lattice site it occupies in GaAs. There are several interstitial sites in the zincblende structure of GaAs: tetrahedral (T), bond centered (BC), anti-bonding (AB) among others (c.f. Article III). Experimental techniques commonly used to identify lattice sites of impurities in crystalline solids are either based on channeling of charged particles (ions or electrons) or on probing the atomic environment of the impurity atom, e.g. in X-ray absorption fine structure (XAFS) techniques.

The literature on lattice location of Mn in GaAs is contradictory. The first reports are on pure Ga-substitutional incorporation (by XAFS [50]) and mixed Ga-substitutional (majority) and T interstitial (minority) occupancy (by ion channeling [48] and XAFS [51]). There are two inequivalent T sites in zincblende GaAs: one coordinated by four As neighbors (T_{As}), the other by Ga neighbors (T_{Ga}) (c.f. Article III). More recently, XAFS experiments confirmed the mixed occupancy and identified the T_{Ga} interstitial site [52, 53]. However, on the theoretical side, *ab initio* calculations yielded an energy 0.35 eV lower for Mn in T_{As} sites compared to T_{Ga} [47], which is consistent with the expectation of having the Mn cations (substitutional and interstitial) coordinated by four As anions. This inconsistency

among XAFS experiments, and of these with theory, is very likely a consequence of the limitations of the technique in distinguishing the chemical nature of the neighbors with a small difference in atomic number, which is the case for Ga and As. Establishing the lattice location of Mn in GaAs will require the use of a technique which can unambiguously distinguish the two T sites.

1.3.4 Mn aggregation and MnAs phase segregation

As mentioned above, annealing $Ga_{1-x}Mn_xAs$ at $\sim$200°C generally increases T_C. However, comparing the T_C after thermal annealing at temperatures between 160°C and 220°C, it was found that T_C actually decreases with increasing annealing temperature [14]. Increasing even more the annealing temperature ($>$ 280°C) eventually leads to an actual decrease of T_C. This indicates the existence of a second process, with an activation energy slightly above that of the out-diffusion of the compensating defect. It has been suggested that this second process is related to Mn aggregation (or segregation). It is however unclear what type of aggregation it is, i.e. whether it is only chemical or also structural. Ion-channeling experiments have shown that part of the substitutional Mn converts to a random fraction at 282°C, most likely due to cluster formation [48]. This indicates that phase segregation starts already at relatively low temperatures. On the other hand, transmission electron microscopy (TEM) experiments [54] have shown that upon thermal annealing at 500°C, only Mn-rich zincblende (Mn,Ga)As clusters ($\sim$ 3 nm) are formed which are coherent with the GaAs matrix (i.e. only chemical segregation occurs). Increasing the annealing temperature up to 600°C leads to the formation of larger (10-20 nm) MnAs secondary phases.

1.4 Structure and magnetism of transition-metal doped ZnO and GaN

This section reviews the current understanding of wide-gap DMS materials focusing on the most intensively studied wide-gap hosts, ZnO and GaN, doped with the most common magnetic impurities, the 3*d* transition metals Mn, Fe and Co.

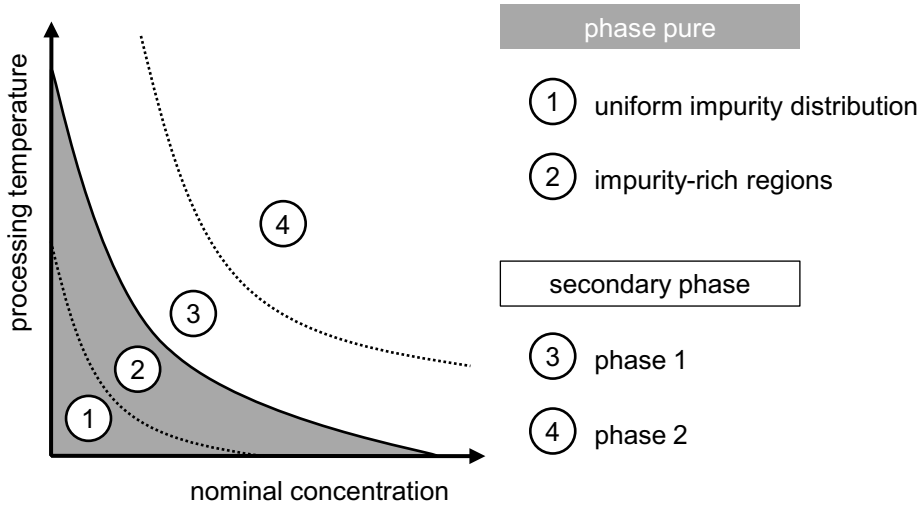

Figure 1.4: Schematic representation of the structural phase diagram of a DMS material.

1.4.1 Structural phase diagram

Both ZnO and GaN crystallize in the wurtzite (hexagonal) structure, where the cations (Zn and Ga) are tetrahedrally coordinated by the anions (O and N) and vice versa. Although less commonly, GaN can also be "forced" into the metastable zincblende (cubic) structure, when epitaxially grown on zincblende substrates such as GaAs or 3C-SiC.

ZnO and GaN can be doped with transition metal impurities either during growth or by ion implantation after growth. The resulting material has general formula $C_{1-x}M_xA$, where C is the cation (Zn in ZnO and Ga in GaN), M is the transition-metal with concentration x and A is the anion (O in ZnO and N in GaN). Typical transition metal concentrations are between 0.01 (1%) and 0.1 (10%). Common methods for epitaxial thin film growth include, for example, pulsed laser deposition (PLD), sputtering and chemical vapor deposition (CVD) for ZnO and molecular beam epitaxy (MBE) and metalorganic vapor phase epitaxy (MOVPE) for GaN.

A generic structural phase diagram of transition-metal doped ZnO or GaN is represented in Fig. 1.4. The gray area corresponds to the phase-pure region, where the transition metal impurities substitute one of the host's constituents, maintaining the crystal structure of the host. For example, for ZnO doped with an atomic concentration x of Co impurities

substituting Zn atoms, the phase-pure region would correspond to wurtzite $Zn_{1-x}Co_xO$. The impurities may be randomly distributed i.e. x is uniform across the material [region (1)] or, for sufficiently high concentrations or precessing temperatures, aggregate in impurity-rich regions where the local concentration of Co impurities is higher than x [region (2)]. For sufficiently high processing temperatures or concentration (white region), the transition metal impurities may segregate into small precipitates of a secondary phase. Depending on various factors,[1] different secondary phases may form [regions (3) and (4)].

1.4.1.1 Impurity lattice sites in the phase-pure region

In the phase-pure region of the phase diagram, impurities may substitute atoms of the host or occupy interstitial sites. The lattice sites occupied by the transition metal impurities then determine the magnetic behavior of the material at two levels. First, by determining the impurity's electronic structure and crystal field, the occupied lattice site defines the localized magnetic moment and its single-ion magnetism (c.f. section 1.4.2.3). Second and more importantly in the context of ferromagnetic DMS, by determining also the impurity's position in the host band structure, it determines its electrical character and the type and strength of the magnetic interactions between localized magnetic moments, i.e. the collective magnetism (c.f. section 1.4.2.1).

The current understanding of the lattice location of transition-metal doped GaN and ZnO is quite different from that of Mn-doped GaAs, where Mn is known to occupy both Ga-substitutional and T interstitial sites. It is generally accepted that $3d$ transition metals, including Mn, Fe and Co, occupy *only* cation substitutional sites, as expected from the chemical similarities between the impurities and the host cations. This has been confirmed experimentally, mostly based on X-ray absorption fine structure (XAFS) experiments but also on ion channeling experiments, and appears to be independent of the doping method, i.e. either during growth (e.g. [55–67]) or by ion implantation (e.g. [68–71]).

Although this cation substitution by transition metals in wide-gap semiconductors is relatively well established, some observations do not completely conform to it. In ZnO, X-ray absorption near-edge structure spectroscopy (XANES) [57, 72] and X-ray photoelectron spectroscopy (XPS)

[1] Including not only processing temperature and impurity concentration but also others such as the preparation method.

[73] experiments have shown that Mn impurities can be incorporated in ZnO with charge states of up to 4+. However, Zn-substitutional Mn is expected to have a 2+ charge state with the 2+/3+ and 3+/4+ donor levels below the valence band maximum (thus not ionized) [74]. Similarly, X-ray absorption near-edge structure spectroscopy (XANES) experiments have shown that the average charge state of Mn in wurtzite GaN is not exactly 3+, which is the expected neutral state of Mn impurities in Ga sites, but 3.3+. These results can be seen to indicate that minority fractions may occupy non-cation-substitutional sites, with higher charges states. In fact, in zincblende GaN, the evidence that Mn impurities occupy non-cation-substitutional sites is even more convincing. It has been reported based on X-ray absorption near-edge structure XANES that, in $Ga_{1-x}Mn_xN$ with $x = 0.025$, a small fraction of the Mn impurities are located in interstitial sites, forming dimers with Ga-substitutional impurities [66]. In another study, X-ray absorption fine structure (EXAFS) experiments detected a remarkably high fraction of 75% of the Mn impurities in anion (N) substitutional sites [75].

Clarifying the lattice location of the transition metal impurities in ZnO and GaN is of fundamental importance for the DMS field. Not only does the magnetic behavior of the impurities directly depend on the lattice sites they occupy, transition metal impurities in lattice sites other than cation-substitutional may behave as self-compensating defects. In the case of Mn-doped GaN, for example, interstitial or N-substitutional Mn is expected to act as donor and therefore compensate (deep) acceptor Ga-substitutional Mn, changing its charge state from Mn_{Ga}^{3+} to Mn_{Ga}^{2+}. Because the type of magnetic interactions between Ga-substitutional Mn moments is determined by the Mn charge state, i.e. ferromagnetic for Mn_{Ga}^{3+} (although with a very low T_C) and antiferromagnetic for Mn_{Ga}^{2+} (c.f. section 1.4.2.3), a non-Ga-substitutional fraction, even if minority, may have a dramatic effect on the magnetic order of Mn-doped GaN.

1.4.1.2 Transition-metal aggregation and phase segregation

Increasing the processing temperature (of growth, implantation or annealing) increases the mobility of the transition metal impurities, and consequently the probability of segregation. This segregation may be only chemical, i.e. the crystal structure is maintained and only the local impurity concentration varies across the material, alternating between impurity-rich and impurity-poor regions [region (2) in Fig. 1.4]. This has been observed,

for example in Co-doped ZnO [56] and Mn-doped GaN [76]. In DMS literature, this type of chemical segregation is generally referred to as *spinodal decomposition*, regardless of the aggregation mechanism. For sufficiently high concentration and temperature, phase segregation may occur, i.e. the impurities precipitate in nanocomposites with a well defined interface with the host structure [regions (3) and (4) in Fig. 1.4]. Phase segregation has been observed, for example, in ZnO doped with Mn [69, 77], Fe [34, 78–80] and Co [33, 81], as well as GaN doped with Mn [75], Fe [35] and Co [82]. The segregated phases observed in ZnO and GaN doped with Mn, Fe and Co, are either elemental metal clusters, e.g. α-Fe (bcc) or hcp Co, or precipitates of a binary (e.g. Mn_2O_3) or ternary (e.g. $ZnFe_2O_4$) compounds involving the host constituents. A particularly interesting example of phase segregation is Fe-implanted ZnO, in which the Fe impurities may segregate both in metal clusters and compound precipitates, depending on the annealing conditions. Zhou *et al.* [34, 78–80] have shown that sufficiently high processing temperatures and Fe concentrations lead to the formation of α-Fe clusters [what would be region (3) in Fig. 1.4]. At even higher temperatures and for sufficiently long annealing times, these α-Fe clusters are oxidized and then converted to precipitates of the spinel ferrite $ZnFe_2O_4$ which are crystallographically oriented with respect to the ZnO host [what would be region (4) in Fig. 1.4].

Impurity segregation is of fundamental importance in the context of DMS materials. In fact, when impurity segregation occurs, the material is no longer considered a dilute magnetic semiconductor (c.f. section 1.1).

1.4.2 Magnetism

Probably the most important parameter for magnetic order in *dilute* magnetic systems is the range of the magnetic interactions: short-range interactions only produce order at high concentrations of magnetic impurities (high x); long-range interactions produce magnetic order for more diluted systems (lower x) but require a mediation mechanism.

Short-range interactions Since (at least) the majority of the transition-metal impurities occupy cation-substitutional sites (section 1.4.1.1), the interactions with the shortest range are those between nearest-cation-neighbors via a superexchange bond, i.e. via the anion (O or N) $2p$ states. Magnetic order occurs above the percolation threshold ($x_p = 0.20$ for wurtzite ZnO or GaN [83]), where nearest-cation-neighbor paths link the transition-metal cations throughout the crys-

tal. However, most reports of room temperature ferromagnetism in transition-metal doped ZnO and GaN fall well below the percolation threshold ($x < 0.10 < x_p = 0.20$). In this concentration range, most of the transition-metal cations are either isolated or in small complexes, i.e. dimers, trimers etc. For example, the concentration of isolated ions and dimers in wurtzite ZnO or GaN is given by $x_{\text{isolated}} = x(1-x)^{12}$ and $x_{\text{dimers}} = 12x^2(1-x)^{18}$, respectively [84].

Long-range interactions According to the established theories of magnetism, long-range interactions are mediated by itinerant carriers, i.e. conduction electrons in RKKY exchange in metals, and valence-band holes in *p-d* Zener exchange in narrow-gap DMS systems (section 1.3.1). Indeed, one of the major contributions to the boom in the wide-gap DMS field was the prediction of ferromagnetism above room temperature in Mn-doped ZnO and GaN, based on *p-d* Zener exchange [20]. However, this prediction was based on the condition of high concentration of valence-band holes ($p \gtrsim 3.5 \times 10^{20}$ cm^{-3}). This condition has not been met so far because of the difficulties in producing highly *p*-type ZnO and GaN.

1.4.2.1 High temperature ferromagnetism

Ferromagnetism at room temperature was first reported in 2001 in TiO_2 doped with 7% Co and, after that, in virtually any of the attempted combinations of wide-gap semiconductor hosts and 3*d* transition metals (cf. e.g. the reviews [21–24]). These results are remarkably surprising for several reasons. The magnetic order is ferromagnetic, whereas superexchange in transition-metal oxides and nitrides is typically antiferromagnetic. In any case, magnetic order appears far below x_p, which implies that the magnetic interactions are long-range. However, most of the reports are in insulator materials, i.e. in the absence of free carriers to mediate such long-range interactions. Moreover, the ferromagnetic order persists above room temperature, i.e. well above any other type of dilute magnetic materials at this level of dilution.

This unexpected high-temperature ferromagnetism in wide-gap DMS was initially regarded with skepticism and the belief that it was associated with segregated magnetic phases or measurement artifacts. The main criticism was based on the general irreproducibility that characterized these reports, with different groups claiming existence and absence of ferromagnetism in virtually the same materials. It did not take long, however, for

this skepticism to be silenced by hundreds of reports claiming the observation of intrinsic ferromagnetism. Together with the enormous volume of experimental research, the theory of dilute magnetic semiconductors also evolved at different fronts. Following the prediction of room-temperature ferromagnetism in highly *p*-type Mn-doped ZnO and GaN based on the *p-d* Zener model, a long series of *ab initio* calculations found a ferromagnetic ground state for dilute transition-metal spins, even in the absence of band carriers (c.f. [85] for a recent review). However, given the difficulties of density functional theory (DFT) in reproducing even basic material parameters of wide-gap materials, such as the bandgap itself, these predictions in the context of magnetism (considerably more complex) were regarded with caution. In the following years a number of models emerged, which were fundamentally different from that of *p-d* Zener exchange. Aiming at describing the observed room temperature ferromagnetism while at the same time accounting for the difficulties in achieving experimental reproducibility, these models share one common characteristic: the presence of lattice defects other than the magnetic impurities, e.g. vacancies, self-interstitials and grain boundaries. Because the type and concentration of such defects strongly depend on the growth methods and conditions and are in general difficult to monitor and control, defect-related order mechanisms could in principle explain the difficulties in reproducing the ferromagnetic properties. These models can be divided in four types:

Bound magnetic polaron (BMP) model (Coey *et. al* [86]), where the localized magnetic moments of the transition-metal impurities interact with electrons associated with defects which form an impurity band. Since these defect electrons occupy large orbits, each defect can interact with several dopant moments and form a magnetic polaron. Ferromagnetism results from the percolation of such polarons. The concept of magnetic polarons was originally proposed in the context of magnetic semiconductors by Kasuya *et al.* [87] such as Eu-Chalcogenides, and later extended to the context of dilute magnetic semiconductors such as $Cd_{1-x}Mn_xSe$ and $Cd_{1-x}Mn_xTe$ (Dietl *et al.* [88] and Golnik *et al.* [89]). However, the exchange energy density necessary to produce high-temperature ferromagnetism in a wide-gap DMS via a BMP mechanism (at a few % of transition-metal doping) corresponds to a magnetic exchange much stronger than that observed in the strongest known ferromagnetic materials [90].

A variant of the BMP model (Panguluri *et. al* [91]) in which no mag-

netic impurities are required; the localized moments arise from electrons associated with defects and are coupled via an impurity or conduction band.

Spin-split impurity band (SIB) model (Edwards and Katsnelson [92]), which is based on a local density of states associated with defects where the density of states at the Fermi level is sufficient to satisfy the Stoner criterion.

Charge-transfer ferromagnetism (CTF) model (Coey *et. al* [93,94]) is also a Stoner-like mechanism. It requires two distinct types of defects, one that creates a narrow impurity band and another to play the role of charge reservoir. If both types of defects are present, electrons can be transfered to or from the reservoir until the filling level of the impurity band satisfies the spontaneous spin-split criterion. In dilute magnetic semiconductors, the impurity band can originate, for example, at grain boundaries, while mixed-valence impurities may behave as charge reservoirs.

With the development of these models, some experimental evidence has emerged which, although indirectly, supports the picture of defect-related ferromagnetism: by varying the defect concentration, it is in some cases possible to turn the ferromagnetic behavior "on" and "off" [95–98].

1.4.2.2 Non-intrinsic ferromagnetism

With a persistent irreproducibility regarding the conditions under which ferromagnetic order could be observed, the initial skepticism regained strength in the mid 2000s. In fact, some of the most active groups in reporting room temperature ferromagnetism in the first half of the decade, later became some of the most convincing in demonstrating its absence in carefully characterized materials. It is fair to say that no direct evidence has been found that wide-gap DMS materials are intrinsically ferromagnetic at room temperature: no magnetoresistance has been observed at room temperature; there are no clear signs of an anomalous Hall effect either; and none of these reports of ferromagnetism lead to the demonstration of a device structure working at room temperature. On the other hand, a number of sources of non-intrinsic ferromagnetism were identified and became well documented, namely various experimental artifacts and different forms of non-uniformity of the magnetic impurity distribution.

Experimental artifacts. The large majority of the reports of high temperature ferromagnetism in DMS materials is based on the observation of a magnetic hysteresis. However, the magnitude of these hystereses typically falls within the range where experimental artifacts may also contribute to ferromagnetic-like signals. In this context, experimental artifacts can be distinguished between (1) setup-related artifacts leading to the misidentification of the magnetic state of a sample [31, 32] and (2) magnetic contamination, i.e. magnetic material which is accidentally incorporated in the sample bulk or deposited on its surface and, therefore, is not accounted for in its nominal composition [30–32]. These experimental artifacts are investigated and described in detail in Article I (section 3.4).

Non-uniform impurity distribution. Transition-metal aggregation and segregation (c.f. section 1.4.1.2) may also result in non-intrinsic ferromagnetic-like behavior. If the segregated secondary phase is ferromagnetic or ferrimagnetic, the system composed of these nanoprecipitates embedded in the semiconductor host will show superparamagnetic behavior, which may be perceived as ferromagnetism. Superparamagnetic secondary phases have been observed for most $3d$ transition-metals in ZnO and GaN, in particular Mn [69, 75, 77], Fe [34, 35, 78–80] and Co [33, 81, 82]. The case of simple impurity aggregation without phase segregation (as in spinodal decomposition) is somewhat less obvious. By locally decreasing the distance between nearest (localized) moments, impurity aggregation may enhance the magnetic interactions within these impurity-rich regions and thus produce magnetic order at very low nominal concentrations. This has been suggested to be the origin of the ferromagnetism observed, for example, in Co-doped ZnO [56] and Mn-doped GaN [76]. Although the $3d$ transition metals in oxides and nitrides tend to couple antiferromagnetically by superexchange, there may be uncompensated spins in particular antiferromagnetic spin-arrangements which can add up to a nonvanishing net moment. Note that a poor crystalline quality may facilitate aggregation and phase segregation: transition-metal impurities may decorate or diffuse along extended defects such as dislocations or grain boundaries. This could explain the inverse correlation between crystalline quality and the appearance of high-temperature ferromagnetism in wide-gap DMS materials.

ion	host	S	D [meV]	$g_{\parallel}$	$g_{\perp}$	Ref.
Fe^{3+}	ZnO	5/2	-0.0074	2.0062	2.0062	[100]
Mn^{2+}	ZnO	5/2	-0.0027	2.0016	2.0016	[101]
Fe^{3+}	GaN	5/2	-0.0093	1.990	1.997	[102]
Mn^{3+}	GaN	2	0.27	1.91	1.98	[103]
Co^{2+}	ZnO	3/2	0.341	2.2384	2.2768	[104]
Co^{2+}	ZnO	3/2	0.342	2.238	2.2755	[105]

Table 1.1: Experimentally determined parameters of the effective spin Hamiltonian (1.1) for Mn, Fe and Co ions in ZnO and GaN.

1.4.2.3 Paramagnetism, antiferromagnetic interactions and low-temperature ferromagnetism

In the last few years, some of the most influential groups in the DMS field have focused on studying the phase-pure region of the phase diagram of the most popular wide-gap DMS materials, namely Co- and Mn-doped ZnO and Mn-doped GaN. However, none of these carefully characterized materials have shown high-temperature ferromagnetism. Instead, only paramagnetism [36, 37, 99], nearest-cation-neighbor antiferromagnetic interactions [38–41, 99]), or at best, ferromagnetic order with very low T_C (e.g. $T_C < 10$ K in Mn-doped GaN [42]) were observed.

Paramagnetism. In the low concentration regime, isolated transition-metal impurities are paramagnetic. Since ZnO and GaN are wurtzite materials, transition-metal impurities in substitutional sites are subject to a trigonal crystal field. Combined with spin-orbit interaction, this anisotropic crystal field induces a strong magnetic anisotropy, which can be described by a zero-field splitting of the fundamental state and by an anisotropic effective g-factor in an effective spin Hamiltonian H_s of the form

$$H_s = \mu_B g_{\parallel} H_z S_z + \mu_B g_{\perp} (H_x S_x + H_y S_y) + D S_z^2 \,, \tag{1.1}$$

where S is the spin quantum number and D describes the zero-field splitting and $g_{\parallel}$ and $g_{\perp}$ are the effective g-factors for directions of magnetic field parallel and perpendicular to the wurtzite c-axis, respectively. This effective spin Hamiltonian contains only the terms of more importance in

the description of the magnetization. More detailed spin Hamiltonians link the phenomenological parameters of (1.1) with the properties of the crystal and magnetic ions, which may include, for example, hyperfine interactions and Jahn Teller effects. Some published values of the parameters of the effective spin-Hamiltonian (1.1) are given in Table 1.1 for Mn, Fe and Co ions in ZnO and GaN. Magnetic ions with $S = 5/2$ (Mn^{2+} and Fe^{3+}) have two orders of magnitude smaller zero-field splitting than other spin configurations with $S = 3/2$ and $S = 2$. The g-factors for $S = 5/2$ spin configuration are also nearly independent of the direction of magnetic field, and the values of $g_{\|}$ and $g_{\perp}$ are close to 2. The magnetization of these $S = 5/2$ ions remains almost isotropic even in the strongly anisotropic wurtzite structure and can be described by a Brillouin function. For ions with $S = 2$ (Mn^{3+}, Fe^{2+} and Co^{3+}) and $S = 3/2$ (Co^{2+}), the zero field splitting is of the order of 0.3 meV, which, as shown in section 4.5.2.2 induces a strong magnetic anisotropy which requires a somewhat more complex description.

Nearest-cation-neighbor antiferromagnetic interactions For sufficiently high concentrations, the transition-metal paramagnetic moments are perturbed by nearest-cation-neighbor antiferromagnetic interactions (e.g. in Co-doped ZnO [39–41], Mn-doped ZnO [99] and Mn-doped GaN [38]), which can be inferred from the magnetization data as a decrease in effective moment per transition-metal atom. This is consistent with the antiferromagnetic nature of the corresponding oxides (MnO and CoO) and nitrides (MnN), with Néel temperatures of 116 K, 291 K [106] and 650 K [107] respectively, and demonstrates that the magnetic interactions between the localized $3d$ moments in nearest-cation-neighbor sites are dominated by indirect superexchange via the anion (O or N) $2p$ states.

The case of Mn-doped GaN is particularly interesting. The type of magnetic interactions between Ga-substitutional Mn moments changes between ferromagnetic and antiferromagnetic depending on the Mn charge state. Under stringent growth conditions minimizing the formation of compensating defects, Mn impurities are incorporated as Mn^{3+} ($3d^4$) moments which couple ferromagnetically ($T_C < 10$ K) [42]. More commonly, such stringent growth conditions are not satisfied and compensating defects are formed, e.g. N vacancies (donors). The Mn impurities are then incorporated as compensated Mn^{2+} ($3d^5$) moments and only nearest-cation-neighbor antiferromagnetic interactions are observed [38].

1.5 Current goals and challenges

Based on sections 1.3 and 1.4, the major challenges/goals currently facing the DMS field can be divided between narrow-gap and wide-gap DMS and summarized as follows.

In narrow-gap DMS:

I - To increase the Curie temperature above the current record value of 185 K in Mn-doped GaAs. This may be achieved by increasing spin (Mn) and hole densities, which is directly related to the balance between the Mn fractions in substitutional and interstitial sites.

In wide-gap DMS:

II - To find intrinsic ferromagnetism above room temperature in a wide-gap DMS which gathers the consensus of the magnetism community, i.e. in which phase segregation and experimental artifacts can be undeniably ruled out. Among the numerous combinations of materials and preparation methods this prototypical DMS could be searched for, the emerging picture of defect-related ferromagnetism points towards disordered systems.

III - To establish the understanding of the magnetism in the phase-pure region of the DMS phase diagram. This involves a detailed investigation of the lattice sites occupied by the transition-metal impurities, of how uniformly they are distributed across the host material, and of the type and strength of the magnetic interactions in representative impurity-host combinations.

Bibliography

[1] H. Ohno, "Making nonmagnetic semiconductors ferromagnetic," *Science*, vol. 281, p. 951, 1998.

[2] I. Zutic, J. Fabian, and S. Das Sarma, "Spintronics: Fundamentals and applications," *Rev. Mod. Phys.*, vol. 76, p. 323, 2004.

[3] D. D. Awschalom and M. E. Flatté, "Challenges for semiconductor spintronics," *Nat. Phys.*, vol. 3, p. 153, 2007.

[4] J. K. Furdyna, "Diluted magnetic semiconductors," *J. Appl. Phys.*, vol. 64, p. R29, 1988.

[5] G. Medvedkin, T. Ishibashi, T. Nishi, K. Hayata, Y. Hasegawa, and K. Sato, "Room temperature ferromagnetism in novel diluted magnetic semiconductor $Cd_{1-x}Mn_xGeP_2$," *Jpn. J. Appl. Phys. Part 2 - Lett.*, vol. 39, p. L949, 2000.

[6] A. Haury, A. Wasiela, A. Arnoult, J. Cibert, S. Tatarenko, T. Dietl, and Y. dAubigne, "Observation of a ferromagnetic transition induced by two-dimensional hole gas in modulation-doped CdMnTe quantum wells," *Phys. Rev. Lett.*, vol. 79, p. 511, 1997.

[7] D. Ferrand, J. Cibert, C. Bourgognon, S. Tatarenko, A. Wasiela, G. Fishman, A. Bonanni, H. Sitter, S. Kolesnik, J. Jaroszyski, A. Barcz, and T. Dietl, "Carrier-induced ferromagnetic interactions in p-doped $Zn_{1-x}Mn_xTe$ epilayers," *J. Cryst. Growth*, vol. 214, p. 387, 2000.

[8] H. Ohno and F. Matsukura, "A ferromagnetic III-V semiconductor: (Ga,Mn)As," *Solid State Commun.*, vol. 117, p. 179, 2001.

[9] H. Ohno, H. Munekata, T. Penney, S. Vonmolnar, and L. L. Chang, "Magnetotransport properties of p-type (In,Mn)As diluted magnetic III-V semiconductors," *Phys. Rev. Lett.*, vol. 68, p. 2664, 1992.

[10] H. Ohno, A. Shen, F. Matsukura, A. Oiwa, A. Endo, S. Katsumoto, and Y. Iye, "(Ga,Mn)As: A new diluted magnetic semiconductor based on GaAs," *Appl. Phys. Lett.*, vol. 69, p. 363, 1996.

[11] S. Ghosh and P. Bhattacharya, "Surface-emitting spin-polarized $In_{0.4}Ga_{0.6}As$/GaAs quantum-dot light-emitting diode," *Appl. Phys. Lett.*, vol. 80, p. 658, 2002.

[12] D. Chiba, F. Matsukura, and H. Ohno, "Electric-field control of ferromagnetism in (Ga,Mn)As," *Appl. Phys. Lett.*, vol. 89, p. 162505, 2006.

[13] K. C. Hall, J. P. Zahn, A. Gamouras, S. March, J. L. Robb, X. Liu, and J. K. Furdyna, "Ultrafast optical control of coercivity in GaMnAs," *Appl. Phys. Lett.*, vol. 93, p. 032504, 2008.

[14] M. Wang, R. P. Campion, A. W. Rushforth, K. W. Edmonds, C. T. Foxon, and B. L. Gallagher, "Achieving high Curie temperature in (Ga,Mn)As," *Appl. Phys. Lett.*, vol. 93, p. 132103, 2008.

[15] V. Novak, K. Olejnik, J. Wunderlich, M. Cukr, K. Vyborny, A. W. Rushforth, K. W. Edmonds, R. P. Campion, B. L. Gallagher, J. Sinova, and T. Jungwirth, "Curie point singularity in the temperature derivative of resistivity in (Ga,Mn)As," *Phys. Rev. Lett.*, vol. 101, p. 077201, 2008.

[16] T. Schallenberg and H. Munekata, "Preparation of ferromagnetic (In,Mn)As with a high Curie temperature of 90 K," *Appl. Phys. Lett.*, vol. 89, p. 042507, 2006.

[17] T. Dietl, D. D. Awschalom, M. Kaminska, and H. Ohno, *Semiconductors and Semimetals*. Elsevier, 2008.

[18] T. Jungwirth, K. Y. Wang, J. Masek, K. W. Edmonds, J. Konig, J. Sinova, M. Polini, N. A. Goncharuk, A. H. MacDonald, M. Sawicki, A. W. Rushforth, R. P. Campion, L. X. Zhao, C. T. Foxon, and B. L. Gallagher, "Prospects for high temperature ferromagnetism in (Ga,Mn)As semiconductors," *Phys. Rev. B*, vol. 72, p. 165204, 2005.

[19] Y. Matsumoto, M. Murakami, T. Shono, T. Hasegawa, T. Fukumura, M. Kawasaki, P. Ahmet, T. Chikyow, S. Koshihara, and H. Koinuma, "Room-temperature ferromagnetism in transparent transition metal-doped titanium dioxide," *Science*, vol. 291, p. 854, 2001.

[20] T. Dietl, H. Ohno, F. Matsukura, J. Cibert, and D. Ferrand, "Zener model description of ferromagnetism in zinc-blende magnetic semiconductors," *Science*, vol. 287, pp. 1019–1022, 2000.

[21] S. J. Pearton, C. R. Abernathy, D. P. Norton, A. F. Hebard, Y. D. Park, L. A. Boatner, and J. D. Budai, "Advances in wide bandgap materials for semiconductor spintronics," *Mater. Sci. Eng. R-Rep.*, vol. 40, p. 137, 2003.

[22] W. Prellier, A. Fouchet, and B. Mercey, "Oxide-diluted magnetic semiconductors: a review of the experimental status," *J. Phys.-Condes. Matter*, vol. 15, p. R1583, 2003.

[23] S. J. Pearton, W. H. Heo, M. Ivill, D. P. Norton, and T. Steiner, "Dilute magnetic semiconducting oxides," *Semicond. Sci. Technol.*, vol. 19, p. R59, 2004.

[24] C. Liu, F. Yun, and H. Morkoc, "Ferromagnetism of ZnO and GaN: A review," *J. Mater. Sci.-Mater. Electron.*, vol. 16, p. 555, 2005.

[25] K. Sato and H. Katayama-Yoshida, "Material design of gan-based ferromagnetic diluted magnetic semiconductors," *Jpn. J. Appl. Phys.*, vol. 40, p. L485, 2001.

[26] K. Sato and H. Katayama-Yoshida, "First principles materials design for semiconductor spintronics," *Semicond. Sci. Technol.*, vol. 17, p. 367, 2002.

[27] S. Dhar, O. Brandt, M. Ramsteiner, V. F. Sapega, and K. H. Ploog, "Colossal magnetic moment of Gd in GaN," *Phys. Rev. Lett.*, vol. 94, p. 037205, 2005.

[28] H. Pan, J. B. Yi, L. Shen, R. Q. Wu, J. H. Yang, J. Y. Lin, Y. P. Feng, J. Ding, L. H. Van, and J. H. Yin, "Room-Temperature Ferromagnetism in Carbon-Doped ZnO," *Phys. Rev. Lett.*, vol. 99, p. 127201, 2007.

[29] M. Venkatesan, C. B. Fitzgerald, and J. M. D. Coey, "Unexpected magnetism in a dielectric oxide," *Nature*, vol. 430, p. 630, 2004.

[30] D. W. Abraham, M. M. Frank, and S. Guha, "Absence of magnetism in hafnium oxide films," *Appl. Phys. Lett.*, vol. 87, p. 252502, 2005.

[31] A. Ney, T. Kammermeier, V. Ney, K. Ollefs, and S. Ye, "Limitations of measuring small magnetic signals of samples deposited on a diamagnetic substrate," *J. Magn. Magn. Mater.*, vol. 320, p. 3341, 2008.

[32] M. A. Garcia, E. Fernandez Pinel, J. de la Venta, A. Quesada, V. Bouzas, J. F. Fernandez, J. J. Romero, M. S. Martin Gonzalez, and J. L. Costa-Kramer, "Sources of experimental errors in the observation of nanoscale magnetism," *J. Appl. Phys.*, vol. 105, p. 013925, 2009.

[33] S. Zhou, K. Potzger, J. von Borany, R. Grotzschel, W. Skorupa, M. Helm, and J. Fassbender, "Crystallographically oriented Co and Ni nanocrystals inside ZnO formed by ion implantation and postannealing," *Phys. Rev. B*, vol. 77, p. 035209, 2008.

[34] S. Zhou, K. Potzger, G. Talut, H. Reuther, J. von Borany, R. Groetzschel, W. Skorupa, M. Helm, J. Fassbender, N. Volbers, M. Lorenz, and T. Herrmannsdoerfer, "Fe-implanted ZnO: Magnetic precipitates versus dilution," *J. Appl. Phys.*, vol. 103, p. 023902, 2008.

[35] A. Bonanni, A. Navarro-Quezada, T. Li, M. Wegscheider, Z. Matej, V. Holy, R. T. Lechner, G. Bauer, M. Rovezzi, F. D'Acapito, M. Kiecana, M. Sawicki, and T. Dietl, "Controlled Aggregation of Magnetic Ions in a Semiconductor: An Experimental Demonstration," *Phys. Rev. Lett.*, vol. 101, p. 135502, 2008.

[36] W. Stefanowicz, D. Sztenkiel, B. Faina, A. Grois, M. Rovezzi, T. Devillers, F. d'Acapito, A. Navarro-Quezada, T. Li, R. Jakiela, M. Sawicki, T. Dietl, and A. Bonanni, "Structural and paramagnetic properties of dilute $Ga_{1-x}Mn_xN$," *Phys. Rev. B*, vol. 81, p. 235210, 2010.

[37] A. Ney, T. Kammermeier, K. Ollefs, S. Ye, V. Ney, T. C. Kaspar, S. A. Chambers, F. Wilhelm, and A. Rogalev, "Anisotropic paramagnetism of Co-doped ZnO epitaxial films," *Phys. Rev. B*, vol. 81, p. 054420, 2010.

[38] S. Granville, B. J. Ruck, F. Budde, H. J. Trodahl, and G. V. M. Williams, "Nearest-neighbor Mn antiferromagnetic exchange in $Ga_{1-x}Mn_xN$," *Phys. Rev. B*, vol. 81, p. 184425, 2010.

[39] A. Ney, K. Ollefs, S. Ye, T. Kammermeier, V. Ney, T. C. Kaspar, S. A. Chambers, F. Wilhelm, and A. Rogalev, "Absence of Intrinsic Ferromagnetic Interactions of Isolated and Paired Co Dopant Atoms in $Zn_{1-x}Co_xO$ with High Structural Perfection," *Phys. Rev. Lett.*, vol. 100, p. 157201, 2008.

[40] P. Sati, C. Deparis, C. Morhain, S. Schafer, and A. Stepanov, "Antiferromagnetic interactions in single crystalline $Zn_{1-x}Co_xO$ thin films," *Phys. Rev. Lett.*, vol. 98, p. 137204, 2007.

[41] Q. Xu, S. Zhou, D. Marko, K. Potzger, J. Fassbender, M. Vinnichenko, M. Helm, H. Hochmuth, M. Lorenz, M. Grundmann, and H. Schmidt, "Paramagnetism in Co-doped ZnO films," *J. Phys. D-Appl. Phys.*, vol. 42, p. 085001, 2009.

[42] E. Sarigiannidou, F. Wilhelm, E. Monroy, R. M. Galera, E. Bellet-Amalric, A. Rogalev, J. Goulon, J. Cibert, and H. Mariette, "Intrinsic ferromagnetism in wurtzite (Ga,Mn)N semiconductor," *Phys. Rev. B*, vol. 74, p. 041306, 2006.

[43] J. Okabayashi, A. Kimura, O. Rader, T. Mizokawa, and A. Fujimori, "Core-level photoemission study of $Ga_{1-x}Mn_xAs$," *Phys. Rev. B*, vol. 58, p. R4211, 1998.

[44] M. Linnarsson, E. Janzen, B. Monemar, M. Kleverman, and A. Thilderkvist, "Electronic structure of the GaAs:Mn-Ga center," *Phys. Rev. B*, vol. 55, p. 6938, 1997.

[45] C. Zener, "Interaction Between the d Shells in the Transition Metals," *Phys. Rev.*, vol. 81, p. 440, 1951.

[46] T. Hayashi, Y. Hashimoto, S. Katsumoto, and Y. Iye, "Effect of low-temperature annealing on transport and magnetism of diluted magnetic semiconductor (Ga,Mn)As," *Appl. Phys. Lett.*, vol. 78, p. 1691, 2001.

[47] K. W. Edmonds, P. Boguslawski, K. Y. Wang, R. P. Campion, S. N. Novikov, N. R. S. Farley, B. L. Gallagher, C. T. Foxon, M. Sawicki,

T. Dietl, M. B. Nardelli, and J. Bernholc, "Mn Interstitial Diffusion in (Ga,Mn)As," *Phys. Rev. Lett.*, vol. 92, p. 037201, 2004.

[48] K. M. Yu, W. Walukiewicz, T. Wojtowicz, I. Kuryliszyn, X. Liu, Y. Sasaki, and J. K. Furdyna, "Effect of the location of Mn sites in ferromagnetic $Ga_{1-x}Mn_xAs$ on its Curie temperature," *Phys. Rev. B*, vol. 65, p. 201303, 2002.

[49] R. E. Goacher, S. Hegde, H. Luo, and J. A. Gardella, "Diffusion of Mn in GaAs studied by quantitative time-of-flight secondary ion mass spectrometry," *J. Appl. Phys.*, vol. 106, p. 044302, 2009.

[50] R. Shioda, K. Ando, T. Hayashi, and M. Tanaka, "Local structures of III-V diluted magnetic semiconductors $Ga_{1-x}Mn_xAs$ studied using extended x-ray-absorption fine structure," *Phys. Rev. B*, vol. 58, no. 3, p. 1100, 1998.

[51] R. Bacewicz, A. Twarog, A. Malinowska, T. Wojtowicz, X. Liu, and J. K. Furdyna, "Local structure of Mn in (Ga, Mn)As probed by X-ray absorption spectroscopy," *J. Phys. Chem. Sol.*, vol. 66, no. 11, p. 2004, 2005.

[52] K. Lawniczak-Jablonska, J. Libera, A. Wolska, M. T. Klepka, R. Jakiela, and J. Sadowski, "The ratio of interstitial to substitutional site occupation by Mn atoms in GaAs estimated by EXAFS," *Rad. Phys. Chem.*, vol. 78, no. Suppl. 10, p. S80, 2009.

[53] A. Wolska, K. Lawniczak-Jablonska, M. T. Klepka, R. Jakiela, J. Sadowski, I. N. Demchenko, E. Holub-Krappe, A. Persson, and D. Arvanitis, "XANES studies of Mn K and L3,2 edges in the (Ga,Mn)As layers modified by high temperature annealing," *Act. Phys. Pol.*, vol. 114, no. 2, p. 357, 2008.

[54] A. Kwiatkowski, D. Wasik, M. Kaminska, R. Bozek, J. Szczytko, A. Twardowski, J. Borysiuk, J. Sadowski, and J. Gosk, "Structure and magnetism of MnAs nanocrystals embedded in GaAs as a function of post-growth annealing temperature," *J. Appl. Phys.*, vol. 101, p. 113912, 2007.

[55] T. Shi, S. Zhu, Z. Sun, S. Wei, and W. Liu, "Structures and magnetic properties of wurtzite $Zn_{1-x}Co_xO$ dilute magnetic semiconductor nanocomposites," *Appl. Phys. Lett.*, vol. 90, p. 102108, 2007.

[56] Z. Sun, W. Yan, G. Zhang, H. Oyanagi, Z. Wu, Q. Liu, W. Wu, T. Shi, Z. Pan, P. Xu, and S. Wei, "Evidence of substitutional Co ion clusters in $Zn_{1-x}Co_xO$ dilute magnetic semiconductors," *Phys. Rev. B*, vol. 77, p. 245208, 2008.

[57] N. R. S. Farley, K. W. Edmonds, A. A. Freeman, G. van der Laan, C. R. Staddon, D. H. Gregory, and B. L. Gallagher, "Magnetic properties of sol-gel-derived doped ZnO as a potential ferromagnetic semiconductor: a synchrotron-based study," *New J. Phys.*, vol. 10, p. 055012, 2008.

[58] J. H. Guo, A. Gupta, P. Sharma, K. V. Rao, M. A. Marcus, C. L. Dong, J. M. O. Guillen, S. M. Butorin, M. Mattesini, P. A. Glans, K. E. Smith, C. L. Chang, and R. Ahuja, "X-ray spectroscopic study of the charge state and local ordering of room-temperature ferromagnetic Mn-doped ZnO," *J. Phys.: Condens. Matter.*, vol. 19, p. 172202, 2007.

[59] H. Ofuchi, Z. W. Jin, T. Fukumura, M. Kawasaki, Y. Matsumoto, T. Hasegawa, H. Fujioka, M. Oshima, and H. Koinuma, "Fluorescence EXAFS study on local structures around Mn and Fe atoms doped in ZnO," *Phys. Scr.*, vol. T115, p. 614, 2005.

[60] J. C. Pivin, G. Socol, I. Mihailescu, P. Berthet, F. Singh, M. K. Patel, and L. Vincent, "Structure and magnetic properties of ZnO films doped with Co, Ni or Mn synthesized by pulsed laser deposition under low and high oxygen partial pressures," *Thin Solid Films*, vol. 517, p. 916, 2008.

[61] M. Sato, H. Tanida, K. Kato, T. Sasaki, Y. Yamamoto, S. Sonoda, S. Shimizu, and H. Hori, "Local structure around Mn in ferromagnetic GaMnN film studied by X-ray absorption fine structure," *Jpn. J. Appl. Phys. Part 1 - Regul. Pap. Short Notes Rev. Pap.*, vol. 41, p. 4513, 2002.

[62] X. Biquard, O. Proux, J. Cibert, D. Ferrand, H. Mariette, R. Giraud, and B. Barbara, "Local structure and valence state of mn in $ga_{1-x}mn_xn$ epilayers," *J. Supercond.*, vol. 16, p. 127, 2003.

[63] S. Kuroda, E. Bellet-Amalric, X. Biquard, J. Cibert, R. Giraud, S. Marcet, and H. Mariette, "Optimization of the growth of Ga1-

xMnxN epilayers using plasma-assisted MBE," *Phys. Status Solidi B-Basic Res.*, vol. 240, p. 443, 2003.

[64] A. Titov, E. Kulatov, Y. Uspenskii, X. Biquard, D. Halley, S. Kuroda, E. Bellet-Amalric, H. Mariette, and J. Cibert, "Pre-edge features in X-ray absorption structure of Mn in GaMnN, GaMnAs and GeMn," *J. Magn. Magn. Mater.*, vol. 300, p. 144, 2006.

[65] J. Hwang, Y. Ishida, Y. Osafune, T. Mizokawa, A. Fujimori, Y. Takeda, K. Terai, S. Fujimori, Y. Saitoh, Y. Muramatsu, A. Tanaka, T. Kondo, H. Munekata, M. Hashimoto, H. Tanaka, S. Hasegawa, and H. Asahi, "Photoemission and X-ray absorption studies of the electronic structure of GaN-based diluted magnetic semiconductors," *Phys. Status Solidi B-Basic Solid State Phys.*, vol. 243, p. 1696, 2006.

[66] S. Wei, W. Yan, Z. Sun, Q. Liu, W. Zhong, X. Zhang, H. Oyanagi, and Z. Wu, "Direct determination of Mn occupations in $Ga_{1-x}Mn_xN$ dilute magnetic semiconductors by x-ray absorption near-edge structure spectroscopy," *Appl. Phys. Lett.*, vol. 89, p. 121901, 2006.

[67] S. Kuroda, S. Marcet, E. Bellet-Amalric, J. Cibert, H. Mariette, S. Yamamoto, T. Sakai, T. Ohshima, and H. Itoh, "Structural analysis of (Ga,Mn)N epilayers and self-organized dots using MeV ion channeling," *Phys. Status Solidi A-Appl. Mat.*, vol. 203, p. 1724, 2006.

[68] A. Singh, R. Kumar, P. Thakur, N. Brookes, K. Chae, and W. Choi, "NEXAFS and XMCD studies of single-phase Co doped ZnO thin films," *J. Phys.: Condens. Matter.*, vol. 21, p. 185005, 2009.

[69] J. A. Sans, G. Martinez-Criado, J. Susini, R. Sanz, J. Jensen, I. Minguez, M. Hernandez-Velez, A. Labrador, and P. Carpentier, "Thermal instability of implanted Mn ions in ZnO," *J. Appl. Phys.*, vol. 107, p. 023507, 2010.

[70] J. Baik, S. Kim, Y. Koo, T. Kang, and J. Lee, "Evidence of mn occupation of Ga site in ferromagnetic (Ga, Mn)N semiconductor observed by EXAFS," *Electrochem. Solid State Lett.*, vol. 7, p. G313, 2004.

[71] C. Liu, E. Alves, A. Ramos, M. da Silva, J. Soares, T. Matsutani, and M. Kiuchi, "Lattice location and annealing behavior of Mn implanted

GaN," *Nucl. Instrum. Methods Phys. Res. Sect. B-Beam Interact. Mater. Atoms*, vol. 191, p. 544, 2002.

[72] P. Thakur, K. H. Chae, J.-Y. Kim, M. Subramanian, R. Jayavel, and K. Asokan, "X-ray absorption and magnetic circular dichroism characterizations of Mn doped ZnO," *Appl. Phys. Lett.*, vol. 91, p. 162503, 2007.

[73] H. T. Cao, Z. L. Pei, J. Gong, C. Sun, R. F. Huang, and L. S. Wen, "Preparation and characterization of Al and Mn doped ZnO transparent conducting oxide films," *J. Solid State Chem.*, vol. 177, p. 1480, 2004.

[74] T. Graf, S. T. B. Goennenwein, and M. S. Brandt, "Prospects for carrier-mediated ferromagnetism in GaN," *Phys. Status Solidi B-Basic Res.*, vol. 239, p. 277, 2003.

[75] F. Takano, H. Ofuchi, J. Lee, K. Takita, and H. Akinaga, "Growth and characterization of Mn-doped cubic-GaN," *Physica B*, vol. 376, p. 658, 2006.

[76] G. Martinez-Criado, A. Somogyi, S. Ramos, J. Campo, R. Tucoulou, M. Salome, J. Susini, M. Hermann, M. Eickhoff, and M. Stutzmann, "Mn-rich clusters in GaN: Hexagonal or cubic symmetry?," *Appl. Phys. Lett.*, vol. 86, p. 131927, 2005.

[77] Y. Wang, J. Zou, Y. J. Li, B. Zhang, and W. Lu, "Mn behaviors in Mn-implanted ZnO," *Acta Mater.*, vol. 57, p. 2291, 2009.

[78] K. Potzger, S. Zhou, H. Reuther, K. Kuepper, G. Talut, M. Helm, J. Fassbender, and J. D. Denlinger, "Suppression of secondary phase formation in Fe implanted ZnO single crystals," *Appl. Phys. Lett.*, vol. 91, p. 062107, 2007.

[79] S. Zhou, K. Potzger, H. Reuther, G. Talut, F. Eichhorn, J. von Borany, W. Skorupa, M. Helm, and J. Fassbender, "Crystallographically oriented magnetic ZnFe2O4 nanoparticles synthesized by Fe implantation into ZnO," *J. Phys. D-Appl. Phys.*, vol. 40, p. 964, 2007.

[80] S. Zhou, K. Potzger, G. Talut, H. Reuther, K. Kuepper, J. Grenzer, Q. Xu, A. Muecklich, M. Helm, J. Fassbender, and E. Arenholz, "Ferromagnetism and suppression of metallic clusters in Fe implanted

ZnO - a phenomenon related to defects?," *J. Phys. D-Appl. Phys.*, vol. 41, p. 105011, 2008.

[81] R. P. Borges, B. Ribeiro, A. R. G. Costa, C. Silva, R. C. da Silva, G. Evans, A. P. Goncalves, M. M. Cruz, and M. Godinho, "Magnetic and transport properties of transition-metal implanted ZnO single crystals," *Eur. Phys. J. B*, vol. 79, p. 185, 2011.

[82] W. Kim, H. J. Kang, S. K. Noh, J. Song, and C. S. Kim, "Magnetic clusters in Co ion-implanted GaN," *J. Magn. Magn. Mater.*, vol. 310, p. E729, 2007.

[83] C. D. Lorenz, R. May, and R. M. Ziff, "Similarity of percolation thresholds on the HCP and FCC lattices," *J. Stat. Phys.*, vol. 98, p. 961, 2000.

[84] R. E. Behringer, "Number of Single, Double, and Triple Clusters in a System Containing Two Types of Atoms," *J. Chem. Phys*, vol. 29, p. 537, 1958.

[85] K. Sato, L. Bergqvist, J. Kudrnovsky, P. H. Dederichs, O. Eriksson, I. Turek, B. Sanyal, G. Bouzerar, H. Katayama-Yoshida, V. A. Dinh, T. Fukushima, H. Kizaki, and R. Zeller, "First-principles theory of dilute magnetic semiconductors," *Rev. Mod. Phys.*, vol. 82, p. 1633, 2010.

[86] J. M. D. Coey, M. Venkatesan, and C. B. Fitzgerald, "Donor impurity band exchange in dilute ferromagnetic oxides," *Nat. Mater.*, vol. 4, no. 2, pp. 173–179, 2005.

[87] T. Kasuya and A. Yanase, "Anomalous Transport Phenomena in Eu-Chalcogenide Alloys," *Rev. Mod. Phys.*, vol. 40, p. 684, 1968.

[88] T. Dietl and J. Spalek, "Effect of Fluctuations of Magnetization on the Bound Magnetic Polaron - Comparison with Experiment," *Phys. Rev. Lett.*, vol. 48, p. 355, 1982.

[89] A. Golnik, J. Gaj, M. Nawrocki, R. Planel, and C. Benoit a la Guillaume, "Optical observation of a magnetic molecule in $Cd_{1-x}Mn_xTe$," *J. Phys. Soc. Jpn.*, vol. 49, p. 819, 1980.

[90] J. M. D. Coey in *Handbook of Spin Transport and Magnetism* (E. I. Tsymbal and I. Zutic, eds.), ch. Magnetism of Dilute Oxides, Chapman and Hall/CRC, 2011.

[91] R. P. Panguluri, P. Kharel, C. Sudakar, R. Naik, R. Suryanarayanan, V. M. Naik, A. G. Petukhov, B. Nadgorny, and G. Lawes, "Ferromagnetism and spin-polarized charge carriers in In_2O_3 thin films," *Phys. Rev. B*, vol. 79, p. 165208, 2009.

[92] D. M. Edwards and M. I. Katsnelson, "High-temperature ferromagnetism of sp electrons in narrow impurity bands: application to CaB_6," *J. Phys.-Condes. Matter*, vol. 18, p. 7209, 2006.

[93] J. M. D. Coey, K. Wongsaprom, J. Alaria, and M. Venkatesan, "Charge-transfer ferromagnetism in oxide nanoparticles," *J. Phys. D-Appl. Phys.*, vol. 41, p. 134012, 2008.

[94] J. M. D. Coey, P. Stamenov, R. D. Gunning, M. Venkatesan, and K. Paul, "Ferromagnetism in defect-ridden oxides and related materials," *New J. Phys.*, vol. 12, p. 053025, 2010.

[95] N. Khare, M. J. Kappers, M. Wei, M. G. Blamire, and J. L. MacManus-Driscoll, "Defect-induced ferromagnetism in co-doped ZnO," *Adv. Mater.*, vol. 18, p. 1449, 2006.

[96] L. E. Halliburton, N. C. Giles, N. Y. Garces, M. Luo, C. C. Xu, L. H. Bai, and L. A. Boatner, "Production of native donors in ZnO by annealing at high temperature in Zn vapor," *Appl. Phys. Lett.*, vol. 87, p. 172108, 2005.

[97] D. A. Schwartz and D. R. Gamelin, "Reversible 300 K ferromagnetic ordering in a diluted magnetic semiconductor," *Adv. Mater.*, vol. 16, p. 2115, 2004.

[98] R. P. Borges, R. C. Da Silva, S. Magalhaes, M. M. Cruz, and M. Godinho, "Magnetism in Ar-implanted ZnO," *J. Phys.-Condes. Matter*, vol. 19, p. 476207, 2007.

[99] T. C. Droubay, D. J. Keavney, T. C. Kaspar, S. M. Heald, C. M. Wang, C. A. Johnson, K. M. Whitaker, D. R. Gamelin, and S. A. Chambers, "Correlated substitution in paramagnetic Mn^{2+}-doped ZnO epitaxial films," *Phys. Rev. B*, vol. 79, p. 155203, 2009.

[100] R. Heitz, A. Hoffmann, and I. Broser, "Fe^{3+} center in ZnO," *Phys. Rev. B*, vol. 45, p. 8977, 1992.

[101] E. Chikoidze, H. J. V. Bardeleben, Y. Dumont, P. Galtier, and J. L. Cantin, "Magnetic interactions in $Zn_{1-x}Mn_xO$ studied by electron paramagnetic resonance spectroscopy," *J. Appl. Phys.*, vol. 97, p. 10D316, 2005.

[102] R. Heitz, P. Thurian, I. Loa, L. Eckey, A. Hoffmann, I. Broser, K. Pressel, B. K. Meyer, and E. N. Mokhov, "Zeeman spectroscopy of the Fe^{3+} center in GaN," *Appl. Phys. Lett.*, vol. 67, p. 2822, 1995.

[103] S. S. Marcet, D. Ferrand, D. Halley, S. Kuroda, H. Mariette, E. Gheeraert, F. J. Teran, M. L. Sadowski, R. M. Galera, and J. Cibert, "Magneto-optical spectroscopy of (Ga,Mn)N epilayers," *Phys. Rev. B*, vol. 74, p. 125201, 2006.

[104] N. Jedrecy, H. J. V. Bardeleben, Y. Zheng, and J. L. Cantin, "Electron paramagneticresonance study of $Zn_{1-x}Co_xO$: A predicted high-temperature ferromagnetic semiconductor," *Phys. Rev. B*, vol. 69, p. R041308, 2004.

[105] P. Sati, R. Hayn, R. Kuzian, S. Rgnier, S. Schafer, A. Stepanov, C. Morhain, C. Deparis, M. Laugt, M. Goiran, and Z. Golacki, "Magnetic Anisotropy of Co2+ as Signature of Intrinsic Ferromagnetism in ZnO :Co," *Phys. Rev. Lett.*, vol. 96, p. 017203, 2006.

[106] C. Kittel, *Introduction to solid state physics*. Wiley, 2004.

[107] K. Suzuki, T. Kaneko, H. Yoshida, Y. Obi, H. Fujimori, and H. Morita, "Crystal structure and magnetic properties of the compound MnN," *J. Alloy. Compd.*, vol. 306, p. 66, 2000.

Chapter 2

Objectives and outline

This work addresses the current goals and challenges facing the DMS field which were described in sections 1.3 and 1.4 and summarized in section 1.5. The objectives of this work (and corresponding research approach and output) can be divided between narrow-gap (A) and wide-gap (B1, B2, B3) DMS.

(A) To determine the lattice location of Mn in GaAs. The goal is to identify the interstitial Mn site and determine its thermal stability for a varying concentration of potentially trapping defects, using the emission channeling technique (described in section 3.3). The results and their implications on the prospects for increasing the Curie temperature of Mn-doped GaAs are presented in section 4.1 (Articles II and III).

(B1) To determine the lattice location of Mn and Co in ZnO and GaN. The goal is to clarify if minority fractions of the 3*d* transition-metal impurities occupy non-cation-substitutional sites. The results and their implications on the current understanding of transition-metal incorporation in ZnO and GaN are presented in section 4.2 (Article IV, V, VI).

(B2) To search for high-temperature intrinsic ferromagnetism in Mn-, Fe- and Co-implanted ZnO and GaN. In line with the emerging picture of defect-related ferromagnetism, the goal is to search for intrinsic ferromagnetism for a varying degree of lattice disorder (defect type and concentration), by covering a wide range of implantation and thermal annealing conditions (c.f. section 3.1), and focusing on the low concentration

regime in order to minimize secondary-phase segregation. Damage formation and annealing are studied using Rutherford backscattering and channeling spectrometry (RBS/C) (described in section 3.2). Superconducting quantum interference device (SQUID) magnetometry is used for magnetic characterization, following strict procedures in order to avoid experimental artifacts (presented in section 3.4, Article I). The results and implications on the prospects for finding a ferromagnetic wide-gap DMS are presented in section 4.3 (Article VII).

(B3) To comprehensively describe the magnetism of wide-gap DMS materials. By combining the techniques and approaches in (A1), (B1) and (B2), the aim is to advance the understanding of representative but poorly understood impurity-host combinations, selected based on the results of (B2) and the available literature. The results are presented in section 4.4 (Articles VIII and IX).

Chapter 3

Experimental techniques

This chapter describes the experimental techniques used in this work. Sample preparation consisted of doping single-crystals and epitaxial thin films by ion implantation (section 3.1). Sample characterization was carried out using Rutherford backscattering and channeling spectrometry (RBS/C) to study the damage formation and recovery (section 3.2), electron emission channeling to study the lattice location of the implanted impurities (section 3.3) and superconducting quantum interference device (SQUID) magnetometry for magnetic characterization (section 3.4).

3.1 Doping technique: ion implantation

Ion implantation follows a simple principle: atoms or molecules are ionized in an ion source, accelerated by the electrostatic field generated by a high-voltage electrode (tens to hundreds of kV), mass-separated by an analyzing magnet, and electromagnetically steered into the target material.

In the context of dilute magnetic semiconductors, ion implantation offers several advantages compared to incorporating the magnetic dopants during growth:

Phase pureness. Because the magnetic dopants can be (randomly) incorporated at low temperature (at least in radiation resistant materials like ZnO and GaN), i.e. below their mobility thresholds, ion implantation may be superior in terms of dopant uniformity and phase pureness, basic conditions to produce an intrinsic DMS. Dopant aggregation during thermal annealing can be controlled by optimizing the thermal budget versus the diffusion coefficients of the implants.

Formation of lattice defects. In addition to doping, ion bombardment produces a variety of lattice defects, the type and amount of which can to some extent be controlled either by tuning the implantation parameters or by post-implantation thermal treatment. Although a major disadvantage when the aim is to electrically and optically dope, lattice defects are considered essential for the ferromagnetism of DMS materials (c.f. section 1.4.2.1).

High reproducibility. A major concern in the DMS field, reproducibility is assured with ion implantation, as it follows a relatively simple principle and because the basic implantation parameters can be precisely monitored and controlled: beam energy, current, and angle (with respect to the sample normal), implanted fluence (total number of atoms per areal unit) and sample temperature.

Versatility. It is compatible with any host material and virtually any dopant element, for a wide range of concentrations. This is particularly useful in a field where it is yet unclear which are the best impurity-host combinations.

Technological applicability. Because ion implantation is a standard technique in semiconductor processing industry, ion-implanted DMS materials are particularly close to technological implementation.

3.1.1 Ion stopping

As a "fast" ion[1] penetrates a solid material, it is "slowed down" and eventually stopped by a series of collisions with the target's nuclei and electrons. These mechanisms determine the dopant distribution in the sample. In the context of ion-implantation, the interaction between incident particle and target material is captured in the concepts of *stopping power* and *energy loss*, which are basically equivalent: the average (kinetic) energy loss of an incident particle per unit path length i.e

$$S(E) = -\frac{dE}{dx}, \tag{3.1}$$

where E is the kinetic energy of the incident particle and x is the path length.[2] The term *stopping power* is used as a property of the material, whereas *energy loss* is used to describe the incident particle.

[1] with a kinetic energy in the keV range and above

[2] The minus sign makes S positive

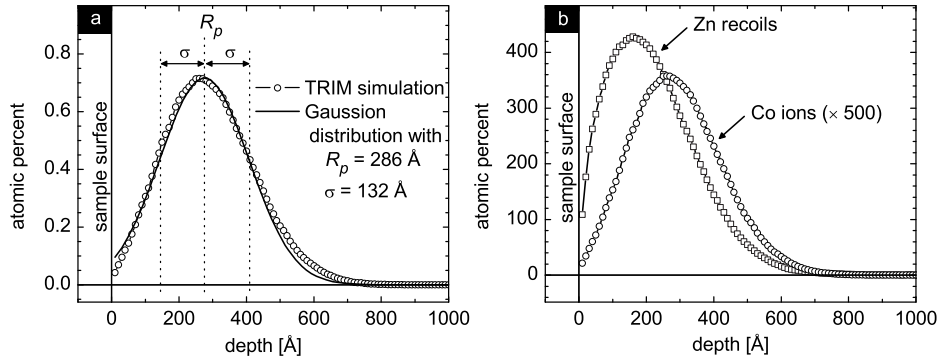

Figure 3.1: Selected outputs of a TRIM [1] simulation for a 60 keV ^{59}Co implantation in ZnO at an angle of 7°, scaled to a fluence of 1×10^{15} at. cm^{-2}: (a) Co depth profile in atomic percent (relative to a ZnO molecule) and Gaussian curve with the mean depth (R_p) and standard deviation (σ) simulated using TRIM; (b) recoiled Zn atoms (by collision with incident Co ions or other Zn recoils) estimated using TRIM's *detailed calculation with full damage cascades* with the default threshold displacement energy (TDE) values of 25 eV and 28 eV for Zn and O atoms, respectively, and the default lattice binding energy (LBE) values of 3 eV for both O and Zn (the Co depth profile is shown for comparison, multiplied by a factor of 500).

3.1.2 Depth profiles

As a representative example, Fig. 3.1 (a) shows the depth profile simulated using TRIM [1] for a 60 keV ^{59}Co implantation in ZnO at an angle of 7° (scaled for a fluence of 1×10^{15} at. cm^{-2}). Implantation depth profiles can be approximated by a Gaussian distribution, with a mean depth and a standard deviation, quoted in the program as *projected ion range* (R_p in Fig. 3.1) and *straggle* (σ in Fig. 3.1), respectively). *Ion range* and *straggle* increase approximately linearly with increasing implantation energy. Note that implanted ions are not only slowed down in the target but also deflected from their initial incident direction, with results in a lateral ion distribution; for the case of Fig. 3.1 the lateral straggle is of about 20 nm. However, because the beam is typically swept over the whole sample area, with typical lateral dimensions of the order of a centimeter, the lateral ion distribution can be considered uniform, i.e. lateral straggle can be ignored. Dopant concentration in implanted systems is typically quoted as the peak concentration x_p (the maximum concentration, approximately at a depth

equal to the *ion range*), which can be estimated based on simulations like that of Fig. 3.1 (a) and the implanted fluence (obtained from integrating the beam current during implantation).

These simulations generally reproduce quite accurately the experimentally determined depth profiles. There are however exceptions. For example, if the implanted species are mobile at the implantation temperature, the depth distribution will be affected by atomic diffusion. Also, for sufficiently high implantation fluences, *sputtering* (ejection of target atoms due to the ion bombardment) becomes non-negligible. As the *sputtering* gradually decreases the sample thickness, the depth distribution widens deeper into the sample. With increasing fluence, a steady-state is eventually reached, where the implanted ions are introduced at the same rate as they are removed by sputtering.

3.1.3 Collision cascades and primary defects

A key parameter in ion implanted systems is beam-induced damage, i.e. lattice defects created during implantation. When a target atom receives significant recoil energies when struck by the incident ion, it is removed from its lattice position and may in addition displace other target atoms, producing a cascade of collisions in the material. These collision cascades are the main cause of damage production during ion implantation in metals and semiconductors. The simplest defects created in collision cascades, also known as primary defects, are the target atoms which are recoiled from their lattice sites and the corresponding vacancies (the empty lattice sites left behind). In order to incorporate primary defect formation in the TRIM simulations, one must input a value for the threshold displacement energy (TDE), i.e. the minimum kinetic energy transferred to a target atom from an incident ion necessary to permanently remove it from its lattice site, thus generating a stable defect. Typical values are about 15 eV for semiconductors and 25 eV for metals. Another important parameter is the lattice binding energy LBE, i.e. the energy that each recoiling target atom loses when it leaves its lattice site and recoils in the target. Typically it is about 1 - 3 eV, but values are not known for most compounds. This energy is assumed to be converted into phonons. Figure 3.1 (b) shows the concentration of recoiled Zn (target) atoms, as simulated by TRIM.[3] Note that

[3]For this simulation, we have used the default values in TRIM for Zn and O: TDE values of 25 eV and 28 eV for Zn and O atoms, respectively, and LBE of 3 eV for both O and Zn. The correct values for ZnO are most likely different. Their determination is

for each recoiled Zn atom, a Zn vacancy is created. The vacancy profile is not shown in Fig. 3.1 (b), as it is nearly the same as that of the Zn recoils. The only noticeable difference is a small (few Å) shift of the recoiled-atom profile deeper into the sample (the predominant recoil direction). Note that what we discussed about Zn recoils and vacancies also applies to the O counterparts as well. Although not exactly quantitative, as the absolute concentration of recoils can vary by an order of magnitude by varying TDE and LBE values within reasonable ranges, such simulations provide a qualitative insight into the basic phenomenon of collision cascades. Two observations are worthy to note: (1) the Co concentration peak is located significantly deeper in the sample (at R_p) compared to the damage peak (at the so-called $R_p/2$ region); (2) the atomic percent of Zn recoils is extremely high ($> 400\%$ with respect to the Zn atoms in the target) even for a relatively low fluence (1×10^{15} at. cm^{-2} which corresponds to $x_p = 0.7$ at.%), meaning that each incident Co ion displaces about 1000 atoms and that in the $R_p/2$ region each Zn atom is an average displaced more than once.

3.1.4 Beam-induced damage: beyond primary defects

Although instrumental for the understanding of defect formation mechanisms, the concepts of *recoiled atoms* and *vacancies* alone do not fully capture the complexity of defect formation. Mobile point defects diffuse across the crystal. Diffusing self-interstitials, for example, may diffuse towards the crystal surface and adsorb from it or may simply fill a vacancy. In either case, because the defect "disappears", it is said to be *annealed*. Interstitials may also aggregate, forming small complexes or larger precipitates. Also vacancies can aggregate, forming small complexes (di-, trivacancies and so on) or larger complexes, knows as *voids*.

There are many different mechanisms by which defects may be either annealed of converted into defects with a different structure and dimensionality. In general, both can occur during ion implantation. The process by which primary defects, such as vacancies and self-interstitials created upon ion bombardment, recombine during or shortly after the evolution of a displacement cascade is known as *dynamic annealing*. Considering for example the case simulated above, it is clear that not all the recoiled atoms become interstitials, as this would correspond to about 400% of the Zn

however highly non-trivial and different values can be found in the literature. We show these simulations as a mere illustration of the basic mechanisms of collision cascades.

atoms in the implantated region. In fact, in Article VII it is shown that, for similar implantation conditions, the crystallinity is barely affected, which reflects the very efficient dynamic annealing in ZnO. The type and amount of defects which remain in the crystal after implantation depend on various factors: target material, implanted ion, ion fluence and energy, beam direction with respect to the the crystal axis, mass of the implanted ions, target temperature, etc. Typically, in the low fluence limit, isolated point defects such as vacancies and interstitials are created. As the fluence increases, defect complexes, extended defects or even amorphous pockets may form. In the limiting case, beam-induced damage leads to amorphization of the implanted layer, if the collision cascades from different impinging ions overlap significantly.

3.1.5 Thermal annealing

The principle of thermal annealing is rather simple: a material is heated up to a certain temperature in order to change its structural characteristics and consequently its electrical, magnetic or mechanical properties. As such, the concept of thermal annealing covers a wide range of material processing methods and procedures, with different aims and applications. In the context of implanted semiconductors, thermal annealing can be used as a means to

Activate dopants by incorporating them in lattice sites where they display the desired properties or by promoting the recombination or out-diffusion of compensating (point) defects such as vacancies, self-interstitials or other impurities.

Overall improvement of structural and electrical properties by removal of point or extended defects which may, for example, behave as scattering or recombination centers, induce stress, etc.

Recrystallize amorphous layers after heavy-ion and/or high-fluence implantation.

Thermal annealing can be performed under different conditions. Basic parameters which can be varied are for example the temperature, duration and atmosphere (vacuum or a gas mixture at a specified pressure). In some cases, capping with proximity or deposited layers is necessary in order to protect the surface from decomposition.

3.2 Defect characterization: Rutherford backscattering and channeling spectrometry (RBS/C)

Rutherford backscattering spectrometry (RBS) is most commonly used to characterize thin films (up to a few μm thick) in terms of thickness and elemental composition. Because it is depth-sensitive, it allows in many cases to determine the depth profile of different constituents. In this work, the technique was used to characterize the implanted layers in terms of beam-induced damage. This is done by exploiting the *ion channeling* effect, in which case the technique is known as Rutherford backscattering and channeling spectrometry (RBS/C). Next we briefly introduce some basic principles of RBS and ion channeling, in particular how the latter can be used in RBS/C to provide information about defects in single-crystals. More details on the theoretical and technical aspects of RBS and RBS/C can be found, for example, in [2–4].

3.2.1 Energy loss and ion backscattering

In a typical RBS experiment, energetic light ions impinge on the target and lose energy as they interact with the particles composing the material. As mentioned in section 3.1.1, the energy loss dE/dx, where E is the kinetic energy of the incident particle and x is the path length, is a sum of two contributions: electronic and nuclear energy loss. For light ions with relatively high energies (100 keV – MeV), the electronic energy loss dominates, while the nuclear energy loss becomes increasingly important as the impinging ion is slowed down (loses energy) in the material. Nuclear loss corresponds to the Coulomb interaction (collision) between an impinging ion and a lattice atom core, both with an effective positive charge. When the mass of the incoming ions is lower than the mass of the lattice atoms, these collisions can result in backscattering of the incoming ions. The ratio between the impinging ion energy before (E_0) and after (E_1) the collision is called the kinematic factor K and is given by

$$K = \frac{E_1}{E_0} = \left[\frac{(M_2^2 - M_1^2 \sin^2\theta)^{1/2} + M_1 \cos\theta}{M_1 + M_2} \right]^2 , \tag{3.2}$$

where M_1 and M_2 are the masses of the impinging ion and of the target atom, respectively, and θ is the *scattering angle*, i.e. the angle between the incident beam and the backscattering beam. The energy of the backscat-

tered ions then depends on two parameters

1. The depth at which the collision took place, which can be deduced from the energy loss dE/dx.

2. The mass of the target atom involved in the collision, which can be deduced from the kinematic factor (3.2).

Two other quantities of interest to interpret an RBS spectrum are the *scattering cross section* $\sigma(\theta)$ and the *depth resolution*. The scattering cross section is related to the number of ions scattered into a solid angle $\mathrm{d}\Omega$ per incident ion, and can be approximated by

$$\sigma(\theta) = \left(\frac{Z_1 Z_2 e^2}{4E}\right)^2 \frac{1}{\sin^4 \theta/2}\,, \tag{3.3}$$

where Z_1 and Z_2 are the atomic numbers of the incident ion and the target atom, respectively. Because of its Z_2 dependence, $\sigma(\theta)$ must be taken into account when determining from an RBS spectrum the relative concentrations of different elements in a layer. Because of its squared dependence in Z_2, the sensitivity of RBS increases considerably from light to heavy target elements. The depth resolution δt can be approximated by

$$\delta t = \frac{\delta E_1}{K(dE/dx)_{\mathrm{in}} + \frac{(dE/dx)_{\mathrm{out}}}{|\cos\theta|}}\,, \tag{3.4}$$

where δE_1 is the energy resolution and $(dE/dx)_{\mathrm{in}}$ and $(dE/dx)_{\mathrm{out}}$ refer to the energy loss on the way in and out of the target.

Typical RBS experiments make use of a beam of $^4\mathrm{He}^+$ ions at an energy of 1–2 MeV, and silicon surface barrier detectors for measuring the backscattered ions. For MeV $^4\mathrm{He}^+$ ions, an energy resolution δE_1 of 15 keV can be obtained with conventional electronic systems. The detector position (the backscattering angle θ) according to the specific aim of the experiment, as a trade-off between mass and depth resolutions. Scattering angles close to 180° (i.e. with the detector close to the incoming beam), maximize the mass resolution. Depth resolution is maximized in glancing geometry, i.e. with the detector at a small exit angle relative to the sample plane.

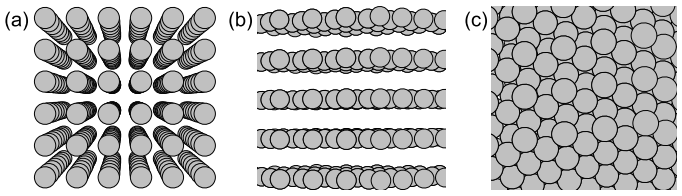

Figure 3.2: Representation of a cubic lattice seen from three different directions: (a) parallel to a crystallographic axis; (b) parallel to a crystal plane; (c) random orientation.

3.2.2 Ion channeling

Channeling is the mechanism by which atomic rows and planes steer energetic charged particles along major crystal axis and planes. Figure 3.2 shows a schematic representation of a lattice, seen from three particular directions: a crystal axis, a crystal plane (off any major axis) and a "random" direction. Because the motion of energetic charged particles in a solid is mainly determined by their Coulomb interaction with the (screened) nuclear charges in the lattice, one can expect that particle propagation is very different among these three types of directions.

Lindhard [5] showed that positively charged particles moving along directions aligned with a crystal axis, can be steered by multiple small-angle collisions with the crystal atoms. The channeling of a positively charged particle in a single-crystal can be summarized in three principles [6]. First, the particle must propagate through an open channel between the rows of atoms - *transparency*. Second, the screened Coulomb potential (repulsive) of the rows of nuclei steers the particle towards the middle of the channel - *steering*. Finally, the principle of *stability* requires that the particle does not approach the rows of atoms too closely, otherwise, instead of a gentle steering via the interaction with the row of atoms, the particle experiences wide-angle deflections in head-on collisions with individual atoms. Such large non-correlated deflections constitute the so called *blocking* effect. These effects are shown schematically in Fig. 3.3. The gentle steering of the impinging ions can be interrupted when these reach regions of the crystal where the periodicity has been broken. The simplest case is that of interstitial atoms in the middle of otherwise "open channels", which increase the probability of large-angle collisions and therefore the backscattering yield. Other point defects, such as substitutional atoms which have relaxed away from their ideal positions due to neighboring vacancies, may

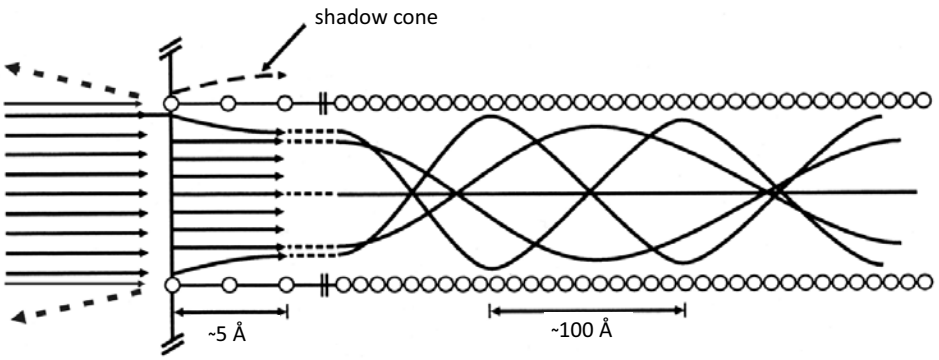

Figure 3.3: Representation of the ion-channeling effect (from [4]). Impinging positively charged ions aligned with a crystallographic axis of the target (singlecrystalline) material are steered by the rows and planes of atoms.

also increase the probability of large-angle collisions. Also extended defects, such as amorphous precipitates or secondary phases which are incoherent with the host structure, increase the backscattering yield by disrupting the translational symmetry of the crystal, i.e. by "obstructing" the crystal's channels.

3.2.3 RBS/C

As an example of how RBS/C can be used to study beam induced damage, Fig. 3.4 shows RBS/C spectra of a ZnO single-crystal, measured with 1.57 MeV $^4He^+$ ions, with the detector in backscattering geometry ($\theta = 160°$). The spectrum with higher backscattering yield was measured with the $^4He^+$ beam impinging at a random orientation, i.e. not aligned with any major crystallographic axis, and is conventionally referred to as the *random* spectrum. Because the kinematic factor [eq. (3.2)] of O is smaller than that of Zn, The O signal appears at lower backscattering energies, superimposed to that of Zn. Because the cross section [eq. (3.3)] of O is much smaller than that of Zn ($\sigma(\mathrm{Zn})/\sigma(\mathrm{O}) = [Z(\mathrm{Zn})/Z(\mathrm{O})]^2 \approx 14$), the O signal is barely visible in the spectrum, despite the equal concentrations of Zn and O. The two spectra with lower backscattering yield were measured with the $^4He^+$ beam aligned with the [0001] axis, for a ZnO singlecrystal before and after implantation. Conventionally referred to as as *channeled* spectra, they can, as described above, provide information about the the crystallinity of

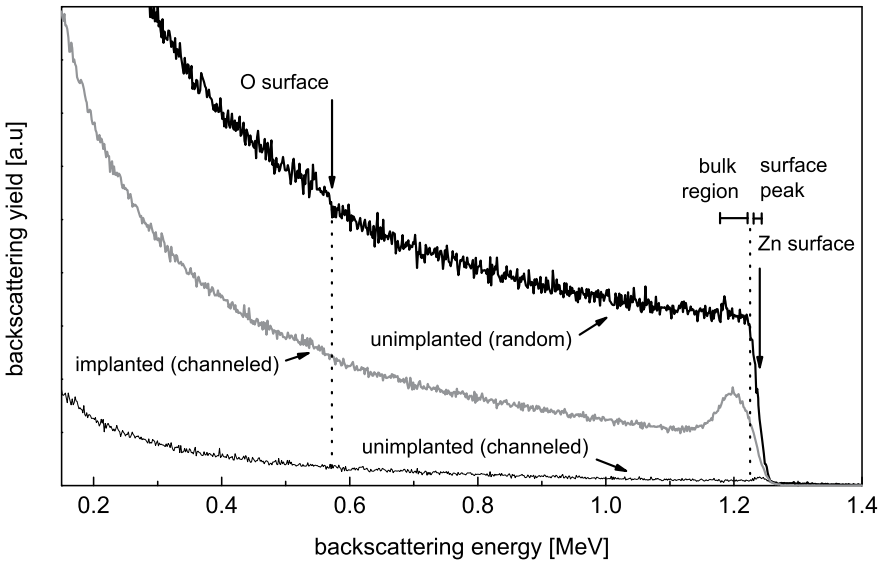

Figure 3.4: RBS/C spectra of a ZnO singlecrystal, measured with 1.57 MeV $^4He^+$ ions, with the detector in backscattering geometry ($\theta = 168°$): random and channeled spectra prior to implantation and channeled spectrum after Fe-implantation to a fluence of 5×10^{15} at. cm^{-2} at 60 keV.

the target material. The "measure" of crystallinity is known as *minimum yield* ($\chi_{\min}$) and is defined as the ratio of the backscattering yield of the channeled to the random spectrum, integrated over a given energy window. Typically two different $\chi_{\min}$ can be defined: (1) the surface $\chi_{\min}$ is calculated by integrating the backscattering yield over an energy window in the near surface region, i.e. for the *surface peak* which is visible in the channeled spectrum of the unimplanted sample in Fig. 3.4 around 1.25 MeV; (2) the bulk $\chi_{\min}$ for an energy window immediately below. In the case of ZnO, because the O signal is much smaller and superimposed on the Zn signal, one can only determine the minimum yield for the Zn sublattice. For the unimplanted sample, the surface and bulk $\chi_{\min}$ are 4–5% and 2–3%, respectively, which is typical for highly crystalline materials. The surface peak (and the fact that the surface $\chi_{\min}$ is higher than the bulk $\chi_{\min}$) is always present, even in perfect crystals. It results from the fact that, eventhough the beam is perfectly aligned with the crystal axis, a fraction of the ions reach the crystal surface very close to the atom rows,

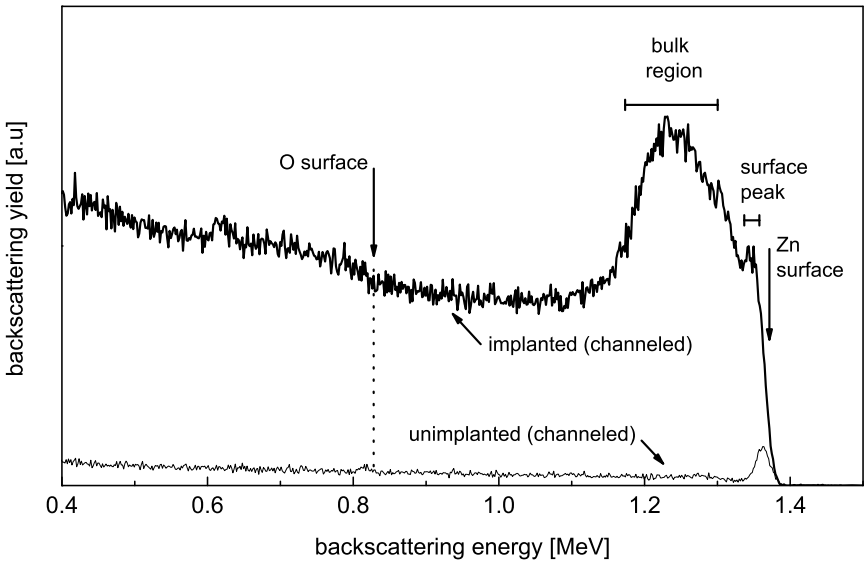

Figure 3.5: RBS/C spectra of a ZnO singlecrystal, measured with 1.57 MeV $^4He^+$ ions, with the detector in glancing geometry ($\theta = 105°$, i.e a 15° exit angle relative to the sample surface): channeled spectra before and after implantation Fe-implantation to a fluence of 5×10^{15} at. cm^{-2} at 60 keV.

and therefore experience large-angle colisions with the first atomic monolayer. After implantation (with 60 keV Fe^+ ions to a fluence of 5×10^{15} at. cm^{-2}), theres an increase in backscatering yield in the surface peak region as well as deeper into the sample, i.e. in the implanted region, which is reflected by the increased surface and bulk $\chi_{\min}$ to 55% and 50% respectively. However the two damage regions are poorly resolved in the spectra measured in backscattering geometry ($\theta = 168°$). Placing the detector at a glancing angle increases the depth resolution [eq. (3.4)]. Figure 3.5 shows the channeled spectra of the same sample, again before and after implantation, measured with the detector at a backscattering angle of 105° (15° exit angle relative to the sample surface). The increased depth resolution allows for the two damage regions to be resolved: (1) the bulk region (i.e. the region of maximum concentration of implanted ions), where the energy loss is maximum as the implanted ions are slowed down to the point that nuclear stopping dominates over electron stopping and the target atoms are thus more efficiently displaced; (2) the near surface region, which acts as

a sink for mobile defects created by the ion bombardment (thus increasing the intensity of the surface peak).

3.3 Impurity lattice location: electron emission channeling

The electron emission channeling technique has been developed for the study of the lattice site location of impurities in single-crystals and offers a number of advantages when compared to other techniques. Because it relies on the direct comparison between experimental and calculated (2-dimensional) patterns, it provides unambiguous and quantitative lattice location superior to more conventional implementations of ion-channeling techniques such as Rutherford backscattering spectrometry (RBS), particle-induced X-ray emission (PIXE) and nuclear reaction analysis (NRA). In addition, Rutherford backscattering and channeling spectrometry (RBS/C), by far the most popular among those, relies on elastic recoil which considerably limits the study of impurity elements lighter than major constituents of the material. This is particularly the case for the systems studied in this work (Mn, Fe and Co impurities in ZnO, GaN and GaAs). Another advantage of electron emission channeling, is its high sensitivity, down to 10^{12} at. cm^{-2}, which makes it particularly suited to study very dilute systems, unlike conventional ion-beam methods. For example, RBS/C requires typical impurity fluences above $10^{14} - 10^{15}$ at. cm^{-2}, i.e. roughly three orders of magnitude higher than emission channeling. The situation is similar for synchrotron radiation techniques such as X-ray absorption fine structure (EXAFS) spectroscopy or X-ray linear dichroism (XLD). Probably one of the strongest features of the emission channeling technique is its applicability to those cases where significant fractions of the impurities occupy more than one lattice site. Although in principle such minority versus majority occupancies can also be quantified using XAFS, unambiguous identification of minority sites is extremely challenging, because the technique relies on complex multiparameter fitting of the spectra using calculated model structures. Other techniques, e.g. electron paramagnetic resonance (EPR) and Mössbauer and perturbed angular correlation (PAC) spectroscopies, are also very sensitive and can in some cases distinguish very well different lattice sites. However, lattice location can only be indirectly inferred from the spectra.

3.3.1 Principles

The channeling of energetic charged particles is introduced in the previous section in the context of ion channeling in Rutherford backscattering

and channeling spectrometry (RBS/C). The general principles described for the channeling of heavy, positive ions apply to the channeling of electrons, which are lighter and negatively charged. Changing the sign of the propagating particle's charge is equivalent to changing the sign of the Coulomb potential: a potential "valley" for a positively charged particle is a potential "hill" for a negatively charged one, and vice versa. The same is to say that negatively charged particles "see" as channels the rows of nuclear charges instead of the space in between. However, although providing an intuitive insight in the elementary phenomena, the classical approach of Lindhard introduced in the previous section does not describe quantitatively *electron* emission channeling, in which quantum effects must be taken in account. Details on the theoretical aspects of emission channeling can be found, for example, in [7].

Several techniques can be applied in *channeling* mode (or geometry) to provide information on the lattice location of impurities: Rutherford backscattering spectrometry (RBS), particle-induced X-ray emission (PIXE) and nuclear reaction analysis (NRA). These more conventional techniques rely on the use of an external *ion* beam and how its interaction with the impurity atoms depends on the beam direction with respect to the lattice. The principle of *emission* channeling is slightly different, in the sense that the channeled particles are emitted from *within* the crystal by a radioactive isotope of the impurity element under study. The emission channeling technique can be applied using either α or electron (β^- or conversion electrons) emitters. In the later case, the technique is known as electron emission channeling, for which the requirement of *stability* (c.f. previous section) determines that the *channeling* and *blocking* effects depend on the initial position and direction of the emitted particle with respect to the lattice, which in turn depends on the lattice site occupied by the radioactive impurity. Figure 3.6 illustrates how such electron *channeling* and *blocking* enable the distinction between, for example, substitutional versus interstitial impurities.

An electron emission channeling experiment can be summarized in four steps:

1. Radioactive electron (β^- or conversion electrons) emitting isotopes are implanted in a single crystal or epitaxial thin film, occupying certain lattice site(s).

2. A fraction of the emitted electrons are channeled along the crystal axes and planes and leave the sample surface describing anisotropic

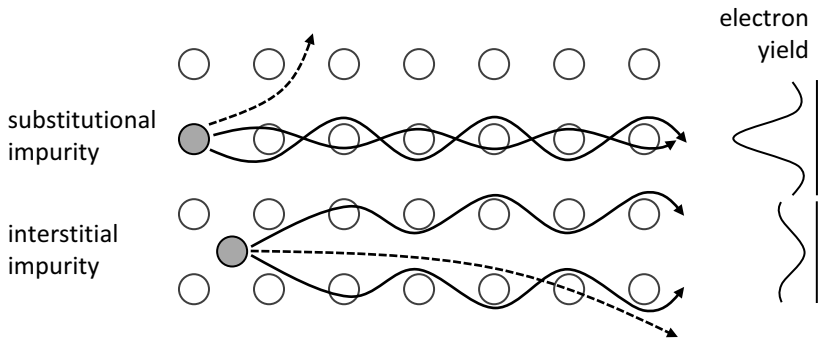

Figure 3.6: Schematic representation of *channeling* and *blocking* effects for substitutional versus interstitial electron emitter impurity. The trajectories of *channeled* (bound state) and *blocked* (free state) electrons are represented by solid lines and dashed lines, respectively. The electron yield profiles as a function of emission angle towards the crystal axis (1-dimensional angular scans) are represented on the right for substitutional versus interstitial emitters.

emission patterns which are characteristic of the emission site and the channeling axis.

3. These anisotropic emission patterns are recorded using a position-sensitive detector around selected crystallographic axes.

4. The lattice site(s) of the impurities is determined by fitting these 2-dimensional experimental patterns with theoretical ones.

Ion implantation (step 1) is described in section 3.1. The remainder of this section is devoted to a short description of the experimental aspects of the electron emission channeling technique (steps 2 to 4). More details on the experimental aspects of emission channeling can be found, for example, in [7–10].

3.3.2 Experimental details

3.3.2.1 Experimental setup

Emission channeling experiments can be performed either on-line or off-line. In on-line experiments, the emission channeling measurements are

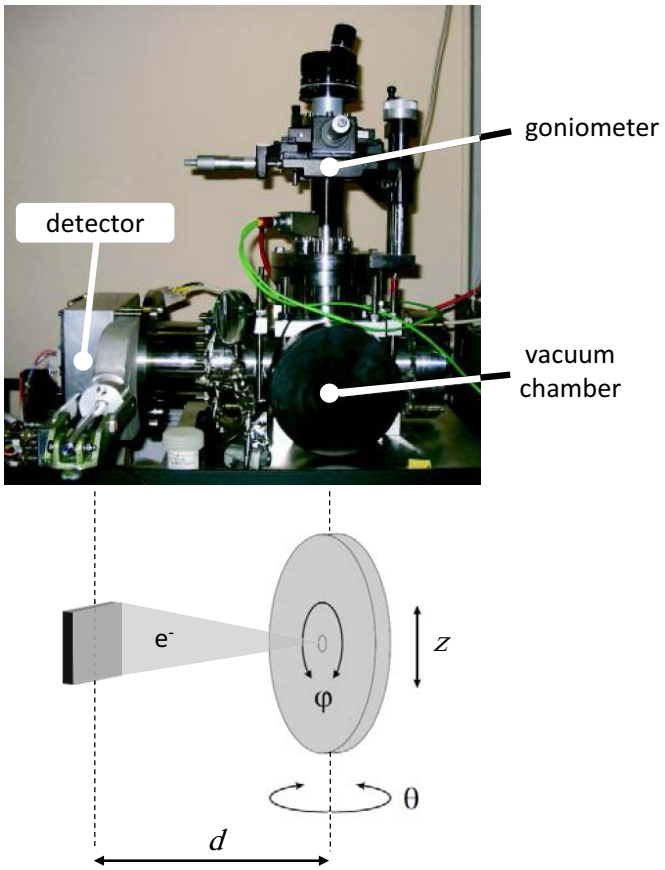

Figure 3.7: (Top) Picture of an off-line electron emission channeling setup with its three basic components: high-vacuum chamber, goniometer and position-sensitive electron detector. (Bottom) Schematics of the detector's sensitive area and sample holder and of the degrees of freedom of the goniometer: vertical position (z) and polar (θ) and azimuthal (φ) rotation.

performed *in-situ*, i.e. in the same chamber as the radioactive implantations. This is necessary for experiments involving relatively short-lived isotopes, i.e. with half-lives of a few hours and below. In off-line experiments, the sample is transferred to an emission channeling setup after implantation with the (long-lived) probe isotope. The concept of such a setup is rather simple and relies on the ability to detect, as a function of angle, electrons emitted from the sample in the vicinity of a crystallographic axis. The three basic components are a high-vacuum chamber, a goniometer to rotate the sample holder, and a position-sensitive electron detector (Fig. 3.7).

High vacuum chamber. Inside a vacuum chamber ($< 10^{-5}$ mbar), the sample is mounted vertically, facing the detector, oriented in such a way that electrons emitted from the sample in the vicinity of a selected crystallographic axis reach the position-sensitive detector. The geometry of the chamber is such that it allows for the emission yield to be recorded as a function of angle in the form of 2-dimensional (2D) patterns.

Goniometer A two-axes goniometer allows the sample to be moved along the vertical direction (z in Fig. 3.7) and around two rotation axes (φ and θ in Fig. 3.7) with a typical angular precision of about 0.05°-0.1°. Note that, because 2D position-sensitive detectors are used, the accuracy of the goniometer does not affect the angular resolution of the measurements. The sample holder is equipped with a tungsten wire resistive heating device, which allows for the measurements to be performed at elevated temperatures and/or after *in-situ* vacuum annealing up to 900°C.

Position-sensitive detector The principle of operation of these detectors is based on integrating an array of separate detector cells (pads or pixels) on a single Si chip and individually contacting them on the surface by a pattern of conducting and insulating layers. The square-shaped sensitive area is $28.6 \times 28.6\,\mathrm{mm}^2$ and consists of 22×22 pixels (thus each of $1.3 \times 1.3\,\mathrm{mm}^2$). The multiplexed readout of all pads is triggered if the signal on the detector back plane, which is common to all pads, exceeds an externally set lower threshold. This readout procedure limits the count rate of the device to a maximum of about 250 events/s, which is sufficient for typical experiments with long-lived isotopes (half-life of several hours and above). This is the case for the

experiments performed in this work using the ^{59}Fe ($t_{1/2} = 44.5$ d) isotope. During the last few years, major technical developments allowed for the implementation of self-triggering readout chips for the Si pad detectors, enabling measurements during and/or immediately after implantation with count rates of up to several kHz. Installed on-line, such a system is able to measure shorter-lived isotopes, as is the case for the experiments performed in this work using ^{56}Mn ($t_{1/2} = 2.56$ h) and ^{61}Co ($t_{1/2} = 1.65$ h) as probe impurities.

3.3.2.2 Angular resolution

The experimental angular resolution is a key parameter in the quantitative analysis of emission channeling patterns. For a position-sensitive detection system, it depends on the distance between sample and detector, the position resolution of the detector, which may vary with energy and nature of the incoming particles, and on the size and shape of the projected beam spot. Assuming that both the position resolution of the detector and the projected beam spot distribution can be approximated as two-dimensional isotropic Gaussian distributions with standard deviations σ_d and σ_b, respectively, the total angular resolution is given by

$$\sigma_{ang} \approx \arctan\left(\frac{\sqrt{\sigma_d^2 + \sigma_b^2}}{d}\right) \approx \frac{\sqrt{\sigma_d^2 + \sigma_b^2}}{d} \tag{3.5}$$

where d is the distance between sample and detector. In most experiments, d is set to ≈ 30 cm in order to cover an angular range of 5°-6°, the relevant range in typical emission channeling patterns. When the channeling effects are very sharp, e.g. for high energy β^- decays, and a higher angular resolution is thus required, d can be set to ≈ 60 cm, which increases the angular resolution by roughly a factor of 2. Since, in either case, the resolution is limited by the size of the pixels ($\sim 1,3$ mm), it makes little difference to use a beam spot which is much smaller. As a trade-off between position resolution and beam transmission, a 1 mm beam spot is typically used, which requires beam collimation during implantation. Assuming that the standard deviations associated with the beam spot (σ_b) and the pixels (σ_d) are about half of their sizes, the angular resolution σ_{ang} is approximately 0.16° for $d = 30$ cm and 0.08° for $d = 60$ cm.

3.3.3 Data analysis procedures

Quantitative lattice location of the radioactive probes is obtained by fitting the theoretical patterns to experimental ones. In the following, we discuss the relevant input parameters for the calculations and describe the fitting procedure.

3.3.3.1 *Manybeam* calculations

Theoretical emission patterns are calculated using the *manybeam* program developed by Hofsäss and Lindner [7–9] and modified by Wahl [11]. The *manybeam* program calculates the angle-dependent emission channeling yields for any emitter lattice position along any crystallographic direction (typically for an angular range of 0° to 3° from the axes in steps of 0.05°).

The starting point for a *manybeam* calculation is the crystallographic structure of the host material. The 3-dimensional structure can be determined experimentally using X-ray diffraction and is well established for the materials used in this work. The *manybeam* formalism uses the 2-dimensional projections with respect to the channeling axes, which can be obtained from the 3-dimensional structures published in the literature. Another important input parameter is the vibration amplitude of the crystal atoms. The one-dimensional root mean square (rms) vibration amplitude u_1 can be determined experimentally from the Debye-Waller factors in X-ray absorption or diffraction experiments. Published values are used as input for the *manybeam* calculations.

The vibration amplitude of the *impurity* atoms can be predicted using the mass-defect approximation. The relation between the one-dimensional rms vibration amplitude u_1 and the Debye temperature Θ_D is given by [12]

$$u_1^2 = \frac{3\hbar T}{M k_B \Theta_D^2}\left[\varphi\left(\frac{\Theta_D}{T}\right) + \frac{\Theta_D}{4T}\right] \tag{3.6}$$

where M is the mass of the element in question, k_B the Boltzmann constant, Θ_D the Debye temperature and $\varphi(x)$ the Debye function defined as

$$\varphi(x) = \frac{1}{x}\int_0^x \frac{t\,dt}{e^t - 1} \tag{3.7}$$

Within the Debye model, the rms vibration amplitude of a mass defect, in this case the substitutional impurity atom which is assumed to be bound to its neighbors with the same elastic constants as the lattice ions, can be

estimated from the effective Debye temperature of the emitter Θ_D^{imp} as:

$$\Theta_D^{imp} = \Theta_D \sqrt{\frac{M}{M'}} \tag{3.8}$$

where Θ_D and M denote the Debye temperature and the mass of the host atom that is substituted by the foreign atom, while M' is the mass of the impurity [13]. The rms vibration amplitude u_1 of the impurity atom can thus be estimated using eq. (3.6) if one replaces the mass M by the impurity mass M' and uses the effective Debye temperature Θ_D^{imp}. Such estimates for the impurity vibration are only reference values. The actual displacement amplitudes are obtained from fitting the experimental patterns with theoretical ones calculated for a set of different rms displacement values. Large deviations (tenths of Å) from these reference values can be associated with static displacement of the impurity due to lattice relaxation in its vicinity. Such lattice relaxation may be caused by the impurity itself (a foreign atom that disturbs the crystal periodicity) or by the interaction between the impurities and neighboring native defects (vacancies and interstitials), i.e. impurity-defect complex formation. In principle, such impurity displacements are better described by a static displacement from the high-symmetry site. However, such relaxation effects may displace the impurities in various directions and by various distances, depending on the specific local structure of each impurity. The measured emission pattern can thus be a superposition of a distribution of sites in the vicinity of a high-symmetry site. In such cases, the occupied site may be relatively well described by the high-symmetry site with an rms displacement larger than the thermal vibration amplitude.

The output of the *manybeam* calculations, for a given material, channeling axis and impurity isotope, is a two-dimensional emission pattern for each impurity lattice site and rms displacement u_1. These patterns are *smoothed* using a Gaussian with $\sigma \simeq 0.1^\circ$ to account for the contribution of the 1 mm beam spot to the experimental angular resolution (see section 3.3.2.2). Higher values of σ may be used in order to account for, e.g., crystal mosaicity and extended damage due to high fluence implantation. The size and shape of the detector pads is taken into account by averaging over the simulated yield falling within the angular range $(0,26^\circ \times 0,26^\circ)$ of one pixel, resulting in the final theoretical emission pattern $\chi^{theo}(\theta,\phi)$. As an example, Fig. 3.8 shows the simulated emission patterns for ^{61}Co, β^- emitter, in different sites of the GaN wurtzite structure, around different

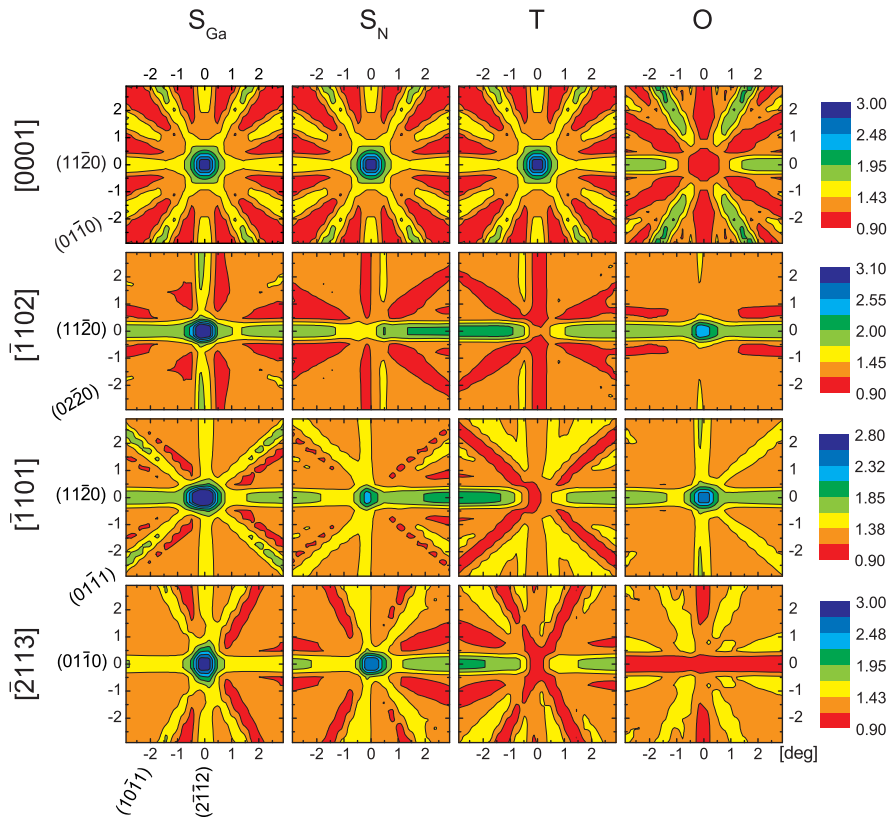

Figure 3.8: Simulated channeling patterns for ^{61}Co, β^- emitter, on substitutional Ga sites (S_{Ga}), substitutional N sites (S_N), and the interstitial T and O sites in the GaN wurtzite structure, around the [0001], [$\bar{1}$102], [$\bar{1}$101] and [$\bar{2}$113] crystallographic directions. Note that the [0001] patterns for the S_{Ga}, S_N and T sites are identical because they are located within the same atomic rows for that direction.

crystallographic directions.

3.3.3.2 Fitting procedures

The *FDD* program was developed by Wahl [14] to perform the quantitative analysis of the experimental 2D patterns $\chi^{exp}(\theta, \phi)$ by fitting a linear combination of the calculated yields $\chi^{theo}(\theta, \phi)$. The fitting routines allow

up to n occupied sites according to

$$\chi^{exp}(\theta,\phi) = S\left[f_{rand} + \sum_{i=1}^{n} f_i \chi_i^{theo}(\theta,\phi)\right] \tag{3.9}$$

where S is a scaling factor and f_i denotes the fraction of emitter atoms occupying the i^{th} site. The random fraction f_{rand} accounts for emitter atoms which do not contribute significantly to the anisotropy of the pattern. These can be either located on sites with very low crystal symmetry or in heavily damaged (or even amorphous) surroundings or have a random occupation of several minority lattice sites. Because the sum of all the fractions must amount to 1, f_{rand} is given by

$$f_{rand} = 1 - \sum_{i=1}^{n} f_i. \tag{3.10}$$

Using non-linear least squares fitting routines, *FDD* determines the best fit values of S, f_i, x_0, y_0 and ϕ_0 simultaneously. Parameters x_0 and y_0 are the coordinates of the channeling axis on the detector plane (i.e. the "center" of the pattern) and ϕ_0 is an azimuthal rotation angle of the pattern with respect to the channeling axis. S, x_0, y_0 and ϕ_0 are always allowed to vary in order to provide correct normalization of the experimental spectra and to achieve optimum translational and azimuthal orientation with respect to the detector. Typically only up to three different sites are considered in the fit, as the fitting routine loses sensitivity with increasing number of sites, i.e. with increasing number of f_i degrees of freedom.

3.3.3.3 Scattered electron background correction

In an emission channeling experiment, two types of electrons reach the detector: *direct* and *scattered* electrons. Those with initial direction in the vicinity of the detection axis are *direct* electrons. The number of *direct* electrons is roughly given by the ratio between the solid angle Ω spanned by the detector relative to the beam spot and the full 4π solid angle into which all the electrons are (almost) isotropically emitted, i.e. $\Omega/4\pi$ of the total number of decays. However, the number of detected electrons is always larger than this estimate. The additional *scattered* electrons are not emitted towards the detector initially, but still reach it after being scattered. The scattering event may occur inside the sample, when an electron is scattered by the host atoms, or outside the sample, by setup parts (including

backscattering from sample holder). These *scattered* electrons constitute an additional isotropic background in the experimental emission yields, which is not taken into account in the theoretical framework of channeling that is implemented in the *manybeam* program. The problem is different for conversion electrons and β^- particles:

Conversion electron decay. For a pure conversion electron decay, it is possible to deduce the total scattering background from the experimental energy spectrum. While, for direct electrons, the energy spectrum consists of a set of narrow peaks at well defined energies, the scattered electrons form tails at lower energies due to the energy lost in the scatter process. It is thus possible to correct for this scattering background by estimating (integrating the counts in the tails) and subtracting it from the experimental yields.

Beta decay Because such a simple estimate is not possible for β^- decays, with continuous energy spectra, De Vries [15] developed the computer program *Pad* based on the Geant4 toolkit (a set of libraries and tools to simulate the interaction of energetic particles with matter) [16,17]. Using the Monte-Carlo method, *Pad* simulates the propagation of electrons emitted from the sample and, among the ones that reach the detector, distinguishes the direct from the scattered ones. This requires detailed input information: the sample's geometry and composition, the β^- decay energy spectrum (isotope-specific) and the exact geometry of the setup, i.e. the position, shape and composition of the setup parts. From the *Pad* simulations it is possible to estimate the background correction factor f as

$$f = \frac{\text{total electrons}}{\text{total electrons} - \text{scattered electrons}} = \frac{\text{total electrons}}{\text{direct electrons}}. \quad (3.11)$$

This f factor can be used to correct the experimental patterns before the fitting or, equivalently, as a rescaling factor of the fractions determined from it.

3.4 Magnetic characterization: superconducting quantum interference device (SQUID) magnetometry

In DMS materials, the already small magnetic moment of a small amount of (presumably) magnetic material (< 1 μm film or implanted layer) is further decreased by the low concentration of magnetic dipoles (such as the localized $3d$ moments of the transition metal impurities) and their small magnetic moment (in many cases, only a fraction of a Bohr magneton). The magnetic moment of a typical DMS sample is usually between 10^{-7} and 10^{-4} emu (10^{-10} and 10^{-7} A m^2), thus requiring the high sensitivity of SQUID magnetometry.

A SQUID magnetometer measures the magnetic moment of a sample by moving it through superconducting detection coils. The detection coils are connected to the SQUID device through superconducting wires, allowing the current from the detection coils to inductively couple to a SQUID sensor (based on a Josephson junction). As the sample moves through the detection coils, the magnetic moment of the sample induces an electric current in the detection coils. The detection coils, the connecting wires and the SQUID input coil form a closed superconducting loop. Any change in the magnetic flux in the detection coils produces a change in the persistent current in the detection circuit, proportional to the change in magnetic flux. Since the SQUID works as a highly linear current-to-voltage converter, the variations in the current in the detection coils produce corresponding variations in the SQUID output voltage which are proportional to the magnetic moment of the sample.

In a fully calibrated system, measurements of the voltage variation as the sample is moved through the detection coils provide a highly accurate measurement of the magnetic moment of the sample (with a resolution down to 10^{-8} emu). However, magnetic contamination and measurement artifacts must be carefully taken into account in the $< 10^{-4}$ emu range. In order for SQUID magnetometry to be used as a reliable tool for the detection of ferromagnetism in DMS materials, it is necessary to develop methods and procedures which ensure that the magnetic signal originating from contamination and other artifacts can be reproducibly kept below a well defined value. This is described next, in Article I.

Article I

Practical limits for detection of ferromagnetism using highly sensitive magnetometry techniques

L. M. C. Pereira,[1,2,3] J. P. Araújo,[2] M. J. Van Bael,[4] K. Temst,[1] and A. Vantomme[1]

[1]*Instituut voor Kern- en Stralingsfysica and INPAC, K.U.Leuven, B-3001 Leuven, Belgium*
[2]*IFIMUP and IN-Institute of Nanoscience and Nanotechnology, Faculdade de Ciências da Universidade do Porto, 4169-007 Porto, Portugal*
[3]*Instituto Tecnológico e Nuclear, 2686-953, Sacavém, Portugal*
[4]*Laboratory of Solid-State Physics and Magnetism and INPAC, K.U.Leuven, 3001 Leuven, Belgium*

Abstract

Over the last ten years, signatures of high temperature ferromagnetism have been found in thin films and nanoparticles of various materials which are non-ferromagnetic in bulk, from semiconductors to superconductors. These studies often involve state-of-the-art magnetometers working close to the limits of their sensitivity, where magnetic contaminations and measurement artefacts become non-negligible. Because such spurious effects may be involved, the reliability of magnetometry techniques for the detection of ferromagnetism in these new magnetic nanomaterials has been questioned. In this paper, we present a detailed study on magnetic contamination arising from sample processing and handling, describing how it may occur and how it can be avoided or otherwise removed. We demonstrate that, when proper procedures are followed, extrinsic magnetic signals can be reproducibly kept below 5×10^{-7} emu (5×10^{-10} Am^2). We also give an overview of the expected levels of contamination when such optimum conditions can not be guaranteed and analyze the characteristics of the resulting magnetic behaviour, discussing which features may or may not be used as criteria to distinguish it from intrinsic ferromagnetism. Although the measurements were performed using superconducting quantum interference device (SQUID) magnetometers, most of what we describe can also be applied when using alternating-gradient force (AGFM) and vibrating-sample (VSM) magnetometers.

Journal of Physics D: Applied Physics **44**, 215001 (2011)

I. INTRODUCTION

Nano-objects with a magnetic signal comparable to that of the diamagnetic substrates on which they are deposited pose new challenges to state-of-the-art magnetometry and its users. With unrivaled sensitivity, superconducting quantum interference device (SQUID) magnetometers have long been proved suitable for the study of nano-versions of well understood materials, e.g., thin films or nanoparticles of magnetic materials and superconductors. However, when studying new materials exhibiting magnetic behaviour close to the limits of SQUID sensitivity, small magnetic contaminations and measurement artefacts must be carefully taken into account. This can be the case when studying, for example, dilute magnetic semiconductors (DMS), undoped oxides and superconductors, claimed to exhibit room temperature ferromagnetism (RT-FM) in thin-film or nanoparticle form. For many of these materials, RT-FM has been reported independently by various groups, the large majority based on SQUID magnetometry. However, an increasing number of reports suggest or even demonstrate that the observed ferromagnetism may originate from extrinsic sources, such as magnetic contamination[1,2] or measurement artefacts.[3]

Typically in these material systems, the already small signal of a small amount of (presumably) magnetic material is further decreased by the low concentration of magnetic dipoles and their small magnetic moment. To illustrate, let us consider a 5×5 mm^2 sample consisting of 10 monolayers of a material with a surface density of 1×10^{15} atoms per cm^2 per monolayer from which 1% are dopant atoms or other magnetic point defects with a magnetic moment of 1 μ_B. Such a sample, be it a continuous thin-film or nanostructures deposited on a diamagnetic substrate, has a total saturation moment of about 2×10^{-7} emu (200 nemu) on a diamagnetic background. This can be thought of as the *nanomagnet* regime, where a nanoscale magnet (nm size) carries a nano-moment (nemu moment). However, this is also the regime where magnetic contamination and measurement artefacts become non-negligible. While some authors continue reporting on the ferromagnetic properties of these new nanomagnets solely based on SQUID measurements, the general opinion is moving towards the notion that finding a signature of ferromagnetism by means of SQUID magnetometry, i.e. a magnetic hysteresis, is only necessary but not sufficient to claim its existence.[3]

Indeed, magnetometry by itself is insufficient to fully establish the magnetic nature of a given material, as it measures the total magnetic moment

without any microscopic information. However, it provides in many cases information that other techniques hardly can assess. X-ray magnetic circular dichroism (XMCD) and polarized neutron reflectometry (PNR) suffer from limited detection power in dilute systems, in addition to the fact that they are only available at synchrotron and neutron facilities, respectively. Mössbauer and perturbed angular correlation (PAC) spectroscopies and other techniques based on hyperfine interactions are only applicable to a limited number of elements of the periodic table. Magneto-transport measurements may indirectly provide information about the magnetic character of a material system but require the input of models which do not exist when the underlying magnetic mechanisms are unknown. In other words, SQUID magnetometry is to a large extent irreplaceable. However, in order to reproducibly establish its reliability limits when measuring very small magnetic moments, the sources of extrinsic magnetism should be investigated and either strategies to minimize them or criteria to identify them should to be outlined.

In this context, extrinsic magnetism can be distinguished between (i) setup-related artefacts leading to the misidentification of the magnetic state of a sample and (ii) magnetic contamination, i.e. magnetic material which is accidentally incorporated in the sample bulk or deposited on its surface and, therefore, is not accounted for in its nominal composition. A number of artefacts and limitations associated with SQUID magnetometers (i) have been identified in previous studies (e.g. Refs. 3–7) as leading to various effects such as a small dependence of the measured magnetic moment on the sample size or shape or signal discontinuities due to automatic scale adjustment. All of these must be taken into account, in particular when high precision is desired. However, with one notable exception, none of these artefacts is capable of emulating ferromagnetism where it does not exist. The exception, recently identified and described in Ref. 3, consists of residual ferromagnetic-like hysteresis attributed to a small magnetic flux trapped in the superconducting coil. Also recently, various sources of magnetic contamination (ii) were identified.[2] The main conclusion from these studies is that artefacts inherent to SQUID magnetometers (i) can result in hysteresis with up to 4×10^{-7} emu of saturation moment, whereas those associated with magnetic contamination (ii) due to sample handling or mounting can be as high as 1×10^{-4} emu. Residual magnetic hysteresis and other artefacts constitute a technical limitation of the setup, and thereby set the lowest achievable limit for detection of ferromagnetism. If SQUID magnetometers are to be used as reliable tools to characterize nanomag-

nets, methods and procedures should be developed which ensure that the magnetic signal originating from contamination can be reproducibly kept below a well defined value, ideally of the same order or smaller than that from artefacts (10^{-7} emu), in order to make full use of the setup sensitivity.

In this paper, we present a detailed study on magnetic contamination (10^{-7} to 10^{-4} emu) arising from sample processing and handling. Purely diamagnetic substrates were used in order to isolate the magnetic contribution from the contaminant material. To ensure a statistically representative sample, we measured more than 50 pieces of commonly used substrates, Al_2O_3, Si, ZnO, MgO and $SrTiO_3$, of various thicknesses and suppliers, subject to various handling, processing and sample-mounting conditions. We investigated how contamination may occur and how it can be avoided or otherwise removed. We also analyzed the characteristics of the contaminant magnetism, discussing which features may or may not be used as criteria to distinguish it from intrinsic ferromagnetism. Although all the measurements were performed using superconducting quantum interference device (SQUID) magnetometers, most of what we describe can be applied when using alternating-gradient force (AGFM) and vibrating-sample (VSM) magnetometers.

II. EXPERIMENTAL DETAILS

The measurements were performed with the commonly used MPMS magnetometers from Quantum Design.[8] The majority was performed with an MPMS-XL (5 T) using the RSO option which provides higher sensitivity compared to the standard dc-transport mode. For comparison and completeness, some measurements were performed with a MPMS-5 (5.5 T), both in RSO and dc-transport modes. The samples consisted of approximately 5×5 mm^2 pieces of the commonly used substrates Al_2O_3, Si, ZnO, MgO and $SrTiO_3$, of various thicknesses ($t = 0.1 - 2$ mm) and suppliers (Crystal GmbH, CrysTec GmbH, MaTecK GmbH and SPC Goodwill Co. Ltd.). Given the large amount of samples, the measurements were simplified whenever possible. In most cases, the parameter to be determined was simply the saturation moment of the ferromagnetic component at 300 K, for which the *M-H* data were measured only for decreasing field (half-loops) and with a small number of field steps. Unless mentioned otherwise, all measurements were performed with the sample plane parallel to the applied field.

III. RESULTS AND DISCUSSION

A. How contamination can occur

1. Sample mounting

It is known that the sample mounting itself can contribute to a FM-like background, even if the sample is not contaminated.[2] As recommended by Quantum Design, clear plastic drinking straws are typically used as sample holders in SQUID magnetometers. Commercial cotton or Kapton® tape are commonly used to hold the sample inside the straw. Both Kapton® and cotton are diamagnetic materials. It is however known that the use of these materials can contribute to a FM-like background with a saturation moment of up to the order of 10^{-5} emu.[2] An alternative is to hold the sample simply by clamping it with the straw itself, avoiding the presence of additional material in the probed region. In principle, the deformations induced in the straw are minimal, behave linearly in field and are virtually temperature independent. However, special care must be taken when applying this method, as straw deformations have been reported to introduce a ferromagnetic-like background with a saturation magnetization of up to 1×10^{-6} emu.[2] Furthermore, this *freestanding* method imposes some constraints on sample size and shape in order to ensure that the sample remains in place. A convenient alternative is to hold the sample with a polyester or cotton thread across the straw, tied around the sample, and held tight and straight by fixing it to the ends of the straw. This contributes with only a small amount of diamagnetic material around the sample, as the contribution from the remaining material cancels out due to its axial symmetry. If the material composing the thread is diamagnetic and free from ferromagnetic contaminations it does not contribute to any FM-like background within SQUID sensitivity. Colored thread should be avoided as some of the commonly used pigments are magnetic. In any case, the materials that are used for sample mounting must always be tested, as they may be contaminated during production or handling in the laboratory. Figure 1 shows the 300 K *M-H* data (magnetic moment as a function of field) of such a thread-mounting scheme, without any sample, to isolate the contribution from the thread. The raw data (a) show an almost perfectly linear behaviour corresponding to a very small diamagnetic susceptibility. Subtracting this diamagnetic (linear) component results in a residual signal (b)

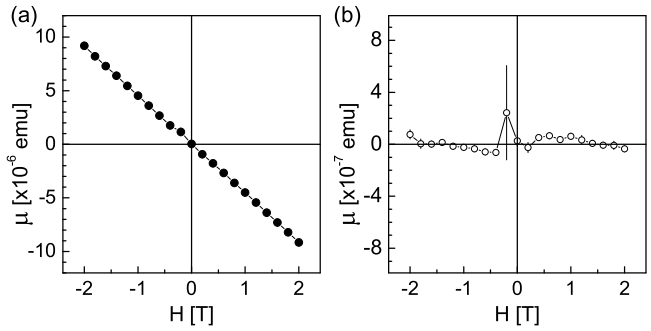

FIG. 1: Example of *M-H* data at 300 K for typical thread-mounting, without any sample in order to isolate the background due to the thread (emu = 10^{-3} A m^2): (a) raw data measured between 2 T and -2 T; (b) after subtraction of the diamagnetic component determined by a linear fit to the raw data. The error bars correspond to the standard deviation of 5 consecutive measurements.

with absolute value below 1×10^{-7} emu, of the order of the system precision. Our tests revealed background levels consistently below 1×10^{-7} emu. Unless mentioned otherwise, all the data that are shown in the following have been measured using this sample-mounting scheme.

2. Cleaving and handling

The simplest and most obvious source of contamination is the contact with Fe-containing tools or setup parts. These can be the sample holder or clamps used during growth or post-growth treatments, tweezers and other tools used to manipulate a sample, or even non-Fe based tools or parts which have previously contacted magnetic materials. Among these, the most common source of contamination is probably the sample cleaving, even when a diamond stencil is used, since it is almost impossible to ensure that the rod, to which the diamond (or SiC piece) is attached, does not touch the sample. If the rod is composed of a ferromagnetic material, e.g., stainless-steel (SS), small magnetic particles can be deposited upon contact, depending on the hardness of the sample material and the pressure involved in the transfer process. Stronger contamination can occur, for example, when a sample is cleaved using a SS blade, a common alternative for substrates thicker than 0.5 mm. In this case, a much larger pressure is applied, as the blade is hammered onto the sample or substrate. The

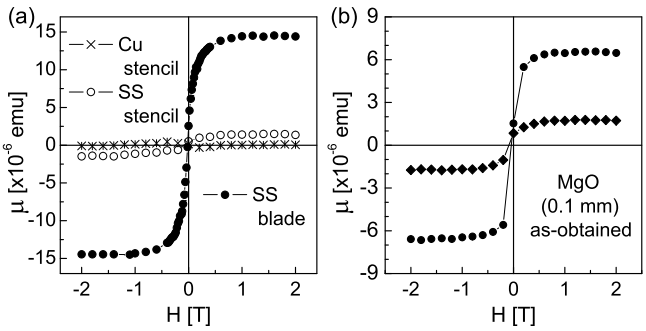

FIG. 2: (a) 300 K *M-H* half-loops of ZnO (0.33 mm) samples which have been cleaved using a diamond-on-Cu stencil and a diamond-on-SS stencil and a $SrTiO_3$ (1 mm) sample cleaved with a SS blade. (b) 300 K *M-H* half-loops of pieces from two different MgO (0.1 mm) substrates, cleaved by simply pressing the very thin substrate while still inside the enclosing paper, as received from the supplier (emu = 10^{-3} A m^2).

effect of cleaving on the magnetic response is illustrated in Fig. 2 (a) which shows the 300 K *M-H* half-loops of ZnO samples which have been cleaved using a Cu stencil (diamond on a Cu rod) or a SS stencil (diamond on a SS rod) and a thick $SrTiO_3$ sample (t = 1 mm) cleaved with a SS blade. The diamagnetic background was estimated by a linear fit between 1 T and 2 T and subtracted from the data. Cleaving ZnO with a Cu stencil did not introduce a measurable contamination. However, cleaving it with a SS stencil resulted in a FM-like signal with a saturation moment of 1.5×10^{-6} emu. Cleaving $SrTiO_3$ with a SS blade resulted in an even stronger contamination (1.4×10^{-5} emu). Similar effects can be induced by contact with parts made of Ni- and Co-containing alloys, typically used in oxide-deposition setups.

Magnetic contamination can also occur when inks or silver paint are used for markings or for electrical contacts, respectively. These can contribute with a few μemu to a FM-like background[2] and should therefore be avoided prior to any magnetic characterization.

3. As-obtained substrates

Surprisingly, some substrates may already be contaminated as received from the supplier. Figure 2 (b) shows the 300 K *M-H* half-loops of pieces

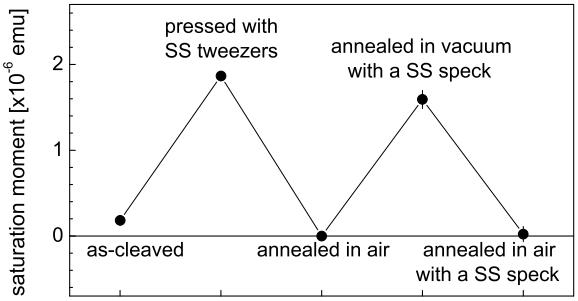

FIG. 3: Saturation moment at 300 K of the same ZnO sample measured in four consecutive stages (emu = 10^{-3} A m^2): as-cleaved using a diamond-on-Cu stencil, pressed with a pair of SS tweezers, annealed at 900 °C in air for 10 min, annealed in vacuum under the same conditions but with a small SS speck on top and, finally, annealed in air once again.

from two different MgO (0.1 mm) substrates. The pieces were cleaved by simply pressing the very thin substrate while still inside the enclosing paper, as received from the supplier, thereby avoiding any contact with a possibly contaminating cutting tool. The saturation moment varies considerably among substrates between 10^{-6} and 10^{-5} emu. By measuring different pieces from the same substrate, we observed that the magnitude of the signal scales with the sample mass within 1%, irrespective of belonging to the border or to the interior of the substrate. This indicates that the contaminant material was uniformly distributed on the substrate surface, most likely during the polishing process. However rare, this shows the importance of a careful pre-characterization of the substrates.

4. High temperature processing / annealing

In general, heating up a sample in contact with metallic parts results in material transfer, even if the contact is point-like. In fact, material can even be evaporated from heated metallic parts and deposited on the sample without direct contact. This applies to high temperature film-growth as well as post-growth annealing. The particular physical and chemical reactions that take place depend on the materials involved and the temperature, atmosphere and duration of the process. Figure 3 shows the saturation moment measured at 300 K of the same ZnO sample in four consecutive stages

of contamination and annealing. The non-magnetic ZnO sample becomes FM after being pressed with SS tweezers. The same occurs after annealing in vacuum at 900 °C for 10 min in contact with a small SS speck (few mg scraped from SS tweezers) placed on the sample surface before annealing and removed afterwards. For both types of contamination, annealing in air renders the sample again non-magnetic, most likely due to either oxidation or desorption of the contaminant material. We observed, although rarely, that annealing in *vacuum* can also reduce the contaminant magnetization, most likely due to desorption. These effects must be considered very carefully when studying, for example, the effect of annealing atmosphere on the magnetic properties of dilute magnetic semiconductors. Such reversibility phenomena can appear to provide evidence for the role of defects, introduced and removed by annealing in different atmospheres, in stabilizing the ferromagnetic state.

In order to minimize contamination, sample-holders made of non-metallic materials such as machinable ceramics should be used at all the steps of sample processing. However, this may be insufficient. Repeated use of the equipment can result in deposition of magnetic material in initially non-magnetic parts. For example, we have observed that, if the annealing setup is not properly cleaned and baked out, magnetic material with up to 5×10^{-6} emu of saturation moment can be deposited on a sample during annealing even when it is performed in vacuum and using a ceramic sample holder.

5. Accidental (re)contamination in metal-free conditions

We have observed that even avoiding the contaminating conditions described above, some samples may accidentally become (re)contaminated. This is likely to originate from Fe-containing dust particles or other airborne magnetic debris easily found in laboratories where magnetic materials are synthesized or characterized. Such contaminant material can deposit on a sample directly or by transfer from otherwise non-magnetic tools or parts. Although the contribution from each of these random events is typically of the order of 10^{-6} emu, they can accumulate, depending on how many processing steps and how much exposure time precedes the magnetic characterization.

6. Summary

Figure 4 (a) summarizes the different levels of contamination discussed above. In general, the oxides appear to suffer from higher contamination levels compared to Si, which reflects that metal particles are more easily abraded by harder materials. Whenever Fe-containing tools were used, the level of contamination reached an order of magnitude of 10^{-5} emu. On the other hand, they can be consistently kept below 1×10^{-6} emu using only tools made of non-magnetic materials such as plastic, carbon fiber or copper. We note, however, that this corresponds to single-event contamination. For real samples, if the magnetic characterization is performed after several processing steps, the effects may accumulate. Moreover, the summary in Fig. 4 (a) does not include the effect of high temperature processing, which by itself can contribute with signals of the order of 10^{-6} emu.

B. How the contaminant material can be removed

So far we demonstrated that the magnetic signal originating from contaminant material can be consistently kept below 1×10^{-6} emu when proper procedures are followed. Nonetheless, real samples may suffer from multiple contamination events and accumulate larger magnetic signals, and in some cases, potentially contaminating conditions simply can not be avoided, e.g., when the substrates are already contaminated as received. In such cases, a suitable cleaning procedure is required for the removal of the contaminant material. Although acid cleaning procedures are standard for Si processing, most of the materials under consideration in this work (oxides) can be degraded by acids. Alternatively, we observed that cleaning the samples in consecutive ultrasound baths of acetone, 2-propanol and ultrapure water, for 5 min each, reduces the contamination considerably. In most cases, repeating this cycle for a number of times reduces it even further. We observed that the magnetic signal originating from the contaminant material reaches a minimum and saturates typically after three cycles. This is illustrated in Fig. 5 (a) where the saturation moment at 300 K is shown for various representative examples after consecutive cleaning cycles: a ZnO sample cleaved with a diamond-on-SS stencil, an MgO (0.1 mm) sample contaminated as received and an MgO (2 mm) sample cleaved with a SS blade. Figure 5 (b) shows the 300 K *M*-*H* half-loops of the MgO (0.1 mm)

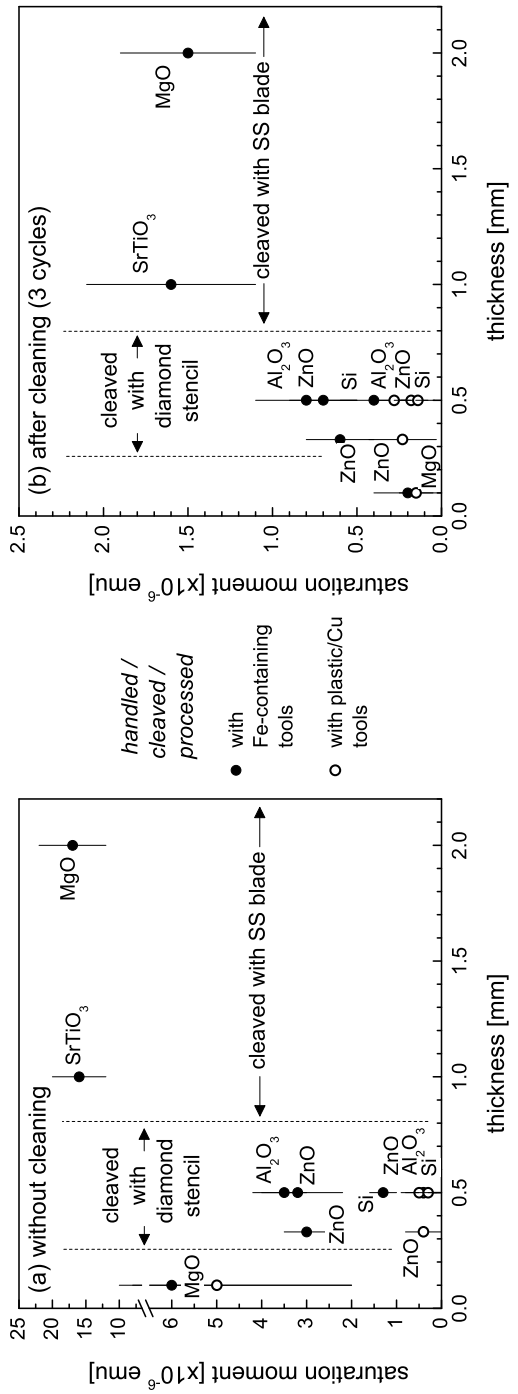

FIG. 4: Summary of the average contamination levels for the different substrate materials and thicknesses before (a) and after (b) three cleaning cycles as described in the text (emu = 10^{-3} A m^2). Averages were taken separately for the samples for which Fe-containing tools were used in any of the processing steps. As indicated, thicker samples (1 and 2 mm) were cleaved using a SS blade, whereas the samples of intermediate thickness (0.33 and 0.5 mm) were cleaved using a diamond stencil (Cu/SS rod for Fe-containing/Fe-free tools). The thinnest MgO substrates (0.1 mm) were cleaved by simply pressing them with plastic tweezers while still inside the enclosing paper, as-received from the supplier. The effect of high temperature processing is not included. The error bars correspond to the standard deviation. Note that the maximum scale in panels (a) and (b) differs by one order of magnitude.

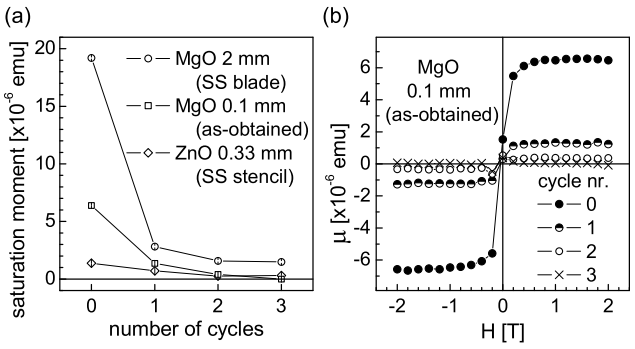

FIG. 5: Representative examples of the effect of the cleaning procedure: (a) saturation moment (300 K) after each cleaning cycle of an MgO (2 mm) sample cleaved using a SS blade, an MgO (0.1 mm) sample contaminated as received by the supplier and a ZnO (0.33 mm) sample cleaved using a diamond-on-SS stencil; (b) 300 K *M-H* half-loops of the MgO (0.1 mm) sample (emu = 10^{-3} A m^2). Each cycle consists of three consecutive ultrasound baths in acetone, 2-propanol and ultrapure water, 5 min each.

sample after each cleaning cycle.

Typically, the cleaning is very efficient when the pressure involved in the process of material transfer is small, as when scratching the back of a substrate with a diamond stencil. However, when the pressure is large enough, e.g., when cleaving a sample by hammering it with a SS blade, or when the contaminated sample has been subject to high temperatures, the contaminating material may not be completely removed. In these cases, as shown in Fig. 6 (a), the strong adhesion with the sample prevents the complete removal of the contaminant material even when new chemicals (to prevent saturation) and higher temperatures (to increase the cleaning efficiency) are used. Moreover, our experience indicates that many short cycles are more efficient than a few long ones, e.g., three 5 min cycles instead of one of 15 min.

As described above, some of the studied samples were accidentally contaminated even in controlled conditions. Figure 6 (b) shows two of these cases. The increase in saturation moment indicates that these samples were contaminated between the end of the corresponding cleaning cycle and the start of the measurement, despite the efforts to avoid contaminating conditions. Interestingly, the nature of the contamination seems to differ from one case to the other. In only one of them, the contaminant material can be removed completely by cleaning.

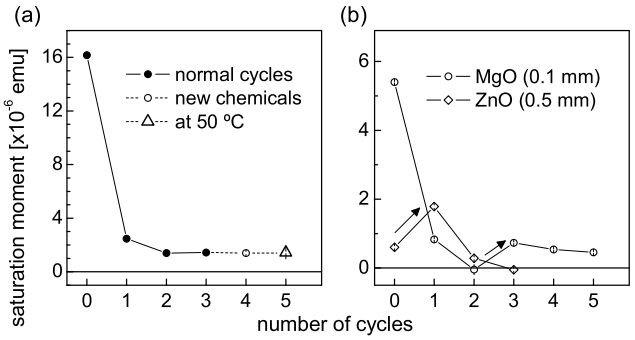

FIG. 6: Saturation moment after each cleaning cycle for two non-typical cases (emu = 10^{-3} A m^2): (a) attempts to eliminate persistent contamination on an MgO (2 mm) substrate (cleaved with a SS blade) using new chemicals (○) and carrying out the baths at 50 °C (△); (b) MgO and ZnO samples accidentally recontaminated between cleaning cycles (↗). Note that the error bars are included (although too small to be visible), taking into account the experimental error and reproducibility limits (of the order of 10^{-7} emu).

Figure 4 (b) gives an overview of the persistent-contamination levels that are achievable with the described cleaning procedure. For the samples that had been in contact with Fe-containing materials, these are of the order of 10^{-6} emu. Remarkably, contamination levels below 5×10^{-7} emu can be consistently achieved after cleaning if the samples have not contacted Fe-containing materials.

The applicability of such cleaning procedures is a trade-off between the required sensitivity for a given experiment and possible undesired effects of the cleaning. The ultrasound bath may damage the sample if it consists, for example, of nanostructures deposited on a substrate with poor adhesion. Also, H diffusion into the sample may be promoted or accelerated by the immersion in water, acetone or 2-propanol, and modify the sample's electrical and magnetic properties. By means of hydrogen forward scattering spectrometry (HFS), we investigated the hydrogenation effects of a 3-cycle cleaning sequence on the different materials used in this study (data not shown). We found that the cleaning procedure does not introduce measurable amounts of H within the HFS sensitivity ($< 1\%$). We note, however, that this is the case for the high-quality single-crystalline materials that we have studied. In real samples, such as thin films and nanostructures deposited onto these substrates, with possibly lower crystalline quality and therefore lower diffusion barriers, hydrogenation may occur.

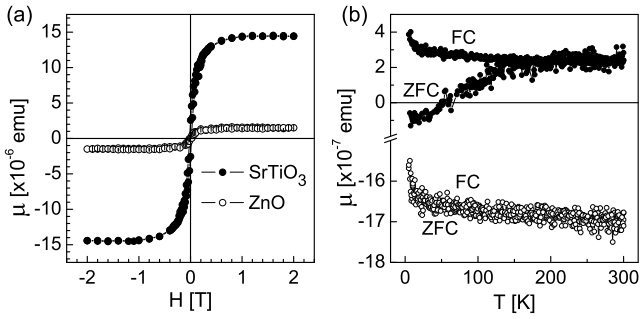

FIG. 7: *M-H* and *M-T* data of a $SrTiO_3$ sample cleaved with a SS blade and a ZnO sample pressed with SS tweezers: (a) 300 K *M-H* full loops (2 T → -2 T → 2T); (b) field-cooled (FC) and zero-field-cooled (ZFC) measurements, with a field of 10 mT (100 Oe) as described in the text (emu = 10^{-3} A m^2). Unlike the *M-H* data (a), the *M-T* data (b) have not been corrected from the diamagnetic component.

C. How to distinguish contaminant from intrinsic ferromagnetism

We have shown that a measurable magnetic contamination will most likely occur if proper procedures are not followed. In general, cleaning procedures can be applied, but in some cases they are unable to completely remove the contaminant material. In other cases, cleaning may not even be an option if it affects the intrinsic properties of the samples. Next, we analyze the magnetic behaviour of the contaminant material, discussing which features may or may not be used as criteria to distinguish it from intrinsic ferromagnetism in these cases where it can not be excluded that measurable contamination has occurred.

1. General M-H and M-T behaviour

Figure 7 shows the typical *M-H* and *M-T* behaviour of two contaminated samples with saturation moment in the 10^{-6} to 10^{-5} emu range. In general, both for weakly and strongly contaminated samples, the *M-H* curves show a coercivity of 10 – 100 mT (100 – 1000 Oe) and a remanence of 10% – 20% of the saturation moment. The field-cooled (FC) and zero-field-cooled (ZFC) measurements[9] of the sample with higher saturation magnetization ($SrTiO_3$) show some degree of irreversibility which disapears

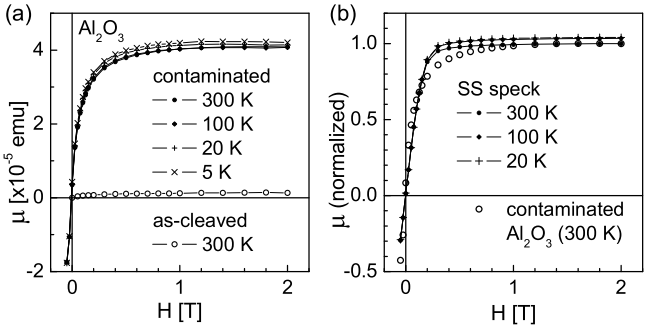

FIG. 8: Comparison between *M-H* data for positive decreasing field at various temperatures: (a) Al_2O_3 sample before (at 300 K) and after (at 5, 20, 100 and 300 K) being contaminated by SS tweezers; (b) 300 K *M-H* data of the contaminated Al_2O_3 sample compared to the 20 K, 100 K and 300 K *M-H* data of a small speck of the SS tweezers tip that caused the contamination (emu = 10^{-3} A m^2).

well below the Curie temperature ($T_C > 300K$). This is consistent with a scenario of superparamagnetic (SPM) behaviour of the metallic particles abraded from the SS blade. The ZnO sample does not show FC-ZFC irreversibility, which could be interpreted as a sign of a fundamentally different type of magnetic behaviour from that of the $SrTiO_3$ sample. We note, however, that the saturation moment of the ZnO sample is much smaller to start with [Fig. 7 (a)], i.e., the SPM component and consequently the expected FC-ZFC splitting are much smaller. Assuming the same linear correspondence between the saturation moment and the FC-ZFC splitting for both samples, the maximum FC-ZFC splitting expected for the ZnO sample is of about 5×10^{-8} emu, smaller than the experimental noise. Therefore, even though the ZnO sample shows measurable coercivity and remanence up to 300 K, FC-ZFC irreversibility is not observed because the possible splitting can not be resolved. We also note that the *M-T* data in Fig. 7 (b) have not been corrected from the diamagnetic component, which results in a shift of the data towards negative μ. This explains why the ZnO moment is negative and the $SrTiO_3$ ZFC curve crosses zero around 50 K. Because the diamagnetic susceptibility is larger for ZnO compared to $SrTiO_3$, this also explains the large off-set between the data for the two materials.

Figure 8 (a) shows the *M-H* data at different temperatures of an Al_2O_3 sample that has been intentionally contaminated using SS tweezers. Aside from a small increase in saturation moment with decreasing temperature (3% between 300 K and 5 K), characteristic of ferromagnetic materials with

a Curie temperature well above 300 K, the measured $\mu(H)$ is virtually temperature independent. For conventional SPM behaviour, $\mu(H)$ is given by a Brillouin function (Langevin in the continuous limit) which is a function of H/T. Therefore, for SPM behaviour, the saturation field at 300 K is expected to be about 60 times that at 5 K. This is clearly not the case; the observed saturation behaviour is the same. This indicates that the contaminant-particle size is above the single-domain regime, i.e., the Brillouin/Langevin behavior of single-domain (macro-spin) SPM particles does not hold. In Fig. 8 (b), the 300 K *M-H* data of the contaminated Al_2O_3 sample are compared to the 20, 100 and 300 K *M-H* data of a small speck of the SS tweezers tip that caused the contamination. The same temperature independence is observed. However, the saturation behaviour differs considerably between bulk and abraded material. This indicates that not only the nature of the contaminant material but also the size and shape of the abraded particles determines its magnetic properties.

In summary, the magnetic behaviour of the contaminant material ranges from SPM-like to weak ferromagnetism. It is generally characterized by a small coercivity and remanence, saturation fields of the order of 1 T and FC-ZFC splitting which may however be too small to be resolved. In some cases, most likely when the Curie temperature of the contaminant material is far beyond the measured range and the contaminant-particle size is above the single-domain regime, the ferromagnetic component of the *M-H* loops is virtually temperature independent. Unfortunately, rather than distinctive, these characteristics are in fact typical of the new magnetic nanomaterials mentioned in the introduction.

2. In-plane vs. out-of-plane anisotropy

Diamagnetism is an isotropic property. Superparamagnetic or ferromagnetic contaminant particles may display some degree of single-particle anisotropy but since they are randomly placed in a sample, their net magnetization should also be isotropic. Therefore, a diamagnetic substrate, even if contaminated with FM material, is not expected to show anisotropic magnetization with respect to the field direction. As such, anisotropy effects could in principle be used as a distinctive feature of intrinsic ferromagnetism. However, as we discuss next, the finite sample size or a non-uniform distribution of the contaminant material can lead to an apparent anisotropy when comparing measurements performed with the field parallel (in-plane)

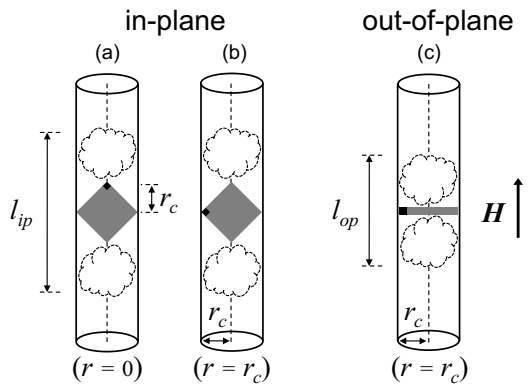

FIG. 9: Diagram illustrating possible sources of *radial* and *axial* anisotropy artefacts for in-plane [(a) and (b)] and out-of-plane (c) measurements, as described in the text. The cylinders represent measuring straws and the samples are depicted in gray. *Radial effects* can be created by the contaminant material (depicted as black squares on the samples edges) at a distance r_c from the sample center and r from the measuring axis (vertical). *Axial effects* can be created, for example, when contaminated cotton is used to hold the sample (depicted above and below the samples), resulting in apparently different sample sizes (l_{ip} and l_{op}).

and normal (out-of plane) to the sample surface.

Similar to other extraction techniques, SQUID magnetometers rely on the response of pickup coils to changes in the magnetic flux as the sample is scanned through the coils. The response depends not only on the magnitude of the sample magnetic moment, i.e., of the ensemble of point dipoles, but also on their orientation and position with respect to the pickup coils. For non-spherical samples this automatically results in an apparent in-plane *vs.* out-of-plane anisotropy, even in the ideal case for which the diamagnetic and ferromagnetic components are uniformly distributed in the sample volume. For typical sample geometries, approximately $5 \times 5 \times 1$ mm^3, the measured magnetization is apparently larger by 3-4% in out-of-plane measurements, as demonstrated theoretically and experimentally in Ref. 7 and 3, respectively. This affects both diamagnetic and ferromagnetic components, and thus emulates a small magnetic anisotropy. Stronger anisotropy effects are created by non-ideal conditions, such as spatial asymmetries or non-uniformities of the ferromagnetic volume. Due to the cylindrical symmetry of the axial second-order gradiometers commonly used in SQUID magnetometers, these anisotropy artefacts can be divided into radial and axial effects.

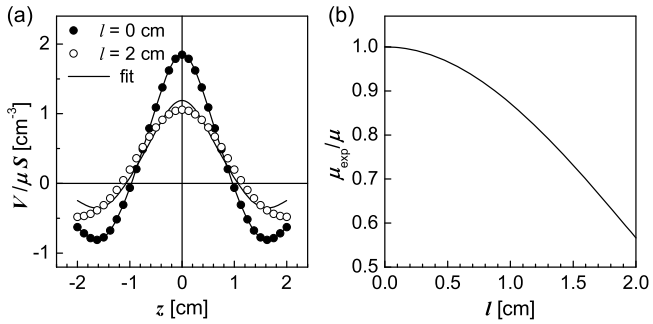

FIG. 10: (a) Response curves ($V(z)$) for scans of two samples with equal magnetic moment μ and different geometries, simulated ($\circ$ and $\bullet$) using the finite elements calculation described in the text and best fits (line) of equation (1) using an algorithm similar to that used by the MPMS MultiVu application to deduce the measured moment $\mu_{\rm exp}$: a point-like dipole ($\bullet$) and a line-like sample with length $l = 2$ cm along the gradiometer axis ($\circ$). (b) Fitted $\mu_{\rm exp}$ as a function of sample length l.

a. Radial effects are observed when the radial distribution of the ferromagnetic volume is significantly different for different measurement geometries. To illustrate, let us consider a square diamagnetic sample, centered within the pickup coils, with a point-like contamination in one of its edges at a distance r_B from the sample center (Fig. 9). By rotating the sample around its center, one can vary the radial distance r, of the ferromagnetic contamination relative to the longitudinal axis of the coils, between 0 and r_c [Fig. 9 (a) and (c)]. Since the magnetic flux across the coils increases with r (cf. Ref. 2), so does the measured moment. As such, in-plane measurements may yield a smaller magnetization if the sample is oriented so that $r = 0$ [Fig. 9 (a)], whereas for out-of-plane measurements, $r = r_c$ always [Fig. 9 (c)]. These radial effects have been discussed in Ref. 2, where a ferromagnetic component up to 40% larger when measuring out-of-plane has been reported. We note, however, that we have not observed a radial anisotropy larger than 10%. We also note that radial effects may as well result in purely in-plane anisotropy, since in-plane rotation around the sample center can also vary r between 0 and r_c [Fig. 9 (a) and (b)].

b. Axial effects are controlled by the longitudinal elongation of the magnetic volume. The response of a point dipole with magnetic moment μ, at point z on the measurement axis and aligned with it, is given by

$$V(z) = \mu S\{2(r_c^2 + z^2)^{-3/2} - [r_c^2 + (z + \Lambda)^2]^{-3/2} - [r_c^2 + (z - \Lambda)^2]^{-3/2}\}, \quad (1)$$

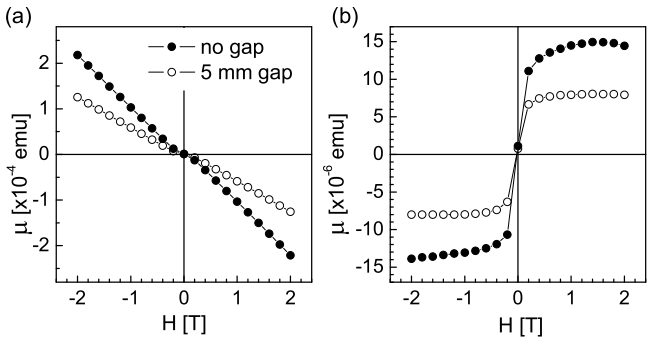

FIG. 11: M-H half-loops of two small cotton pieces inside a measuring straw with no gap (•) and with a 5 mm gap (◦) between them: (a) raw data; (b) data corrected from the diamagnetic component estimated between 1 and 2 T (emu = 10^{-3} A m^2).

where r_c is the coil radius (0.97 cm), Λ is the distance between an outermost coil and the central coils of the gradiometer (1.519 cm) and S is the calibration factor. Finite size samples with length l along the z-axis can be approximated as an ensemble of point dipoles along the sample length l, neglecting the radial dimension. The $V(z)$ scans can thus be simulated using a simple finite elements calculation and fitted to equation (1) using an algorithm similar to that used by the MPMS MultiVu application to deduce the measured moment $\mu_{\rm exp}$. This is shown in Fig. 10 (a) for two limiting cases with equal moment μ: a point-like dipole and a line-like sample with $l = 2$ cm. Figure 10 (b) shows how $\mu_{\rm exp}$ decreases with increasing sample length l. Within normal sample sizes (≤ 0.5 mm) the effect is negligible ($\leq 4\%$). However if the ferromagnetic signal is external to the sample, the effects may become significant. As mentioned above, in order to fix the position and orientation of a sample inside the measuring straw, it is common to use two small pieces of commercial cotton, which is typically contaminated with small ferromagnetic particles. If the sample is fixed between two pieces of cotton (Fig. 9), the distance between the two pieces is very small (of the order of the sample thickess) for out-of-plane measurements, whereas for in-plane measurements, it is increased to about the sample length. In terms of *apparent* sample length, this corresponds to an increase from l_{op} to l_{ip} (Fig. 9). Figure 11 shows the *M-H* half-loops of two small cotton pieces inside a measuring straw, emulating the two measurement geometries: touching (in-plane) and separated by 5 mm (out-of-plane). The anisotropy is close to 100% and affects equally the

diamagnetic and ferromagnetic components.

3. N-shaped $V(z)$ and kinks in $\mu(H)$

None of what we described so far can be used as a distinctive feature of contaminant magnetism. The search for such a fingerprint must therefore be extended to what is *experimentally* characteristic of measuring a contaminated sample, other than the magnetic behaviour itself. Indeed, one such feature has been identified, which results from an axial asymmetry of the ferromagnetic volume with respect to the *center of moment* of the uniformly magnetized diamagnetic (DM) sample. These artefacts have been studied in detail in Ref. 7 and are also discussed in the context of FM contaminations in Ref. 3. To illustrate, let us consider a typical square diamagnetic sample with a FM point-like contamination in one of the edges. Let us also assume that for a given field H_0 within the measured range, the magnetization is zero, i.e., the FM and DM components have the same magnitude but opposite signal, thus canceling each other. If the sample is mounted such that the contaminated edge is at the top or the bottom, the FM and DM *centers of moment* are displaced from each other by about half of the sample length. Therefore, close to H_0, instead of a $V(z)$ shape as in Fig. 10, one measures a superposition of two dipoles with opposite sign and separated by a few millimeters in the z direction. This produces an N-like shape, with a relative (absolute) maximum and a absolute (relative) minimum of comparable magnitude in the vicinity of H_0. This is always visible in the measured $V(z)$ data but can also affect the *M-H* (or similarly the *M-T*) curves as follows. Both *iterative* and *linear* fitting routines calculate the magnetic moment by mathematically fitting equation (1) to the measured response curve. The *linear* routine assumes a perfectly centered sample and therefore uses equation (1). For the *iterative* routine, z is substituted by $(z - z_0)$ in equation (1), where the additional free parameter z_0 accounts for possible sample miscentering along the z-axis. When the latter is used, since it always assumes a $V(z)$ curve with one absolute extremum (Fig. 10), the best fit will be obtained for z_0 equal to the position of the largest of the two extrema. Close to H_0, this results in a large fitted offset with opposite signs below and above H_0 and a discontinuity of the measured magnetic moment. We note, however, that these symptoms can only be interpreted as an indication of an asymmetric distribution of the FM material with respect to the DM substrate which, in many cases but

not necessarily, corresponds to the presence of contaminant material. Also, the absence of such effects can not be interpreted as evidence of absence of contamination. The distribution of the contaminant material projected onto the measurement axis may simply be symmetric enough to escape detection.

IV. CONCLUSIONS

In summary, we have established the practical limits of SQUID magnetometry for the detection of ferromagnetism in nanomaterials deposited on diamagnetic substrates with comparable magnetic signal. We have shown that, when proper procedures are followed, extrinsic magnetic signals can be reproducibly kept below 5×10^{-7} emu (5×10^{-10} Am^2). Although we have described such procedures, the reliability limits should be established independently for the sample processing and handling conditions specific to each experiment, by means of adequate and statistically relevant tests. We suggest that magnetic behaviour should only be reported reasonably above those limits, as we were unable to identify characteristics of the contaminant magnetism which could be generally used as criteria to distinguish it from intrinsic ferromagnetism.

Acknowledgments

This work was supported by FCT Portugal (SFRH/BD/35761/2007, PTDC/FIS/098943/2008, PTDC/CTM-NAN/115125/2009), FWO Flanders, KULeuven projects GOA/2009/006 and INPAC EF/05/005 and the IUAP P6/42 program.

[1] D. W. Abraham, M. M. Frank, and S. Guha, Appl. Phys. Lett. **87**, 252502 (2005).
[2] M. A. Garcia, E. Fernandez Pinel, J. de la Venta, A. Quesada, V. Bouzas, J. F. Fernandez, J. J. Romero, M. S. Martin Gonzalez, and J. L. Costa-Kramer, J. Appl. Phys. **105**, 013925 (2009).
[3] A. Ney, T. Kammermeier, V. Ney, K. Ollefs, and S. Ye, J. Magn. Magn. Mater. **320**, 3341 (2008).
[4] D. P. Osterman and S. J. Williamson, Rev. Sci. Instrum. **54**, 1380 (1983).
[5] A. Zieba, Rev. Sci. Instrum. **64**, 3357 (1993).

[6] L. L. Miller, Rev. Sci. Instrum. **67**, 3201 (1996).
[7] P. Stamenov and J. M. D. Coey, Rev. Sci. Instrum. **77**, 015106 (2006).
[8] Quantum Design, Inc., 11578 Sorrento Valley Road, San Diego, CA, USA.
[9] The following procedure was adopted for the field-cooled (FC) and zero-field-cooled (ZFC) measurements. The samples were demagnetized at 300 K and cooled without an applied magnetic field. After stabilizing the temperature at 5 K, a field of 10 mT (100 Oe) was applied. The magnetic moment was then measured as a function of increasing temperature from 5 K to 300 K - the zero-field-cooled (ZFC) measurement. The sample was then cooled in the same magnetic field and, after stabilizing at 5 K, the magnetic moment was measured again as a function of increasing temperature from 5 K to 300 K - the field-cooled (FC) measurement.

Bibliography

[1] J. F. Ziegler, J. P. Biersack, and U. Littmark, *The stopping and range of ions in solids*. Pergamon Press, New York, 1985.

[2] W. K. Chu, M. A. Nicolet, and J. W. Mayer, *Backscattering Spectrometry*. Academic Press, New York, 1978, 1978.

[3] J. W. Mayer and E. Rimini, *Ion beam handbook for material analysis*. Academic Press, New York, 1977.

[4] L. C. Feldman and J. W. Mayer, *Fundamentals of surface and thin film analysis*. North-Holland, Amsterdam, 1986.

[5] J. Lindhard, "Influence of crystal lattice on motion of energetic charged particles by Jens Lindhard," *Matematisk-fysiske meddelelser udgivet af det Kongelige Danske videnskabernes selskab*, vol. 34, p. 14, 1965.

[6] D. V. Morgan, *Channeling*. John Wiley & Sons, 1973.

[7] H. Hofsäss and G. Lindner, "Emission channeling and blocking," *Phys. Rep.-Rev. Sec. Phys. Lett.*, vol. 201, p. 121, 1991.

[8] H. Hofsäss, U. Wahl, and S. G. Jahn, "Impurity lattice location and recovery of structural defects in semiconductors studied by emission channeling," *Hyperfine Interact.*, vol. 84, p. 27, 1994.

[9] H. Hofsäss, "Emission channeling," *Hyperfine Interact.*, vol. 97, p. 247, 1996.

[10] U. Wahl, "Advances in electron emission channeling measurements in semiconductors," *Hyperfine Interact.*, vol. 129, p. 349, 2000.

[11] U. Wahl, A. Vantomme, J. De Wachter, R. Moons, G. Langouche, J. G. Marques, and J. G. Correia, "Direct evidence for tetrahedral interstitial Er in Si," *Phys. Rev. Lett.*, vol. 79, p. 2069, 1997.

[12] B. T. M. Willis and A. W. Pryor, *The thermal vibrations in Crystallography.* Cambridge University Press, Cambridge, 1975.

[13] O. H. Nielsen, F. K. Larsen, S. Damgaard, J. W. Petersen, and G. Weyer, "Systematic experimental and theoretical studies of the lattice vibrations of host atoms and substitutional Sn impurities in III-V semiconductors," *Z. Phys. B - Cond. Matter*, vol. 52, p. 99, 1983.

[14] U. Wahl, 1992. Ph. D. Thesis, Konstanz Univ., Konstanz.

[15] B. De Vries, 2006. Ph. D. Thesis, Katholieke Univ. Leuven, Leuven.

[16] S. Agostinelli, J. Allison, K. Amako, J. Apostolakis, H. Araujo, P. Arce, M. Asai, D. Axen, S. Banerjee, G. Barrand, F. Behner, L. Bellagamba, J. Boudreau, L. Broglia, A. Brunengo, H. Burkhardt, S. Chauvie, J. Chuma, R. Chytracek, G. Cooperman, G. Cosmo, P. Degtyarenko, A. Dell'Acqua, G. Depaola, D. Dietrich, R. Enami, A. Feliciello, C. Ferguson, H. Fesefeldt, G. Folger, F. Foppiano, A. Forti, S. Garelli, S. Giani, R. Giannitrapani, D. Gibin, J. Cadenas, I. Gonzalez, G. Abril, G. Greeniaus, W. Greiner, V. Grichine, A. Grossheim, S. Guatelli, P. Gumplinger, R. Hamatsu, K. Hashimoto, H. Hasui, A. Heikkinen, A. Howard, V. Ivanchenko, A. Johnson, F. Jones, J. Kallenbach, N. Kanaya, M. Kawabata, Y. Kawabata, M. Kawaguti, S. Kelner, P. Kent, A. Kimura, T. Kodama, R. Kokoulin, M. Kossov, H. Kurashige, E. Lamanna, T. Lampen, V. Lara, V. Lefebure, F. Lei, M. Liendl, W. Lockman, F. Longo, S. Magni, M. Maire, E. Medernach, K. Minamimoto, P. de Freitas, Y. Morita, K. Murakami, M. Nagamatu, R. Nartallo, P. Nieminen, T. Nishimura, K. Ohtsubo, M. Okamura, S. O'Neale, Y. Oohata, K. Paech, J. Perl, A. Pfeiffer, M. Pia, F. Ranjard, A. Rybin, S. Sadilov, E. Di Salvo, G. Santin, T. Sasaki, N. Savvas, Y. Sawada, S. Scherer, S. Seil, V. Sirotenko, D. Smith, N. Starkov, H. Stoecker, J. Sulkimo, M. Takahata, S. Tanaka, E. Tcherniaev, E. Tehrani, M. Tropeano, P. Truscott, H. Uno, L. Urban, P. Urban, M. Verderi, A. Walkden, W. Wander, H. Weber, J. Wellisch, T. Wenaus, D. Williams, D. Wright, T. Yamada, H. Yoshida, and D. Zschiesche, "Geant4-a simulation toolkit," *Nucl. Instrum. Methods Phys. Res. Sect. A-Accel. Spectrom. Dect. Assoc. Equip.*, vol. 506, p. 250, 2003.

[17] J. Allison, K. Amako, J. Apostolakis, H. Araujo, P. A. Dubois, M. Asai, G. Barrand, R. Capra, S. Chauvie, R. Chytracek, G. A. P.

Cirrone, G. Cooperman, G. Cosmo, G. Cuttone, G. G. Daquino, M. Donszelmann, M. Dressel, G. Folger, F. Foppiano, J. Generowicz, V. Grichine, S. Guatelli, P. Gumplinger, A. Heikkinen, I. Hrivnacova, A. Howard, S. Incerti, V. Ivanchenko, T. Johnson, F. Jones, T. Koi, R. Kokoulin, M. Kossov, H. Kurashige, V. Lara, S. Larsson, F. Lei, O. Link, F. Longo, M. Maire, A. Mantero, B. Mascialino, I. McLaren, P. M. Lorenzo, K. Minamimoto, K. Murakami, P. Nieminen, L. Pandola, S. Parlati, L. Peralta, J. Perl, A. Pfeiffer, M. Pia, A. Ribon, P. Rodrigues, G. Russo, S. Sadilov, G. Santin, T. Sasaki, D. Smith, N. Starkov, S. Tanaka, E. Tcherniaev, B. Tome, A. Trindade, P. Truscott, L. Urban, M. Verderi, A. Walkden, J. Wellisch, D. Williams, D. Wright, and H. Yoshida, "Geant4 developments and applications," *IEEE Trans. Nucl. Sci.*, vol. 53, p. 270, 2006.

Chapter 4

Results

In this chapter the results are presented based on the articles that have been published and the manuscripts that have been prepared for publication. The sections follow the same structure as the research objectives in chapter 2: objective (A) corresponds to section 4.1 (Lattice location of Mn in GaAs), objective (B1) to section 4.2 (Lattice location Mn and Co in ZnO and GaN), objective (B2) to section 4.3 (Searching for room-temperature ferromagnetism in Mn-, Fe- and Co-implanted ZnO and GaN), and objective (B3) to section 4.4 (Paramagnetism and antiferromagnetic interactions in Cr-implanted GaN and Fe-implanted ZnO). At the end of this chapter, section 4.5 consists of a more global discussion, bringing together the results on lattice location of transition-metals in narrow-gap GaAs and wide-gap GaN and ZnO, and on the magnetism of dilute magnetic semiconductors.

4.1 Lattice location of Mn in GaAs

This section is composed of articles II and III, on the lattice location of Mn in GaAs using the emission channeling technique (described in section 3.3). The main goal is to identify the interstitial Mn site and determine its thermal stability. Article I presents the results on p^+-GaAs, which in principle most resembles highly Mn-doped GaAs (i.e. typical $Ga_{1-x}Mn_xAs$ DMS samples, grown by low temperature MBE). Article III extends these experiments to semi-insulating and n^+-GaAs, in order to investigate the effect of varying the concentration of potentially trapping defects. Article III also gives an overview of the results in the two articles, and discusses their implications on the prospects for increasing the Curie temperature of $Ga_{1-x}Mn_xAs$.

Article II

Direct identification of interstitial Mn in heavily *p*-type doped GaAs and evidence of its high thermal stability

L. M. C. Pereira,[1,2,3] U. Wahl,[3] S. Decoster,[1] J. G. Correia,[3]
M. R. da Silva,[4] A. Vantomme,[1] and J. P. Araújo[2]

[1]*Instituut voor Kern- en Stralingsfysica and INPAC, K.U.Leuven, B-3001 Leuven, Belgium*
[2]*IFIMUP and IN-Institute of Nanoscience and Nanotechnology, Faculdade de Ciências da Universidade do Porto, 4169-007 Porto, Portugal*
[3]*Instituto Tecnológico e Nuclear, 2686-953, Sacavém, Portugal*
[4]*Centro de Física Nuclear da Universidade de Lisboa, 1649-003 Lisboa, Portugal*

Abstract

We report on the lattice location of Mn in heavily *p*-type doped GaAs by means of β^- emission channeling from the decay of ^{56}Mn. The majority of the Mn atoms substitute for Ga and up to 31% occupy the tetrahedral interstitial site with As nearest neighbors. Contrary to the general belief, we find that interstitial Mn is immobile up to 400°C, with an activation energy for diffusion of 1.7–2.3 eV. Such high thermal stability of interstitial Mn has significant implications on the strategies and prospects for achieving room temperature ferromagnetism in $Ga_{1-x}Mn_xAs$.

Applied Physics Letters **98**, 201905 (2011)

Intensively studied for over a decade, $Ga_{1-x}Mn_xAs$ stands as one of the most well understood dilute magnetic semiconductors (DMS).[1] This sound understanding of $Ga_{1-x}Mn_xAs$ from both a fundamental and applied point of view, supported by an increase of the Curie temperature (T_C) over the years and by the prominent position of GaAs in semiconductor industry, holds the promise of an eventual crossing of the room temperature barrier and direct technological implementation.

It has been theoretically and experimentally established that the T_C of $Ga_{1-x}Mn_xAs$ increases with increasing Mn concentration x and hole concentration p.[2] Thermal annealing near the growth temperature (∼200°C) increases p and consequently T_C, but a significant fraction of Mn atoms remains electrically inactive.[2,3] This partial activation by (∼200°C) annealing was attributed to the out-diffusion of a compensating defect with low thermal stability,[3] with an activation energy of 0.7 eV,[4] which has been identified as interstitial Mn.[4,5]

By studying the lattice location of Mn in heavily p-type doped GaAs, by means of β^- emission channeling, we find evidence of high thermal stability of interstitial Mn.

Emission channeling[6] makes use of charged particles emitted by a radioactive isotope. The screened Coulomb potential of atomic rows and planes determines the anisotropic scattering of the initially isotropically emitted decay particles. Since these channeling and blocking effects strongly depend on the initial position of the emitted particles, they result in emission patterns that are characteristic of the lattice site(s) occupied by the probe atoms.

A fluence of 2×10^{13} cm^{-2} of radioactive ^{56}Mn ($t_{1/2} = 2.56$ h) was implanted at the ISOLDE facility at CERN into heavily p-type doped single-crystalline GaAs:Zn (0.6–2×10^{-3} Ωcm, $p = 1.4$–6×10^{19} cm^{-3}) with an energy of 50 keV, under a tilt angle of 17° to minimize ion channeling. Using MARLOWE,[7] the Mn peak concentration is estimated to be 4.6×10^{18} cm^{-3} at a projected range R_p of 313 Å with a 168 Å straggling. The low Mn concentration allows us to study of the annealing behavior of interstitial Mn (Mn_I) free from phase segregation, which otherwise hinders the quantification of the Mn_I fraction at high annealing temperatures.[5] On the other hand, the high Zn doping renders the material heavily p-type, similar to typical $Ga_{1-x}Mn_xAs$ (DMS) samples. Angular-dependent emission yields of the β^- particles emitted during the decay to stable ^{56}Fe were measured at room temperature, along four crystallographic directions, ⟨100⟩, ⟨111⟩, ⟨110⟩ and ⟨211⟩, in the as-implanted state and after *in situ* cap-

less annealing under vacuum ($< 10^{-5}$ mbar) in steps of 100°C (10 min) up to 600°C. These patterns were recorded using a position- and energy-sensitive detection system similar to that described in Ref. 8. Given the short half-life of ^{56}Mn, this system was installed on-line and upgraded with self-triggering readout chips for the Si pad detectors, enabling measurements during and/or immediately after implantation with count rates of up to several kHz. Quantitative lattice location is provided by fitting the experimental data with theoretical patterns calculated using the *many-beam* formalism for probes occupying different sites with varying root mean square displacement. Calculation and fitting procedures are described in Ref. 6 and Ref. 8, respectively. Details on how the technique discriminates among the possible sites in the GaAs (zincblende) structure are described in Ref. 9.

As a representative example, Fig. 1 compares the normalized experimental β^- emission yields along the four directions [(a)-(d)] measured after 300°C annealing with the best fits of theoretical patterns [(e)-(h)]. These fits correspond to a mixed occupancy of 71% in the substitutional Ga site (S_{Ga}) and 29% in the tetrahedral interstitial site with As nearest neighbors (T_{As}). Simple visual inspection (Fig. 2) shows how the features of the $\langle 211 \rangle$ experimental patterns [(c)-(e)] are reproduced by a superposition of the S_{Ga} and T_{As} simulations [(a) and (b)]. It is also clear that this S_{Ga} + T_{As} superposition converts into a nearly pure S_{Ga} pattern with increasing annealing temperature. Including S_{As}, T_{Ga}, bond centered (BC), anti-bonding (AB) or hexagonal (H) sites, as well as intermediate positions between pairs of these high-symmetry sites, yields only insignificant fit improvements. Possible fractions on these sites are estimated to be below 5%. The overall results are summarized in Fig. 3. Within the experimental error, the total S_{Ga} + T_{As} fraction is 100% for all the annealing steps, confirming negligible occupancy of other sites. Along $\langle 111 \rangle$ and $\langle 100 \rangle$, S_{Ga} and T_{As} are on the same sublattice and therefore the relative fractions on these sites are derived from the fits to the $\langle 110 \rangle$ and $\langle 211 \rangle$ patterns. About 70% of the implanted Mn substitutes for Ga, while the remaining 30% occupies T_{As} sites where it is stable up to 400°C, reducing significantly at 500°C and vanishing at 600°C.

Estimating the activation energy (E_a) associated with Mn_I diffusion requires in principle a detailed knowledge of the concentration profiles of Mn_I and the trapping centers throughout the annealing sequence. However, one can obtain simple estimates for the maximum and minimum E_a values from the following considerations. The total S_{Ga} + T_{As} fraction remains

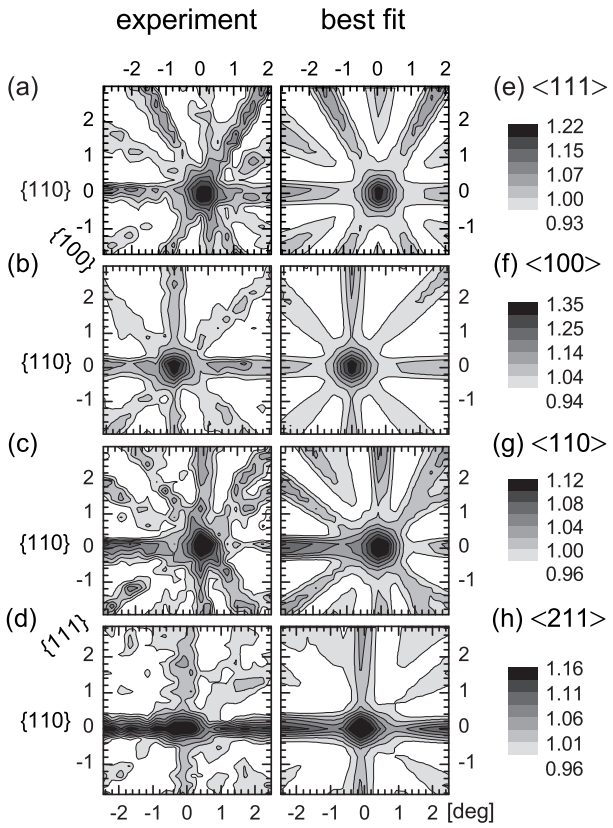

FIG. 1: (a)-(d) Normalized experimental β^- emission channeling patterns in the vicinity of the $\langle 111\rangle$, $\langle 100\rangle$, $\langle 110\rangle$ and $\langle 211\rangle$ directions following annealing at 300°C. (e)-(h) Corresponding best fits yielding 71% and 29% of the Mn atoms on S_{Ga} and T_{As} sites respectively.

constant up to the last annealing stage, indicating that Mn_I converts into Mn_{Ga} by combining with Ga vacancies (V_{Ga}) produced during implantation. Within an Arrhenius model for the thermally activated migration, the fraction $f(T, \Delta t)$ of Mn remaining on T_{Ga} sites after an annealing step of duration Δt at a temperature T is given by

$$f(T, \Delta t) = f_0 \exp[-\nu_0 \Delta t / N \exp(-E_a / k_B T)], \quad (1)$$

where f_0 is the fraction before the annealing step, ν_0 is the attempt frequency, which we take as 10^{12} s^{-1}, *i.e.* of the order of the lattice vibrations, N is the average number of jumps before a Mn_I atom combines with a Ga

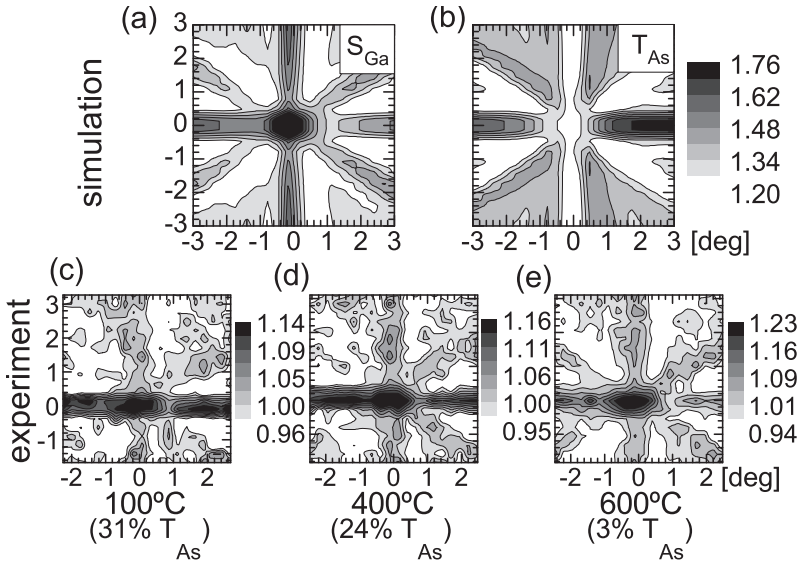

FIG. 2: Comparison between the S_{Ga} (a) and T_{As} (b) simulations and the experimental patterns after 100°C (c), 400°C (d) and 600°C (e) annealing, along the $\langle 211 \rangle$ direction.

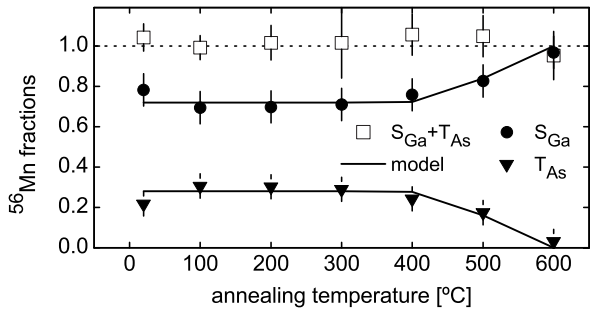

FIG. 3: Fractions of ^{56}Mn on S_{Ga} and T_{As} sites derived from the fits to the experimental patterns: (□) total S_{Ga} + T_{As} fraction derived from the $\langle 111 \rangle$, $\langle 100 \rangle$, $\langle 110 \rangle$ and $\langle 211 \rangle$ best fits; relative fractions on S_{Ga} (•) and T_{As} (▼) averaged from the $\langle 110 \rangle$ and $\langle 211 \rangle$ best fits; (line) Eq. (1) for $N = 2000$ and $E_a = 1.8$ eV.

vacancy and k_B is the Boltzmann constant.[10] Conservative estimates for the minimum and maximum migration energies can be deduced from the two limiting cases for the value of N corresponding to two opposite scenarios before the mobilization of Mn_I: (1) every Mn_I (in T_{As}) has trapped

one mobile V_{Ga} in a neighboring Ga-tetrahedron; (2) Mn_I and V_{Ga} are randomly and independently distributed. The interaction between Mn_I and other ^{56}Mn or ^{56}Fe atoms can probably be neglected since, not only is the average minimum distance between probes very large ($\sim$ 120 Å), the concentration of Ga vacancies is expected to be significantly higher than that of Mn or Fe atoms, i.e., the Mn_I-V_{Ga} interaction dominates.

Case (1) requires a minimum N of one jump of the Mn atom from T_{As} into the Ga vacancy. Case (2) is rather more complex and an accurate solution requires assumptions to be made about the annealing dynamics of V_{Ga}. Nonetheless, one can estimate a maximum value of N from the following. The root-mean-square (rms) distance traveled by a Mn_I atom after N jumps in a 3-dimensional random walk is given by $R_{rms} = \sqrt{N} \times l$, where l is the distance between two T_{As} sites (4.0 Å). The maximum number of jumps is thus related to the maximum distance traveled by a Mn_I atom before combining with a Ga vacancy, for which a limit can be estimated from our data as follows. Long-range diffusion has a strong effect on the emission patterns due to the exponential dependence of β^- dechanneling on the emitter (^{56}Mn) depth. Diffusion of Mn_I to the surface, *i.e.* over a distance of R_p, would lead to an apparent increase of fitted fractions. Conversely, diffusion of a similar magnitude into the bulk would damp this fraction, resulting in the opposite effect. Since the total S_{Ga} + T_{As} fraction remained constant throughout the annealing sequence, one can take R_p as the maximum distance traveled by the Mn_I atoms in the direction perpendicular to the surface. Statistically, only one third of the jumps result in displacements in that direction. The maximum R_{rms} is hence $3 \times R_p$, corresponding to a maximum $N \approx 20000$. Finally, with N between 1 and 20000, Eq. (1) yields an activation energy of 1.7–2.3 eV.

Our results indicate that Mn_I is not the compensating defect that becomes mobile at $\sim$200°C ($E_a = 0.7$ eV) as generally accepted. Interestingly, they do not necessarily disagree with previous element-specific studies on the thermal stability of Mn_I. We note, for example, that although ion channeling measurements qualitatively detected a decrease of the Mn_I fraction after annealing at 282°C,[5] they show that at least a significant fraction actually persisted, i.e, almost 100°C above the temperature at which Mn_I would become mobile if it was the low temperature diffuser. Moreover, in a recent radio-tracer study on the diffusion of Mn in GaAs,[11] the activation energies for the Mn migration were also found to be very high: $\sim$3 eV and higher for the fast and slow components, respectively. However, radio-tracer techniques do not provide direct information on the lattice

sites occupied by the diffusing species. In fact, the fast component in Ref. 11 (with $E_a \approx 3$ eV) more likely corresponds to Frank-Turnbull diffusion of the *substitutional* Mn fraction via interstitial sites, since E_a is well above the maximum estimated here for the direct interstitial diffusion of the *interstitial* Mn fraction (2.3 eV).

We should point out that the Mn peak concentration in our experiment was 4.6×10^{18} cm^{-3} (0.021 %), considerably lower than that of typical $Ga_{1-x}Mn_xAs$ DMS materials (few %). While this successfully avoided phase segregation at high annealing temperatures, thus allowing us to study the onset of mobility of interstitial Mn, one must discuss the generalization of our results to $Ga_{1-x}Mn_xAs$. According to *ab initio* calculations, the effect of higher Mn concentrations is to increase the activation energy (E_a) for Mn_I diffusion due to the decrease in average Mn_I–Mn_{Ga} minimum distance and the resulting increase in Coulomb attraction between oppositely charged Mn_I (double-donor) and Mn_{Ga} (acceptor) defects.[4,12] Therefore, if higher Mn concentrations are to have an effect on E_a, it should be that of increasing it even further above the 0.7 eV determined for the low temperature diffuser.

Finally, showing that interstitial Mn is immobile in GaAs well above 200°C has significant implications as it motivates a reevaluation of the structural effects of low temperature annealing in $Ga_{1-x}Mn_xAs$. This, in turn, may potentially lead to new strategies for achieving pure substitutional doping and higher Curie temperatures.

In summary, we have experimentally established the lattice location of Mn in heavily p-type doped GaAs. We confirmed that the majority of the implanted Mn atoms substitute for Ga and located a significant fraction in the tetrahedral interstitial site with As nearest neighbors. Contrary to the general belief that interstitial Mn is mobile at 200°C, we gave evidence of its high thermal stability, up to 400°C, with an effective activation energy for diffusion of 1.7–2.3 eV.

Acknowledgments

This work was supported by the Portuguese Foundation for Science and Technology (CERN/FP/109272/2009, CERN/FP/116320/2010, SFRH/BD/35761/2007), the Research Foundation - Flanders, the EURONS project (RII3-CT-2004-506065), the SPIRIT (Support of Public and Industrial Research using Ion Beam Technology) project (contract no. 227012), KULeuven projects GOA/2009/006 and INPAC EF/05/005 and

the IUAP P6/42 program.

[1] S. Lee, J. H. Chung, X. Liu, J. K. Furdyna, and B. J. Kirby, Materials Today **12**, 14 (2009).
[2] T. Jungwirth, K. Y. Wang, J. Masek, K. W. Edmonds, J. Konig, J. Sinova, M. Polini, N. A. Goncharuk, A. H. MacDonald, M. Sawicki, et al., Phys. Rev. B **72**, 165204 (2005).
[3] T. Hayashi, Y. Hashimoto, S. Katsumoto, and Y. Iye, Appl. Phys. Lett. **78**, 1691 (2001).
[4] K. W. Edmonds, P. Boguslawski, K. Y. Wang, R. P. Campion, S. N. Novikov, N. R. S. Farley, B. L. Gallagher, C. T. Foxon, M. Sawicki, T. Dietl, et al., Phys. Rev. Lett. **92**, 037201 (2004).
[5] K. M. Yu, W. Walukiewicz, T. Wojtowicz, I. Kuryliszyn, X. Liu, Y. Sasaki, and J. K. Furdyna, Phys. Rev. B **65**, 201303 (2002).
[6] H. Hofsass and G. Lindner, Phys. Rep. **201**, 121 (1991).
[7] M. T. Robinson, Phys. Rev. B **40**, 10717 (1989).
[8] U. Wahl, J. G. Correia, S. Cardoso, J. G. Marques, A. Vantomme, G. Langouche, and ISOLDE Collaboration, Nucl. Instrum. Methods Phys. Res. B **136**, 744 (1998).
[9] U. Wahl, A. Vantomme, G. Langouche, and ISOLDE collaboration, Nucl. Instrum. Methods Phys. Res. B **148**, 492 (1999).
[10] U. Wahl, J. G. Correia, E. Rita, J. P. Araujo, J. C. Soares, and ISOLDE Collaboaration, Nucl. Instrum. Methods Phys. Res. B **253**, 167 (2006).
[11] O. Koskelo, J. Raisanen, F. Tuomisto, J. Sadowski, and ISOLDE Collaboration, Sem. Sci. Tech. **24**, 045011 (2009).
[12] V. I. Baykov, P. A. Korzhavyi, and B. Johansson, Phys. Rev. Lett. **101**, 177204 (2008).

Article III

Stability and diffusion of interstitital and substitutional Mn in GaAs of different doping types

L. M. C. Pereira,[1,2,3] U. Wahl,[3,4] S. Decoster,[1] J. G. Correia,[3,4]
L. M. Amorim,[1] M. R. da Silva,[4] J. P. Araújo,[2] and A. Vantomme[1]

[1]*Instituut voor Kern- en Stralingsfysica and INPAC, K.U.Leuven, 3001 Leuven, Belgium*
[2]*IFIMUP and IN-Institute of Nanoscience and Nanotechnology, DFA-FCUP, 4169-007 Porto, Portugal*
[3]*Instituto Tecnológico e Nuclear, UFA, 2686-953 Sacavém, Portugal*
[4]*Centro de Física Nuclear da Universidade de Lisboa, 1649-003 Lisboa, Portugal*

Abstract

We report on the lattice location of Mn impurities ($< 0.05\%$) in undoped (semi-insulating) and heavily *n*-type doped GaAs, by means of β^- emission channeling. In addition to the majority substituting for Ga, we locate up to 30% of the Mn impurites on tetrahedral interstitial sites with As nearest neighbors. In line with the recently reported high thermal stability of interstitial Mn in heavily *p*-type doped GaAs [L. M. C. Pereira *et al.*, Appl. Phys. Lett. **98**, 201905 (2011)], the interstitial fraction is found to be stable up to 400°C, with an activation energy for diffusion of 1.7–2.3 eV. Since varying the concentration of potentially trapping defects has no measurable effect on the activation energy for diffusion of the interstitial impurities, we conclude that the observed high thermal stability is characteristic of isolated interstitial Mn. Being difficult to reconcile with the general belief that interstitial Mn is the donor defect that out-diffuses at ∼200°C, these findings motivate a careful reassessment of the structural effects of low temperature annealing of $Ga_{1-x}Mn_xAs$.

In preparation for *Physical Review B*

I. INTRODUCTION

One of the most well-understood dilute magnetic semiconductors (DMS), $Ga_{1-x}Mn_xAs$ has become an exceptional material in which to study the physics of carrier-mediated ferromagnetism in semiconductors[1–3] and for the development of proof-of-concept semiconductor-based spintronic devices.[4] Based on this sound understanding of $Ga_{1-x}Mn_xAs$, both fundamental and applied, the increase in Curie temperature (T_C) of the current record value of 190 K to above room temperature remains a major goal in the DMS field.[5]

It has been theoretically and experimentally established that the T_C of $Ga_{1-x}Mn_xAs$ increases with increasing Mn concentration and hole concentration p.[6] More precisely, T_C increases with effective Mn concentration, which takes into account the balance between the fractions of Mn substituting for Ga (Mn_{Ga}) and on interstitial sites (Mn_I). While Mn_{Ga} provides both the localized magnetic moment and the itinerant hole that mediates the magnetic coupling, Mn_I has a two-fold compensating effect: magnetic, as Mn_I-Mn_{Ga} pairs couple antiferromagnetically, and electrical, since double donor Mn_I compensates Mn_{Ga} acceptors. As a consequence of this self-compensation, while the amount of Mn that can be incorporated in high quality $Ga_{1-x}Mn_xAs$ has been remarkably increased throughout the years up to $x \approx 0.10$, p and T_C persistently fail to follow.[6,7] Thermal annealing near the growth temperature (∼200°C) increases p and consequently T_C, but a significant fraction of the initially introduced Mn atoms remains inactive.[6,8] This partial activation by annealing (∼200°C) was attributed to the out-diffusion of a compensating defect with low thermal stability,[8] with an activation energy (E_a) of 0.7 eV,[9] which was suggested to be interstitial Mn.[9,10] This established the belief that pure substitutional Mn doping can be achieved by low-temperature (∼200°C) thermal annealing. Since then, attempts to increase T_C above room temperature have focused on increasing the Mn concentration that can be incorporated in $Ga_{1-x}Mn_xAs$. However, film growth development beyond $x \approx 0.10$ and (and thus of $T_C \approx 190$ K) faces significant technical challenges.[6,11]

Recently, we reported on the lattice location of Mn in heavily p-type doped GaAs.[12] We identified the lattice site occupied by interstitial Mn as the tetrahedral interstitial site with As nearest neighbors (T_{As}) and, more importantly, gave evidence of its high thermal stability, up to 400°C, with an effective activation energy (E_a) for diffusion of 1.7–2.3 eV. Being difficult to reconcile with the general belief that Mn_I is the donor defect that

out-diffuses at ∼200°C with $E_a = 0.7$ eV, these results raise two important questions:

1. What is the origin of such a high activation energy? Is it a characteristic of interstitial Mn in T_{As} sites or is it due to trapping by oppositely charged acceptor defects (i.e. substitutional Mn in $Ga_{1-x}Mn_xAs$ or Zn acceptors in our previous study in heavily p-type doped GaAs)? While the migration barrier for an isolated Mn_I atom was estimated by *ab initio* calculations to be only 0.8 eV,[9] pairing with Mn_{Ga} acceptors was estimated to add up to 0.8 eV of binding energy,[13] which could explain the high effective activation energy for diffusion.

2. What are the implications of such a high thermal stability of interstitial Mn on the strategies and prospects to achieve higher Curie temperatures in $Ga_{1-x}Mn_xAs$? If interstitial Mn is immobile in GaAs up to 400°C (Ref. 12), while Mn clustering is known to set in already at 282°C in $Ga_{1-x}Mn_xAs$ (Ref. 10), can pure substitutional doping be achieved in $Ga_{1-x}Mn_xAs$ by thermal annealing?

We address these questions here by studying, as a function of annealing temperature, the lattice location of Mn in both semi-insulating (SI) and highly n-type doped (n^+) GaAs using β^- emission channeling. Comparing these to our previous results on highly p-type doped (p^+) GaAs,[12] we investigate if the higher thermal stability of interstitial Mn can be ascribed to trapping by electrical defects (question 1). Comparing the thermal stabilities of Mn in interstitial and substitutional sites in GaAs to the temperature regime where Mn aggregation and phase segregation is known to occur in $Ga_{1-x}Mn_xAs$, we discuss if, above its mobility threshold, interstitial Mn atoms are more likely to out-diffuse or aggregate with other Mn atoms (question 2).

II. EXPERIMENT

A. Emission channeling

The emission channeling (EC) technique has been developed to determine the lattice location of impurities in single crystals, making use of the charged particles emitted by a radioactive isotope of the impurity element under study.[14] The screened Coulomb potential of atomic rows and planes

determines the anisotropic scattering of the particles emitted isotropically during decay. Along low-index crystal directions of single crystals, this anisotropic scattering results in well defined channeling or blocking effects. Because these effects strongly depend on the initial position of the emitted particles, they lead to emission patterns which are characteristic of the lattice site(s) occupied by the probe atoms. Angular-dependent emission patterns are recorded along various crystallographic axes using a position- and energy-sensitive detection system similar to that described in Ref. 15. The theoretical emission patterns for probes occupying possible lattice sites are calculated using the *manybeam* formalism for electron channeling in single crystals.[14] Quantitative lattice location is provided by fitting the experimental patterns with theoretical ones using the two-dimensional fit procedure outlined in Ref. 15. Corrections for secondary electrons that reach the detector were implemented by subtracting an isotropic background from every pattern. This secondary electron contribution is estimated based on Geant4[16,17] simulations of electron scattering, taking into account the elemental composition and geometry of the sample, sample holder and vacuum chamber. Several reviews on emission channeling can be found in the literature.[14,18–20]

The technique offers a number of advantages compared to other lattice location techniques. Because EC makes use of 2-dimensional emission patterns (measured using position sensitive detectors) which are directly compared to numerical simulations, it provides unambiguous and quantitative lattice location superior to conventional ion-channeling techniques. In addition, it is extremely sensitive in the sense that it only requires a small number of impurities, down to 10^{10} atoms, which makes it particularly suited to study very dilute systems, unlike conventional ion-channeling and synchrotron based techniques such as X-ray absorption fine structure (XAFS), which require a number of impurities several orders of magnitude above. Probably one of the strongest features of the EC technique is its applicability to those cases where significant fractions of the impurities occupy more than one lattice site. This multi-site lattice location capability of EC has allowed us, for example, to establish the amphoteric (both Ga- and N-substitutional) nature of As in GaN[21] and to identify, in addition to the majority fractions in cation sites, significant fractions of Co and Mn impurities in the anion (O) site in ZnO[22] and of Mn impurities in the anion (N) site of GaN.[23] Although in principle such minority versus majority occupancies can also be quantified using XAFS, unambiguous identification of minority sites is extremely challenging, because the technique relies

on complex multiparameter fitting of the spectra using calculated model structures. For the case of Mn impurities in GaAs in particular, these limitations of XAFS and conventional ion-channeling techniques in identifying minority sites have resulted in either (i) an incomplete identification of the Mn interstitial site or (ii) a proposed identification that conflicts with the theoretical prediction: (i) Based on ion channeling[10] and XAFS[24] experiments, the Mn impurities were found to occupy Ga substitutional sites (majority) and tetrahedral interstitial (T) sites (minority), however without being able to identify which of the two possible T sites, i.e. with Ga (T_{Ga}) or As (T_{As}) nearest neighbors; (ii) Based on XAFS experiments the interstitial site was identified as the T_{Ga}, which is in disagreement with *ab initio* calculations estimating an energy 0.35 eV lower for Mn in T_{As} sites compared to T_{Ga}.[9] This inconsistency among XAFS reports and disagreement with our previous emission channeling results[12] can be explained by the limitations of XAFS in distinguishing the chemical nature of neighbors with similar atomic numbers, as is the case of Ga and As. With emission channeling, the distinction between T_{Ga} and T_{As} sites is achieved as follows. Since the nuclear charges of Ga and As are quite similar the symmetric channeling patterns for the ⟨100⟩ Ga and As rows are quite similar as well (cf. Fig. 2) and are not well-suited to distinguish between S_{Ga} and S_{As} or between T_{Ga} and T_{As} sites. However, in addition to the difference in nuclear charges there is a much more pronounced sublattice-sensitive effect which results from the fact that the channeling patterns of ⟨110⟩ and ⟨211⟩ directions are not mirror-symmetric since the underlying ZnS structure itself lacks the corresponding symmetry.

Examples for possible lattice sites of high symmetry in the GaAs zincblende structure are shown in Fig. 1. In addition to the substitutional Ga (S_{Ga}) and As (S_{As}) sites and the tetrahedral interstitial sites with Ga (T_{Ga}) and As (T_{As}) nearest neighbors, the following interstitial sites are shown: interstitial sites along the ⟨111⟩ direction, i.e. the bond center (BC), antibonding Ga (AB_{Ga}), antibonding As (AB_{As}) and the hexagonal site (H); interstitial sites along the ⟨100⟩ direction, in either the Ga or the As rows, i.e. the split interstitials (SP_{Ga} and SP_{As}), the "C" sites with C_{2v} symmetry (C_{Ga} and C_{As}) and the "Y" sites (Y_{Ga} and Y_{As}). Figure 2 shows the theoretical emission patterns along the ⟨100⟩, ⟨111⟩, ⟨110⟩ and ⟨211⟩ axes for 100% of ^{56}Mn atoms on substitutional sites (S_{Ga} and S_{As}) and tetrahedral interstitial sites (T_{Ga} and T_{As}). Since S_{Ga}, S_{As}, T_{Ga} and T_{As} sites are located on the same row along the ⟨111⟩ axis (Fig. 1), they are all equivalent in the lattice projection onto the plane perpendicular

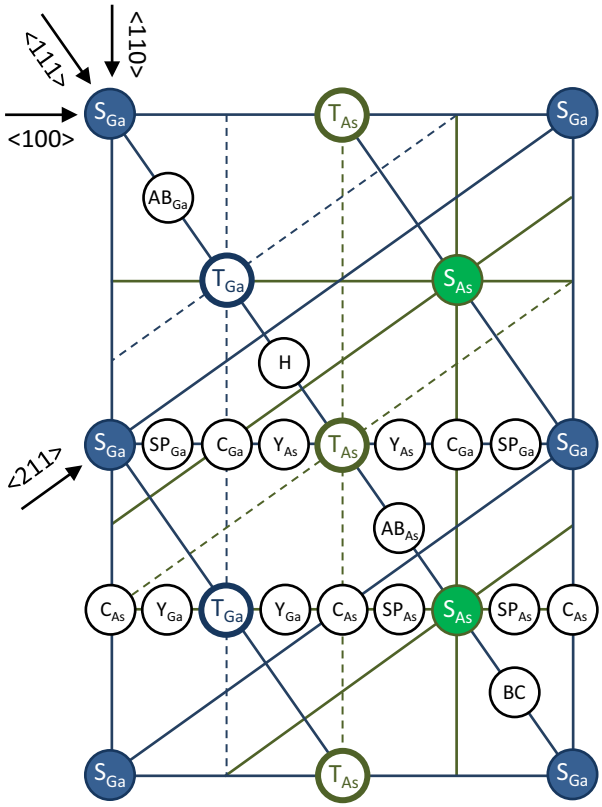

FIG. 1: The {110} planes in the GaAs zincblende lattice, showing the following sites: the substitutional Ga (S_{Ga}) and As (S_{As}) sites; the tetrahedral interstitial sites with Ga (T_{Ga}) and As (T_{As}) nearest neighbors; interstitial sites along the $\langle 111 \rangle$ direction, i.e. the bond center (BC), antibonding Ga (AB_{Ga}), antibonding As (AB_{As}) and the hexagonal site (H); interstitial sites along the $\langle 100 \rangle$ direction, in either the Ga or the As rows, i.e. the split interstitials (SP_{Ga} and SP_{As}), the "C" sites with C_{2v} symmetry (C_{Ga} and C_{As}) and the "Y" sites (Y_{Ga} and Y_{As}). Along the $\langle 100 \rangle$, $\langle 111 \rangle$, $\langle 110 \rangle$ and $\langle 211 \rangle$ directions, the rows of Ga and As atoms are indicated (lines), as well as the rows of the T_{Ga} and T_{As} sites (dashed lines). Note that, along the $\langle 111 \rangle$ direction, the substitutional (S_{Ga} and S_{As}) and tetrahedral interstitial (T_{Ga} and T_{As}) sites are all located on the same row; along the $\langle 100 \rangle$ direction, S_{Ga} is on the same row as T_{As}, and S_{As} is on the same row as T_{Ga}.

to the $\langle 111 \rangle$ direction and, consequently, the corresponding $\langle 111 \rangle$ emission patterns are undistinguishable (Fig. 2, second row). Similarly, along the $\langle 100 \rangle$ direction, because S_{Ga} is on the same row as T_{As}, and S_{As} is on the

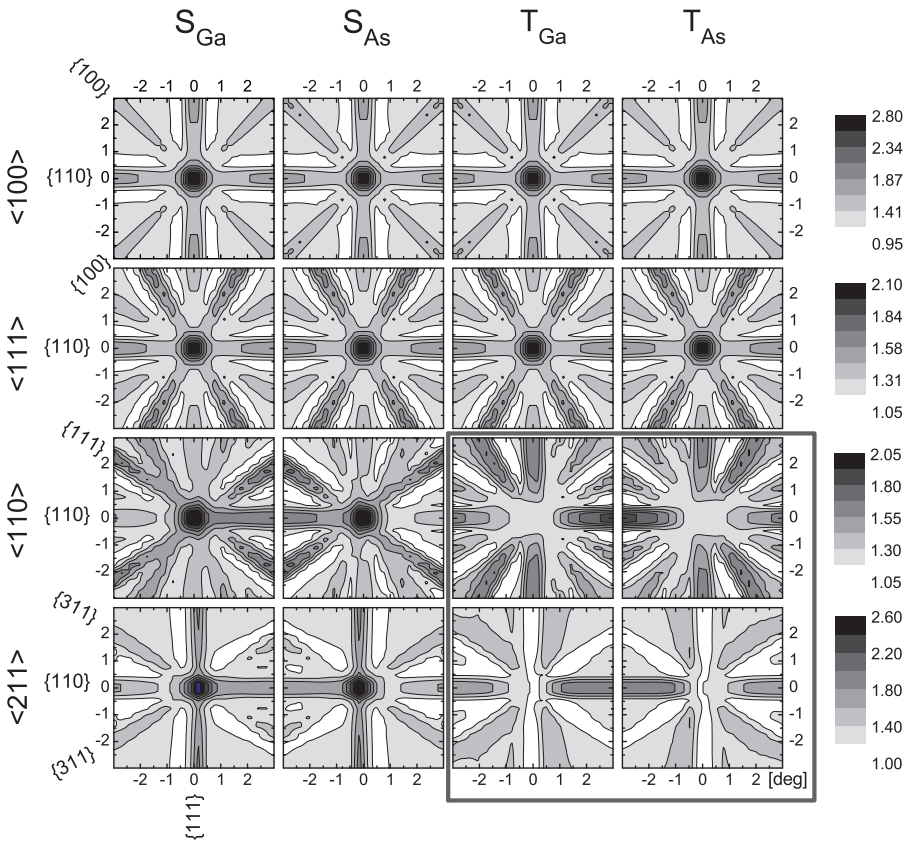

FIG. 2: Simulated emission channeling patterns for 100% of emitter atoms (^{56}Mn) on substitutional Ga (S_{Ga}) and As (S_{As}) sites, and tetrahedral interstitial sites with Ga (T_{Ga}) and As (T_{As}) nearest neighbors, along the $\langle 100\rangle$, $\langle 111\rangle$, $\langle 110\rangle$ and $\langle 211\rangle$ directions.

same row as T_{Ga}, the corresponding $\langle 100\rangle$ emission patterns are undistinguishable of sites. In order to unambiguously distinguish these sites it is thus necessary to measure also along the $\langle 110\rangle$ and $\langle 211\rangle$ directions, which separate the corresponding rows (see the dashed lines in Fig. 1). This results in emission patterns with clearly distinct anisotropies (Fig. 2, third and fourth rows) and thus allows for the unambiguous indentification of the occupied lattice sites. In particular, due to the mirror-asymmetry of the $\langle 110\rangle$ and $\langle 211\rangle$ directions, the two T sites are unambiguoulsy distinguished

(patterns inside the gray square in Fig. 2).

B. Experimental details

Radioactive ^{56}Mn ($t_{1/2} = 2.56$ h) was implanted at the on-line isotope separator facility ISOLDE at CERN, which provides mass-separated beams of radioactive Mn isotopes produced by means of 1.4-GeV proton-induced nuclear fission from uranium carbide UC_2 targets and chemically selective laser ion sources.[26] The samples consisted of $\langle 100 \rangle$ GaAs single crystals, undoped semi-insulating (s.i.) and heavily n-type doped (n^+). Material properties and implantation details are summarized in Table I, where we also include our previous experiments on heavily p-type doped (p^+) GaAs.[12] All implantations were performed at room temperature under a tilt angle of 17°. Angular-dependent emission yields of the β^- particles emitted during decay to stable ^{56}Fe were measured at room temperature, along four crystallographic directions, $\langle 100 \rangle$, $\langle 111 \rangle$, $\langle 110 \rangle$ and $\langle 211 \rangle$, in the as-implanted state and after *in situ* capless annealing under vacuum ($< 10^{-5}$ mbar) for 10 min in steps of 100°C up to 700°C. These patterns were recorded using a position- and energy-sensitive detection system similar to that described in Ref. 15. Given the relatively short half-life of ^{56}Mn, this system was installed on-line and upgraded with self-triggering readout chips for the Si pad detectors, enabling measurements during and/or immediately after implantation with count rates of up to several kHz.

Theoretical patterns were calculated for probes occupying substitutional Ga (S_{Ga}) and As (S_{As}) sites with varying root-mean-square (rms) displacements, the high symmetry interstitial sites described above and interstitial sites resulting from displacements along the $\langle 100 \rangle$ and $\langle 111 \rangle$ directions. The GaAs crystallographic parameters and room temperature atomic displacements used in the *manybeam* simulations can be found in Ref. 27.

III. RESULTS AND DISCUSSION

Next we present and discuss the results in two parts. First we determine the lattice sites occupied by Mn in GaAs, in particular with respect to T_{As} versus T_{Ga} interstitial sites, and compare it to the results of previous studies using XAFS and ion-channeling techniques. We then analyze the changes observed upon annealing in terms of thermal stability and diffusion.

doping type	dopant	resistivity [Ωcm]	carrier concentration [cm^{-3}]	^{56}Mn fluence [at. cm^{-2}]	implantation energy [keV]	projected ion range (R_p) [Å]	projected ion straggling [Å]	peak ^{56}Mn concentration [at. cm^{-3}]
n^+	Te	$0.6 - 2\times10^{-3}$	$1.1 - 5\times10^{18}(e^-)$	2×10^{13}	40	259	141	5.2×10^{18}
s.i.	–	1.4×10^{8}	–	2×10^{13}	30	206	113	7.2×10^{18}
p^+	Zn	$0.6 - 2\times10^{-3}$	$1.4 - 6\times10^{19}(h^+)$	2×10^{13}	50	313	168	4.4×10^{18}

TABLE I: Sample and implantation details. All implantations were performed at room temperature under a tilt angle of 17°. The ^{56}Mn peak concentration and the projected ion range (R_p) and straggling were estimated using SRIM-2008 code.[25] The details of our previous work on p^+ GaAs[12] are also included.

A. Lattice location: substitutional and T interstitial sites

For both n^+ and semi-insulating GaAs, for all four measured directions, the calculated S_{Ga} patterns gave by far the best agreement, showing that the majority of the probe atoms occupy Ga sites, as expected. The fitting routine was then allowed to include, in addition to S_{Ga}, a second lattice site, for which all the simulated sites were tested. The S_{Ga} + T_{As} double occupancy gives the best fit compared to all other combinations and considerably improves the S_{Ga} single-site fit (up to 30% improvement in reduced χ^2). As an example for the good match between experiment and simulated patterns, Fig. 3 compares the normalized experimental β^- emission yields along the four directions [(a)-(d)] of the semi-insulating (s.i.) sample measured following 100°C annealing with the best fits of theoretical patterns [(e)-(h)]. These fits correspond to a mixed occupancy of 70% on substitutional Ga sites (S_{Ga}) and 30% in tetrahedral interstitial sites with As nearest neighbors (T_{As}). Introducing a third site yields only insignificant fit improvements (of the order of 1% improvement in reduced χ^2). Possible fractions on other sites are estimated to be below 5%, which is considered the technique's sensitivity limit for detecting small fractions in minority sites. In particular for T_{As} versus T_{Ga} sites, the fitted T_{Ga} fraction is always below 5% (with an improvement in reduced χ^2 of the order of 1%) when the routine is allowed to include S_{Ga}, T_{As} and T_{Ga} sites simultaneously. This identification of the T_{As} site over T_{Ga} is consistent with our previous results on p^+ GaAs[12] and *ab initio* calculations yielding an energy 0.35 eV lower for Mn in T_{As} sites compared to T_{Ga}.[9] It is indeed natural that, due to the Coulomb interaction, positively charged Mn_I^{2+} defects have a lower energy when coordinated by negatively charged As anions rather than by positively charged Ga cations. It is thus quite surprising that in previous XAFS experiments the identification of S_{Ga} + T_{Ga} occupancy was proposed,[28,29] which most likely results from the limitations of XAFS when it comes to distinguishing the chemical nature of neighbors with similar atomic numbers, as is the case of Ga and As. With emission channeling, the distinction between T_{Ga} and T_{As} sites is a direct structural effect related to the mirror-asymmetry of the ⟨110⟩ and ⟨211⟩ directions of the GaAs lattice, as described above and illustrated in Fig. 1.

We must note, however, that the T_{As} site may be energetically favorable over T_{Ga} only for *isolated* Mn_I defects. For very high Mn concentrations (few %), the probablility of formation of substitutional-interstitial (Mn_{Ga}–Mn_I) pairs or even larger complexes is not negligible. In such complexes,

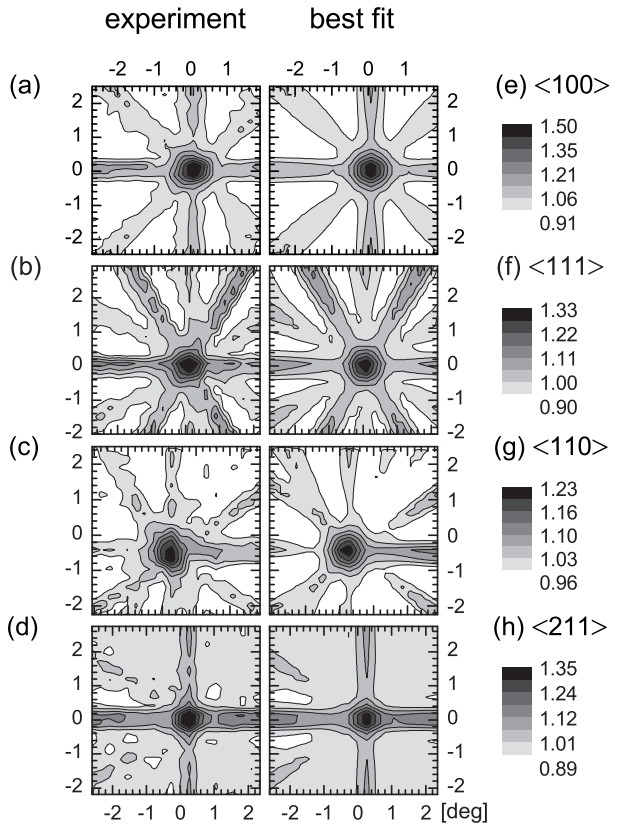

FIG. 3: (a)-(d) Normalized experimental β^- emission channeling patterns (s.i. GaAs) in the vicinity of the $\langle 100 \rangle$, $\langle 111 \rangle$, $\langle 110 \rangle$ and $\langle 211 \rangle$ directions following annealing at 100°C. (e)-(h) Corresponding best fits yielding 70% and 30% of the Mn atoms on S_{Ga} and T_{As} sites respectively.

the Coulomb attraction between oppositely charged Mn_{Ga} acceptors and Mn_I donors may counteract the repulsion between positively charged Mn_I and Ga cations: since the distance between neighboring S_{Ga} and T_{Ga} sites (2.45 Å) is smaller than that between neighboring S_{Ga} and T_{As} sites (2.83 Å), the decrease in Coulomb energy by decreasing the Mn_{Ga}–Mn_I distance may counterbalence the increase in Coulomb energy by changing the Mn_I coordination to Ga cations. Indeed, *ab initio* calculations have predicted that the energy of a Mn_I atom in one of the four T_{Ga} sites neighboring a Mn_{Ga} defect is the same as in one of the six T_{As}.[9] Moreover, it was also predicted that the energy barrier between the two sites is small enough

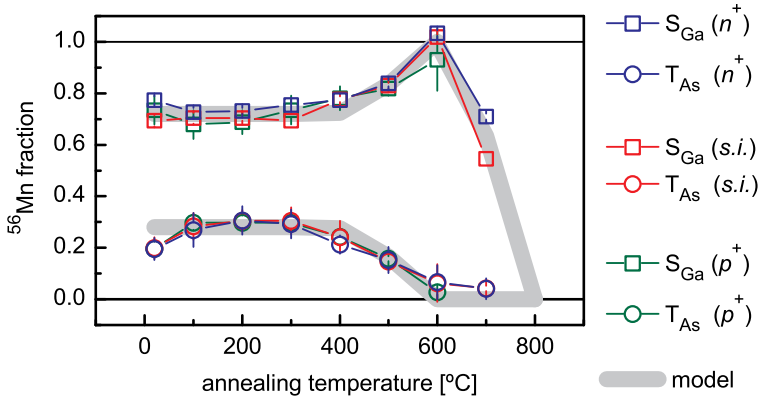

FIG. 4: Fractions of ^{56}Mn in S_{Ga} (□) and T_{As} (○) sites in n^+, semi-insulating and p^+ GaAs, derived from the fits to the experimental patterns. The data for p^+ GaAs are from Ref. 12. The gray line is given by the model of vacancy-limited diffusion of interstitial and substitutional Mn, described in the text.

to allow for Mn_I atoms to swap between the two types of sites even at room temperature.[9] Therefore, one can not exclude that, for very high concentrations of Mn and when Mn_{Ga}–Mn_I pairs *do* form, part of the interstitial fraction occupies T_{Ga} sites.

B. Thermal stability and diffusion

The Ga-substitutional and T_{As} interstitial fractions are shown in Fig. 4, as a function of annealing temperature, for both n^+ and semi-insulating GaAs. The results of our previous experiments on p^+ GaAs are also included.[12] The behavior is strikingly similar for all three doping types and can be divided in three regimes:

$T \leq 300°$C: About 70% of the implanted Mn substitutes for Ga while the remaining 30% occupies T_{As} sites. Within the experimental error, the total S_{Ga} + T_{As} fraction is 100%, which confirms that fractions on other sites are indeed negligible. The kink at 100°C, although within experimental error, is quite reproducible in the three experiments, which indicates that it is not mere scattering of experimental data. An increase in interstitial Mn at the expense of the substitutional fraction can in principle be explained as follows. If the Ga

interstitials created during implantation become mobile at temperatures $\leq 100°$C, during the annealing at 100°C they can migrate and either recombine with Ga vacancies or replace substitutional Mn atoms via a kick-out mechanism ($Mn_{Ga} + Ga_I \rightarrow Mn_I + Ga_{Ga}$). The latter mechanism can thus explain the increase of the interstitial fraction at the expense of substitutional Mn. Note that, due to the Coulomb attraction between (most likely) oppositely charged Ga interstitials (donors) and substitutional Mn (acceptors), this kick-out mechanism may be quite efficient even in the very dilute regime of our samples.

$400°\text{C} \leq T \leq 600°$**C:** The substitutional fraction increases at the expense of the interstitial fraction. At 600°C the interstitial fraction has almost completely converted into substitutional. The fact that the total $S_{Ga} + T_{As}$ fraction remains constant indicates that Mn_I converts into Mn_{Ga} by combining with Ga vacancies (V_{Ga}) created during implantation. We will discuss this mechanism below in terms of the thermal stability and diffusion of Mn_I.

$T > 600°$**C:** While the interstitial fraction remains negligible, the substitutional fraction decreases from nearly 100% at 600°C to nearly 50% at 700°C, in both the n^+ and semi-insulating samples (not measured for p^+ GaAs[12]). We will discuss this below in terms of long-range diffusion of substitutional Mn.

1. Interstitial Mn

The most obvious observation is that the thermal stability of interstitial Mn is independent of the electrical doping of the material. Interpreting this independence on the doping type requires a closer look at the concentrations of the potential trapping acceptor and donor defects. The order of magnitude of the dopant (Zn and Te) concentrations can be estimated from the quoted carrier concentration (before implantation) assuming a 100% activation. After implantation, the $Mn_{Ga}(Mn_I)$ fraction contributes with the corresponding acceptor(donor) concentration. Note that, although deep centers introduced during implantation are likely to shift the Fermi level towards the middle of the bandgap, thus reducing the number of free carriers, the concentration of *charged* donors (Te_{As} and Mn_I) and acceptors (Zn_{Ga} and Mn_{Ga}) is in principle unaffected, because shallow donors/acceptors re-

doping type	acceptor dopant	acceptor concentration [at. cm^{-3}]	donor dopant	donor concentration [at. cm^{-3}]	Mn_{Ga} (acceptor) peak concentration [at. cm^{-3}]	Mn_I (donor) peak concentration [at. cm^{-3}]	mean acceptor-donor distance [Å]	mean donor-donor distance [Å]
n^+	Te	-	Te	$1.1 - 5\times10^{18}$	3.2×10^{18}	1.6×10^{18}	85	65
s.i.	-	-	-	-	4.7×10^{18}	2.0×10^{18}	79	54
p^+	Zn	$1.4 - 6\times10^{19}$	-	-	3.8×10^{18}	1.4×10^{18}	34	90

TABLE II: Estimated acceptor (Zn_{Ga} and Mn_{Ga}) and donor (Te_{As} and Mn_I) concentrations and mean donor-donor and acceptor-acceptor distances. The dopant (Zn and Te) concentrations were estimated from the quoted carrier concentration assuming a 100% activation. The Mn_{Ga} and Mn_I peak concentrations were estimated from the ^{56}Mn peak concentration (Table I) and the S_{Ga} and T_{As} fractions measured for the annealing temperatures $100 - 300$°C (i.e., $x_p \times fraction$). The mean acceptor-acceptor and donor-donor distances are estimated from the total acceptor (Zn_{Ga} and Mn_{Ga}) the donor (Te_{As} and Mn_I) concentrations, respectively, assuming a random distribution of all four defects. The values corresponding to our previous work on p^+ GaAs[12] are also included.

main positively/negatively charged when the Fermi level moves deeper into the bandgap. The concentration of potential trapping defects, i.e. charged donors (Te_{As} and Mn_I) and acceptors (Zn_{Ga} and Mn_{Ga}) are compiled in Table II, as well as the corresponding mean donor-donor and acceptor-acceptor distances. Since varying the concentration of potential trapping defects by an order of magnitude (and thus the mean distance between them and the Mn_I defects by almost a factor of 3) produced no measurable change in the thermal stability of Mn_I, these can be ignored in the following modeling of the Mn_I migration.

As mentioned above, the fact that the total S_{Ga} + T_{As} fraction remains constant indicates that Mn_I converts into Mn_{Ga} by combining with Ga vacancies (V_{Ga}) created during implantation. However, estimating the migration barrier of Mn_I, i.e. the activation energy (E_a) for free interstitial diffusion, requires that the concentration profiles of both Mn_I and V_{Ga} (before each of the annealing steps) are known. Nevertheless, using the model which we applied to the p^+ case,[12] one can still obtain simple estimates for the maximum and minimum E_a values as follows. Within an Arrhenius model for the thermally activated migration, the fraction $f(T, \Delta t)$ of Mn remaining on T_{As} sites after an annealing step of duration Δt at a temperature T is given by

$$f(T, \Delta t) = f_0 \exp[-\nu_0 \Delta t / N \exp(-E_a / k_B T)], \quad (1)$$

where f_0 is the fraction before the annealing step, ν_0 is the attempt frequency, which we take as 10^{12} s^{-1}, *i.e.* of the order of the lattice vibrations, N is the average number of jumps before a Mn_I atom combines with a Ga vacancy and k_B is the Boltzmann constant.[30] Conservative estimates for the minimum and maximum migration energies can be deduced from the two limiting cases for the value of N corresponding to two opposite scenarios before the mobilization of Mn_I: (1) every Mn_I (in T_{As}) has trapped one mobile V_{Ga} in a neighboring Ga-tetrahedron; (2) Mn_I and V_{Ga} are randomly and independently distributed. Case (1) requires a minimum N of one jump of the Mn atom from T_{As} into the Ga vacancy. Case (2) is more complex and an accurate solution requires assumptions to be made about the annealing dynamics of V_{Ga}. Nonetheless, one can estimate a maximum value of N from the following reasoning. The root-mean-square (rms) distance traveled by a Mn_I atom after N jumps in a 3-dimensional random walk is given by $R_{rms} = \sqrt{N} \times l$, where l is the distance between two T_{As} sites (4.0 Å). The maximum number of jumps is thus related to the maximum distance traveled by a Mn_I atom before combining with a

Ga vacancy, for which a limit can be estimated from our data as follows. Long-range diffusion has a strong effect on the emission patterns due to the exponential dependence of β^- dechanneling on the emitter (^{56}Mn) depth. Diffusion of Mn_I to the surface, *i.e.* over a distance of R_p, would lead to an apparent increase of fitted fractions. Conversely, diffusion of a similar magnitude into the bulk would damp this fraction, resulting in the opposite effect. Since the total S_{Ga} + T_{As} fraction remained constant throughout the annealing sequence, one can take R_p as the maximum distance traveled by the Mn_I atoms in the direction perpendicular to the surface. Statistically, only one third of the jumps result in displacements in that direction. The maximum R_{rms} is hence $3 \times R_p$, corresponding to a maximum N of the order of 20000. With N between 1 and 20000, Eq. (1) yields an activation energy of 1.7–2.3 eV, just as in p^+ GaAs.[12]

The main conclusion from the analysis above is that the high activation energy for Mn_I diffusion in GaAs (1.7–2.3 eV), determined here and in Ref. 12, can not be ascribed to acceptor trapping, since varying the acceptor concentration by an order of magnitude had no measurable effect. Such high activation energy for diffusion should thus be a characteristic of isolated interstitial Mn (answering question 1 in the Introduction). This does not mean that trapping of Mn_I impurities by acceptor defects does not happen in general. In the low concentration regime studied here, it is very likely that trapping does not occur simply because Mn_I defects combine with Ga vacancies before being trapped by substitutional acceptors. Indeed, MARLOWE[31] simulations of the distribution of the implanted ^{56}Mn impurities and of the Ga vacancies created upon implantation yield a mean distance between a Mn impurity and the nearest Ga vacancy of the order of 2 Å, i.e. much smaller than the distance between Mn impurities and the nearest substitutional acceptors. Even though in practice the mean Mn_I–V_{Ga} distance is larger than 2 Å due to vacancy annealing, these estimates are a good indicator that, indeed, Mn_I impurities combine with Ga vacancies before being trapped by substitutional acceptors, thus explaining the equal diffusion behavior for the different doping types. On the other hand, for higher Mn concentrations (or more precisely: higher Mn_{Ga} acceptor concentrations) trapping is very likely to occur. We discuss this in more detail below, together with the general implications of this high thermal stability on the strategies to increase T_C in ferromagnetic $Ga_{1-x}Mn_xAs$.

2. Substitutional Mn

The decrease in the substitutional Mn fraction from nearly 100% at 600°C to nearly 50% at 700°C indicates Mn diffusion, either to (i) the sample bulk or to (ii) the surface. Electrons emitted from deeper within the sample (i) are subject to stronger dechanneling, which results in a decreased fitted fraction. Electrons emitted from the first few atomic layers at the surface (ii) do not experience channeling effects and thus contribute with an isotropic ("random") pattern, which would also lead to a decreased fitted fraction. In principle, Mn clustering into a phase that is incoherent with the GaAs structure could also explain the decreased substitutional fraction. Clustering, however, is extremely unlikely in our samples, given the very small Mn concentrations ($< 0.05\%$). Also material degradation (due to loss of As during annealing in vacuum) could in principle result in enhanced dechanneling and thus a decreased fitted fraction. We have tested this hipothesis by performing ^{73}As:GaAs emission channeling experiments under the same annealing conditions: the ^{73}As substitutional fraction, nearly 100% at 600°C did not decrease upon annealing up to 750°C, which shows that the decrease in substitutional Mn fraction can not be ascribed to sample degradation.

Diffusion of substitutional Mn in GaAs can be modeled by a Frank-Turnbull mechanism: a Mn atom "jumps" from the substitutional site and diffuses through interstitial sites until being trapped by a Ga vacancy (V_{Ga}), thus becoming substitutional (Mn_{Ga}) again. The next "diffusion step" occurs when the atom leaves the vacancy again and finds another one. Considering the V_{Ga} concentration fixed, such a process follows an Arrhenius behavior. The corresponding activation energy is given by the binding energy of the Mn impurity to V_{Ga} plus the migration energy of interstitial Mn diffusion. The Mn_{Ga} fraction measured after an annealing step of duration Δt at a temperature T is thus given by Eq. 1, where N is in this case the number of steps until the ^{56}Mn emitter is either too deep to contribute with a measurable channeling effect, or at the surface. Assuming that the concentration of Ga vacancies that survived annealing up to 700°C is residual, only one diffusion step is required, i.e. $N = 1$. As such, Eq. 1 yields $E_a = 2.9$ eV (c.f. Fig. 4), which is in agreement with a recent radio-tracer study on the diffusion of Mn in GaAs,[32] yielding and activation energy of $\sim$3 eV.

3. Comparison to higher Mn concentrations

When discussing the implications of our results on the strategies for increasing T_C in $Ga_{1-x}Mn_xAs$ (question 2 in the Introduction), one must take into account how the mobility of both interstitial and substitutional Mn may be affected by increasing the Mn concentration from $< 0.05\%$ (this work) up to a few % in ferromagnetic $Ga_{1-x}Mn_xAs$.

Interstitial Mn. Increasing the Mn concentration up to a few % reduces the mean distance between isolated Mn_I atoms and their closest Mn_{Ga} neighbors down to the order of the lattice constant. The activation energy for diffusion of a Mn_I donor can respond to one such nearby Mn_{Ga} acceptor in two stages, i.e. *before* and *after* the Mn_I–Mn_{Ga} nearest-neighbor pair is formed. Before the pair is formed, the positively Mn_I donor is subject to an attractive Coulomb interaction with the negatively charged Mn_{Ga} acceptor, which in principle *decreases* the energy barrier for migration towards Mn_{Ga}. Once the pair is formed, the same attractive Coulomb potential increases the activation energy for diffusion by the pair binding energy. Such binding energies can be as high as 0.8 eV, depending on the structure of the Mn_I–Mn_{Ga} complex, as calculated in Ref. 13. According to the calculations in Ref. 9, the presence of other nearby Mn_{Ga} acceptors reduces somewhat the binding energy (as the Coulomb attraction they exert on the Mn_I donor counteracts that within the pair), but the activation energy for diffusion still remains higher that that of isolated Mn_I, which we determined here to be 1.7–2.3 eV.

Substitutional Mn. In principle, strain and alloying effects resulting from an increasing Mn concentration decrease the activation energy for diffusion of substitutional Mn, i.e. favor the diffusion towards aggregation and eventual segregation into secondary phases. Indeed, it has been observed in $Ga_{1-x}Mn_xAs$ ($\sim$8% Mn) that part of the substitutional Mn fraction converts to random clusters already at 282°C,[10] i.e well below the 600 – 700 °C interval (determined here) in which susbtitutional Mn becomes mobile in the very dilute regime. Similarly, Mn clustering in $Ga_{1-x}Mn_xAs$ ($\sim$12% Mn) has been suggested to account for the decrease in T_C with increasing annealing temperatures between 160°C and 220°C.[11]

In short, we have determined here that isolated Mn_I in GaAs has a high migration energy (1.7–2.3 eV) and it has been predicted[11,13] that

Mn_I–Mn_{Ga} complex formation, which is favored in high Mn concentration $Ga_{1-x}Mn_xAs$, increases its activation energy for diffusion even further. This implies that the annealing temperatures required to induce the out-diffusion of interstitial Mn in $Ga_{1-x}Mn_xAs$ are within the range which is known to induce Mn segregation. This is however in disagreement with the established belief that thermal annealing of $Ga_{1-x}Mn_xAs$ at ∼200°C removes interstitial Mn by inducing its out-diffusion (with an activation energy of 0.7 eV).

Other hints can be found in the literature which indicate that interstitial Mn is *not* removed by low temperature (∼200°C) annealing. Although ion channeling measurements qualitatively detected a decrease of the Mn_I fraction after annealing at 282 °C,[10] they show that at least a significant fraction actually persisted, i.e, almost 100 °C above the temperature at which Mn_I would become mobile if it was the low temperature diffuser. Moreover, using secondary ion-mass spectrometry (SIMS), the out-diffusion of Mn in $Ga_{1-x}Mn_xAs$ was indeed found to be almost negligible below 400°C,[33] with a diffusion coefficient at 200°C that is at least four orders of magnitude smaller than the one derived for the out-diffusion of the donor defect in Ref. 9.

A scenario that would conform to all the observations summarized above is that the defect which out-diffuses at ∼200°C is not interstitial Mn but another compensating defect. In this scenario, Mn_I becomes mobile at slightly higher temperatures and, instead of out-diffusing as generally accepted, it is captured by substitutional Mn, forming complexes which may in fact play the role of seeds for nucleation and segregation of MnAs phases, which takes place at even higher temperatures.[34] In order to complete this scenario, one must identify a defect, other than interstitial Mn, that (i) is created in sufficient abundance during $Ga_{1-x}Mn_xAs$ growth, (ii) compensates substitutional Mn acceptors both electrically and magnetically and (iii) is removed by low temperature (∼200°C) annealing. A detailed discussion is out of the scope of this paper, but for the sake of completeness, we will briefly describe how a defect consisting of non-substitutional (excess) As forming complexes with substitutional Mn fulfills all these three conditions. Low temperature molecular beam epitaxy (LT-MBE) growth of GaAs (∼200°C), as is required for $Ga_{1-x}Mn_xAs$ with high Mn content, produces excess As in the % range[35] [condition (i)]. Excess non-substitutional As atoms, known to act as deep donors,[36,37] were found to form paramagnetic complexes with Mn_{Ga} in $Ga_{1-x}Mn_xAs$,[38] thus compensating Mn_{Ga} both electrically and magnetically [condition (ii)]. Non-substitutional As

in GaAs is known to be removed by thermal annealing in the 200 – 220 °C range,[39] and indeed in Ref. 38, the dissociation of these complexes during 260°C annealing was correlated with the increase in hole concentration and T_C [condition (iii)].

IV. CONCLUSIONS

We have experimentally determined the lattice location of Mn impurities ($< 0.05\%$) in undoped (semi-insulating) and heavily n-type doped GaAs, as a function of annealing temperature up to ∼700°C. In addition to the majority substituting for Ga, a significant fraction occupies tetrahedral interstitial sites with As nearest neighbors. Similar to our recent results on heavily p-type doped GaAs, the interstitial fraction is stable up to 400°C, with an activation energy for diffusion of 1.7–2.3 eV. Substitutional Mn becomes mobile at higher temperatures (∼700°C) with an activation energy of ∼3 eV.

Since varying the doping type of GaAs, and thus the concentration of potential trapping defects, has no measurable effect on the activation energy for diffusion of the interstitial fraction (as long as the recombination with nearby Ga vacancies is concerned), we conclude that the observed high thermal stability is characteristic of isolated interstitial Mn. In $Ga_{1-x}Mn_xAs$ materials with high Mn concentrations, although the electric fields induced by neighboring substitutional Mn acceptors may reduce the migration barrier of interstitial Mn donors, this would in principle favor complex formation. This, in turn, has previously been predicted to increase the activation energy for out-diffusion of interstitial Mn compared to when the defect is isolated.

Being difficult to reconcile with the general belief that interstitial Mn is the donor defect that out-diffuses at ∼200°C, these findings motivate a careful reassessment of the structural effects of low temperature annealing of $Ga_{1-x}Mn_xAs$. A thermal stability of interstitial Mn above 200°C has major implications on the prospects for increasing T_C in $Ga_{1-x}Mn_xAs$. If interstitial Mn remains in the matrix after low temperature annealing, full activation of the nominal Mn concentration may still be achieved by alternative post-growth processing methods. Since it is believed that a T_C of 300 K can be achieved with $x \approx 0.10$ of purely substitutional Mn, such post-growth processing may potentially allow for the realization of room temperature ferromagnetism in $Ga_{1-x}Mn_xAs$ without further film growth development, as it is currently possible to grow high quality films with

$x > 0.10$ – of which a fraction is however incorporated interstitially.

Acknowledgments

This work was supported by the Portuguese Foundation for Science and Technology (CERN/FP/109272/2009, CERN/FP/116320/2010, SFRH/BD/35761/2007), the Research Foundation - Flanders, the EURONS project (RII3-CT-2004-506065), the SPIRIT (Support of Public and Industrial Research using Ion Beam Technology) project (contract no. 227012), KULeuven projects GOA/2009/006 and INPAC EF/05/005 and the IUAP P6/42 program.

[1] T. Dietl, H. Ohno, F. Matsukura, J. Cibert, and D. Ferrand, Science **287**, 1019 (2000).
[2] K. Sato, P. H. Dederics, and H. Katayama-Yoshida, Europhys. Lett. **61**, 403 (2003).
[3] K. Alberi, K. M. Yu, P. R. Stone, O. D. Dubon, W. Walukiewicz, T. Wojtowicz, X. Liu, and J. K. Furdyna, Phys. Rev. B **78**, 075201 (2008).
[4] T. Dietl, D. D. Awschalom, M. Kaminska, and H. Ohno, *Spintronics*, vol. 82 (Academic Press, 2008).
[5] T. Dietl, Nat. Mater. **9**, 965 (2010).
[6] T. Jungwirth, K. Y. Wang, J. Masek, K. W. Edmonds, J. Konig, J. Sinova, M. Polini, N. A. Goncharuk, A. H. MacDonald, M. Sawicki, et al., Phys. Rev. B **72**, 165204 (2005).
[7] H. Ohno, A. Shen, F. Matsukura, A. Oiwa, A. Endo, S. Katsumoto, and Y. Iye, Appl. Phys. Lett. **69**, 363 (1996).
[8] T. Hayashi, Y. Hashimoto, S. Katsumoto, and Y. Iye, Appl. Phys. Lett. **78**, 1691 (2001).
[9] K. W. Edmonds, P. Boguslawski, K. Y. Wang, R. P. Campion, S. N. Novikov, N. R. S. Farley, B. L. Gallagher, C. T. Foxon, M. Sawicki, T. Dietl, et al., Phys. Rev. Lett. **92**, 037201 (2004).
[10] K. M. Yu, W. Walukiewicz, T. Wojtowicz, I. Kuryliszyn, X. Liu, Y. Sasaki, and J. K. Furdyna, Phys. Rev. B **65**, 201303 (2002).
[11] M. Wang, R. P. Campion, A. W. Rushforth, K. W. Edmonds, C. T. Foxon, and B. L. Gallagher, Appl. Phys. Lett. **93**, 132103 (2008).
[12] L. M. C. Pereira, U. Wahl, S. Decoster, J. G. Correia, M. R. da Silva, A. Vantomme, and J. P. Araújo, Appl. Phys. Lett. **98**, 201905 (2011).
[13] V. I. Baykov, P. A. Korzhavyi, and B. Johansson, Phys. Rev. Lett. **101**, 177204 (2008).
[14] H. Hofsass and G. Lindner, Phys. Rep. **201**, 121 (1991).

[15] U. Wahl, J. G. Correia, S. Cardoso, J. G. Marques, A. Vantomme, G. Langouche, and ISOLDE Collaboration, Nucl. Instrum. Methods Phys. Res. B **136**, 744 (1998).
[16] S. Agostinelli, J. Allison, K. Amako, J. Apostolakis, H. Araujo, P. Arce, M. Asai, D. Axen, S. Banerjee, G. Barrand, et al., Nucl. Instrum. Methods Phys. Res. Sect. A-Accel. Spectrom. Dect. Assoc. Equip. **506**, 250 (2003).
[17] J. Allison, K. Amako, J. Apostolakis, H. Araujo, P. A. Dubois, M. Asai, G. Barrand, R. Capra, S. Chauvie, R. Chytracek, et al., IEEE Trans. Nucl. Sci. **53**, 270 (2006).
[18] H. Hofsass, U. Wahl, and S. G. Jahn, Hyperfine Interact. **84**, 27 (1994).
[19] H. Hofsass, Hyperfine Interact. **97**, 247 (1996).
[20] U. Wahl, Hyperfine Interact. **129**, 349 (2000).
[21] U. Wahl, J. G. Correia, J. P. Araujo, E. Rita, and S. J. C, Appl. Phys. Lett. **90**, 181934 (2007).
[22] L. M. C. Pereira, U. Wahl, S. Decoster, J. G. Correia, L. M. Amorim, M. R. da Silva, J. P. Araujo, and A. Vantomme, Phys. Rev. B **84**, 125204 (2011).
[23] L. M. C. Pereira, U. Wahl, S. Decoster, J. G. Correia, M. R. da Silva, , J. P. Araújo, and A. Vantomme, Article V (unpublished).
[24] R. Bacewicz, A. Twarog, A. Malinowska, T. Wojtowicz, X. Liu, and J. K. Furdyna, J. Phys. Chem. Sol. **66**, 2004 (2005).
[25] J. F. Ziegler, J. P. Biersack, and M. D. Ziegler, *The Stopping and Range of Ions in Matter* (Lulu Press, 2009).
[26] V. N. Fedoseyev, K. Batzner, R. Catherall, A. H. M. Evensen, D. ForkelWirth, O. C. Jonsson, E. Kugler, J. Lettry, V. I. Mishin, H. L. Ravn, et al., Nucl. Instrum. Methods Phys. Res. Sect. B-Beam Interact. Mater. Atoms **126**, 88 (1997).
[27] U. Wahl, A. Vantomme, G. Langouche, and ISOLDE collaboration, Nucl. Instrum. Methods Phys. Res. B **148**, 492 (1999).
[28] K. Lawniczak-Jablonska, J. Libera, A. Wolska, M. T. Klepka, R. Jakiela, and J. Sadowski, Rad. Phys. Chem. **78**, S80 (2009).
[29] A. Wolska, K. Lawniczak-Jablonska, M. T. Klepka, R. Jakiela, J. Sadowski, I. N. Demchenko, E. Holub-Krappe, A. Persson, and D. Arvanitis, Act. Phys. Pol. **114**, 357 (2008).
[30] U. Wahl, J. G. Correia, E. Rita, J. P. Araujo, J. C. Soares, and ISOLDE Collaboaration, Nucl. Instrum. Methods Phys. Res. B **253**, 167 (2006).
[31] M. T. Robinson, Phys. Rev. B **40**, 10717 (1989).
[32] O. Koskelo, J. Raisanen, F. Tuomisto, J. Sadowski, and ISOLDE Collaboration, Sem. Sci. Tech. **24**, 045011 (2009).
[33] R. E. Goacher, S. Hegde, H. Luo, and J. A. Gardella, J. Appl. Phys. **106**, 044302 (2009).
[34] A. Kwiatkowski, D. Wasik, M. Kaminska, R. Bozek, J. Szczytko, A. Twardowski, J. Borysiuk, J. Sadowski, and J. Gosk, J. Appl. Phys. **101**, 113912 (2007).
[35] Kin Man Yu, M. Kaminska, and Z. Liliental-Weber, J. Appl. Phys. **72**, 2850

(1992).
[36] S. Ohagan and M. Missous, J. Appl. Phys. **75**, 7835 (1994).
[37] H. Shimizu, T. Hayashi, T. Nishinaga, and M. Tanaka, Appl. Phys. Lett. **74**, 398 (1999).
[38] Y. Ishiwata, M. Watanabe, R. Eguchi, T. Takeuchi, Y. Harada, A. Chainani, S. Shin, T. Hayashi, Y. Hashimoto, S. Katsumoto, et al., Phys. Rev. B **65**, 233201 (2002).
[39] J. C. Bourgoin, H. J. Vonbardeleben, and D. Stievenard, J. Appl. Phys. **64**, R65 (1988).

4.2 Lattice location of Mn and Co in ZnO and GaN

This section is composed of articles IV, V and VI, on the lattice location of Mn and Co in ZnO and GaN using the emission channeling technique (described in section 3.3). Article IV presents the results for Mn and Co in ZnO; article V for Mn and Article VI for Co in GaN. Article VI gives an overview of the results in all three articles (for Mn and Co in ZnO and GaN) and of previous emission channeling studies on the lattice location of Fe (between Mn and Co in the periodic system) in ZnO and GaN. Article VI also discusses the implications of these results on the current understanding of transition-metal incorporation in wide-gap oxides and nitrides.

Article IV

Mixed Zn and O substitution of Co and Mn in ZnO

L. M. C. Pereira,[1,2,3] U. Wahl,[2,4] S. Decoster,[1] J. G. Correia,[2,4]
L. M. Amorim,[1] M. R. da Silva,[4] J. P. Araújo,[3] and A. Vantomme[1]

[1]*Instituut voor Kern- en Stralingsfysica and INPAC, K.U.Leuven, 3001 Leuven, Belgium*
[2]*Instituto Tecnológico e Nuclear, UFA, 2686-953 Sacavém, Portugal*
[3]*IFIMUP and IN-Institute of Nanoscience and Nanotechnology, Department of Physics and Astronomy, Faculdade de Ciências da Universidade do Porto, 4169-007 Porto, Portugal*
[4]*Centro de Física Nuclear da Universidade de Lisboa, 1649-003 Lisboa, Portugal*

Abstract

The physical properties of an impurity atom in a semiconductor are primarily determined by the lattice site it occupies. In general, this occupancy can be correctly predicted based on chemical intuition, but not always. We report on one such exception in the dilute magnetic semiconductors (DMS) Co- and Mn-doped ZnO, experimentally determining the lattice location of Co and Mn using β^- emission channeling from the decay of radioactive ^{61}Co and ^{56}Mn implanted at the ISOLDE facility at CERN. Surprisingly, in addition to the majority substituting for Zn, we find up to 18% (27%) of the Co (Mn) atoms in O sites, which is virtually unaffected by thermal annealing up to 900°C. We discuss how this anion site configuration, which had never been considered before for any transition metal in any metal oxide material, may in fact have a low formation energy. This suggests a change in paradigm regarding transition metal incorporation in ZnO and possibly other oxides and wide-gap semiconductors.

Physical Review B **84**, 125204 (2011)

I. INTRODUCTION

Among the many combinations of host materials and transition metal dopants investigated in the past two decades, Co- and Mn-doped ZnO are currently two of the most intensively studied dilute magnetic semiconductors (DMS). However, despite major developments in both synthesis and characterization methods, the magnetism of wide-gap semiconductors remains one of the most controversial topics in condensed matter physics.[1]

Key to the understanding of DMS materials, is the local structure of the transition metal (TM) atoms in the host semiconductor matrix. The occupied lattice site determines the electronic structure of the impurity atom, and consequently its electrical and magnetic character. Intrinsic point defects, e.g. vacancies and self-interstitials, may form complexes with an impurity atom and change its charge state and magnetic moment or even mediate magnetic interactions. Another crucial parameter in DMS materials, the impurity spatial distribution (dilution versus aggregation), depends on the diffusivity of the impurity atoms, which in turn is controlled by the thermal stability of their local structure configuration(s). Stemming from a growing awareness of this complex influence on the magnetic properties, the lattice location of $3d$ transition metals in ZnO has been extensively studied in the last few years mostly based on X-ray absorption fine structure (XAFS) techniques, e.g. Refs. 2–4 for Co and Refs. 5–7 for Mn, incorporated either during growth[2–6,8] or by ion implantation.[7,9] When secondary phase segregation is avoided, all $3d$ TMs, including Co and Mn, were always found to substitute Zn, independently of the growth method,[10] as expected from the chemical similarities between the impurities and the host elements. The Zn substitution by Co^{2+} impurities has also been inferred from electron paramagnetic resonance (EPR) experiments (e.g. Refs. 11,12 and references therein) and confirmed by X-ray linear dichroism (XLD) measurements.[13] However, some observations do not completely conform to the scenario where all impurities occupy Zn substitutional sites in ZnO. X-ray absorption near-edge structure spectroscopy (XANES)[4,14] and X-ray photoelectron spectroscopy (XPS)[15] experiments have shown that Mn impurities can be incorporated in ZnO with charge states of up to 4+. Because Zn-substitutional Mn is expected to have a 2+ charge state with the 2+/3+ and 3+/4+ donor levels below the valence band maximum (thus not ionized),[16] these reports indicate that minority fractions may in fact occupy other lattice sites.

Here we report on the lattice location of ion-implanted Co and Mn in

ZnO, in the as-implanted state and after thermal annealing up to 900°C, using the emission channeling (EC) technique.

II. EXPERIMENT

Emission channeling[17] makes use of the charged particles emitted by a radioactive isotope. The screened Coulomb potential of atomic rows and planes determines the anisotropic scattering of the particles emitted isotropically during decay. Since these channeling and blocking effects strongly depend on the initial position of the emitted particles, they result in emission patterns that are characteristic of the lattice site(s) occupied by the probe atoms. The EC technique is ideal to study the lattice location of transition metals in semiconductors, as we have shown, for example, for Fe,[18] Cu[19] and Ag[20] in ZnO. It is particularly suited for those cases where significant fractions of the transition metal atoms occupy more than one lattice site (e.g. Ref. 21). For Mn impurities specifically, this multi-site lattice location capability has recently allowed us to locate a fraction of implanted Mn on the bond-centered (BC) site in Ge[22] and to unambiguously identify the interstitial Mn site in GaAs and quantitatively study its thermal stability.[23]

Commercially available ZnO wurtzite [0001] single-crystals (CrysTec GmbH), hydrothermally grown and Zn-face polished, were implanted at room temperature at the on-line isotope separator facility ISOLDE at CERN. As a Mn probe, we implanted radioactive ^{56}Mn ($t_{1/2} = 2.56$ h) and measured the β^- particles emitted during the decay to stable ^{56}Fe. For Co, we implanted the precursor isotope ^{61}Mn with the decay chain ^{61}Mn (0.71 s) $\rightarrow$ ^{61}Fe (6 min) $\rightarrow$ ^{61}Co (1.6 h) $\rightarrow$ ^{61}Ni (stable). In order to ensure that the contributions of ^{61}Mn and ^{61}Fe β^- particles to the channeling patterns were negligible, the measurements started only after a waiting period of approximately 30-60 min. The β^- decay of ^{61}Fe transfers a recoil energy of about 103 eV to its ^{61}Co daughter. This is well above the threshold displacement energy of ZnO (57 eV)[24] and is therefore sufficiently high to re-implant the ^{61}Co atoms, ensuring that they do not inherit the ^{61}Fe lattice site. The ^{61}Mn (^{56}Mn) implantations were performed under a tilt angle of 17° with respect to the surface normal in order to minimize ion channeling, with an energy of 60 keV (50 keV) and a fluence of 2×10^{13} cm^{-2}, resulting in a peak concentration of 6×10^{18} cm^{-3} (7×10^{18} cm^{-3}) at a projected range R_p of 278 Å (246 Å) with a 125 Å (115 Å) straggling, estimated using the MARLOWE code.[25] The low concentration regime used

in this study (below 1×10^{19} cm^{-3}) allows us to investigate the lattice location of Co and Mn free from phase segregation, which typically occurs for concentrations of the order of 10^{21} cm^{-3} (i.e. three orders of magnitude higher) and above.[26]

Angular-dependent emission yields of the β^- particles emitted during decay were measured at room temperature, along four crystallographic directions, [0001], [$\underline{1}$102], [$\underline{1}$101] and [$\underline{2}$113], in the as-implanted state and after *in situ* capless annealing in vacuum ($< 10^{-5}$ mbar) at temperatures up to 900°C. These patterns were recorded using a position- and energy-sensitive detection system similar to that described in Ref. 27. Given the relatively short half-life of ^{56}Mn and ^{61}Co, this system was installed on-line and upgraded with self-triggering readout chips for the Si pad detectors, enabling measurements during and/or immediately after implantation with count rates of up to several kHz.

III. RESULTS AND DISCUSSION

Quantitative lattice location is provided by fitting the experimental patterns with theoretical ones using the two-dimensional fit procedure outlined in Ref. 27. The theoretical patterns were calculated using the *many-beam* formalism[17] for probes occupying various sites in the ZnO (wurtzite) structure described in Ref. 28: substitutional Zn (S_{Zn}) and O (S_O) sites with varying root-mean-square (rms) displacements, the main interstitial sites, i.e. tetrahedral (T), octahedral (O), hexagonal (H), bond-centered (BC) and anti-bonding (AB), as well as interstitial sites resulting from displacements along the c or the basal directions. For all four measured directions in both ^{61}Co:ZnO and ^{56}Mn:ZnO, the calculated S_{Zn} patterns gave by far the best agreement, showing that the majority of the probe atoms occupy S_{Zn} sites, as expected. The fitting routine was then allowed to include, in addition to S_{Zn}, an additional lattice site, for which all the simulated sites were tested. The S_{Zn} + S_O double occupancy gives the best fit compared to all other combinations and considerably improves the S_{Zn} single-site fit. This is illustrated in Fig. 1, which shows the reduced χ^2 of the fit as we *move* the non-S_{Zn} site along the c-axis between two neighboring S_{Zn} sites. Data are shown only for the off-surface directions [$\underline{1}$102], [$\underline{1}$101] and [$\underline{2}$113], since the [0001] patterns are not sensitive to displacements of the probe atoms along the c-axis. Consistently for all three directions, the best fits are clearly centered on the S_O site. In fact, the relative improvement in χ^2 is correlated with the spatial separation of Zn and O rows along the

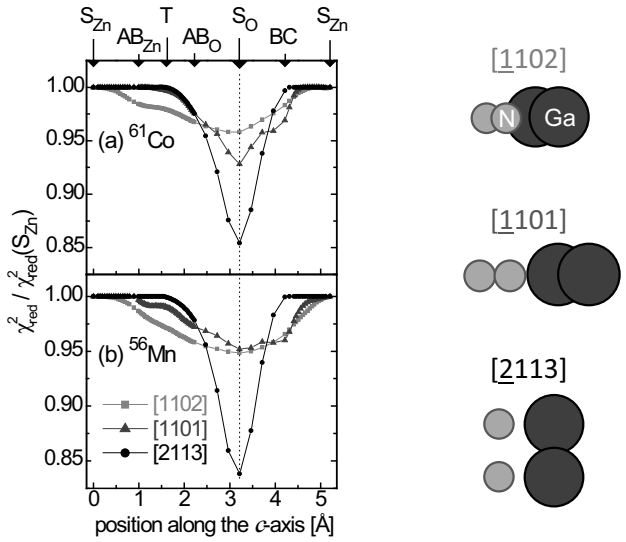

FIG. 1: *Left* - Reduced χ^2 of the fits to the ^{61}Co:ZnO (a) and ^{56}Mn:ZnO (b) data (800°C annealing step), in the vicinity of the [$\underline{1}$102], [$\underline{1}$101] and [$\underline{2}$113] directions. Each data point corresponds to the best fit obtained using two given sites, with the corresponding two fractions as free parameters. The site pairs are composed of S_{Zn} plus each of the simulated sites along the *c*-axis: the S_O and the T sites, the BC and AB sites along the *c*-axis and a number of intermediate positions. The reduced χ^2 (*y*-axis) of these two-sites fits have been normalized to that of the one-site (S_{Zn}) fit. The *x*-axis corresponds to the position (along the *c*-axis) of the non-S_{Zn} site used in each fit. *Right* - Projection of the ZnO lattice on the plane perpendicular to each direction, showing that the separation between Zn and O sublattices is maximized for [$\underline{2}$113].

channeling axis (Fig. 1), being most pronounced for the [$\underline{2}$113] direction. A similar behavior is observed for displacements along the basal directions, with the best fit consistently centered on the S_O site. As an example for the good match between experiment and simulated patterns, Fig. 2 compares the β^- emission yields of ^{61}Co:ZnO along the four measured directions with the best fits of theoretical patterns, obtained for 82% of the ^{61}Co atoms on S_{Zn} (Co_{Zn}) and 18% on S_O sites (Co_O). Introducing a third site yields only insignificant fit improvements. Possible fractions on other sites are estimated to be below 5%.

In Fig. 3 we have compiled the Co and Mn fractions on S_{Zn} and S_O sites as a function of annealing temperature. Within experimental error, both the Co_O and Mn_O fractions remain constant around 16% and 24%,

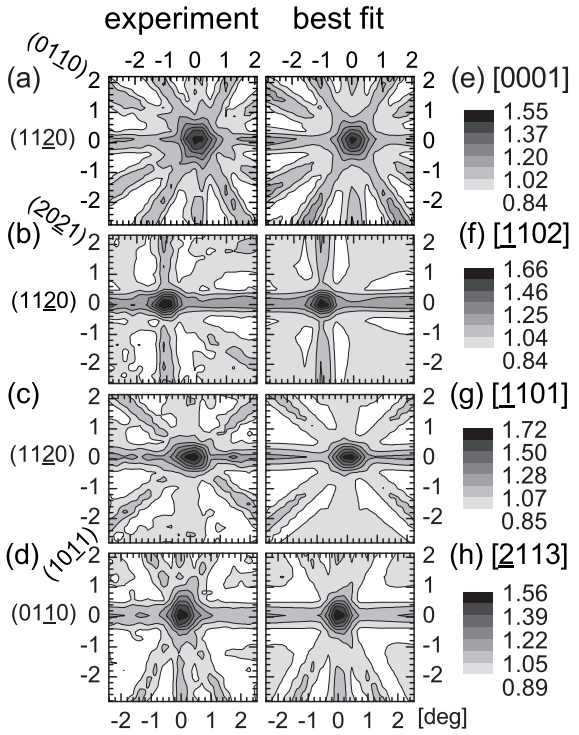

FIG. 2: (a)-(d) Normalized experimental ^{61}Co β^- emission channeling patterns in the vicinity of the [0001], [$\underline{1}$102], [$\underline{1}$101] and [$\underline{2}$113] directions following annealing at 800°C. (e)-(h) Corresponding best fits with 82% and 18% of the ^{61}Co atoms on S_{Zn} and S_O sites, respectively.

respectively, up to the highest temperature annealing step. The best fits are obtained for rms displacements of Co_{Zn} and Mn_{Zn} from ideal S_{Zn} sites between 0.06 Å and 0.09 Å. Although the fitting is less sensitive to rms displacements of the Co_O and Mn_O minority fractions, it indicates that these may be isotropically scattered by up to 0.25 Å around the ideal O sites. Based on the thermal vibration amplitudes of $u_1(Zn) = 0.08$ Å and $u_1(O) = 0.08 - 0.09$ Å for Zn and O, respectively,[29] we conclude that, while Co_{Zn} and Mn_{Zn} atoms are incorporated in ideal Zn sites, some degree of lattice relaxation may take place in the vicinity of Co_O and Mn_O atoms.

It is interesting to compare this behavior to that of Fe, which is positioned between Co and Mn in the periodic system. In our previous EC experiments on ^{59}Fe:ZnO, the maximum fraction of Fe on substitutional O sites compatible with the experimental data is less than 5%, which is

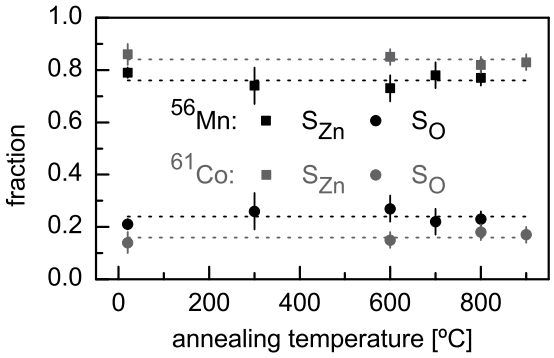

FIG. 3: Fractions of ^{56}Mn and ^{61}Co atoms on S_{Zn} and S_O sites following each annealing step. The dashed lines correspond to the mean fractions, averaged from the values for the different annealing steps.

considered below the sensitivity limit of the technique.[18] The average β^- energies for ^{61}Co and ^{56}Mn are 460 keV and 831 keV respectively, and are thus significantly larger than the one for ^{59}Fe, which is 118 keV. Since a higher β^- energy results in narrower channeling effects, the experimental patterns from ^{61}Co and ^{56}Mn are less resolved than those previously measured for ^{59}Fe. In order to exclude that this would influence the analysis, we carried out a ^{56}Mn:ZnO EC experiment with increased angular resolution. To do so, we doubled the distance between the sample and the detector (from 30 cm to 60 cm), thus improving the angular resolution by approximately a factor of two. The analysis of this high-resolution data confirms the S_O occupancy and, in fact the experimental patterns even allow for its visual identification. This is illustrated in Fig. 4, which compares calculated patterns for ^{56}Mn probes on S_{Zn} and S_O to experimental patterns from which the S_{Zn} component has been subtracted. The S_{Zn}-subtracted patterns are remarkably similar to S_O and very different from S_{Zn} patterns, which unambiguously confirms the S_O occupancy.

Finding significant fractions of Co and Mn atoms on O sites is remarkably surprising. Not only has it never been observed, it has never even been considered since the Zn substitution was regarded as obvious and taken for granted. Moreover, experimentally identifying a minority site in cases of double occupancy is extremely challenging. These two factors (being unexpected and difficult to detect) could explain why such anion site minority fractions may have passed undetected in previous studies on the lattice location of Mn and Co in ZnO, incorporated either during growth (e.g.

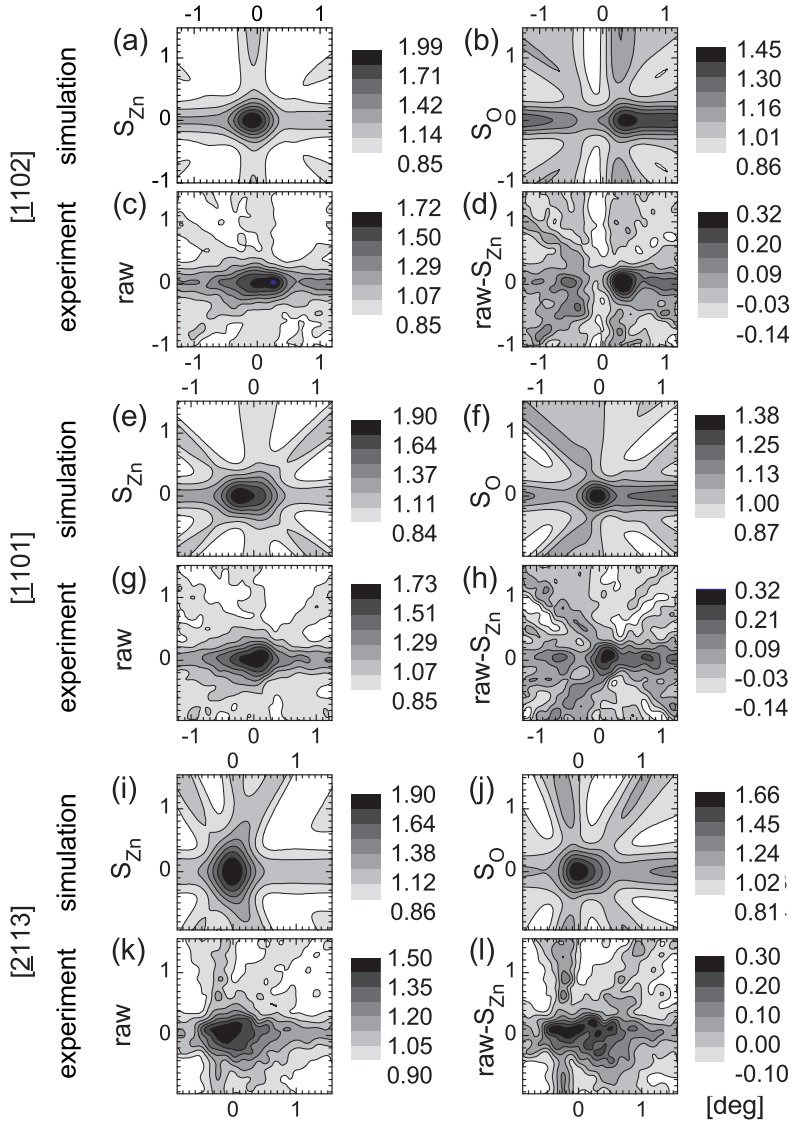

FIG. 4: Comparison of the experimental and calculated patterns of the high resolution, as-implanted ^{56}Mn:ZnO experiment: calculated [$\underline{1}$102], [$\underline{1}$101] and [$\underline{2}$113] patterns for 100% of ^{56}Mn probes on S_{Zn} [(a), (e), (i)] and S_O sites [(b), (f), (j)]; normalized experimental patterns [(c), (g), (k)]. Patterns [(d), (h), (l)] result from subtracting the fitted S_{Zn} component from the experimental patterns. For all three directions, this allows for the visual identification of the S_O occupancy, i.e. patterns (d), (h) and (l) reproduce the distinctive features of the S_O patterns (b), (f) and (j), respectively.

Refs. 2–6,8) or by ion implantation (e.g. Refs. 7,9).

Generally, in compound semiconductors, the lattice sites of impurities are determined by chemical similarities and matching of size and electronegativity with the host atoms. Not only are Co and Mn 3*d* metals like Zn, they are very similar to Zn and very different from O in terms of electronegativity and ionic radii, which in principle makes it energetically unfavorable for Co and Mn impurities to be incorporated on O sites. The non-equilibrium nature of ion implantation may have an influence, but it does not explain why, under the same conditions, the S_O occupancy is observed for Mn and Co and not for Fe. The case that has been studied theoretically which most resembles Mn_O and Co_O defects is the Zn antisite (Zn_O). Depending on the growth conditions (Zn- or O-rich) and Fermi level, either 2^+, 3^+ or 4^+ charge states of Zn_O can be stable, with the $4^+/3^+$ and $3^+/2^+$ transition levels deep in the bandgap.[30–33] These calculations predicted that the formation energy of Zn_O^{4+} can in fact be very small, even negative, under metal-rich conditions and for a Fermi level close to the valence band maximum. Therefore, if the $4^+/3^+$ and $3^+/2^+$ transition levels of Co_O and Mn_O are shallower than those of Zn_O, it is conceivable that the formation energies of Co_O and Mn_O may indeed be small enough to allow for sizable concentrations, even with the Fermi level close to the conduction band minimum, which is typically the case for ZnO (intrinsically *n*-type). On the other hand, the $4^+/3^+$ and $3^+/2^+$ levels of Fe_O may be located deeper in the bandgap and therefore not be ionized when the Fermi level is close to the conduction band minimum. Based on the Zn_O case, this would result in a higher formation energy of Fe_O compared to Co_O and Mn_O, and thus decrease its concentration below the detection limit.

An important consequence of the discussion in the previous paragraph is that O-substitution can thus explain the observed 4+ charge state of minority fractions of Mn impurities in ZnO thin films.[4,14,15] Moreover, the fact that for those studies the impurities were not incorporated by ion implantation but during growth, indicates that minority anion substitution may be a general phenomenon in transition metal doped ZnO. In principle, the concentration of transition metal impurities in anion sites depends on (1) the energy cost of incorporating an atom of a given impurity element in an O site and (2) the available energy, i.e. the characteristic energy scale of the impinging impurity atoms. The energy cost (1) depends on (i) the "chemistry" of the impurity-host combination, which for the ZnO host case appears to favor Co and Mn over Fe, based on our results and the discussion of the previous paragraph, and (ii) the tendency of the growth or

doping process to form O vacancies which can be filled by transition metal impurities (for doping during growth this is favored in O-poor conditions; in ion implanted systems O vacancies are created by the ion bombardement). The available energy (2) depends primarily on the growth or doping method and conditions, increasing with the characteristic order of magnetiude of impinging atom energies: 0.1 eV for molecular beam epitaxy (MBE), 1 eV for sputtering deposition, 10 eV for pulsed laser deposition (PLD) and 1 keV for ion implantation.

Because the magnetic and electric behavior of Co and Mn impurities depend primarily on the lattice site(s) they occupy, our results have direct implications on the field of dilute magnetic semiconductors. For example, anion site Mn and Co are likely to behave as multiple-donor defects in ZnO and thus contribute to preventing the realization of *p*-type conduction (by acceptor co-doping) in TM-doped ZnO, which is considered crucial to establish ferromagnetic order via *p*-*d* Zener exchange.[34] A similar case is the well known double-donor Mn interstitial in (Ga,Mn)As which compensates for acceptor substitutional Mn both electrically and magnetically, thus decreasing the Curie temperature.[35] Also in Mn-doped GaN, the presence of donor defects controls the charge state of cation (Ga) substitutional Mn, hence the type of magnetic interactions: ferromagnetic for Mn^{3+},[36] antiferromagnetic for Mn^{2+}.[37]

IV. CONCLUSIONS

In summary, we have experimentally established the lattice location of implanted Co and Mn in ZnO in the low concentration regime ($< 10^{18}$ cm^{-3}). Surprisingly, in addition to the majority on substitutional Zn sites, we find up to 18% (27%) of the Co (Mn) atoms on substitutional O sites, which is virtually unaffected by thermal annealing up to 900°C. Because this minority anion site substitution has never even been considered, it challenges our current understanding of transition metal incorporation in ZnO and wide-gap semiconductors in general. In particular, these results motivate a theoretical assessment of the formation energies of these defects, as well as an experimental reassessment of the lattice location of Mn and Co in wide-gap semiconductors, its dependence on preparation techniques and growth conditions, and its influence on the magnetic properties of wide-gap DMS materials.

Acknowledgments

This work was supported by the Portuguese Foundation for Science and Technology (PTDC/FIS/66262/2006, CERN/FP/116320/2010, SFRH/BD/35761/2007), the Research Foundation - Flanders (FWO), the EURONS project (RII3-CT-2004-506065), the SPIRIT project (contract no. 227012), KULeuven projects GOA/2009/006 and INPAC EF/05/005 and the IUAP P6/42 program.

[1] T. Dietl, Nat. Mater. **9**, 965 (2010).
[2] T. Shi, S. Zhu, Z. Sun, S. Wei, and W. Liu, Appl. Phys. Lett. **90**, 102108 (2007).
[3] Z. Sun, W. Yan, G. Zhang, H. Oyanagi, Z. Wu, Q. Liu, W. Wu, T. Shi, Z. Pan, P. Xu, et al., Phys. Rev. B **77**, 245208 (2008).
[4] N. R. S. Farley, K. W. Edmonds, A. A. Freeman, G. van der Laan, C. R. Staddon, D. H. Gregory, and B. L. Gallagher, New J. Phys. **10**, 055012 (2008).
[5] J. H. Guo, A. Gupta, P. Sharma, K. V. Rao, M. A. Marcus, C. L. Dong, J. M. O. Guillen, S. M. Butorin, M. Mattesini, P. A. Glans, et al., J. Phys.: Condens. Matter. **19**, 172202 (2007).
[6] H. Ofuchi, Z. W. Jin, T. Fukumura, M. Kawasaki, Y. Matsumoto, T. Hasegawa, H. Fujioka, M. Oshima, and H. Koinuma, Phys. Scr. **T115**, 614 (2005).
[7] J. A. Sans, G. Martinez-Criado, J. Susini, R. Sanz, J. Jensen, I. Minguez, M. Hernandez-Velez, A. Labrador, and P. Carpentier, J. Appl. Phys. **107**, 023507 (2010).
[8] J. C. Pivin, G. Socol, I. Mihailescu, P. Berthet, F. Singh, M. K. Patel, and L. Vincent, Thin Solid Films **517**, 916 (2008).
[9] A. P. Singh, R. Kumar, P. Thakur, N. B. Brookes, K. H. Chae, and W. K. Choi, J. Phys.: Condens. Matter. **21**, 185005 (2009).
[10] A. Ney, M. Opel, T. C. Kaspar, V. Ney, S. Ye, K. Ollefs, T. Kammermeier, S. Bauer, K.-W. Nielsen, S. T. B. Goennenwein, et al., New J. Phys. **12**, 013020 (2010).
[11] P. Sati, R. Hayn, R. Kuzian, S. Regnier, S. Schafer, A. Stepanov, C. Morhain, C. Deparis, M. Laugt, M. Goiran, et al., Phys. Rev. Lett. **96**, 017203 (2006).
[12] N. Jedrecy, H. J. von Bardeleben, Y. Zheng, and J. L. Cantin, Phys. Rev. B **69**, 041308 (2004).
[13] A. Ney, K. Ollefs, S. Ye, T. Kammermeier, V. Ney, T. C. Kaspar, S. A. Chambers, F. Wilhelm, and A. Rogalev, Phys. Rev. Lett. **100**, 157201 (2008).
[14] P. Thakur, K. H. Chae, J.-Y. Kim, M. Subramanian, R. Jayavel, and K. Asokan, Appl. Phys. Lett. **91**, 162503 (2007).
[15] H. T. Cao, Z. L. Pei, J. Gong, C. Sun, R. F. Huang, and L. S. Wen, J. Solid State Chem. **177**, 1480 (2004).

[16] T. Graf, S. T. B. Goennenwein, and M. S. Brandt, Phys. Status Solidi B-Basic Res. **239**, 277 (2003).
[17] H. Hofsass and G. Lindner, Phys. Rep. **201**, 121 (1991).
[18] E. Rita, U. Wahl, J. G. Correia, E. Alves, and J. C. Soares, Appl. Phys. Lett. **85**, 4899 (2004).
[19] U. Wahl, E. Rita, J. G. Correia, E. Alves, and J. G. Soares, Phys. Rev. B **69**, 012102 (2004).
[20] E. Rita, U. Wahl, A. M. L. Lopes, J. P. Araujo, J. G. Correia, E. Alvesa, J. C. Soares, and ISOLDE Collaboration, Physica B **340**, 240 (2003).
[21] S. Decoster, S. Cottenier, B. De Vries, H. Emmerich, U. Wahl, J. G. Correia, and A. Vantomme, Phys. Rev. Lett. **102**, 065502 (2009).
[22] S. Decoster, S. Cottenier, U. Wahl, J. G. Correia, L. M. C. Pereira, C. Lacasta, M. R. Da Silva, and A. Vantomme, Appl. Phys. Lett. **97**, 151914 (2010).
[23] L. M. C. Pereira, U. Wahl, S. Decoster, J. G. Correia, M. R. da Silva, A. Vantomme, and J. P. Araújo, Appl. Phys. Lett. **98**, 201905 (2011).
[24] D. R. Locker and J. M. Meese, IEEE Trans. Nucl. Sci. **NS19**, 237 (1972).
[25] M. T. Robinson, Phys. Rev. B **40**, 10717 (1989).
[26] S. Zhou, K. Potzger, J. von Borany, R. Groetzschel, W. Skorupa, M. Helm, and J. Fassbender, Phys. Rev. B **77**, 035209 (2008).
[27] U. Wahl, J. G. Correia, S. Cardoso, J. G. Marques, A. Vantomme, G. Langouche, and ISOLDE Collaboration, Nucl. Instrum. Methods Phys. Res. B **136**, 744 (1998).
[28] U. Wahl, A. Vantomme, G. Langouche, J. P. Araujo, L. Peralta, J. G. Correia, and ISOLDE Collaboration, J. Appl. Phys. **88**, 1319 (2000).
[29] U. Wahl, E. Rita, J. G. Correia, E. Alves, J. P. Araujo, and ISOLDE Collaboration, Appl. Phys. Lett. **82**, 1173 (2003).
[30] A. Janotti and C. G. Van de Walle, Phys. Rev. B **76**, 165202 (2007).
[31] F. Oba, A. Togo, I. Tanaka, J. Paier, and G. Kresse, Phys. Rev. B **77**, 245202 (2008).
[32] F. Oba, M. Choi, A. Togo, A. Seko, and I. Tanaka, J. Phys.: Condens. Matter **22**, 384211 (2010).
[33] R. Vidya, P. Ravindran, H. Fjellvag, B. G. Svensson, E. Monakhov, M. Ganchenkova, and R. M. Nieminen, Phys. Rev. B **83**, 045206 (2011).
[34] T. Dietl, H. Ohno, F. Matsukura, J. Cibert, and D. Ferrand, Science **287**, 1019 (2000).
[35] T. Jungwirth, K. Y. Wang, J. Masek, K. W. Edmonds, J. Konig, J. Sinova, M. Polini, N. A. Goncharuk, A. H. MacDonald, M. Sawicki, et al., Phys. Rev. B **72**, 165204 (2005).
[36] E. Sarigiannidou, F. Wilhelm, E. Monroy, R. M. Galera, E. Bellet-Amalric, A. Rogalev, J. Goulon, J. Cibert, and H. Mariette, Phys. Rev. B **74**, 041306 (2006).
[37] S. Granville, B. J. Ruck, F. Budde, H. J. Trodahl, and G. V. M. Williams, Phys. Rev. B **81**, 184425 (2010).

Article V

Evidence of N substitution by Mn in wurtzite GaN

L. M. C. Pereira,[1,2,3] U. Wahl,[2,4] S. Decoster,[3] J. G. Correia,[2,4]
M. R. da Silva,[4] A. Vantomme,[3] and J. P. Araújo[1]

[1]*IFIMUP and IN-Institute of Nanoscience and Nanotechnology, Department of Physics and Astronomy, Faculdade de Ciências da Universidade do Porto, 4169-007 Porto, Portugal*
[2]*Instituto Tecnológico e Nuclear, UFA, 2686-953 Sacavém, Portugal*
[3]*Instituut voor Kern- en Stralingsfysica and INPAC, K.U.Leuven, 3001 Leuven, Belgium*
[4]*Centro de Física Nuclear da Universidade de Lisboa, 1649-003 Lisboa, Portugal*

Abstract

We report on the lattice location of Mn in wurtzite GaN using β^- emission channeling. In addition to the majority substituting for Ga, we locate up to 20% of the Mn atoms in N sites. We suggest that the incorporation of Mn in N sites is favored under sufficiently high concentrations of N vacancies, and stabilized by a highly charged state of the Mn cations. Since N substitution by Mn impurities in wurtzite GaN had never been observed experimentally or even considered theoretically before, it challenges the current paradigm of transition-metal incorporation in widegap dilute magnetic semiconductors.

In preparation for *Physical Review Letters*

Dilute magnetic semiconductors (DMS) continue to challenge our understanding of how transition-metal impurities behave in widegap nitrides and oxides, both in terms of magnetism and structure.[1] With ferromagnetism being reported well above the ordering temperatures of any other type of dilute magnetic materials, widegap DMSs still divide the magnetics community between those who report it and those who report its absence (see e.g. Ref. 1–5 for recent discussions). On the structure side, only in the last few years has a more consistent picture of the structural phase-diagram of some widegap DMSs started to emerge, with phenomena such as spinodal decomposition and other types of chemical and structural phase-segregation being carefully documented (see e.g. Ref. 1 and references therein). It is however at the very genesis of both the magnetic and structural properties of widegap DMS that some of the most puzzling reports can be found: the lattice sites occupied by the transition-metal impurities. By determining the impurity's electronic structure and the energy barriers which it must overcome in order to diffuse, the impurity's lattice site directly controls its magnetism and aggregation behavior. Although it is generally accepted that 3*d* transition metals such as Mn and Co substitute the cation in widegap nitrides and oxides (e.g. Ga in GaN and Zn in ZnO), some reports suggest that this is not a general rule (see Ref. 6 for a recent discussion on ZnO).

One of the most well understood widegap DMS, Mn-doped GaN is also one of those that best illustrate the open questions regarding (i) the magnetism, (ii) phase pureness and (iii) the lattice location of the magnetic impurities. Despite the many reports of ferromagnetism at and above room temperature (i), recent studies on carefully characterized materials found only paramagnetism,[2] antiferromagnetic interactions,[7] or at best, ferromagnetic order with very low Curie temperature ($T_C < 10$ K).[8] Mn-doped GaN is also an interesting system in which to study "subtle" forms of impurity segregation (ii), using for example synchrotron radiation,[9] which can easily pass undetected using more conventional characterization techniques. Regarding the lattice location of the Mn impurities (iii), although the majority of the reports are consistent with cation (Ga) substitution (e.g. Refs. 2,3,10,11 based on X-ray absorption fine structure (XAFS), Refs. 12,13 on ion-channeling, and Ref. 14 on electron-channeling), some observations do not completely conform to it. This is particularly the case for zincblende GaN, for which there are strong indications that Mn impurities may occupy non-Ga-substitutional sites. Based on XANES experiments, it has been reported that small fractions of the Mn impurities are located in interstitial

sites.[15] In Ref. 16, extended X-ray absorption fine structure (EXAFS) experiments detected a remarkably high fraction of 75% of the Mn impurities in anion (N) substitutional sites. However, the unambiguous identification of a minority site in cases of double occupancy poses a number of challenges to XAFS techniques such as XANES and EXAFS. In addition, it is unknown if the non-Ga substitution observed in the zincblende GaN may also occour in the wurtzite structure, which is by far more commonly used in the context of GaN-based applications and DMS.

Here we report on the lattice location of Mn impurities in epitaxial thin films of wurtzite GaN, using the emission channeling technique. The aim is to determine if and which non-Ga-substitutional sites may be occupied by Mn impurities in the wurtzite lattice, using a technique which has been specifically developed for lattice location of impurities in single-crystalline materials. Measurements were carried out in the as-implanted state and after thermal annealing up to 900 °C in order to investigate the thermal stability of the Mn impurities in the respective lattice sites. We focus on the low concentration regime (below 1×10^{19} cm^{-3}, i.e. $< 0.03\%$) in order to minimize possible effects of Mn segregation.

Emission channeling[17] makes use of the charged particles emitted by a decaying radioactive isotope. The screened Coulomb potential of atomic rows and planes determines the anisotropic scattering of the particles emitted isotropically during decay. Because these channeling and blocking effects strongly depend on the initial position of the emitted particles, they result in emission patterns which are characteristic of the lattice site(s) occupied by the probe atoms. We have previously used the emission channeling technique to determine the lattice location of other impurities in GaN (e.g. Fe[18], As[19] and several rare earths[20]). The technique is particularly suited for those cases where significant fractions of the impurity atoms occupy more than one lattice site. For Mn impurities in particular, this multi-site lattice location capability has recently allowed us to locate a fraction of implanted Mn on the bond-centered (BC) interstitial site in Ge,[21] in anion-substitutional sites (Oxygen sites) in ZnO,[6] as well as to unambiguously identify the interstitial Mn site in GaAs and quantitatively study its thermal stability.[22]

Epitaxial thin films of wurtzite [0001] GaN grown on sapphire were implanted at room temperature with a fluence of 2×10^{13} cm^{-2} of radioactive ^{56}Mn ($t_{1/2} = 2.56$ h), at the on-line isotope separator facility ISOLDE at CERN. The implantations were performed under a tilt angle of 17° to minimize ion channeling, using an energy of 50 keV, resulting in a peak

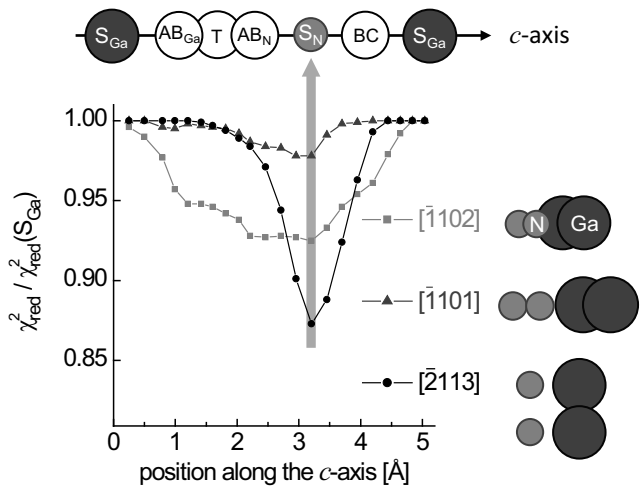

FIG. 1: Reduced χ^2 of the fits to the experimental emission yields in the vicinity of the $[\bar{1}102]$, $[\bar{1}101]$ and $[\bar{2}113]$ directions (following 600°C annealing). Each data point corresponds to the best fit obtained using two given sites, with the corresponding two fractions as free parameters. The site pairs are composed of S_{Ga} plus each of the simulated sites along the c-axis (depicted above the plot): the S_N and the T sites, the BC and AB sites along the c-axis and a number of intermediate positions. The x-axis corresponds to the position (along the c-axis) of the non-S_{Ga} site used in each fit. The reduced χ^2 (y-axis) of these two-sites fits are normalized to that of the one-site (S_{Ga}) fit. The non-equivalent rows of Ga and N atoms, projected on the plane perpendicular to each of the axes, are also shown (*right*). Note that the separation between Ga and N rows is maximized along the $[\bar{2}113]$ axis.

concentration of 7×10^{18} cm^{-3} at a projected range R_p of 247 Å with a 114 Å straggling, as estimated using the MARLOWE code.[23] Angular-dependent emission yields of the β^- particles emitted during decay to stable ^{56}Fe were measured at room temperature, along four crystallographic directions, [0001], $[\bar{1}102]$, $[\bar{1}101]$ and $[\bar{2}113]$, in the as-implanted state and after *in situ* capless annealing in vacuum ($< 10^{-5}$ mbar) at 300°C, 600°C, 700°C, 800°C and 900°C. The patterns were recorded using a position- and energy-sensitive detection system similar to that described in Ref. 24. Given the short half-life of ^{56}Mn, this system was installed on-line and upgraded with self-triggering readout chips for the Si pad detectors, enabling measurements during and/or immediately after implantation with count rates of up to several kHz.

Quantitative lattice location is provided by fitting the experimental pat-

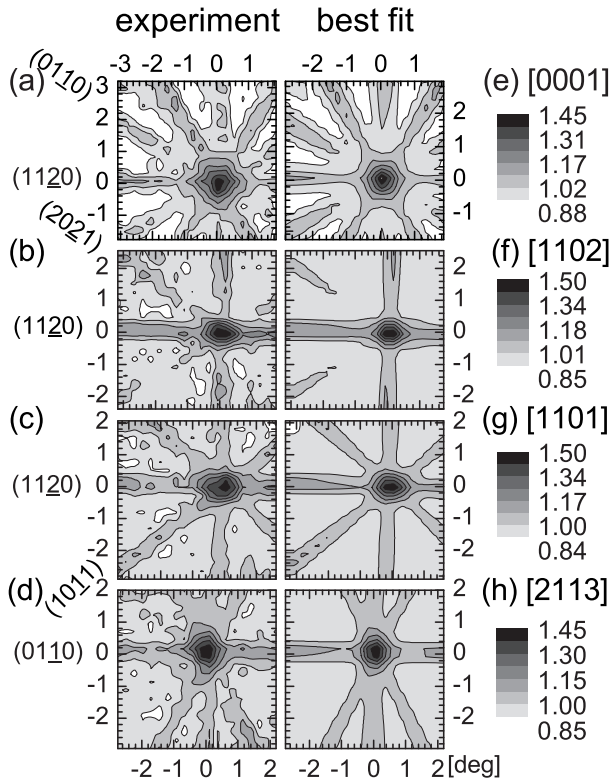

FIG. 2: (a)-(d) Normalized experimental ^{56}Mn β^- emission channeling patterns in the vicinity of the [0001], [$\bar{1}$102], [$\bar{1}$101] and [$\bar{2}$113] directions following annealing at 600 °C. (e)-(h) Corresponding best fits with 81% and 19% of the ^{56}Mn atoms on S_{Ga} and S_N sites, respectively.

terns with theoretical ones using the two-dimensional fit procedure outlined in Ref. 24. The theoretical patterns were calculated using the *many-beam* formalism[17] for probes occupying various sites in the wurtzite GaN structure:[25] substitutional Ga (S_{Ga}) and N (S_N) sites with varying root-mean-square displacements, the main interstitial sites, i.e., tetrahedral (T), octahedral (O), hexagonal (H), bond-centered (BC) and anti-bonding (AB), as well as interstitial sites resulting from displacements along the *c* or the basal directions. For all four measured directions, the calculated S_{Ga} patterns gave by far the best agreement, showing that the majority of the probe atoms occupy S_{Ga} sites, as expected. The fitting routine was then allowed to include, in addition to S_{Ga}, an additional lattice site, for which all simulated sites were considered. Consistently for all measured direc-

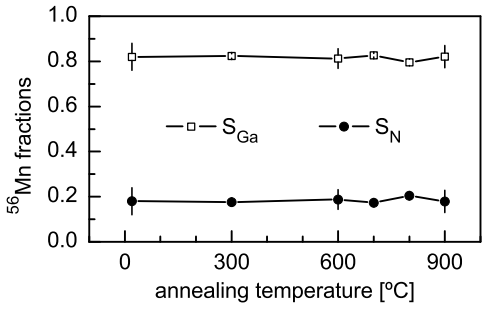

FIG. 3: Fractions of ^{56}Mn impurities on S_{Ga} and S_N sites following each annealing step.

tions, the S_{Ga} + S_N double occupancy gives the best fit compared to all other combinations and considerably improves the S_{Ga} single-site fit. This is illustrated in Fig. 1, which shows the reduced χ^2 of the fit as we *move* the non-S_{Ga} site along the *c*-axis between two neighboring S_{Ga} sites. Consistently for all three directions, the best fits are centered in the S_N site. The sensitivity of the fit (in terms of magnitude and "width" of the improvement in χ^2) is correlated with the spatial separation between Ga and N rows along the channeling axis (Fig. 1), being most pronounced for the [$\bar{2}$113] direction. As an example of the good match between experiment and simulated patterns, Fig. 2 compares the normalized experimental β^- emission yields of ^{56}Mn:GaN, following annealing at 600 °C, along the four measured directions [(a)-(d)] with the best fits of theoretical patterns [(e)-(h)]. The best fit is obtained for 81% of the ^{56}Mn atoms on S_{Ga} (Mn_{Ga}) and 19% on S_N sites (Mn_N). Introducing a third site yields only insignificant fit improvements. Possible fractions in other sites are estimated to be below 5%. Figure 3 shows the fractions of ^{56}Mn probes in S_{Ga} and S_N sites as a function of annealing temperature. Within experimental error, the Mn_N fraction remains constant around 20%, up to highest annealing temperature of 900°C.

Chemically, 3*d* transition metals such as Mn are much more similar to Ga (a post-transition metal) than they are to N (a non-metal). In particular, the electronegativity and ionic radii of Mn are much closer to those of Ga compared to N, which in principle makes it energetically unfavorable for Mn impurities to be incorporated in N sites. Because anion substitution by 3*d* transition metals in GaN is so unexpected, theoretical considerations of the phenomena are very scarce, specially for wurtzite GaN. For

zincblende GaN, the calculated total energies for Mn in Ga and N sites indicate, as expected, that Ga substitution is more favorable.[26] However, the calculations in Ref. 26 do not consider charged Mn_N defects. The defect that most resembles Mn_N, for which different charge states have been considered, is the Ga antisite (Ga_N). It has been shown that varying the charge state from neutral to 4+ considerably decreases the formation energy of Ga_N in wurtzite GaN (from ~ 8 eV to ~ 1 eV, under Ga-rich/N-poor conditions).[27] Such highly charged states are only stable for a Fermi level sufficiently close to the valence band, i.e. in the presence of acceptors states to which the Ga_N electrons can be transfered. In Mn-doped GaN, that role can be played by the deep acceptor levels of Mn_{Ga} defects (the Ga-substitutional fraction). On the other hand, the requirement of N-poor growth is in agreement with Ref. 16. There, N-substitution by Mn (in zincblende GaN) was only observed in thin films grown under N-poor conditions. In other words, increasing the concentration of N vacancies (which can be "filled" by Mn impurities), decreases the formation energy of Mn_N defects, increasing its concentration. In the present study, the required N vacancies were in principle created upon $^{56}Mn^+$ ion bombardment. Note, nonetheless, that the incorporation of Mn impurities in N sites cannot be considered a direct effect of ion implantation, since it was not observed for Fe under very similar experimental conditions.[18] Fe is a $3d$ transition metal as well, with an atomic mass which is similar to that of Mn and thus similar incorporation kinetics. A more detailed description of the conditions under which N substitution by Mn impurities occurs in wurtzite GaN will require the assessment of the formation energies of such defects, as well as an experimental reassessment of the lattice location of Mn in GaN for different preparation methods and growth conditions, carefully taking into consideration the possibility of anion substitution.

Together with our recent report on O-substitutional Mn and Co in ZnO,[6] these results suggest that anion substitution by $3d$ transition-metals may be a general phenomenon in widegap nitrides and oxides. However, because it is both highly unexpected and difficult to detect with conventional techniques, anion substitution by transition metals may have so far passed undetected in these materials. Although there is in principle no reason to consider anion substitution as a potential route towards room temperature ferromagnetism, a comprehensive description of the phenomenon is fundamental for the understanding of widegap DMS materials. For example, it has been predicted that electron delocalization increases the range of the magnetic interactions between anion-substitutional compared to cation-

substitutional Mn impurities in zincblende GaN, potentially leading to spin-glass behavior in anion-substituted Ga(Mn,N).[26] Indeed, magnetometry measurements in Ref. 16 indicate that while cation-substituted (Ga,Mn)N is not ferromagnetic down to 5 K, anion-substituted Ga(Mn,N) displays some degree of magnetic irreversibility at low temperatures (5 K). In a slightly different context, because anion-substitutional transition-metals are likely to behave as donors (see previous paragraph), they may also play an important role in terms of electrical (self-)compensation. For example, such defects may contribute to preventing the realization of *p*-type conduction (e.g. in Mg co-doped GaN), which is considered crucial to establish ferromagnetic order via *p*-*d* Zener exchange in Mn-doped GaN and ZnO.[28] In Mn-doped GaN, in particular, it is relatively well established that the type of magnetic interactions between Ga-substitutional Mn moments is determined by the Mn charge state, which in turn depends on the concentration of compensating donor defects.[3] Under stringent growth conditions that minimize the concentration of compensating donors such as N vacancies and H impurities (donors), Mn impurities are incorporated as Mn^{3+}. In such cases, ferromagnetic interactions[3] and low temperature order ($T_C < 10$ K)[8] can be observed. More commonly, such stringent growth conditions are not satisfied and Mn impurities are incorporated as compensated Mn^{2+}, for which only nearest-cation-neighbor antiferromagnetic interactions are observed.[3,7] Being a potential donor defect, Mn_N may also compensate Mn_{Ga}^{3+} impurities, i.e. turning ferromagnetically interacting Mn_{Ga}^{3+} into antiferromagnetically interacting Mn_{Ga}^{2+}. Such electric and magnetic self-compensation by N-substitutional Mn in GaN is very similar to that of interstitial Mn in GaAs, also a donor which compensates acceptor and ferromagnetically interacting Ga-substitutional Mn.[29]

In summary, we have experimentally demonstrated that, in addition to the majority substituting for the cation (Ga), minority fractions (up to 20%) of ion-implanted Mn impurities occupy anion (N) sites in wurtzite GaN. Both Ga- and N-substitutional fractions are virtually unafected by thermal annealing up to 900°C. Together with recent reports on anion substitution by Mn and Co in ZnO, these results challenge the current paradigm of transition-metal incorporation in widegap nitrides and oxides, with profound implications on our understanding of magnetic interactions and self-compensation effects in widegap DMS.

acknowledgments

This work was supported by the Portuguese Foundation for Science and Technology (PTDC/FIS/66262/2006, CERN/FP/116320/2010, SFRH/BD/35761/2007), the Research Foundation - Flanders (FWO), the EURONS project (RII3-CT-2004-506065), the SPIRIT project (contract no. 227012), KULeuven projects GOA/2009/006 and INPAC EF/05/005 and the IUAP P6/42 program.

[1] T. Dietl, Nat. Mater. **9**, 965 (2010).
[2] W. Stefanowicz, D. Sztenkiel, B. Faina, A. Grois, M. Rovezzi, T. Devillers, F. d'Acapito, A. Navarro-Quezada, T. Li, R. Jakiela, et al., Phys. Rev. B **81**, 235210 (2010).
[3] A. Bonanni, M. Sawicki, T. Devillers, W. Stefanowicz, B. Faina, T. Li, T. E. Winkler, D. Sztenkiel, A. Navarro-Quezada, M. Rovezzi, et al., Phys. Rev. B **84**, 035206 (2011).
[4] L. M. C. Pereira, T. Som, J. Demeulemeester, M. J. Van Bael, K. Temst, and A. Vantomme, J. Phys.-Condes. Matter **23**, 346004 (2011).
[5] L. M. C. Pereira, J. P. Araujo, M. J. Van Bael, K. Temst, and A. Vantomme, J. Phys. D-Appl. Phys. **44**, 215001 (2011).
[6] L. M. C. Pereira, U. Wahl, S. Decoster, J. G. Correia, L. M. Amorim, M. R. da Silva, J. P. Araujo, and A. Vantomme, Phys. Rev. B **84**, 125204 (2011).
[7] S. Granville, B. J. Ruck, F. Budde, H. J. Trodahl, and G. V. M. Williams, Phys. Rev. B **81**, 184425 (2010).
[8] E. Sarigiannidou, F. Wilhelm, E. Monroy, R. M. Galera, E. Bellet-Amalric, A. Rogalev, J. Goulon, J. Cibert, and H. Mariette, Phys. Rev. B **74**, 041306 (2006).
[9] G. Martinez-Criado, A. Somogyi, S. Ramos, J. Campo, R. Tucoulou, M. Salome, J. Susini, M. Hermann, M. Eickhoff, and M. Stutzmann, Appl. Phys. Lett. **86**, 131927 (2005).
[10] O. Sancho-Juan, O. Martinez-Criado, A. Cantarero, N. Garro, M. Salome, J. Susini, D. Olguin, S. Dhar, and K. Ploog, Phys. Rev. B **83**, 172103 (2011).
[11] N. Smolentsev, G. Smolentsev, S. Wei, and A. V. Soldatov, Physica B **406**, 2843 (2011).
[12] C. Liu, E. Alves, A. Ramos, M. da Silva, J. Soares, T. Matsutani, and M. Kiuchi, Nucl. Instrum. Methods Phys. Res. Sect. B-Beam Interact. Mater. Atoms **191**, 544 (2002).
[13] S. Kuroda, S. Marcet, E. Bellet-Amalric, J. Cibert, H. Mariette, S. Yamamoto, T. Sakai, T. Ohshima, and H. Itoh, Phys. Status Solidi A-Appl. Mat. **203**, 1724 (2006).
[14] T. Niermann, D. Mai, M. Roever, M. Kocan, J. Zenneck, J. Malindretos,

A. Rizzi, and M. Seibt, J. Appl. Phys. **103**, 073520 (2008).
[15] S. Wei, W. Yan, Z. Sun, Q. Liu, W. Zhong, X. Zhang, H. Oyanagi, and Z. Wu, Appl. Phys. Lett. **89**, 121901 (2006).
[16] F. Takano, H. Ofuchi, J. Lee, K. Takita, and H. Akinaga, Physica B **376**, 658 (2006).
[17] H. Hofsass and G. Lindner, Phys. Rep. **201**, 121 (1991).
[18] U. Wahl, A. Vantomme, G. Langouche, J. G. Correia, and L. Peralta, Appl. Phys. Lett. **78**, 3217 (2001).
[19] U. Wahl, J. G. Correia, J. P. Araujo, E. Rita, and S. J. C, Appl. Phys. Lett. **90**, 181934 (2007).
[20] U. Wahl, E. Alves, K. Lorenz, J. G. Correia, T. Monteiro, B. De Vries, A. Vantomme, and R. Vianden, Mat. Sci. Eng. B **105**, 132 (2003).
[21] S. Decoster, S. Cottenier, U. Wahl, J. G. Correia, L. M. C. Pereira, C. Lacasta, M. R. Da Silva, and A. Vantomme, Appl. Phys. Lett. **97**, 151914 (2010).
[22] L. M. C. Pereira, U. Wahl, S. Decoster, J. G. Correia, M. R. da Silva, A. Vantomme, and J. P. Araujo, Appl. Phys. Lett. **98**, 201905 (2011).
[23] M. T. Robinson, Phys. Rev. B **40**, 10717 (1989).
[24] U. Wahl, J. G. Correia, S. Cardoso, J. G. Marques, A. Vantomme, G. Langouche, and ISOLDE Collaboration, Nucl. Instrum. Methods Phys. Res. B **136**, 744 (1998).
[25] U. Wahl, A. Vantomme, G. Langouche, J. Araujo, L. Peralta, J. G. Correia, and ISOLDE Collaboration, J. Appl. Phys. **88**, 1319 (2000).
[26] C. Y. Fong, V. A. Gubanov, and C. Boekema, J. Electron. Mater. **29**, 1067 (2000).
[27] S. Limpijumnong and C. G. Van de Walle, Phys. Rev. B **69**, 035207 (2004).
[28] T. Dietl, H. Ohno, F. Matsukura, J. Cibert, and D. Ferrand, Science **287**, 1019 (2000).
[29] T. Jungwirth, K. Y. Wang, J. Masek, K. W. Edmonds, J. Konig, J. Sinova, M. Polini, N. A. Goncharuk, A. H. MacDonald, M. Sawicki, et al., Phys. Rev. B **72**, 165204 (2005).

Article VI

Cation versus anion substitution of transition metals in GaN and ZnO

L. M. C. Pereira,[1,2,3] U. Wahl,[2] J. G. Correia,[2]
S. Decoster,[3] A. Vantomme,[3] and J. P. Araújo[1]

[1]*IFIMUP and IN-Institute of Nanoscience and Nanotechnology, Department of Physics and Astronomy, Faculdade de Ciências da Universidade do Porto, 4169-007 Porto, Portugal*
[2]*Instituto Tecnológico e Nuclear, UFA, 2686-953 Sacavém, Portugal*
[3]*Instituut voor Kern- en Stralingsfysica and INPAC, K.U.Leuven, 3001 Leuven, Belgium*

Abstract

The magnetism of dilute magnetic semiconductors (DMS) is determined by the lattice sites occupied by the magnetic dopant atoms. While the majority site can in principle be predicted based on chemical similarities with the host elements and is usually simple to confirm experimentally, minority sites are far more complicated to predict, detect and identify. Here we report on the lattice location of Co in GaN using β^- emission channeling from the decay of implanted ^{61}Co. In addition to the majority in cation (Ga) sites, we find up to 17% of the Co impurities in anion (N) sites, which is unaffected by thermal annealing up to 900°C. Although contrary to the general belief that transition metal impurities substitute only the cation in semiconductors like GaN and ZnO, these results are in line with recent reports of anion substitution by Mn in GaN (Article V, unpublished) and by Mn and Co in ZnO [L. M. C. Pereira *et al.*, Phys. Rev. B **84**, 125204 (2011)]. We give an overview of the recent emission channeling studies on the lattice location of the main magnetic dopants Mn, Fe and Co in GaN and ZnO and propose a basic mechanism controlling the majority-cation versus minority-anion substitutional incorporation of transition metal impurities in wide-gap nitrides and oxides.

In preparation for *Physical Review B*

I. INTRODUCTION

Despite major developments in growth, doping and characterization methods, the magnetism of wide-gap dilute magnetic semiconductors (DMS) remains one of the most controversial topics in condensed matter physics,[1] mostly as a consequence of the many contradictory reports on supposedly very similar materials. While a significant part of it can be explained on the basis of extrinsic magnetism,[2–4] this irreproducibility is also generally accepted to be a consequence of the strong dependence of the DMS magnetism on the local structure around the magnetic dopants, which is not trivial to control. So far, however, this dependency has only been discussed in terms of dopant uniformity (dilution versus clustering)[1] and possible interactions between the dopant atoms and intrinsic defects (e.g. point defects[5] and extended defects[6]). Regarding the actual lattice sites occupied by the transition metal impurities, which is in fact what primarily determines their magnetic character, cation substitution has always been taken for granted based on the chemical similarities between the host cations and the transition metal dopants.

The lattice site(s) occupied by the magnetic impurities determine the magnetic behavior of DMS materials at two levels. First, by determining the impurity's electronic structure and crystal field, the occupied lattice site defines the localized magnetic moment and its single-ion magnetism. Second and more importantly, by determining also the impurity's position in the host band structure, it controls its electrical character and the type and strength of the magnetic interactions between localized magnetic moments, i.e. the collective magnetism. The canonical and relatively well understood example is the *narrow-gap* Mn-doped GaAs ($Ga_{1-x}Mn_xAs$). Here, Mn can occupy both Ga-substitutional and As-tetrahedral interstitial sites.[7] Substitutional Mn provides both the localized magnetic moment and the itinerant hole that mediates the magnetic coupling via *p-d* Zener exchange.[8] On the other hand, interstitial Mn has a two-fold compensating effect: magnetic, as substitutional-interstitial Mn pairs couple antiferromagnetically, thus decreasing the effective magnetic dopant concentration x_{eff}, and electrical, since interstitial Mn is a double donor which compensates substitutional Mn acceptors, thus decreasing the hole concentration p.[9] Because a significant fraction of the Mn impurities is incorporated in interstitial sites during $Ga_{1-x}Mn_xAs$ growth,[9] the Curie temperature of the material, which increases with x_{eff} and p, is determined by the balance between interstitial and substitutional Mn fractions.[9] The current

understanding of Mn-, Fe- and Co-doped GaN and ZnO, representative of the *wide-gap* DMS family, is quite different. It is generally accepted that 3*d* transition metals, including Mn, Fe and Co, occupy only cation-substitutional sites, i.e. substitute Ga in GaN and Zn in ZnO, as expected from the chemical similarities between the impurities and the host elements. This has been confirmed experimentally, mostly based on X-ray absorption fine structure (XAFS) but also on ion channeling experiments, and appears to be independent of the doping method, i.e. either during growth (e.g. Refs. 10–19) or by ion implantation (e.g. Refs. 20–23). A representative example among the many wide-gap DMS compounds is the intensively studied Mn-doped GaN ($Ga_{1-x}Mn_xN$). In samples where secondary phase segregation has been avoided, both XAFS[14–17] and ion channeling[19,23] experiments confirmed the expected cation (Ga) substitution by Mn impurities. The type of magnetic interactions between Ga-substitutional Mn moments is determined by the Mn charge state, which in turn depends on the concentration of compensating donor defects.[14] Under stringent growth conditions that minimize the concentration of compensating donors such as N vacancies and H impurities (donors), Mn impurities are incorporated as Mn^{3+}. In such cases, ferromagnetic interactions[14] and low temperature order ($T_C < 10$ K)[24] can be observed. More commonly, such stringent growth conditions are not satisfied and Mn impurities are incorporated as compensated Mn^{2+}, for which only nearest-cation-neighbor antiferromagnetic interactions are observed,[14,25] similar to, e.g., Cr^{3+} in GaN.[26] Although this cation-substitution by transition metals in wide-gap semiconductors is quite well established, some observations do not completely conform to it. Taking the Mn-doped GaN example again, there are strong indications that Mn impurities may occupy non-Ga-substitutional sites. Based on XANES experiments, it has been reported that small fractions of the Mn impurities are located in interstitial sites in zincblende GaN.[27] Also in zincblende GaN, extended X-ray absorption fine structure (EXAFS) experiments detected a remarkably high fraction of 75% of the Mn impurities in anion (N) substitutional sites.[28] However, the unambiguous identification of a minority site in cases of double occupancy poses a number of challenges to XAFS techniques such as XANES and EXAFS. Very recently, we have reported on the lattice location of Mn in wurtzite GaN using the emission channeling (EC) technique.[29] In addition to the majority substituting for Ga (cation), we found significant fractions (20%) of Mn impurities in N (anion) sites. Similarly, we have also reported minority anion (O) substitution by Co (18%) and Mn (27%) impurities in wurtzite ZnO.[30] On the other

hand, experiments on the lattice location of Fe (under similar conditions to those on Mn and Co) in both GaN[31] and ZnO[32] did not reveal anion-site fractions above the sensitivity of the technique (5%). Altogether, these reports challenge the generally accepted scenario where 3*d* transition metals occupy only cation-substitutional sites in wide-gap nitrides and oxides.

Here we investigate the lattice location of implanted Co in GaN using the emission channeling (EC) technique. The aim is to determine to what extent the differences observed between Mn,[30] Fe[32] and Co[30] in ZnO, and Mn[29] and Fe[31] in GaN, are impurity- and host-dependent. In a second part of this paper, we compare the results for these six impurity-host combinations and propose a basic principle controlling the majority-cation versus minority-anion substitutional incorporation of transition metals in wide-gap nitrides and oxides.

II. EXPERIMENT

A. Emission channeling

The emission channeling (EC) technique was developed to determine the lattice location of impurities in single crystals, making use of the charged particles emitted by a radioactive isotope of the impurity element under study.[33] The screened Coulomb potential of atomic rows and planes determines the anisotropic scattering of the particles emitted isotropically during the radioactive decay. Along low-index crystal directions of single crystals, this anisotropic scattering results in well defined channeling or blocking effects. Because these effects strongly depend on the initial position of the emitted particles, they result in emission patterns which are characteristic of the lattice site(s) occupied by the probe atoms. Angular-dependent emission patterns are recorded along various crystallographic axes using a position- and energy-sensitive detection system similar to that described in Ref. 34. The theoretical emission patterns for probes occupying possible lattice sites are calculated using the *manybeam* formalism for electron channeling in single crystals.[33] Quantitative lattice location is provided by fitting the experimental patterns with theoretical ones using the two-dimensional fit procedure outlined in Ref. 34. Corrections for secondary electrons that reach the detector were implemented by subtracting an isotropic background from every pattern. This secondary electron contribution is estimated based on Geant4[35,36] simulations of electron scattering, taking into account the elemental composition and geometry of the

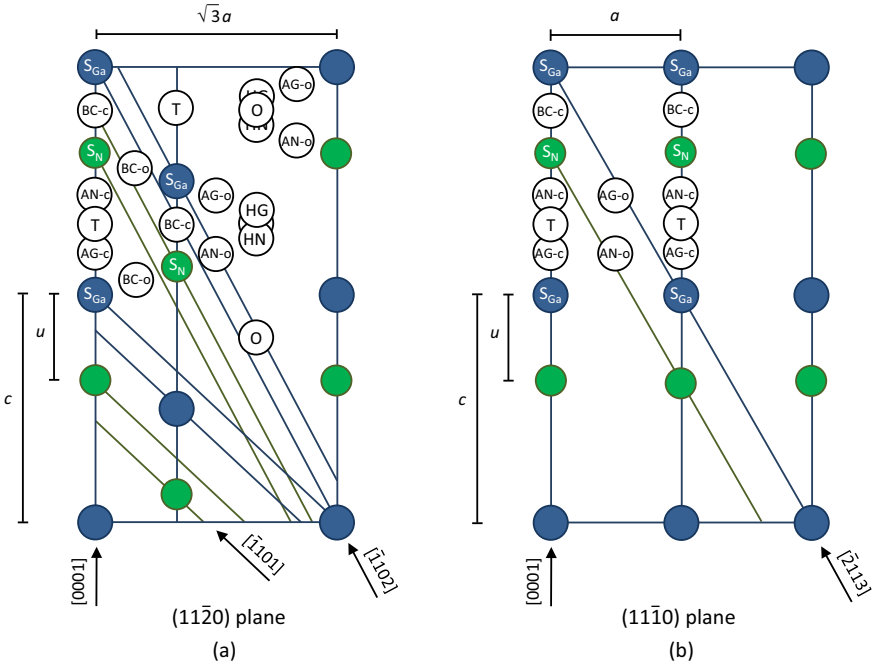

FIG. 1: The (11$\bar{2}$0) (a) and (11$\bar{1}$0) (b) planes of the GaN wurtzite lattice, showing the substitutional Ga (S_{Ga}) and N (S_N) sites as well as the following interstitial sites: bond center BC, antibonding Ga (AG) and antibonding N (AN), octahedral (O), tetrahedral (T) and hexagonal (HZ and HO). "-c" denotes sites along the *c*-axis and "-o" along the basal directions, i.e. off the *c*-axis. Note that in (a) the O sites are very close to the HG and HN sites so the corresponding circles overlap. Along the [$\bar{1}$102], [$\bar{1}$101] and [$\bar{2}$113] directions, the rows of Ga and N atoms are indicated. Note that along the [0001] direction the Ga and N rows coincide.

sample, sample holder and vacuum chamber. Several reviews on emission channeling can be found in the literature.[33,37–39]

Examples for possible lattice sites of higher symmetry in the GaN wurtzite structure are shown in Fig. 1. In addition to substitutional Ga (cation) and N (anion) sites, the following interstitial sites are shown: bond-centered sites along the *c*-axis and the basal directions, abbreviated BC-c and BC-o, antibonding sites AG-c, AN-c, AG-o, and AN-o, the hexagonal sites HG and HN.[40] T and O sites, which have been considered previously as possible sites for native Ga and N interstitials[40] are also shown. Figure 2 shows the theoretical emission patterns along the [0001], [$\bar{1}$102], [$\bar{1}$101] and [$\bar{2}$113] axes for 100% of ^{61}Co atoms on substitutional Ga sites S_{Ga},

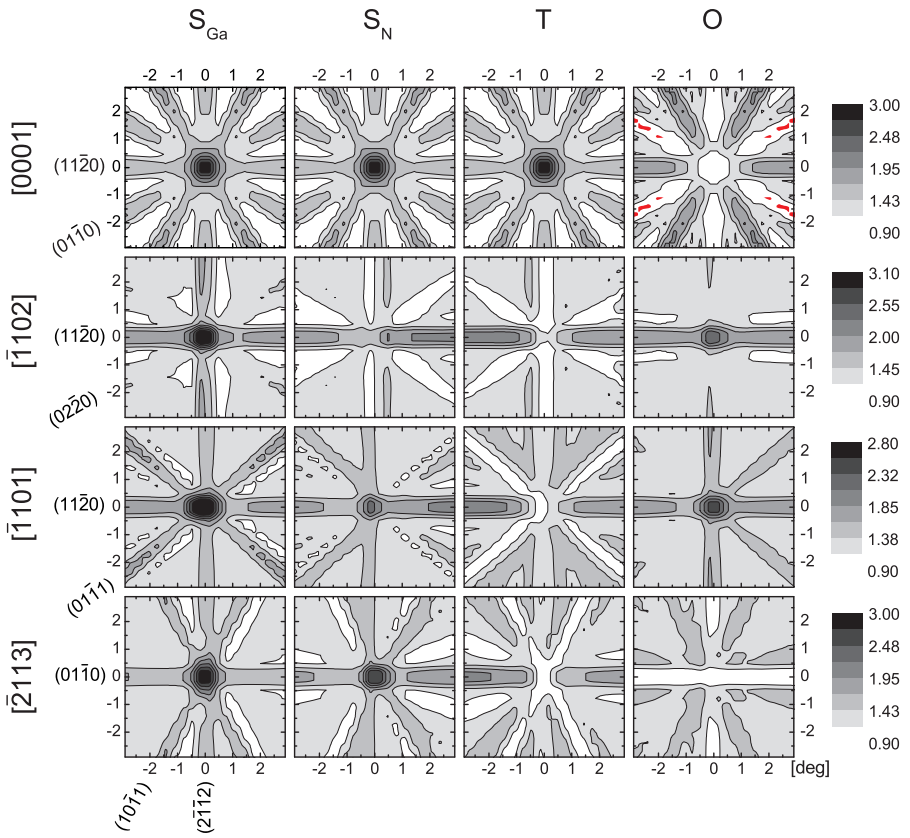

FIG. 2: Simulated channeling patterns for 100% of emitter atoms (^{61}Co) on substitutional Ga sites S_{Ga}, substitutional N sites S_N, and the interstitial T and O sites.

substitutional N sites S_N, and the interstitial T and O sites. Because Ga and N substitutional sites (S_{Ga} and S_N) and the interstitial sites along the *c*-axis (e.g. BC-c and T) are all equivalent in the lattice projection onto the plane perpendicular to the [0001] direction, the corresponding [0001] emission patterns are undistinguishable (Fig. 2, first row). The same holds for the interstitial sites along the main interstitial axis parallel to the *c*-axis (e.g. O, HG, HN). In order to unambiguously distinguish the lattice sites in wurtzite crystals it is thus necessary to measure also along other directions, such as the [$\bar{1}$102], [$\bar{1}$101] and [$\bar{2}$113] axis. As shown in Fig. 2 these direc-

tions separate the different lattice sites. In particular, all three directions separate the two rows of Ga atoms from the two rows of N. This results in emission patterns with distinct anisotropies (Fig. 2, second to forth row) and thus allows for the unambiguous identification of the occupied lattice sites. Moreover, comparing the fit results for as many as four different directions allows us to verify the consistency of the analysis in terms of site identification and occupancy quantification.

The EC technique has been extensively applied to the lattice location of impurities in the wurtzite materials GaN and ZnO, from transition metals (Mn,[29,30] Fe,[31,32] Co,[30] Cu,[41] Ag[42]), to rare earths (Pr,[43] Nd,[44] Pm,[44] Eu,[44] Er[44]), to group II (Ca, Sr)[45] and group V (As,[46,47] Sb[48]) dopants. It offers a number of specific advantages compared to other lattice location techniques. Since EC makes use of 2-dimensional emission patterns (measured using position sensitive detectors) which are directly compared to simulations, it provides unambiguous and quantitative lattice location superior to conventional ion-channeling techniques, where usually only 1-dimensional angular scans can be measured. In addition, it is extremely sensitive in the sense that it requires only a small number of impurities, down to 10^{10} atoms, which makes it particularly suited to study very dilute systems, unlike synchrotron based techniques such as extended X-ray absorption fine structure (EXAFS) spectroscopy or X-ray linear dichroism (XLD). Probably one of the strongest features of the EC technique is its applicability to those cases where significant fractions of the impurities occupy more than one lattice site. This multi-site lattice location capability of EC has allowed us, for example, to establish the amphoteric nature of As in GaN (substituting both Ga and N)[47] and, as discussed in depth in this paper, to identify, in addition to the majority fractions in cation sites, significant fractions (approximately 20% – 30%) of Co and Mn impurities in the anion (O) site in ZnO[30] and of Mn impurities in the anion (N) site of GaN.[29] Although in principle such minority versus majority occupancies can also be quantified using EXAFS, unambiguous identification of minority sites is extremely challenging, because the technique relies on complex multiparameter fitting of the spectra using calculated model structures.

B. ^{61}Co:GaN experimental details

The samples consisted of epitaxial thin films of wurtzite [0001] GaN grown on sapphire. In order to dope the samples with ^{61}Co we implanted the precursor isotope ^{61}Mn with the decay chain ^{61}Mn (0.71 s)

$\rightarrow$ ^{61}Fe (6 min) $\rightarrow$ ^{61}Co (1.6 h) $\rightarrow$ ^{61}Ni (stable). The implantations were carried out at the on-line isotope separator facility ISOLDE at CERN, which provides mass-separated beams of radioactive Mn isotopes produced by means of 1.4-GeV proton-induced nuclear fission from uranium carbide UC_2 targets and chemically selective laser ion sources.[49] In order to ensure that the contributions of ^{61}Mn and ^{61}Fe β^- particles to the channeling patterns were negligible, the measurements started only after a waiting period of approximately 30-60 min. The β^- decay of ^{61}Fe transfers a recoil energy of about 103 eV to its ^{61}Co daughter. This ensures that the ^{61}Co atoms are re-implanted, i.e. that they do not inherit the ^{61}Fe lattice site. The implantations were performed at room temperature, under a tilt angle of 17° with respect to the surface normal in order to minimize ion channeling, with an energy of 50 keV and a fluence of 2×10^{13} cm^{-2}, resulting in a peak concentration of 7×10^{18} cm^{-3} at a projected range R_p of 236 Å with a 109 Å straggling, estimated using the MARLOWE code.[50] The low concentration regime (below 1×10^{19} cm^{-3}, i.e. $< 0.03\%$) allows us to study the lattice location of Co free from phase segregation.

Angular-dependent emission yields of the β^- particles emitted during decay were measured at room temperature, along four crystallographic directions, [0001], [$\bar{1}$102], [$\bar{1}$101] and [$\bar{2}$113], in the as-implanted state and after *in situ* capless annealing in vacuum ($< 10^{-5}$ mbar) at 600°C and 900°C. These patterns were recorded using a position- and energy-sensitive detection system similar to that described in Ref. 34. Given the relatively short half-life of ^{61}Co, this system was installed on-line and upgraded with self-triggering readout chips for the Si pad detectors, enabling measurements during and/or immediately after implantation with count rates of up to several kHz.

Theoretical patterns were calculated for probes occupying substitutional Ga (S_{Zn}) and N (S_O) sites with varying root-mean-square (rms) displacements, the main interstitial sites described above and interstitial sites resulting from displacements along the c or the basal directions. The GaN crystallographic parameters and room temperature atomic displacements used in the manybeam simulations can be found in Ref. 51.

III. RESULTS

Considering only one lattice site, the calculated S_{Ga} patterns gave by far the best agreement for all four measured directions, showing that the majority of the probe atoms occupy S_{Ga} sites, as expected. The fitting

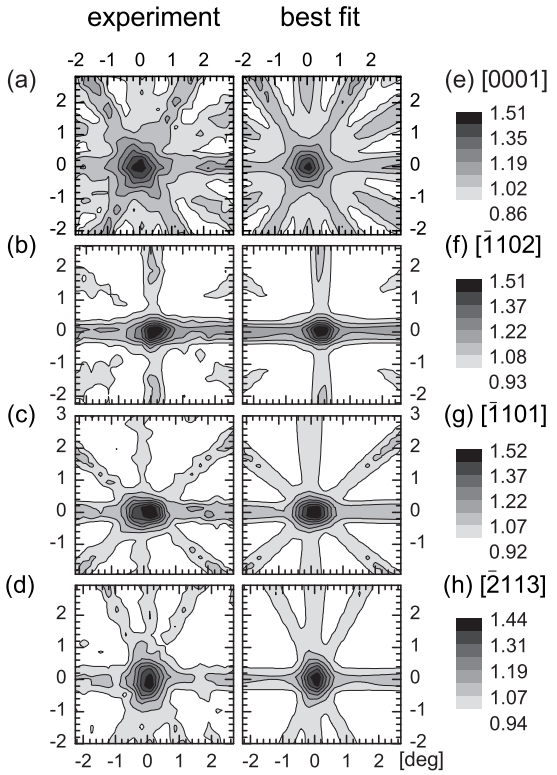

FIG. 3: (a)-(d) Normalized experimental ^{61}Co β^- emission channeling patterns in the vicinity of the [0001], [$\bar{1}$102], [$\bar{1}$101] and [$\bar{2}$113] directions following annealing at 600°C. (e)-(h) Corresponding best fits with 85% and 15% of the ^{61}Co atoms on S_{Ga} and S_N sites, respectively.

routine was then allowed to include, in addition to S_{Ga}, an additional lattice site, for which all the simulated sites were considered. Consistently for all measured directions, the $S_{Ga} + S_N$ double occupancy gives the best fit compared to all other combinations and considerably improves the S_{Ga} single-site fit, with up to 10% lower reduced χ^2. As an example for the good match between experiment and simulated patterns, Fig. 3 compares the β^- emission yields of ^{61}Co:GaN (following annealing at 600°C) along the four measured directions with the best fits of theoretical patterns, obtained for 85% of the ^{61}Co atoms on S_{Ga} (Co_{Ga}) and 15% on S_N sites (Co_N). Introducing a third site yields only insignificant fit improvements. Possible fractions on other sites are estimated to be below 5%.

In Fig. 4 (a) we compile the Co fractions on S_{Ga} and S_N sites as a

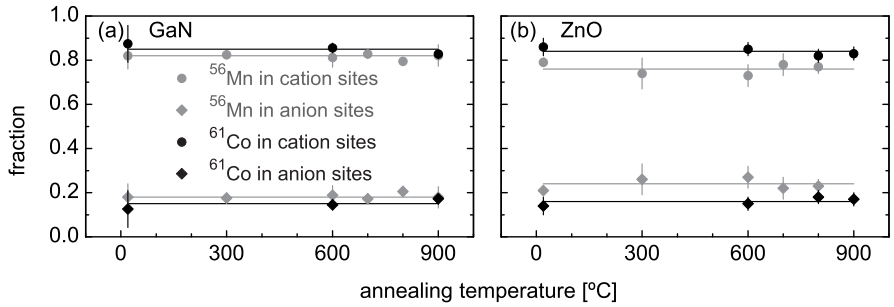

FIG. 4: Fractions of ^{61}Co and ^{56}Mn atoms in S_{Ga} and S_N sites in GaN (a) and in S_{Zn} and S_O sites in ZnO (b) following the various annealing steps. The lines correspond to the mean fractions, averaged from the values for the different annealing steps. The data for ^{56}Mn:GaN are from Ref. 30 and for ^{61}Co:ZnO and ^{56}Mn:GaN are from Ref. 29.

function of annealing temperature, and compare to our previous results for Mn impurities.[29] Within experimental error, the Co_N fraction remains constant around 15% up to the highest temperature annealing step, similar to what was observed for Mn.[29]

IV. DISCUSSION

A. Overview of experimental results on Mn/Fe/Co in GaN/ZnO

Although very intriguing, this anion (N) substitution of Co in GaN is consistent with our recent reports on minority anion substitution by Mn in GaN[29] and by Co and Mn in ZnO[30], also using the emission channeling technique. However, no such anion substitutional fractions have been detected in the large majority of the studies based on XAFS and ion-channeling on the lattice location of Co and Mn impurities incorporated either during growth (e.g. Refs. 10–19) or by ion implantation (e.g. Refs. 20–23). The only report on anion substitution detected by XAFS is for Mn-doped *zincblende* GaN grown by molecular beam epitaxy (MBE) in N-poor conditions.[28] We note, however, that XAFS (EXAFS, more precisely) was able to identify anion substitution in Ref. 28 because the corresponding fraction was remarkably high (75%). This raises an important question of how small can the anion-substitutional fraction be and still be detected by XAFS. Since identifying a minority site in cases of double occupancy is in

general extremely challenging for XAFS techniques, one can argue that anion-subsitutional fractions (significant but still below detection limit) may have simply escaped detection in other studies on the lattice location of Mn and Co impurities in wurtzite GaN and ZnO. Other techniques, e.g. electron paramagnetic resonance (EPR) and Mössbauer and perturbed angular correlation (PAC) spectroscopies, are also very sensitive and can in some cases distinguish very well the components corresponding to different lattice sites. However, lattice location can only be indirectly inferred from the spectra.

There is still another type of techniques which may provide useful (although indirect) information on anion versus cation substitution. If the charge state of anion substitutional impurities is different from that of cation substitutional, techniques such as X-ray photoelectron spectroscopy (XPS) and X-ray absorption near-edge structure spectroscopy (XANES) should be able to detect them, and indeed one can find indications in the literature that they have. X-ray absorption near-edge structure spectroscopy (XANES)[12,52] and X-ray photoelectron spectroscopy (XPS)[53] experiments have shown that Mn impurities can be incorporated in ZnO with charge states of up to 4^+. Because Zn-substitutional Mn is expected to have a 2^+ charge state with the $2^+/3^+$ and $3^+/4^+$ donor levels below the valence band maximum (thus not ionized),[54] these reports indicate that minority fractions may in fact occupy a different lattice site with a 4^+ charge state. As we suggested in Ref. 30 and in more detail below, this is indeed the expected charge state for Mn impurities in O sites. Similarly, it has also been reported that the average charge state of Mn in high crystalline quality $Ga_{1-x}Mn_xN$ is not exactly 3^+ but 3.3^+.[18] Although this was interpreted as resulting from electron transfer from Ga-substitutional Mn impurities to the N neighbors, it may as well indicate the contribution from a minority anion fraction in a 4^+ charge state. (Mn_{Ga} is usually in the 2^+ (Ref. 25) or 3^+ (Ref. 24) charge state; the $3^+/4^+$ donor level is very deep in the bandgap, hence Mn_{Ga}^{4+} charge state is only observed in *p*-type (Mg co-doped) GaN.[55]) It is important to note that for all the studies discussed in this paragraph, the impurities were incorporated during growth, not by ion implantation, which is a strong indication that minority anion substitution may be a relatively general phenomenon.

Altogether, these results challenge our understanding of cation versus anion substitution of 3*d* transition metals in GaN and ZnO and possibly other wide-gap semiconductors. Before discussing possible mechanisms responsible for these effects and how they depend on the growth/doping

methods and conditions, let us briefly summarize the EC results on the lattice location of the 3*d* transition metals Mn ($Z = 25$), Fe ($Z = 26$) and Co ($Z = 27$) in GaN and ZnO. Figure 4 compiles the anion versus cation fractions of ^{56}Mn and ^{61}Co impurities in GaN (a) and ZnO (b) from the as-implanted state to up to 900°C annealing. For Fe, which is positioned between Co and Mn in the periodic system, our EC experiments did not detect anion fractions above 5% (the sensitivity limit of EC) in either GaN[31] or ZnO.[32] These EC results can be summarized in three main observations:

1. Unlike Fe, significant fractions of Mn and Co impurities (15%–30%) occupy anion sites in GaN and ZnO.

2. For all four cases, Mn and Co impurities have a high thermal stability in both cation and anion sites (measured up to 800°C for Mn in ZnO and 900°C for the other three).

B. Proposed physical mechanism

Generally, in compound semiconductors, the lattice sites of impurities are determined by chemical similarities and matching of size and electronegativity with the host atoms. Because Co and Mn are quite similar to Ga and Zn and very different from N and O in terms of electronegativity and ionic radii, it is in principle energetically unfavorable for Co and Mn impurities to be incorporated in anion sites.

Since anion substitution by 3*d* transition metals in GaN and ZnO is so unexpected, theoretical considerations of the phenomena are very scarce. For zincblende GaN, the calculated total energies for Mn in Ga and N sites indicate, as expected, that Ga substitution is more favorable.[60] However, the calculations in Ref. 60 do not consider charged Mn_N defects. The defects that most resemble anion-substitutional transition-metals, for which different charge states have been considered, are the cation antisites (Zn_O in ZnO[57,61–63] and Ga_N in GaN[56]). Depending on the growth conditions (metal rich or poor) and Fermi level, charge states of up to 4^+ can be stable [Fig. 5 (a)], with the $3^+/4^+$ and $2^+/3^+$ transition levels deep in the bandgap [Fig. 5 (a) and (b)]. All these calculations predicted that the formation energy of the antisites can in fact be small, even negative for Zn_O, under metal-rich conditions and for a Fermi level close to the valence band maximum (VBM). Extrapolating these results on the post-transition metals Zn and Ga to the transition-metals Mn, Fe and Co is not straightforward.

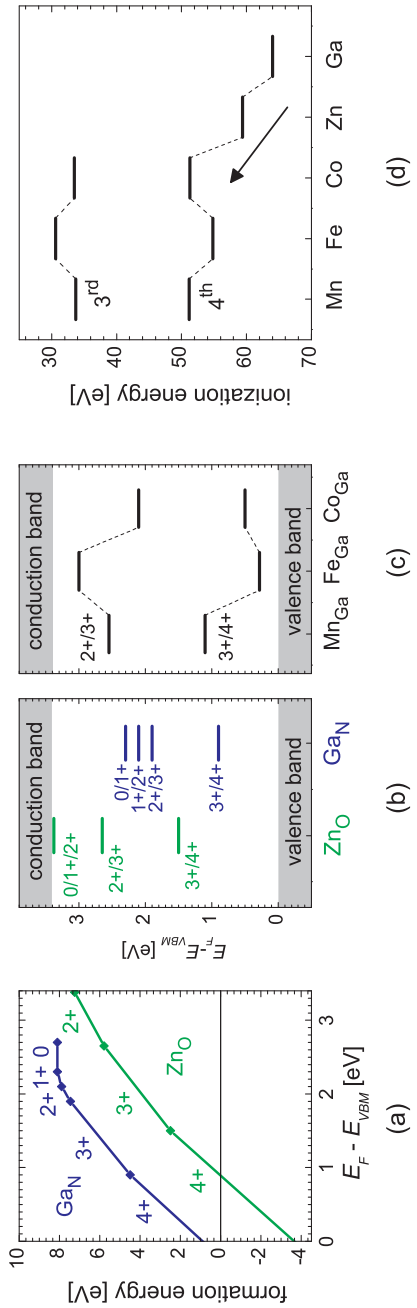

FIG. 5: (a) Formation energies of Ga antisites (Ga_N) in GaN[56] and of Zn antisites (Zn_O) in ZnO,[57] under metal-rich conditions, as a function of Fermi level (E_F) with respect to the valence band maximum (E_{VBM}). Note that only the charge state with the lowest formation energy is shown, from neutral to 4^+. (b) Charge transfer levels of the Zn and Ga antisites extracted from (a). (c) Charge transfer levels of Ga substitutional Mn, Fe and Co.[58] (d) Ionization energies of free Mn, Fe, Co, Zn and Ga ions.[59]

There is one important difference: whereas the 3*d* shells of Zn and Ga are closed, for the transition metals they are open. Nevertheless, in the 4^+ charge state (the most stable for Zn_O[57,61–63] and Ga_N[56]), all of these (Mn, Fe and Co as well as Zn and Ga,) have open 3*d* shells. One can thus expect that the behavior of these elements in anion sites is qualitatively similar, except for a chemical (3*d* occupancy) dependence of the position of the $0/1^+/2^+/3^+/4^+$ levels. Assuming that this is the case, one can then suggest the following two conditions for anion-substitution by Mn, Fe and Co in GaN and ZnO:

N- or O-poor conditions or, equivalently, sufficiently high concentration of N or O vacancies. This is in agreement with Ref. 28, where N-substitution by Mn (in zincblende GaN) was only observed in thin films grown under N-poor conditions. In other words, increasing the concentration of N vacancies (which can be "filled" by Mn impurities), decreases the formation energy of Mn_N, increasing its concentration. In the present study, as well as in Refs. 29 and 30, the required N and O vacancies were in principle created upon ion bombardment by the radioactive probes ($^{56}Mn^+$ and $^{61}Mn^+$). Note, nonetheless, that the incorporation of Mn impurities in N sites cannot be considered a direct effect of ion implantation, since it was not observed for Fe under very similar experimental conditions, neither in GaN[31] nor ZnO.[32] Fe has an atomic mass which is similar to those of Mn and Co and thus similar incorporation kinetics.

Fermi level sufficiently close to the VBM , i.e. in the presence of acceptor states to which the electrons from the anion-substitutional cations (the transition-metal impurities) can be transfered. Usually, the Fermi level of *undoped* GaN and ZnO is well above the VBM due to the presence of donor defects (e.g. native anion vacancies), i.e. this condition is not satisfied. On the other hand, in *transition-metal doped* GaN and ZnO, the acceptors states which are required to stabilize the anion-substitutional fraction may in principle be provided by the cation-substitutional fraction (with the deep acceptor levels $2^+/3^+$ in GaN and $1^+/2^+$ in ZnO). This requires that the anion-substitutional donor levels are above (in energy) the cation-substitutional acceptor levels. However, these acceptor levels are typically very deep, even closer to the conduction band minimum (CBM) than they are to the VBM [e.g. Fig. 5 (c) for values calculated for GaN[58]], which means that for this Fermi level condition

to be satisfied (in the general case, i.e. without additional acceptor doping), the anion-substitutional donor levels of the transition-metal impurities must be closer to the CBM (i.e. shallower) than those of the antisites [Fig. 5 (b)]. Although the transition levels have never been calculated for anion-substitutional Mn, Fe or Co impurities in GaN or ZnO, some arguments can be drawn from which one can infer their positions in the bandgap, i.e. (i) if the levels are indeed closer to the CBM than are those of the antisites and (ii) how they differ from Mn to Fe to Co. The trend among Mn, Fe and Co in anion sites (ii) can in principle be inferred from the transition levels for the cation-substitutional case [e.g. Fig. 5 (c) for GaN[58]]. Interestingly, they follow quite well the trend in ionization energies of the free ions (Fig 5 (d)). The $2^+/3^+$ level is shallower for Fe compared to Mn and Co, relative to the CBM (to which the electron can be transfered) the same way the 3$^{\text{rd}}$ ionization energy of Fe (from Fe^{2+} to Fe^{3+}) is smaller than those of Mn and Co. Conversely, the $3^+/4^+$ level is deeper for Fe compared to Mn and Co the same way the 4$^{\text{th}}$ ionization energy of Fe (from Fe^{3+} to Fe^{4+}) is larger than those of Mn and Co. This correspondence is not at all surprising, since the chemical trends of *deep* impurity levels are largely determined by the electronic structure of the free atoms/ions, due to the strong electronic localization.[64] From this relation between transition levels and ionization energies, one can also infer how the $3^+/4^+$ levels of anion site Mn, Fe and Co compare to the levels $3^+/4^+$ of the Zn and Ga antisites (ii): since the 4$^{\text{th}}$ ionization energy increases from Ga to Zn to the three 3*d* transition metals [indicated by the arrow in Fig. 5 (d)], one can expect that the $3^+/4^+$ levels of 3*d* transition metals in anion sites are indeed shallower than those of the antisites.

This simple scheme agrees with our experimental observation (1) quite well. If the Fermi level lies above the 4+/3+ level of anion site Fe, and below those of Co and Mn, only Co and Mn will be ionized in the 4+ charge state for which the formation energies can be small enough to allow for sizable concentrations of these defects to be created [observation (1)]. Extrapolating this principle to the other elements in the 3*d* series, one can expect that anion site fractions are likely to increase (decrease) with decreasing (increasing) atomic number Z, as the $3^+/4^+$ levels move closer to (further from) the CBM.[58] The available experimental data is in agreement with this expectation: on the higher Z side of the 3*d* series, our previous emission channeling experiments on the lattice location of Cu ($Z = 29$) in

ZnO did not detect anion (O) substitutional fractions. Emission channeling experiments on the lattice location of Ni in GaN and ZnO are currently underway which will complete the higher Z side of the $3d$ series. Suitable isotopes for emission channeling experiments on the lattice location of the lighter $3d$ transition metals (Sc, Ti, V and Cr) are currently unavailable.

Regarding the high thermal stability of Mn and Co impurities on anion sites, up to 900°C [observation (2)], it suggests that for the relevant DMS concentration range (few %) it may not be possible to remove anion site defects by post-growth thermal annealing without at the same time inducing phase segregation, which normally occurs at such high temperatures.

Finally, even though there seems to exist a physical mechanism capable of creating sizable anion-site fractions under near-equilibrium growth conditions, as well as some experimental observations supporting it, a definite generalization of these effects will require further theoretical and experimental investigation. This includes, in particular, the assessment of the formation energies of anion-substitutional transition-metal defects, as well as an experimental reassessment of the lattice location of Mn and Co in GaN and ZnO for different preparation methods and growth conditions, carefully taking into consideration the possibility of anion substitution.

V. CONCLUSIONS

We have experimentally established the lattice location of implanted Co in wurtzite GaN in the low concentration regime (below 1×10^{19} cm^{-3}, i.e. $< 0.03\%$). In addition to the majority on substitutional Ga sites, we find up to 17% of the Co atoms on substitutional N sites, which is virtually unaffected by thermal annealing up to 900°C. Combining these results with those of previous emission channeling experiments on the lattice location of Mn, Fe and Co in wurtzite GaN and ZnO, the following conclusions can be drawn:

1. Unlike Fe, minority fractions of implanted Mn and Co impurities (15% – 30%) occupy anion sites in GaN and ZnO.

2. In the low concentration regime ($< 0.03\%$), Mn and Co impurities have a high thermal stability in both cation and anion sites (up to 900°C).

Although anion site fractions of GaN and ZnO materials are highly unexpected, a number of arguments can be put forward which suggest that

anion-substitutional Co and Mn defects may indeed have low formation energies. Moreover, anion substitution may explain previous experimental observations of high charge states of Mn and Co impurities in GaN and ZnO, up to 4+, which are hardly compatible with cation substitution. Nevertheless, definite generalization of these effects will require the assessment of the formation energies of these defects, as well as an experimental reassessment of the lattice location of Mn and Co in GaN and ZnO for different preparation methods and growth conditions, carefully taking into consideration the possibility of anion substitution.

The most direct implications of anion substitution by Mn and Co in GaN and ZnO concern the field of dilute magnetic semiconductors. Not only does the magnetic behavior of magnetic impurities depend directly on the lattice site they occupy, self-compensation effects by minority anion substitution may change the charge state of the majority cation-substitutional fraction and thus indirectly control their magnetic interactions and order mechanisms.

Acknowledgments

This work was supported by the Portuguese Foundation for Science and Technology (PTDC/FIS/66262/2006, CERN/FP/116320/2010, SFRH/BD/35761/2007), the Research Foundation - Flanders (FWO), the EURONS project (RII3-CT-2004-506065), the SPIRIT project (contract no. 227012), KULeuven projects GOA/2009/006 and INPAC EF/05/005 and the IUAP P6/42 program.

[1] T. Dietl, Nat. Mater. **9**, 965 (2010).
[2] A. Ney, T. Kammermeier, V. Ney, K. Ollefs, and S. Ye, J. Magn. Magn. Mater. **320**, 3341 (2008).
[3] M. A. Garcia, E. Fernandez Pinel, J. de la Venta, A. Quesada, V. Bouzas, J. F. Fernandez, J. J. Romero, M. S. Martin Gonzalez, and J. L. Costa-Kramer, J. Appl. Phys. **105**, 013925 (2009).
[4] L. M. C. Pereira, J. P. Araujo, M. J. Van Bael, K. Temst, and A. Vantomme, J. Phys. D: Appl. Phys. **44**, 215001 (2011).
[5] J. M. D. Coey, M. Venkatesan, and C. B. Fitzgerald, Nat. Mater. **4**, 173 (2005).
[6] J. M. D. Coey, P. Stamenov, R. D. Gunning, M. Venkatesan, and K. Paul, New J. Phys. **12**, 053025 (2010).

[7] L. M. C. Pereira, U. Wahl, S. Decoster, J. G. Correia, M. R. da Silva, A. Vantomme, and J. P. Araújo, Appl. Phys. Lett. **98**, 201905 (2011).
[8] T. Dietl, H. Ohno, F. Matsukura, J. Cibert, and D. Ferrand, Science **287**, 1019 (2000).
[9] T. Jungwirth, K. Y. Wang, J. Masek, K. W. Edmonds, J. Konig, J. Sinova, M. Polini, N. A. Goncharuk, A. H. MacDonald, M. Sawicki, et al., Phys. Rev. B **72**, 165204 (2005).
[10] T. Shi, S. Zhu, Z. Sun, S. Wei, and W. Liu, Appl. Phys. Lett. **90**, 102108 (2007).
[11] Z. Sun, W. Yan, G. Zhang, H. Oyanagi, Z. Wu, Q. Liu, W. Wu, T. Shi, Z. Pan, P. Xu, et al., Phys. Rev. B **77**, 245208 (2008).
[12] N. Farley, K. Edmonds, A. Freeman, G. van der Laan, C. Staddon, D. Gregory, and B. Gallagher, New J. Phys. **10**, 055012 (2008).
[13] J. C. Pivin, G. Socol, I. Mihailescu, P. Berthet, F. Singh, M. K. Patel, and L. Vincent, Thin Solid Films **517**, 916 (2008).
[14] A. Bonanni, M. Sawicki, T. Devillers, W. Stefanowicz, B. Faina, T. Li, T. E. Winkler, D. Sztenkiel, A. Navarro-Quezada, M. Rovezzi, et al., Phys. Rev. B **84**, 035206 (2011).
[15] O. Sancho-Juan, O. Martinez-Criado, A. Cantarero, N. Garro, M. Salome, J. Susini, D. Olguin, S. Dhar, and K. Ploog, Phys. Rev. B **83**, 172103 (2011).
[16] W. Stefanowicz, D. Sztenkiel, B. Faina, A. Grois, M. Rovezzi, T. Devillers, F. d'Acapito, A. Navarro-Quezada, T. Li, R. Jakiela, et al., Phys. Rev. B **81**, 235210 (2010).
[17] N. Smolentsev, G. Smolentsev, S. Wei, and A. V. Soldatov, Physica B **406**, 2843 (2011).
[18] X. Biquard, O. Proux, J. Cibert, D. Ferrand, H. Mariette, R. Giraud, and B. Barbara, J. Supercond. **16**, 127 (2003).
[19] S. Kuroda, S. Marcet, E. Bellet-Amalric, J. Cibert, H. Mariette, S. Yamamoto, T. Sakai, T. Ohshima, and H. Itoh, Phys. Status Solidi A-Appl. Mat. **203**, 1724 (2006).
[20] A. Singh, R. Kumar, P. Thakur, N. Brookes, K. Chae, and W. Choi, J. Phys.: Condens. Matter. **21**, 185005 (2009).
[21] J. A. Sans, G. Martinez-Criado, J. Susini, R. Sanz, J. Jensen, I. Minguez, M. Hernandez-Velez, A. Labrador, and P. Carpentier, J. Appl. Phys. **107**, 023507 (2010).
[22] J. Baik, S. Kim, Y. Koo, T. Kang, and J. Lee, Electrochem. Solid State Lett. **7**, G313 (2004).
[23] C. Liu, E. Alves, A. Ramos, M. da Silva, J. Soares, T. Matsutani, and M. Kiuchi, Nucl. Instrum. Methods Phys. Res. Sect. B-Beam Interact. Mater. Atoms **191**, 544 (2002).
[24] E. Sarigiannidou, F. Wilhelm, E. Monroy, R. M. Galera, E. Bellet-Amalric, A. Rogalev, J. Goulon, J. Cibert, and H. Mariette, Phys. Rev. B **74**, 041306 (2006).
[25] S. Granville, B. J. Ruck, F. Budde, H. J. Trodahl, and G. V. M. Williams,

Phys. Rev. B **81**, 184425 (2010).
[26] L. M. C. Pereira, T. Som, J. Demeulemeester, M. J. Van Bael, K. Temst, and A. Vantomme, J. Phys.-Condes. Matter **23**, 346004 (2011).
[27] S. Wei, W. Yan, Z. Sun, Q. Liu, W. Zhong, X. Zhang, H. Oyanagi, and Z. Wu, Appl. Phys. Lett. **89**, 121901 (2006).
[28] F. Takano, H. Ofuchi, J. Lee, K. Takita, and H. Akinaga, Physica B **376**, 658 (2006).
[29] L. M. C. Pereira, U. Wahl, S. Decoster, J. G. Correia, J. P. da Silva, M Rand Araújo, and A. Vantomme, (Article V, unpublished).
[30] L. M. C. Pereira, U. Wahl, S. Decoster, J. G. Correia, L. M. Amorim, M. R. da Silva, J. P. Araujo, and A. Vantomme, Phys. Rev. B **84**, 125204 (2011).
[31] U. Wahl, A. Vantomme, G. Langouche, J. G. Correia, and L. Peralta, Appl. Phys. Lett. **78**, 3217 (2001).
[32] E. Rita, U. Wahl, J. Correia, E. Alves, and J. Soares, Appl. Phys. Lett. **85**, 4899 (2004).
[33] H. Hofsass and G. Lindner, Phys. Rep. **201**, 121 (1991).
[34] U. Wahl, J. G. Correia, S. Cardoso, J. G. Marques, A. Vantomme, G. Langouche, and ISOLDE Collaboration, Nucl. Instrum. Methods Phys. Res. B **136**, 744 (1998).
[35] S. Agostinelli, J. Allison, K. Amako, J. Apostolakis, H. Araujo, P. Arce, M. Asai, D. Axen, S. Banerjee, G. Barrand, et al., Nucl. Instrum. Methods Phys. Res. Sect. A-Accel. Spectrom. Dect. Assoc. Equip. **506**, 250 (2003).
[36] J. Allison, K. Amako, J. Apostolakis, H. Araujo, P. A. Dubois, M. Asai, G. Barrand, R. Capra, S. Chauvie, R. Chytracek, et al., IEEE Trans. Nucl. Sci. **53**, 270 (2006).
[37] H. Hofsass, U. Wahl, and S. G. Jahn, Hyperfine Interact. **84**, 27 (1994).
[38] H. Hofsass, Hyperfine Interact. **97**, 247 (1996).
[39] U. Wahl, Hyperfine Interact. **129**, 349 (2000).
[40] P. Boguslawski, E. L. Briggs, and J. Bernholc, Phys. Rev. B **51**, 17255 (1995).
[41] U. Wahl, E. Rita, J. Correia, E. Alves, and J. Soares, Phys. Rev. B **69**, 012102 (2004).
[42] E. Rita, U. Wahl, A. Lopes, J. Araujo, J. Correia, E. Alves, J. Soares, and ISOLDE Collaboration, Physica B **340**, 240 (2003).
[43] U. Wahl, A. Vantomme, G. Langouche, J. P. Araujo, L. Peralta, J. G. Correia, and ISOLDE Collaboration, J. Appl. Phys. **88**, 1319 (2000).
[44] U. Wahl, E. Alves, K. Lorenz, J. G. Correia, T. Monteiro, B. De Vries, A. Vantomme, and R. Vianden, Mat. Sci. Eng. B **105**, 132 (2003).
[45] B. De Vries, A. Vantomme, U. Wahl, J. G. Correia, J. P. Araujo, W. Lojkowski, and D. Kolesnikov, J. Appl. Phys. **100**, 023531 (2006).
[46] U. Wahl, E. Rita, J. G. Correia, A. C. Marques, E. Alves, J. C. Soares, and ISOLDE Collaboration, Phys. Rev. Lett. **95**, 215503 (2005).
[47] U. Wahl, J. G. Correia, J. P. Araujo, E. Rita, and S. J. C, Appl. Phys. Lett. **90**, 181934 (2007).
[48] U. Wahl, J. G. Correia, T. Mendonca, and S. Decoster, Appl. Phys. Lett. **94**,

261901 (2009).
[49] V. N. Fedoseyev, K. Batzner, R. Catherall, A. H. M. Evensen, D. ForkelWirth, O. C. Jonsson, E. Kugler, J. Lettry, V. I. Mishin, H. L. Ravn, et al., Nucl. Instrum. Methods Phys. Res. Sect. B-Beam Interact. Mater. Atoms **126**, 88 (1997).
[50] M. T. Robinson, Phys. Rev. B **40**, 10717 (1989).
[51] U. Wahl, A. Vantomme, G. Langouche, J. Araujo, L. Peralta, J. G. Correia, and ISOLDE Collaboration, J. Appl. Phys. **88**, 1319 (2000).
[52] P. Thakur, K. H. Chae, J.-Y. Kim, M. Subramanian, R. Jayavel, and K. Asokan, Appl. Phys. Lett. **91**, 162503 (2007).
[53] H. T. Cao, Z. L. Pei, J. Gong, C. Sun, R. F. Huang, and L. S. Wen, J. Solid State Chem. **177**, 1480 (2004).
[54] T. Graf, S. T. B. Goennenwein, and M. S. Brandt, Phys. Status Solidi B-Basic Res. **239**, 277 (2003).
[55] B. Han, R. Y. Korotkov, B. W. Wessels, and M. P. Ulmer, Appl. Phys. Lett. **84**, 5320 (2004).
[56] S. Limpijumnong and C. G. Van de Walle, Phys. Rev. B **69**, 035207 (2004).
[57] R. Vidya, P. Ravindran, H. Fjellvag, B. G. Svensson, E. Monakhov, M. Ganchenkova, and R. M. Nieminen, Phys. Rev. B **83**, 045206 (2011).
[58] U. Gerstmann, A. T. Blumenau, and H. Overhof, Phys. Rev. B **63**, 075204 (2001).
[59] D. P. Lide, ed., *CRC Handbook of Chemistry and Physics* (CRC PRESS, 2004), 84th ed.
[60] C. Y. Fong, V. A. Gubanov, and C. Boekema, J. Electron. Mater. **29**, 1067 (2000).
[61] A. Janotti and C. G. Van de Walle, Phys. Rev. B **76**, 165202 (2007).
[62] F. Oba, A. Togo, I. Tanaka, J. Paier, and G. Kresse, Phys. Rev. B **77**, 245202 (2008).
[63] F. Oba, M. Choi, A. Togo, A. Seko, and I. Tanaka, J. Phys.: Condens. Matter **22**, 384211 (2010).
[64] P. Vogl, Fertkorperprobleme-Adv. Solid State Phys. **21**, 191 (1981).

4.3 Searching for room-temperature ferromagnetism in Mn-, Fe- and Co-implanted ZnO and GaN

This section is composed of article VII, on the search for room-temperature ferromagnetism in Mn-, Fe- and Co-implanted ZnO and GaN. In line with the emerging picture of defect-related ferromagnetism, the goal is to search for intrinsic ferromagnetism under a varying degree of lattice disorder (defect type and concentration), by sweeping a wide range of implantation and thermal annealing conditions. This study focuses on the low concentration regime in order to minimize secondary-phase segregation. Damage formation and annealing are studied using Rutherford backscattering and channeling spectrometry (RBS/C) (described in section 3.2). Superconducting quantum interference device (SQUID) magnetometry is used for magnetic characterization (described in section 3.4), following strict procedures in order to avoid ferromagnetic-like signals from setup-related artifacts or magnetic contamination (described in Article I).

Article VII

Searching for room temperature ferromagnetism in transition metal implanted ZnO and GaN

L. M. C. Pereira,[1,2,3] J. P. Araújo,[2] U. Wahl,[3]
M. J. Van Bael,[4] K. Temst,[1] and A. Vantomme[1]

[1]*Instituut voor Kern- en Stralingsfysica and INPAC, K.U.Leuven, 3001 Leuven, Belgium*
[2]*IFIMUP and IN-Institute of Nanoscience and Nanotechnology, Department of Physics and Astronomy, Faculdade de Ciências da Universidade do Porto, 4169-007 Porto, Portugal*
[3]*Instituto Tecnológico e Nuclear, UFA, 2686-953 Sacavém, Portugal*
[4]*Laboratory of Solid-State Physics and Magnetism and INPAC, K.U.Leuven, 3001 Leuven, Belgium*

Abstract

Significant progress in the field of wide-gap dilute magnetic semiconductors hangs on the discovery of a system which not only shows high-temperature ferromagnetism but is also simple to prepare and thus easy to reproduce. Ion implantation is both a relatively simple and a highly reproducible doping method. Here we report on the search for high-temperature ferromagnetism in Mn-, Fe- and Co-implanted ZnO and GaN, prepared under a wide range of implantation and post-processing conditions. We focused on the low concentration regime ($\sim 0.3 - 8\%$) in order to avoid phase segregation and applied strict experimental procedures to avoid ferromagnetic contamination. Despite the wide range of materials, implantation and post-processing conditions, none of the prepared DMS systems showed room-temperature ferromagnetism. In aggreement with other comprehensive reports of absence of ferromagnetism in wide-gap DMS materials prepared by various methods, these results support the view that the often observed high-temperature ferromagnetism is not intrinsic.

In preparation for *Journal of Applied Physics*

I. INTRODUCTION

The magnetism of wide-gap semiconductors doped with transition metals, or dilute magnetic semiconductors (DMS), remains one of the most puzzling and controversial topics in magnetism today.[1] Despite the more than ten years of intense research and significant developments in both synthesis and characterization methods, none of the wide-gap DMS systems which have been reported to be ferromagnetic at room temperature gathers the consensus of the magnetism community.

The basic condition for the technological application of DMS materials is an ordering temperature (Curie temperature T_C) compatible with device operation, i.e. above room temperature. Following the first report of high temperature ferromagnetism in Co-doped TiO_2[2] and the prediction by Dietl *et al.*[3] that highly p-type Mn-doped ZnO and GaN could attain a T_C above room temperature, ferromagnetism at and above room temperature was reported in a rapidly growing number of wide-gap DMS materials (cf. e.g. the reviews Refs. 4–7). Although virtually any of the attempted impurity-host DMS combinations was sooner or later reported to display room temperature ferromagnetism, materials like Co- and Mn-doped ZnO and Mn- and Fe-doped GaN received particular attention. This preference can be attributed to various factors, the most important probably being the early predictions of room temperature ferromagnetism in ZnO and GaN, by Dietl *et al.*[3] in *p*-type materials (c.f. Ref. 1 for a recent review) and by Sato *et al.*[8,9] even in the absence of additional carrier doping (c.f. Ref. 10 for a recent review). In addition, ZnO and GaN based DMS materials were (and are) particularly attractive due to their compatibility with existing semiconductor heterostructure technology. However, as the understanding of the magnetism in these materials deepened, issues of irreproducibility and instability became increasingly evident. As the origin of the observed ferromagnetism became increasingly debated, a number of non-intrinsic sources of ferromagnetism were identified and became well documented: magnetic contamination,[11–14] measurement artifacts ,[12,13] spinodal decomposition (e.g. in Co-doped ZnO[15] and Mn-doped GaN[16]) and secondary phase formation (e.g. in Fe- and Co-doped ZnO[17,18] and Fe in GaN[19]). On the other hand, several comprehensive studies on carefully characterized phase-pure materials found only paramagnetism (e.g. in Mn-doped GaN[20] and Co-doped ZnO[21]), antiferromagnetic interactions (e.g. in Mn- and Cr-doped GaN[22,23] and in Co- and Fe-doped ZnO[24–28]), or at best, ferromagnetic order with very low T_C (e.g. $T_C < 10$ K in Mn-doped GaN[29]).

On the theoretical side, as the conditions for *p-d* Zener exchange proposed by Dietl *et al.*, i.e. the high concentration of valence-band holes, are generally *not* satisfied in ZnO and GaN, various other models have been proposed. Aiming at describing the observed room temperature ferromagnetism while at the same time accounting for the difficulties in achieving experimental reproducibility, these models share one common characteristic: the presence of lattice defects other than the magnetic impurities, e.g. vacancies, self-interstitials and grain boundaries. Because the type and concentration of such defects strongly depend on the growth methods and conditions and are in general difficult to monitor and control, defect-related order mechanisms could in principle explain the difficulties in reproducing the ferromagnetic properties. Some models rely on the interplay between such defects and the magnetic impurities, e.g. the bound magnetic polaron (BMP)[30] and the charge-transfer ferromagnetism (CTF) models.[31,32] Others require the presence of only one type of defect, e.g. the spin-split impurity band (SIB) model[33] and a variant of the BMP model.[34] With the development of these models, some experimental evidence has been reported which, although indirectly, supports this picture of defect-related ferromagnetism: by varying the defect concentration it is in some cases possible to turn "on" and "off" the ferromagnetic behavior.[35–38]

Given the general irreproducibility which characterizes the field, and that limited experimental evidence exists that DMS materials are intrinsically ferromagnetic at room temperature, *significant progress in the field depends on the discovery of a DMS system which is not only ferromagnetic at room temperature but is also simple to prepare and thus easy to reproduce*. Among the numerous combinations of materials and preparation methods this prototypical DMS could be searched for, the emerging picture of defect-related ferromagnetism seems to point towards disordered systems. In this context, ion implantation offers some advantages compared to incorporating the magnetic dopants during growth. Not only is it a relatively simple and highly reproducible process,[39] ion bombardment produces a variety of lattice defects, the type and amount of which can be controlled to some extent either by tuning the implantation parameters (e.g. target temperature and incident beam energy and angle) or by post-implantation thermal treatment. In addition, as the magnetic dopants can be (randomly) incorporated at low temperature (at least in radiation resistant materials like ZnO and GaN), i.e. below their mobility thresholds, ion implantation may be superior in terms of dopant uniformity and phase pureness, basic conditions to produce an intrinsic DMS. Ion implantation is

also the standard doping technique in integrated circuit technology, which brings ion-implanted *ferromagnetic* DMS materials particularly close to technological implementation.

In this paper we present an extensive search for room temperature ferromagnetism in common wide-gap DMS systems, using ion implantation as doping method. We focused on the (relatively) low concentration regime ($\sim 0.3 - 8\%$) in order to minimize phase segregation and varied the major material parameters:

- host wide-gap semiconductors: ZnO and GaN;
- magnetic dopants ($3d$ transition metals): Mn, Fe and Co;
- dopant concentration: $\sim 0.3 - 8\%$ by varying fluence ($10^{14} - 10^{16}$ at. cm^{-2}) and implantation energy (60–180 keV);
- co-doping with potential electronic dopants in ZnO: Al (donor) and N (acceptor);
- amount of beam-induced damage: by thermal annealing up to 900°C, characterized using Rutherford backscattering spectrometry and channeling (RBS/C).

The magnetic characterization was performed using superconducting quantum interference device (SQUID) magnetometry, under strict experimental procedures in order to minimize ferromagnetic contamination and measurement artifacts (described in Ref. 14).

II. EXPERIMENTAL DETAILS: SAMPLE PREPARATION

As host materials we used commercial ZnO wurtzite [0001] single-crystals (CrysTec GmbH), hydrothermally grown and Zn-face polished, as well as high-quality epitaxial GaN [0001] thin films (2 μm thick), grown on an Al_2O_3 [0001] by metalorganic vapor phase epitaxy (MOVPE).

Table I lists the implanted samples and corresponding implantation parameters, which are motivated and described in the next section. Table I also lists the depth-profile parameters simulated using SRIM.[40] The sample names are according to the implanted transition metal ("M" for Mn, "F" for Fe and "C" for Co), fluence in units of 1×10^{14} at. cm^{-2}, and host compound ("Z" for ZnO and "G" for GaN). A suffix "180" is added to the names

Sample	Host	Dopant	Energy [keV]	Fluence [at. cm^{-2}]	x_p	R_p [nm]	straggle [nm]
M5Z	ZnO	Mn	60	5×10^{14}	0.0034	30	14
M10Z	ZnO	Mn	60	1×10^{15}	0.0068	30	14
M50Z	ZnO	Mn	60	5×10^{15}	0.034	30	14
F5Z	ZnO	Fe	60	5×10^{14}	0.0034	29	14
F10Z	ZnO	Fe	60	1×10^{15}	0.0069	29	14
F50Z	ZnO	Fe	60	5×10^{15}	0.034	29	14
C5Z	ZnO	Co	60	5×10^{14}	0.0035	28	13
C10Z	ZnO	Co	60	1×10^{15}	0.0070	28	13
C50Z	ZnO	Co	60	5×10^{15}	0.035	28	13
F10Z180	ZnO	Fe	180	1×10^{15}	0.0027	82	35
F50Z180	ZnO	Fe	180	5×10^{15}	0.013	82	35
F100Z180	ZnO	Fe	180	1×10^{16}	0.027	82	35
M50A50Z	ZnO	Mn	60	5×10^{15}	0.034	30	14
		Al	30	5×10^{15}	0.029	30	15
F50A50Z	ZnO	Fe	60	5×10^{15}	0.034	29	14
		Al	30	5×10^{15}	0.029	30	15
C50A50Z	ZnO	Co	60	5×10^{15}	0.035	28	13
		Al	30	5×10^{15}	0.029	30	15
M50N50Z	ZnO	Mn	60	5×10^{15}	0.034	30	14
		N	17	5×10^{15}	0.028	30	15
F50N50Z	ZnO	Fe	60	5×10^{15}	0.034	29	14
		N	17	5×10^{15}	0.028	30	15
C50N50Z	ZnO	Co	60	5×10^{15}	0.035	28	13
		N	17	5×10^{15}	0.028	30	15
M5G	GaN	Mn	60	5×10^{14}	0.0035	29	13
M10G	GaN	Mn	60	1×10^{15}	0.0070	29	13
M50G	GaN	Mn	60	5×10^{15}	0.035	29	13
F5G	GaN	Fe	60	5×10^{14}	0.0036	28	13
F10G	GaN	Fe	60	1×10^{15}	0.0072	28	13
F50G	GaN	Fe	60	5×10^{15}	0.036	28	13
C5G	GaN	Co	60	5×10^{14}	0.0037	27	13
C10G	GaN	Co	60	1×10^{15}	0.0075	27	13
C50G	GaN	Co	60	5×10^{15}	0.037	27	13

TABLE I: Sample list, indicating implanted element, energy and fluence. The peak concentration normalized to the cation (Zn or Ga) concentration (x_p), projected ion range (R_p) and ion straggle were estimated using SRIM[40].

of the samples implanted at 180 keV instead of 60 keV. The co-implanted samples are also named according to the co-dopant ("A" for Al and "N" for N). For ZnO, each entry in Table I corresponds to two samples, one for the structural characterization and the other for magnetometry measurements. For GaN, each entry corresponds to 4 samples, i.e. (structural + magnetic characterization) $\times$ (2 different annealing atmospheres).

A. Implantation parameters

The dopant concentration depends, in ion-implanted systems, on both the number and the depth distribution of the implanted ions. The number of ions can be controlled by measuring the current on the target, i.e the sample or sample holder, and is typically quoted in terms of *fluence* (atoms per areal unit). The depth distribution, for a given impurity-host combination, depends on the energy of the incident ion beam as well as its orientation with respect to the crystal structure. In amorphous materials the depth distribution can be approximated by a Gaussian function with a mean depth (ion range R_p) and a depth standard deviation (ion *straggle*) which increase with beam energy (conversely, the peak concentration x_p decreases with increasing beam energy). In single-crystalline materials, implantation aligned with major crystallographic axes or planes, which is known as *channeled implantation* as the ions tend to be *channeled* and reach deeper into the sample, results in depth profiles which can deviate considerably from a Gaussian. When the beam is at least a few degrees off any low-index crystallographic axis or plane, which is known as *random implantation*, the resulting depth distribution can be approximated by that which would result from implanting the amorphous counterpart of the material. The advantage of random implantation is that it is less dependent on small variations of implantation angle, and is thus superior in terms of reproducibility. For that reason, all implantations in this study were performed at a 10° angle relative to the surface normal (c-axis).

In industrial applications of ion implantation (mostly Si wafer processing), beam energies can vary over several orders of magnitude, from 0.1 keV up to 1000 keV. Most applications are limited to the 10-200 keV range. In this study, most transition metal implantations are performed at 60 keV. Since defect accumulation depends on beam energy, implantations were also performed at 180 keV in the Fe-doped ZnO system, for comparison.

With fixed implantation angle and energy, varying the implanted fluence varies the dopant concentration, which can be estimated using SRIM

code.[40] In transition metal implanted ZnO and GaN with a peak concentration of ∼10% and higher, phase segregation occurs already at relatively low annealing temperatures (700–900°C).[17,18,41–45] Since temperatures in the 700–900° range are normally required for significant damage recovery in ZnO and GaN, this study focuses on the peak-concentration range of the order of $\sim 0.1 - 10\%$ which, for Mn, Fe and Co implanted at 60 keV and 180 keV in ZnO and GaN, corresponds to fluences between 5×10^{14} and 1×10^{16} at. cm^{-2} (c.f. Table I).

In general, defect accumulation depends on the implantation temperature. Increasing the implantation temperature tends to decrease the accumulated damage, as it favors dynamic annealing by increasing the atomic mobility (e.g. Ref. 46). However, controlling and monitoring the temperature at the sample surface during implantation is far from trivial. For simplicity and reproducibility, all implantations were performed at room temperature in this study.

B. Thermal annealing

The main goal of this study is to search for high temperature ferromagnetism under a varying degree of lattice disorder, which can be accomplished by thermal annealing. Annealing of implantation damage in ZnO and GaN is however rather complex. The general rule of thumb is that temperatures of around two thirds of the melting point (in units of K) are required to remove extended defects in semiconductors. For ZnO and GaN, this corresponds to about 1200°C[47] and 1500–1600°C,[48,49] respectively. However, already at 700–900°, annealing of transition-metal implanted ZnO and GaN leads to (undesired) secondary phase segregation[17,18,41–45] and may, in addition be counteracted by material decomposition (e.g N loss from the GaN surface[50]). In order to obtain significant damage recovery while avoiding surface decomposition and phase segregation, thermal annealing was carried out as follows. After being characterized in the as-implanted state, the ZnO and GaN samples were annealed for 10 min in vacuum ($< 10^{-5}$ mbar), in steps of 100°C from 300°C to 900°C. Given the tendency for surface decomposition in GaN under vacuum annealing at high temperatures, a separate set of GaN samples were annealed at 900°C for 30 min under N_2 flow, after being annealed in vacuum up to 600°C.

C. Al and N co-implantation in transition-metal implanted ZnO

Since transition-metal doped ZnO has also been reported to show room temperature ferromagnetism when co-doped with Al (donor) and N (acceptor) (e.g. Refs. 51–55), a set of ZnO samples implanted with Mn, Fe or Co to a fluence of 5×10^{15} at. cm^{-2} were co-implanted with Al or N, also to a fluence of 5×10^{15} at. cm^{-2}. Based on SRIM[40] simulations, the implantation energies were selected in order to maximize the overlap between the transition metal and the Al/N profile (Table I). Note that since we have not characterized these samples in terms of carrier type and concentration, we can not establish a correlation between activated donor/acceptor concentrations and the presence or absence of high temperature ferromagnetism.

III. EXPERIMENTAL DETAILS: CHARACTERIZATION

Given the large amount of samples (27), which multiplies by the number of annealing stages (8 for ZnO samples and 9 for GaN samples) giving a total of 216 sample-temperature combinations, we characterized only a selected set of these. Magnetic characterization was performed on all the samples, in the as-implanted state and following annealing at 300°C, 600°C and 900°C. The aim of the RBS/C measurements was mostly to investigate to what extent the thermal annealing was able to recover the sample crystallinity, i.e. if the magnetic characterization was indeed performed for a varying level of lattice disorder, from highly disordered to highly crystalline, as desired. Therefore, RBS/C measurements were performed for all the annealing steps but only for the highest fluence (for which the beam-induced damage is maximum and the recovery should be minimum compared to the other fluences) of each dopant-compound combination. The set of co-implanted ZnO samples were not characterized by RBS/C, since the relatively low fluence (5×10^{15} at. cm^{-2}) of the much lighter (Al and N) co-implants is not expected to considerably change the damage accumulation and annealing behavior. All ZnO samples implanted at 180 keV (three different fluences) were measured by RBS/C.

A. SQUID magnetometry

The magnetic characterization was performed using a superconducting quantum interference device (SQUID) magnetometer (*Quantum De-*

sign MPMS XL-5) following strict procedures in order to avoid magnetic contamination and other experimental artifacts.[14] These procedures were developed based on statistically relevant tests, which allowed us to determine the practical limits of SQUID magnetometry for the detection of ferromagnetism under various sample preparation, processing and handling conditions. The measurements were performed with the field perpendicular to the *c*-axis, i.e., parallel to the sample plane. The field-dependent measurements were performed with decreasing field.

B. Rutherford backscattering and channeling spectrometry (RBS/C)

Defect formation and annealing were characterized using Rutherford backscattering and channeling spectrometry (RBS/C), with a 1.57 MeV He^+ beam and two detectors, at backscattering angles of 168° and 105°. The 168° backscattering geometry was used to determine the channeling minimum yield $\chi_{\min}$ along the [0001] axis. The minimum yield $\chi_{\min}$ is the ratio of the backscattering yield with the ion beam aligned with the crystal axis to that of random beam incidence, and it is a measure of the lattice disorder induced by ion implantation.[56] The 105° glancing angle geometry (15° relative to the sample surface) of the second detector provides a better depth resolution and thus allows us to study the evolution of the damage as a function of depth.

IV. RESULTS

A. Damage accumulation and annealing

Figures 1 (a) and 2 (a) show representative RBS/C spectra in backscattering geometry (168°) of unimplanted and implanted/annealed ZnO (Fig. 1) and GaN (Fig. 2) samples. Figure 1 shows data of sample C50Z (5×10^{15} cm^{-2} Co-implanted ZnO); the data are similar for Mn and Fe. Figure 2 shows data of sample M50G (5×10^{15} cm^{-2} Mn-implanted GaN); the data is similar for Fe and Co. As typical for ZnO[57] and GaN,[58] lattice disorder in the Zn/Ga sublattice accumulates in two regions: in the crystal bulk (bulk peak), where the energy loss is maximum; near the sample surface (surface peak), which acts as a sink for mobile defects created by the ion bombardment. This bimodal damage accumulation is particularly clear in

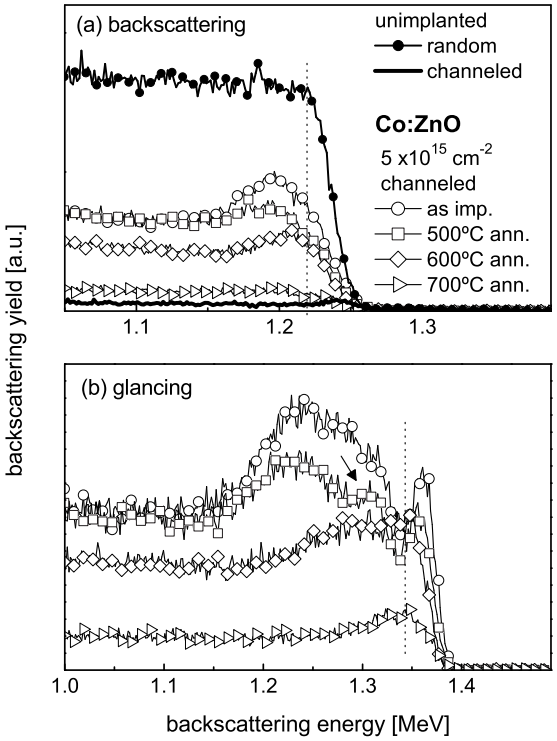

FIG. 1: (a) RBS/C spectra in backscattering geometry (168°) in channeling orientation of an unimplanted ZnO sample and sample C50Z (5×10^{15} cm^{-2} Co-implanted ZnO) after different annealing stages, compared to the random spectrum of the unimplanted sample. The dashed line separates the surface and bulk energy windows used to calculate the corresponding $\chi_{\min}$. (b) RBS/C spectra in glancing geometry (15° with respect to the sample surface) in channeling orientation of the same sample C50Z and same annealing stages. The arrow indicates the position of the middle defect peak (MDP) region, discussed in the text.

the spectra measured in glancing geometry, with higher depth resolution [Fig. 1 (b) and 2 (b)]. It is also particularly clear in the ZnO samples Fe-implanted at 180 keV [Fig. 3 (a)], where the Fe profile reaches deeper in the sample and the surface and bulk regions are thus better resolved in the RBS/C spectra. As usual in cases of bimodal damage accumulation, the channeling minimum yield $\chi_{\min}$ is determined separately for the two regions, i.e. surface and bulk, from the RBS/C spectra in backscattering geometry. Bulk $\chi_{\min}$ are compiled in Fig. 4 (a) and surface $\chi_{\min}$ in Fig. 4

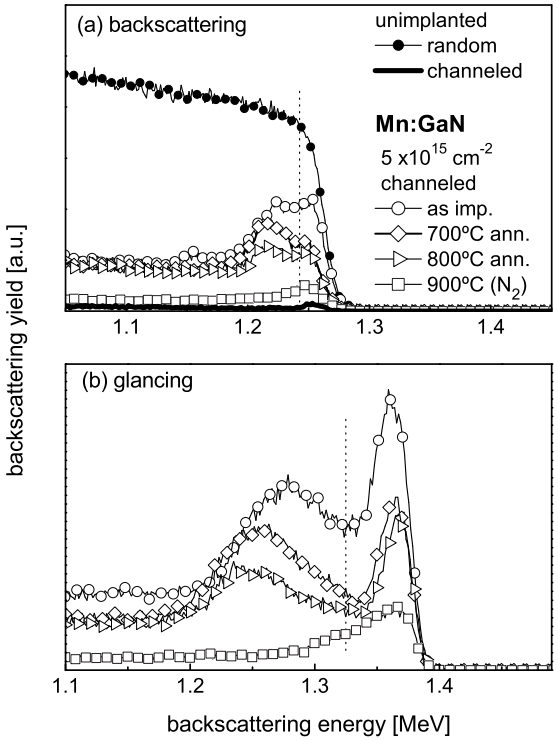

FIG. 2: (a) RBS/C spectra in backscattering geometry (168°) in channeling orientation of an unimplanted GaN sample and sample M50G (5×10^{15} cm^{-2} Mn-implanted GaN) at different annealing stages, compared to the random spectrum of the unimplanted sample. The dashed line separates the surface and bulk energy windows used to calculate the corresponding $\chi_{\min}$. (b) RBS/C spectra in glancing geometry (15° with respect to the sample surface) in channeling orientation of the same sample C50Z and same annealing stages.

(b) for the three transition metal dopants in ZnO and all annealing steps up to 900°C. Similarly bulk $\chi_{\min}$ and surface $\chi_{\min}$ are compiled in Fig. 5 for GaN.

The overall behavior is similar for both host materials and for all three transition metal dopants (Mn, Fe and Co). Both ZnO and GaN remain crystalline even after a relatively high fluence implantation (5×10^{15} cm^{-2}), as the backscattering yield in the as-implanted state is well below the random level (which would correspond to amorphization). This reflects the efficient *dynamic annealing* which characterizes ZnO and GaN and is responsible

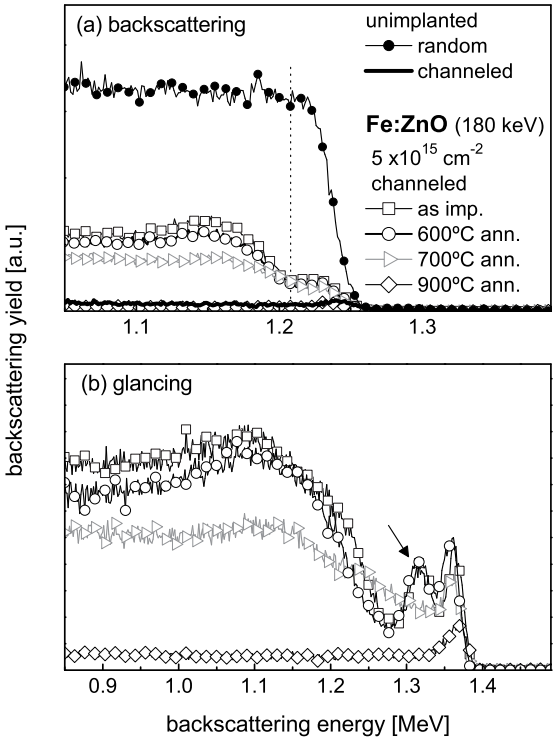

FIG. 3: (a) RBS/C spectra in backscattering geometry (168°) in channeling orientation of an unimplanted ZnO sample and sample Z50Z180 (5×10^{15} cm^{-2} Fe-implanted ZnO at 180 keV) at different annealing stages, compared to the random spectrum of the unimplanted sample. The dashed line separates the surface and bulk energy windows used to calculate the corresponding $\chi_{\min}$. (b) RBS/C spectra in glancing geometry (15° with respect to the sample surface) in channeling orientation of the same sample Z50Z180 and same annealing stages. The arrow indicates the position of the middle defect peak (MDP) region, discussed in the text.

for its known high radiation resistance. Still, significant lattice disorder is induced upon implantation in the ion range region (bulk $\chi_{\min} > 50$ %), which in turn is significantly recovered upon thermal annealing, with the main difference between ZnO and GaN being the temperature range at which the major recovery starts (600°C in ZnO and 700°C in GaN). These and other differences are discussed next as we analyze the damage build-up and annealing for ZnO and GaN separately.

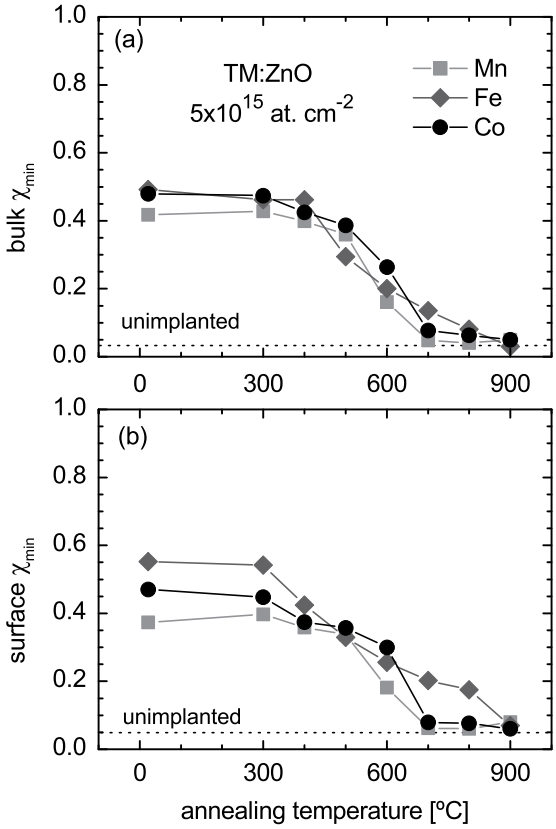

FIG. 4: (a) Bulk and (b) surface $\chi_{\min}$ of samples M50Z, F50Z and C50Z, i.e. 5×10^{15} cm^{-2} Mn-, Fe- and Co-implanted ZnO, respectively, as a function of annealing temperature.

1. ZnO

The most important observation with regards to the main purpose of this work, i.e. searching for ferromagnetism under a varying degree of crystallinity, is that thermal annealing is able to progressively vary the bulk $\chi_{\min}$ (i.e. the relative disorder in the region of interest, the dopant end of range region) from highly disordered (40%–50%) in the as-implanted state to virtually perfectly crystalline after 900°C annealing (3%–5%), similar to the unimplanted sample (3%) [Fig. 4 (a)]. It is also important to note that no major differences can be observed between the three different transition metal impurities. For the 180 keV implantations (Fig. 6), $\chi_{\min}$ increases

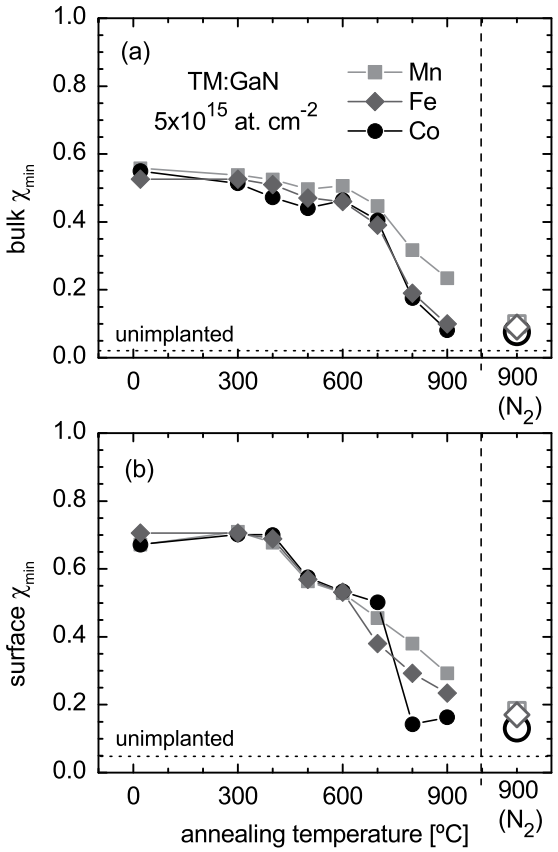

FIG. 5: (a) Bulk and (b) surface $\chi_{\min}$ of samples M50G, F50G and C50G, i.e. 5×10^{15} cm^{-2} Mn-, Fe- and Co-implanted GaN, respectively, as a function of annealing temperature. Full symbols correspond to vacuum annealing; open symbols correspond to annealing in N_2 flow.

with implanted fluence as expected, and the annealing behavior is virtually the same as for 60 keV. It is interesting to note that a higher implantation energy results in a lower bulk $\chi_{\min}$ (49% for 60 keV and 29% for 180 keV 5×10^{15} cm^{-2} Fe-implantation). This appears to be somehow counterintuitive, as a higher energy of the impinging ions implies that a larger energy is deposited in the target material and, consequently, that more damage is created. Note however that increasing the implantation energy increases the width of the bulk damage peak (related to the also increased ion straggle). Therefore, although the number of displaced atoms per impinging atom

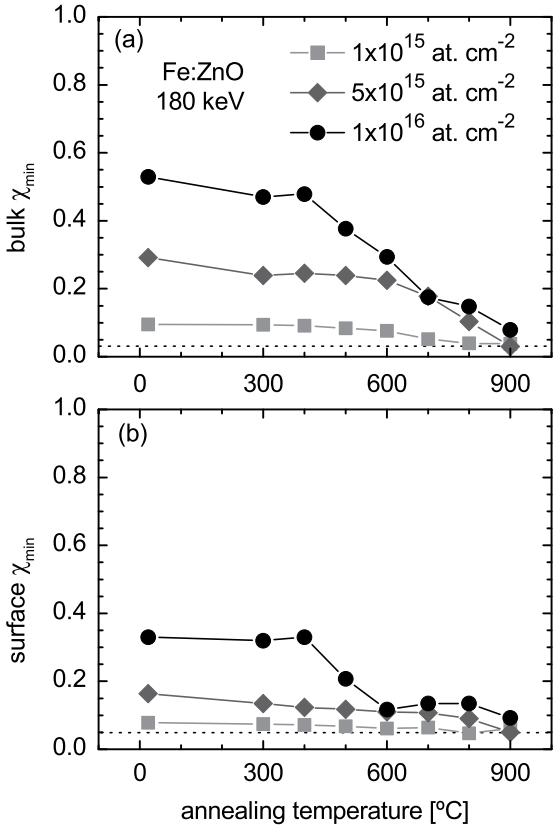

FIG. 6: (a) Bulk and (b) surface $\chi_{\min}$ of samples F10Z180, F50Z180 and F100Z180, i.e. Fe-implanted ZnO (180 keV implantations) to fluences of 1×10^{15} cm^{-2}, 5×10^{15} cm^{-2} and 1×10^{16} cm^{-2}, respectively.

necessarily increases with implantation energy, the bulk $\chi_{\min}$ (which is more directly related to the concentration than it is to the total number of defects) does not in this case.

Looking in somewhat more detail at the evolution of the damage in the bulk region upon annealing, it appears that for all three transition metals [Fig. 1 (b) for Co] the damage in the ion range region survives annealing up to higher temperatures compared to the region between the ion range and the surface. This can be attributed to trapping of lattice defects (such as vacancies and self-interstitials) by the transition-metal impurities. This is particularly clear for Fe, which we have studied in more detail in Ref. 28.

Another interesting feature of the ZnO spectra is the appearance of a third damage peak, between the common surface and bulk peaks (indicated by arrows in Figs. 1 and 3). This *middle defect peak* (MDP) was also observed in Au-implanted ZnO by Kucheyev *et al.* in Ref. 57 and by us in Ref. 28. In Ref. 57, the MDP was attributed to a localized band of lattice defects, which nucleates in the near surface region due to incomplete dynamic annealing during ion bombardment. This in turn is likely to result from the spatial separation between vacancies and interstitials in the collision cascades, which creates an excess of vacancies closer to the surface and an excess of interstitials near the ion end of range. The MDP is particularly well resolved in the samples implanted with Fe with an energy of 180 keV [Fig. 3 (b)], as the bulk and surface regions are better separated, which shows in addition that the MDP-related damage is annealed at 700°C.

2. GaN

Not only is $\chi_{\min}$ in as-implanted GaN (53%–55%) [Fig. 5 (a)] higher than in ZnO (41%–49%) [Fig. 4 (a)], major recovery starts at higher temperatures (700°C in GaN and 600°C in ZnO). In addition, thermal annealing is less efficient in recovering the crystallinity of GaN. Annealing in vacuum up to 900°C results in a bulk $\chi_{\min}$ of 8%–23%, considerably higher than for ZnO (bulk $\chi_{\min}$ of 3%–5%); annealing in N_2 flow is more efficient (bulk $\chi_{\min}$ of 7%–10%), but still significantly higher than the 2.5% prior to implantation.

The higher degree of beam-induced disorder in GaN compared to ZnO is even more noticeable in the surface region, with GaN showing a higher surface $\chi_{\min}$ from the as-implanted state up to the last annealing step [Fig. 5 (b)]. This is also visible in the RBS/C spectra measured in glancing angle geometry [Fig. 2 (b)], with a surface peak which is more intense than the bulk peak, as opposed to the ZnO case [Fig. 1 (b)]. The difference between host materials is consistent with the lower surface amorphization threshold observed by Kucheyev *et al.* in GaN[58] compared to ZnO,[57] which is probably associated with a higher tendency for N loss in the GaN surface upon ion bombardment, compared to O loss in ZnO.

The trapping of native defects by the implanted impurities, discussed above for ZnO, can also be inferred from the GaN data. The arrows in Fig. 2 show that the damage in the Mn end of range region is annealed at higher temperatures compared to the damage in the region between the Mn end of range and the surface.

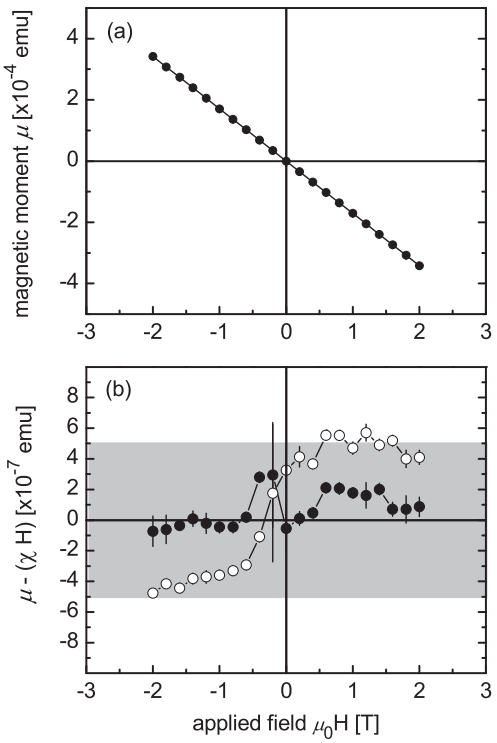

FIG. 7: (a) Representative examples of (a) $\mu(H)$ data as measured at 300 K (sample C50Z) and (b) ferromagnetic-like component obtained by subtracting the linear component estimated between 1 and 2 T (sample C50Z as implanted (•) and sample M50Z following 900°C annealing (○)). The gray region indicates the range corresponding to magnetic contamination and instrumental limits.[14]

B. Magnetic characterization

Figure 7 (a) shows typical $\mu(H)$ data measured at 300 K, dominated by the diamagnetic susceptibility of the ZnO substrate (similar for the GaN grown on Al_2O_3 substrates). Since, to a good approximation, the diamagnetic susceptibility χ does not depend on the applied field H in ZnO and Al_2O_3, one can search for a possible residual ferromagnetic-like component (i.e. a saturating hysteresis) by estimating χ from the linear fit of the data between 1 and 2 T, where the ferromagnetic component is in principle saturated, and plotting $(\mu(H) - \chi H)$. Examples of such residual signals are shown in Fig. 7 (b) for the samples which showed the lowest $(7(5) \times 10^{-8}$

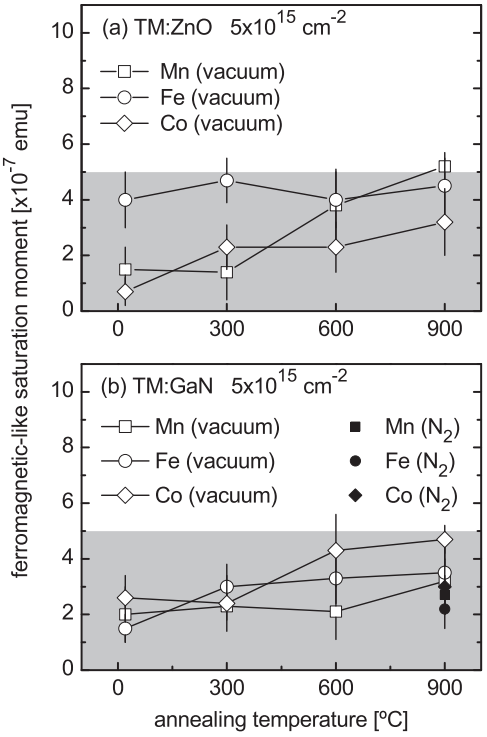

FIG. 8: Representative examples of the saturation moment of the ferromagnetic-like component of the *M-H* data as a function of annealing temperature, for (a) samples M50Z, F50Z and C50Z (5×10^{15} cm-2 Mn-, Fe-, and Co-implanted ZnO, respectively) and (b) samples M50G, F50G and C50G (5×10^{15} cm-2 Mn-, Fe-, and Co-implanted GaN, respectively). Open symbols correspond to vacuum annealing and full symbols to annealing in N_2 flow. The gray region indicates the range corresponding to magnetic contamination and instrumental limits.[14]

emu) and highest ($5.2(5) \times 10^{-7}$ emu) saturation moment, which can be taken as the $\mu(H = 0)$ value extrapolated from the linear fit between 1 and 2 T. We have shown in Ref. 14 that such residual ferromagnetic-like signals with a saturation moment of the order of 5×10^{-7} emu can be attributed to magnetic contamination or measurement artifacts. Most of the samples in the present study had a saturation moment in that range, i.e. did not exhibit ferromagnetic behavior (at 300 K) above the experimental detection limit. For the few samples which did, we implanted new samples under the same conditions. This second set of samples had saturation magnetization

fluence [at. cm^{-2}]	$\mu_{\rm at}$ [μ_B]
5×10^{14}	0.43
1×10^{15}	0.22
5×10^{15}	0.043
1×10^{16}	0.022

TABLE II: Maximum magnetic moment per implanted transition-metal atom $\mu_{\rm at}$, in case the observed residual hystereses (with a saturation moment of the order of 5×10^{-7} emu) would originate from intrinsic, doping-related ferromagnetism.

below 5×10^{-7} emu, with the exception of 5×10^{15} cm^{-2} Fe-implanted ZnO (F50Z); a third F50Z sample was prepared, which showed a saturation moment below 5×10^{-7}. In addition, all samples that showed a saturation moment above 5×10^{-7} at some annealing stage were cleaned using the protocol described in Ref. 14. After the cleaning procedure, the saturation moment of all the samples decreased significantly, most of them to below 5×10^{-7} emu. The saturation moment of samples C50Z and M50G, representative of all the other samples, is plotted in Fig. 8 as a function of annealing temperature. The slight increase in saturation moment with increasing annealing temperature reflects the increase in number of processing steps, i.e. of contaminating events. We conclude that none of the samples showed intrinsic ferromagnetism above the experimental detection limit; the ferromagnetism observed in some samples can be attributed to magnetic contamination, as extensively discussed in Ref. 14. However, one can not exclude that the residual hystereses are at least partially due to intrinsic ferromagnetism induced by the magnetic doping. Table II lists the maximum ferromagnetic saturation moment per implanted transition metal consistent with a detection limit of 5×10^{-7} emu for samples of approximately 5×5 mm^2.

V. DISCUSSION

Despite the wide range of implantation and post-processing conditions, none of the impurity-host combinations showed measurable room-temperature ferromagnetism. In particular, even though we covered a wide range of density and type of beam-induced damage by varying the implanted fluence and the annealing temperature, no sign of defect-related

ferromagnetism could be observed. This strongly suggests that the high temperature ferromagnetism reported in various ion-implanted DMS systems can be attributed to magnetic contamination (as observed here) and to ferromagnetic secondary phases (as demonstrated for example in Refs. 17,18,41–45). Based on the present study alone, the conclusion that transition-metal doped ZnO and GaN are not ferromagentic at room temperature can only be drawn for relatively low fluence ion-implanted materials. However, if even such a simple and reproducible preparation technique such as ion implantation has allowed for such a spread of contradictory reports, one may ask what fraction of the reports of room temperature ferromagnetism in wide gap DMS materials prepared by other methods can actually be ascribed to intrinsic ferromagnetism.

The absence of high temperature ferromagnetism raises another question: what is then the magnetic behavior of these materials? We have not addressed this here, but a number of comprehensive reports exist on wide-gap DMS materials either doped during growth or by ion implantation (e.g. Fe- and Co-doped ZnO[21,24–28] and Mn- and Cr-doped GaN[20,22,23]) seem to provide a general and rather consistent answer. For sufficiently low concentrations, the isolated transition-metal impurities, the large majority of which in cation-substitutional sites,[59–63] behave as localized paramagnetic moments.[20,21,23,28] With increasing concentration and the consequent decrease of the mean distance between the impurities in the lattice, this paramagnetism is affected by strong *antiferromagnetic* interactions between the localized magnetic moments of nearest-cation-neighbor impurities.[22–28] The dominance of antiferromagnetic over ferromagnetic interactions between nearest-cation-neighbor transition metals in oxides and nitrides can hardly be considered surprising, since most transition-metal oxides and nitrides are indeed antiferromagnetic. On the other hand, the proposed mechanisms of longer-ranged ferromagnetic interactions between transition metal impurities depend on conditions which are not necessarily satisfied in wide-gap DMS materials. Transition metals form deep levels in the ZnO and GaN bandgap and therefore do not introduce the *p*-holes required to mediate ferromagnetic *p-d* Zener interaction. Regarding bound magnetic polaron (BMP) models, the exchange energy density necessary to produce high-temperature ferromagnetism with a few percent of transition-metal doping corresponds to a magnetic exchange much stronger than that observed in the strongest of the known ferromagnetic materials.[64]

It appears that for high-temperature ferromagnetism to be achieved in these materials, a different mechanism should be explored that does not

rely on ordered 3*d* local moments and Heisenberg-type exchange as in *p-d* Zener exchange and BMP models. The charge-transfer ferromagnetism (CTF) model,[64] a Stoner-type mechanism, seems to offer just that. It requires two distinct types of defects, one that creates a narrow impurity band and another to play the role of charge reservoir. If both types of defects are present, electrons can be transferred to or from the reservoir until the filling level of the impurity band satisfies the spontaneous spin-splitting criterion. Indeed, most 3*d* transition metals have more than one charge state within the bandgap of wide-gap semiconductors (e.g. Fe^{2+} and Fe^{3+} in ZnO[18] and Mn^{2+} and Mn^{3+} in GaN[22,29]) and could thus play the role of charge reservoirs. However, it remains to be demonstrated if one such type of defect does exist which creates an impurity band that can be spontaneously spin-split. Based on the results presented by us here and in Refs. 23 and Refs. 28, beam-induced defects do not seem to satisfy those requirements.

VI. CONCLUSIONS

In summary, none of the wide-gap DMS systems prepared by ion implantation of Mn, Fe and Co in ZnO and GaN showed measurable room temperature ferromagnetism. Given the wide range of material, implantation and post-processing parameters covered in this study, these results strongly suggest that ion-implanted wide-gap DMS materials are not ferromagnetic at room temperature. In agreement with other comprehensive reports of absence of ferromagnetism in wide-gap DMS prepared by various other methods, our findings support the view that the high temperature ferromagnetism often observed in wide-gap DMS materials is not intrinsic.

Acknowledgments

This work was supported by the Portuguese Foundation for Science and Technology (PTDC/FIS/66262/2006, SFRH/BD/35761/2007), the Research Foundation - Flanders (FWO), the EURONS project (RII3-CT-2004-506065), the SPIRIT project (contract no. 227012), KULeuven projects GOA/2009/006 and INPAC EF/05/005 and the IUAP P6/42 pro-

gram.

[1] T. Dietl, Nat. Mater. **9**, 965 (2010).
[2] Y. Matsumoto, M. Murakami, T. Shono, T. Hasegawa, T. Fukumura, M. Kawasaki, P. Ahmet, T. Chikyow, S. Koshihara, and H. Koinuma, Science **291**, 854 (2001).
[3] T. Dietl, H. Ohno, F. Matsukura, J. Cibert, and D. Ferrand, Science **287**, 1019 (2000).
[4] S. J. Pearton, C. R. Abernathy, D. P. Norton, A. F. Hebard, Y. D. Park, L. A. Boatner, and J. D. Budai, Mater. Sci. Eng. R-Rep. **40**, 137 (2003).
[5] W. Prellier, A. Fouchet, and B. Mercey, J. Phys.-Condens. Matter **15**, R1583 (2003).
[6] S. J. Pearton, W. H. Heo, M. Ivill, D. P. Norton, and T. Steiner, Semicond. Sci. Technol. **19**, R59 (2004).
[7] C. Liu, F. Yun, and H. Morkoc, J. Mater. Sci.-Mater. Electron. **16**, 555 (2005).
[8] K. Sato and H. Katayama-Yoshida, Jpn. J. Appl. Phys. **40**, L485 (2001).
[9] K. Sato and H. Katayama-Yoshida, Semicond. Sci. Technol. **17**, 367 (2002).
[10] K. Sato, L. Bergqvist, J. Kudrnovsky, P. H. Dederichs, O. Eriksson, I. Turek, B. Sanyal, G. Bouzerar, H. Katayama-Yoshida, V. A. Dinh, et al., Rev. Mod. Phys. **82**, 1633 (2010).
[11] D. W. Abraham, M. M. Frank, and S. Guha, Appl. Phys. Lett. **87**, 252502 (2005).
[12] A. Ney, T. Kammermeier, V. Ney, K. Ollefs, and S. Ye, J. Magn. Magn. Mater. **320**, 3341 (2008).
[13] M. A. Garcia, E. Fernandez Pinel, J. de la Venta, A. Quesada, V. Bouzas, J. F. Fernandez, J. J. Romero, M. S. Martin Gonzalez, and J. L. Costa-Kramer, J. Appl. Phys. **105**, 013925 (2009).
[14] L. M. C. Pereira, J. P. Araujo, M. J. Van Bael, K. Temst, and A. Vantomme, J. Phys. D: Appl. Phys. **44**, 215001 (2011).
[15] Z. Sun, W. Yan, G. Zhang, H. Oyanagi, Z. Wu, Q. Liu, W. Wu, T. Shi, Z. Pan, P. Xu, et al., Phys. Rev. B **77**, 245208 (2008).
[16] G. Martinez-Criado, A. Somogyi, S. Ramos, J. Campo, R. Tucoulou, M. Salome, J. Susini, M. Hermann, M. Eickhoff, and M. Stutzmann, Appl. Phys. Lett. **86**, 131927 (2005).
[17] S. Zhou, K. Potzger, J. von Borany, R. Grotzschel, W. Skorupa, M. Helm, and J. Fassbender, Phys. Rev. B **77**, 035209 (2008).
[18] S. Zhou, K. Potzger, G. Talut, H. Reuther, J. von Borany, R. Groetzschel, W. Skorupa, M. Helm, J. Fassbender, N. Volbers, et al., J. Appl. Phys. **103**, 023902 (2008).
[19] A. Bonanni, A. Navarro-Quezada, T. Li, M. Wegscheider, Z. Matej, V. Holy, R. T. Lechner, G. Bauer, M. Rovezzi, F. D'Acapito, et al., Phys. Rev. Lett.

101, 135502 (2008).
[20] W. Stefanowicz, D. Sztenkiel, B. Faina, A. Grois, M. Rovezzi, T. Devillers, F. d'Acapito, A. Navarro-Quezada, T. Li, R. Jakiela, et al., Phys. Rev. B **81**, 235210 (2010).
[21] A. Ney, T. Kammermeier, K. Ollefs, S. Ye, V. Ney, T. C. Kaspar, S. A. Chambers, F. Wilhelm, and A. Rogalev, Phys. Rev. B **81**, 054420 (2010).
[22] S. Granville, B. J. Ruck, F. Budde, H. J. Trodahl, and G. V. M. Williams, Phys. Rev. B **81**, 184425 (2010).
[23] L. M. C. Pereira, T. Som, J. Demeulemeester, M. J. Van Bael, K. Temst, and A. Vantomme, J. Phys.: Condens. Matter **23**, 346004 (2011).
[24] A. Ney, K. Ollefs, S. Ye, T. Kammermeier, V. Ney, T. C. Kaspar, S. A. Chambers, F. Wilhelm, and A. Rogalev, Phys. Rev. Lett. **100**, 157201 (2008).
[25] P. Sati, C. Deparis, C. Morhain, S. Schafer, and A. Stepanov, Phys. Rev. Lett. **98**, 137204 (2007).
[26] Q. Xu, S. Zhou, D. Marko, K. Potzger, J. Fassbender, M. Vinnichenko, M. Helm, H. Hochmuth, M. Lorenz, M. Grundmann, et al., J. Phys. D-Appl. Phys. **42**, 085001 (2009).
[27] H. B. de Carvalho, M. P. F. de Godoy, R. W. D. Paes, M. Mir, A. Ortiz de Zevallos, F. Iikawa, M. J. S. P. Brasil, V. A. Chitta, W. B. Ferraz, M. A. Boselli, et al., J. Appl. Phys. **108**, 079906 (2010).
[28] (Article IX, unpublished).
[29] E. Sarigiannidou, F. Wilhelm, E. Monroy, R. M. Galera, E. Bellet-Amalric, A. Rogalev, J. Goulon, J. Cibert, and H. Mariette, Phys. Rev. B **74**, 041306 (2006).
[30] J. M. D. Coey, M. Venkatesan, and C. B. Fitzgerald, Nat. Mater. **4**, 173 (2005).
[31] J. M. D. Coey, K. Wongsaprom, J. Alaria, and M. Venkatesan, J. Phys. D-Appl. Phys. **41**, 134012 (2008).
[32] J. M. D. Coey, P. Stamenov, R. D. Gunning, M. Venkatesan, and K. Paul, New J. Phys. **12**, 053025 (2010).
[33] D. M. Edwards and M. I. Katsnelson, J. Phys.-Condens. Matter **18**, 7209 (2006).
[34] R. P. Panguluri, P. Kharel, C. Sudakar, R. Naik, R. Suryanarayanan, V. M. Naik, A. G. Petukhov, B. Nadgorny, and G. Lawes, Phys. Rev. B **79**, 165208 (2009).
[35] N. Khare, M. J. Kappers, M. Wei, M. G. Blamire, and J. L. MacManus-Driscoll, Adv. Mater. **18**, 1449 (2006).
[36] L. E. Halliburton, N. C. Giles, N. Y. Garces, M. Luo, C. C. Xu, L. H. Bai, and L. A. Boatner, Appl. Phys. Lett. **87**, 172108 (2005).
[37] D. A. Schwartz and D. R. Gamelin, Adv. Mater. **16**, 2115 (2004).
[38] R. P. Borges, R. C. Da Silva, S. Magalhaes, M. M. Cruz, and M. Godinho, J. Phys.-Condens. Matter **19**, 476207 (2007).
[39] L. Rubin and J. Poate, Indust. Phys. **9**, 12 (2003).
[40] J. P. Biersack and L. Haggmark, Nucl. Instr. and Meth. **174**, 257 (1980).
[41] R. P. Borges, B. Ribeiro, A. R. G. Costa, C. Silva, R. C. da Silva, G. Evans,

A. P. Goncalves, M. M. Cruz, and M. Godinho, Eur. Phys. J. B **79**, 185 (2011).
[42] Y. Wang, J. Zou, Y. J. Li, B. Zhang, and W. Lu, Acta Mater. **57**, 2291 (2009).
[43] G. Talut, H. Reuther, A. Muecklich, F. Eichhorn, and K. Potzger, Appl. Phys. Lett. **89**, 161909 (2006).
[44] W. Kim, H. J. Kang, S. K. Noh, J. Song, and C. S. Kim, J. Magn. Magn. Mater. **310**, E729 (2007).
[45] W. Kim, H. J. Kang, S. K. Noh, J. Song, and C. S. Kim, J. Magn. Magn. Mater. **316**, E199 (2007).
[46] W. Jiang and W. J. Weber, Nucl. Instrum.Nucl. Instrum. Methods Phys. Res. B **242**, 431 (2006).
[47] R. H. Lamoreaux, D. L. Hildenbrand, and L. Brewer, J. Phys. Chem. Ref. Data **16**, 419 (1987).
[48] J. A. Van Vechten, Phys. Rev. B **7**, 1479 (1973).
[49] K. Harafuji, T. Tsuchiya, and K. Kawamura, J. Appl. Phys. **96**, 2501 (2004).
[50] J. S. Williams, Mater. Sci. Eng. A **253**, 8 (1998).
[51] Y. Tian, Y. Li, M. He, I. A. Putra, H. Peng, B. Yao, S. A. Cheong, and T. Wu, Appl. Phys. Lett. **98**, 162503 (2011).
[52] M. H. N. Assadi, Y. B. Zhang, and S. Li, J. Appl. Phys. **106**, 093911 (2009).
[53] W. Xue-Tao, Z. Li-Ping, Y. Zhi-Gao, Y. Zhi-Zhen, and Z. Bing-Hui, J. Inorg. Mater. **25**, 711 (2010).
[54] S. Chattopadhyay, T. K. Nath, A. J. Behan, J. R. Neal, D. Score, Q. Feng, A. M. Fox, and G. A. Gehring, J. Magn. Magn. Mater. **323**, 1033 (2011).
[55] Z. L. Lu, W. Miao, W. Q. Zou, M. X. Xu, and F. M. Zhang, J. Alloy. Compd. **494**, 392 (2010).
[56] W. K. Chu, J. W. Mayer, and M. A. Nicolet, *Backscattering Spectrometry* (Academic, New York, 1978).
[57] S. O. Kucheyev, J. S. Williams, C. Jagadish, J. Zou, C. Evans, A. J. Nelson, and A. V. Hamza, Phys. Rev. B **67** (2003).
[58] S. O. Kucheyev, J. S. Williams, C. Jagadish, J. Zou, and G. Li, Phys. Rev. B **62**, 7510 (2000).
[59] E. Rita, U. Wahl, J. G. Correia, E. Alves, and J. C. Soares, Appl. Phys. Lett. **85**, 4899 (2004).
[60] L. M. C. Pereira, U. Wahl, S. Decoster, J. G. Correia, L. M. Amorim, M. R. da Silva, J. P. Araujo, and A. Vantomme, Phys. Rev. B **84**, 125204 (2011).
[61] U. Wahl, A. Vantomme, G. Langouche, J. G. Correia, and L. Peralta, Appl. Phys. Lett. **78**, 3217 (2001).
[62] (Article V, unpublished).
[63] (Article VI, unpublished).
[64] J. M. D. Coey, P. Stamenov, R. D. Gunning, M. Venkatesan, and K. Paul, New J. Phys. **12**, 053025 (2010).

4.4 Paramagnetism and antiferromagnetic interactions in Cr-implanted GaN and Fe-implanted ZnO

In the previous section (Article VII), we have shown that, despite the wide range of implantation and post-processing conditions, none of the impurity-host combinations was ferromagnetic at room temperature. This raises several questions. If not high temperature ferromagnetism, what *is* the magnetic behavior of these materials in the phase-pure region of the phase diagram? What is the magnetic behavior of isolated transition-metal impurities and what type of magnetic interactions (ferro- or antiferromagnetic, short- or long-range) exist between them? How is the magnetism of the transition-metal impurities affected by other lattice defects? These questions have been addressed already for some of the most intensively studied materials, such as Co- and Mn-doped ZnO and Mn-doped GaN (c.f. section 1.4.2). The aim of the this section is to contribute to a more general picture of wide-gap DMS, by comprehensively investigating other representative impurity-hot combinations which are not as well-understood, namely Cr-implanted GaN (in article VIII) and Fe-implanted ZnO (in article IX).

The interest of Cr-doped GaN derives from the fact that nearly all the available literature on this system consists of reports of (supposedly intrinsic) high-temperature ferromagnetism, unlike systems such as Co- and Mn-doped ZnO and Mn-doped GaN, for which reports of absence of ferromagnetism have been accumulating. While focusing on the *intrinsic* origin of the observed ferromagnetism by investigating possible secondary-phase formation, these studies lack however a comprehensive analysis of the magnetic behavior itself, particularly with respect to other potential sources of non-intrinsic ferromagnetism.

Fe-implanted ZnO, on the other hand, is a remarkably rich DMS system in which to study the magnetism of both the phase-pure and the phase-segregated regions of the phase diagram. On the phase-pure region, Fe impurities may be incorporated in ZnO both as Fe^{2+} and Fe^{3+}, making it a potentially suitable mixed-valency impurity in charge-transfer ferromagnetic (CFT) systems (c.f. section 1.4.2.1). On the phase-segregation side of the phase diagram, ferromagnetic-like behavior has been shown to originate from superparamagnetic precipitates formed at sufficiently high processing temperatures and Fe concentrations: α-Fe clusters which are oxidized and then converted to the spinel ferrite $ZnFe_2O_4$ with increasing

annealing temperature and time.

Article VIII

Paramagnetism and antiferromagnetic interactions in Cr-doped GaN

L. M. C. Pereira,[1,2,3] T. Som,[1,4] J. Demeulemeester,[1]
M. J. Van Bael,[5] K. Temst,[1] and A. Vantomme[1]

[1]*Instituut voor Kern- en Stralingsfysica and INPAC, K.U.Leuven, B-3001 Leuven, Belgium*
[2]*IFIMUP and IN-Institute of Nanoscience and Nanotechnology, Faculdade de Ciências da Universidade do Porto, 4169-007 Porto, Portugal*
[3]*Instituto Tecnológico e Nuclear, 2686-953, Sacavém, Portugal*
[4]*Institute of Physics, Bhubaneswar 751005, Orissa, India*
[5]*Laboratory of Solid-State Physics and Magnetism and INPAC, K.U.Leuven, 3001 Leuven, Belgium*

Abstract

We report on the magnetic and structural properties of Cr-doped GaN prepared by ion implantation of epitaxial thin films. Based on a detailed analysis of the magnetometry data, we demonstrate that the magnetic interactions between Cr moments in GaN are antiferromagnetic (AFM). Increasing the Cr fractional concentration up to 0.35, we observe that strong nearest cation neighbor AFM coupling leads to a decrease of the effective moment per Cr atom. The uncompensated Cr moments exhibit paramagnetic behavior and we discuss to what extent the effects of an anisotropic crystal field and AFM interactions can be inferred from the magnetization data. We discuss the observed changes in magnetic and structural properties induced by thermal annealing in terms of defect annealing and Cr agglomeration.

Journal of Physics-Condensed Matter **23**, 346004 (2011)

I. INTRODUCTION

Over the past decade, the magnetism of wide-gap semiconductors doped with 3*d* transition metals, or dilute magnetic semiconductors (DMS), has become one of the most controversial topics in condensed matter physics. Despite the remarkable volume of experimental and theoretical research and significant developments in synthesis and characterization methods, the origin of high-temperature ferromagnetism in wide-gap DMS remains far from consensual.[1]

Soon after the first report on Co-doped TiO_2,[2] ferromagnetism at and above room temperature was reported in many other wide-gap DMS materials (cf. e.g. the reviews Refs. 3–6). Research in the ensuing years followed two main directions, the search (i) for new DMS materials displaying signatures of high-temperature ferromagnetic order (e.g. Gd-doped GaN,[7] C-doped ZnO,[8] and undoped HfO_2[9]) and (ii) for the origin and control of ferromagnetism in those systems regarded as most attractive (e.g. Co- and Mn-doped ZnO[10] and Mn-doped GaN[11]). However, as the understanding of some of the most intensively studied materials deepened, issues of irreproducibility and instability became common features of these materials. A number of non-intrinsic sources of ferromagnetism were identified and became well documented: magnetic contaminations,[12–15] measurement artifacts,[13,14] spinodal decomposition (e.g. in Co-doped ZnO[16]) and secondary phase formation (e.g. in ZnO doped with Fe, Co and Ni[17–19]). On the other hand, studies on well characterized DMS materials (single-phase and homogeneous) found only paramagnetism (e.g. in Mn-doped GaN[20] and Co-doped ZnO[21]), antiferromagnetic interactions (e.g. in Mn-doped GaN[22] and in Co-doped ZnO[23–26]), or at best, ferromagnetic order with very low Curie temperature (e.g. in Mn-doped GaN[11]). Consequently, the current view on wide-gap DMS is moving towards the belief that the often observed high-temperature ferromagnetism may be non-intrinsic.[1] Key to solving this controversy is a systematic and detailed mapping of the type and strength of the magnetic interactions in the most representative combinations of magnetic dopants and wide-gap semiconductor hosts. In this sense, Cr-doped GaN is an interesting case. Far from being one of the most intensively studied cases, it has accumulated a significant amount of reports of high-temperature ferromagnetism.[27–33] However, while focusing on the *intrinsic* origin of the observed ferromagnetic signatures by demonstrating the absence of secondary-phase formation, these studies lack a deeper analysis of the magnetic behavior itself.

Transition metals can be incorporated in GaN during growth[27–31] or by ion implantation.[32,33] The advantage of ion implantation with respect to the production of uniform and single-crystalline DMS nanolayers is that it is less likely to suffer from the formation of secondary phases. Ion bombardment inevitably leads to lattice disorder, a major concern when electrical and optical dopants are introduced by ion implantation.[34] For magnetic doping, however, lattice disorder is believed to be crucial in establishing the ferromagnetic order, either in the form of point[35] or extended[36] defects. Depending on the implantation conditions, different types of defects can be produced in ion-implanted GaN. At the low fluence end, isolated[37] or clustered[38] point defects are typically observed. As the fluence increases, bands of large planar defects are formed parallel to the basal plane of GaN.[38] Ion-implanted DMS materials are thus interesting systems in which to study the interplay between magnetic dopants and lattice defects.

The most straightforward and reproducible parameter to control, in order to tune the amount and type of ion-beam damage, is temperature, either during implantation or during subsequent thermal annealing.[39] Typically, the accumulation of stable defects in irradiated semiconductors, which can eventually result in amorphization, can be reduced by increasing the implantation temperature. In GaN, the accumulated damage decreases rather sharply as the irradiation temperature is increased up to 300°C and more slowly above that.[40] On the other hand, high-fluence ion implantation at elevated temperatures (550°C) has been reported to induce dramatic erosion of GaN.[41] Implantation temperatures around 300°C can thus be expected to yield a good compromise between avoiding amorphization and minimizing surface erosion of GaN. Further control over beam-induced damage is typically realized by thermal treatment. Annealing of implantation disorder in GaN is, however, a rather complex problem. The rule of thumb is that temperatures of around two thirds of the melting point (in units of K) are required to remove extended defects in compound semiconductors. For GaN, this corresponds to about 1600°C, based on its calculated melting point.[42] However, annealing of GaN at such high temperatures is counteracted by material decomposition involving loss of nitrogen from the GaN surface (e.g Ref. 43). In addition, high temperature annealing may result in undesired segregation of Cr or CrN secondary phases.[44] Therefore, when studying the magnetism of ion-implanted GaN DMS materials and its dependence on defect concentration, optimum annealing conditions are those providing a significant degree of damage recovery while avoiding surface decomposition and phase segregation.

In this paper, we analyze the magnetic and structural properties of Cr-doped GaN thin films, produced by implanting Cr^+ ions in epitaxial GaN thin films. Covering a wide range of Cr fractional concentrations (0.005 – 0.35), from the very dilute regime to well above the site percolation threshold (0.20), and focusing on an in-depth analysis of the magnetometry data, we aim at identifying the type of magnetic interactions between Cr moments in GaN. Combined with the structural characterization of as-implanted and annealed samples by means of X-ray diffraction (XRD) and Rutherford backscattering and channeling spectrometry (RBS/C), we investigate how the magnetic behavior is influenced by thermal annealing.

II. EXPERIMENTAL RESULTS

A. Sample preparation and structural characterization

High-quality epitaxial GaN (0001) thin films were grown by metalorganic vapor phase epitaxy (MOVPE). Two wafers were grown using different substrates: a 2 μm thick GaN (0001) layer on an Al_2O_3 (0001) substrate and an 800 nm GaN (0001) layer on a Si (111) substrate using a AlN/AlGaN intermediate layer. Pieces from each of the wafers were implanted at 300°C with Cr^+ ions with an energy of 80 keV to fluences ranging from 1×10^{15} to 7×10^{16} at. cm^{-2}. The implantations were performed under an angle of 7° with respect to the surface normal in order to minimize ion channeling.[45] Using the TRIM code[46] to simulate the Gaussian-like ion distribution, we estimated a projected range of $R_P = 38$ nm, a longitudinal straggling of 17 nm and peak concentrations (x_p) ranging from 0.005 to 0.35. Table I lists the implanted samples and the corresponding fluences and x_p. All samples were studied in the as-implanted state and after thermal annealing at 800°C in N_2 flow for 2.5 hours, using a GaN proximity cap to minimize surface degradation. In order to avoid sample contamination with ferromagnetic impurities,[15] the implantations were carried out using a Mo sample-holder and the samples were placed in a ceramic boat during annealing. Each entry in Table I corresponds to two samples, one for the structural characterization and the other for magnetometry measurements. The samples reserved for the magnetic characterization were handled with non-metallic tweezers in order to avoid magnetic contamination.[15]

Defect formation and recovery were studied using Rutherford backscattering and channeling spectrometry (RBS/C), with a 1.57 MeV He^+ beam. Figure 1 shows examples of spectra obtained in random and channeled ge-

name	substrate	fluence [at. cm^{-2}]	peak concentration (x_p)
S1	Si	1×10^{15}	0.005
A1	Al_2O_3	1×10^{15}	0.005
S4	Si	4×10^{15}	0.02
A4	Al_2O_3	4×10^{15}	0.02
S10	Si	1×10^{16}	0.05
A10	Al_2O_3	1×10^{16}	0.05
S20	Si	2×10^{16}	0.10
A20	Al_2O_3	2×10^{16}	0.10
S40	Si	4×10^{16}	0.20
A40	Al_2O_3	4×10^{16}	0.20
S70	Si	7×10^{16}	0.35
A70	Al_2O_3	7×10^{16}	0.35

TABLE I: Sample list. Naming is according to substrate, S for silicon and A for Al_2O_3, and implanted fluence, in units of 1×10^{15} at. cm^{-2}. All implantations were performed at 300°C.

ometries (a) and summarizes the results in terms of damage accumulation and recovery both in the near-surface (first few monolayers) and bulk (end of range) regions (b). It is clear that implanting at 300°C successfully suppresses amorphization, as both near-surface and bulk disorder exhibit saturation at levels which are considerably below the random level. In addition, there is no sign of dramatic surface erosion. This can be inferred from the position of the bulk damage peak relative to the surface. If the film erosion had reached depths of the order of the ion range, the bulk damage peak would have shifted towards the surface as has been reported in Ref. 47. Furthermore, within the experimental uncertainty (< 30 nm) the film thickness does not decrease after implantation, even to the maximum fluence. Showing that film erosion was minimal has two important practical consequences. Not only does it show that the nominal Cr content was conserved, it also validates the simulated Cr depth profiles and peak concentrations, calculated assuming a constant film thickness. Regarding the choice of annealing treatment, Fig. 1 also shows that while providing a significant reduction of the lattice disorder in the Cr-doped region [depicted by $\downarrow$ in Fig. 1 (b)], it kept the near-surface damage peak below random levels.

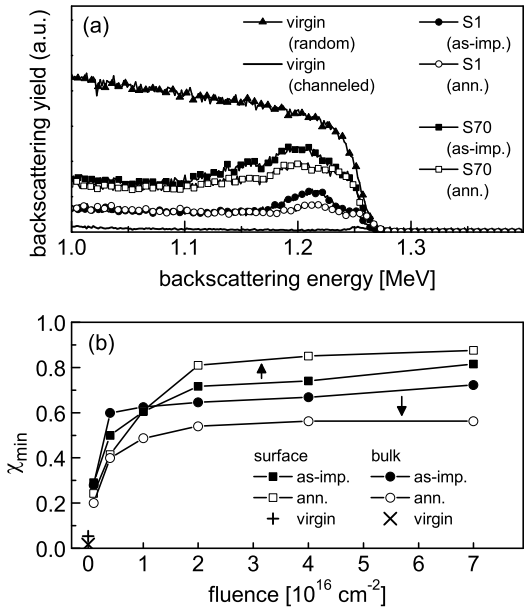

FIG. 1: (a) Selected RBS/C spectra: random and channeled spectra of a virgin (unimplanted) GaN sample and channeled spectra of the samples with the lowest (S1, 1×10^{15} cm^{-2}) and the highest (S70, 7×10^{16} cm^{-2}) implanted fluence, before and after annealing at 800° C. (b) Minimum yield ($\chi_{\min}$) determined from both the near-surface and bulk peaks of disorder, before and after annealing, as a function of implanted fluence.

Possible formation of Cr or CrN precipitates was investigated using conventional X-ray diffraction (XRD). Other than those associated with the GaN layers and the substrate, no additional peaks could be resolved, either before or after annealing (data not shown). Only typical signs of reduced crystalline quality due to implantation were observed. Although thermal annealing of similar wide-gap semiconductors implanted with transition metals can result in the formation of small precipitates which are difficult to detect with conventional XRD (e.g. Co-, Ni- and Fe-implanted ZnO in Refs. 17–19), Cr was found to be very stable in substitutional sites in GaN, at least up to annealing temperatures of 825°C.[31] The presence of Cr or CrN precipitates in our samples is thus highly unlikely, both before and after annealing (800°C). However, although very unlikely in the as-implanted state, the formation of (substitutional) Cr-rich regions during annealing can not be excluded. Such substitutional clusters would be coherent with

the GaN matrix and thus difficult to detect by diffraction techniques. This chemical phase separation by aggregation of the transition-metal dopants, known as spinodal decomposition in DMS literature, has been observed in a number of DMS materials, including Cr[44] and Fe[48] doped GaN.

From the structural characterization described in this section we can conclude that, in terms of implantation conditions, we have successfully avoided both amorphization and significant surface erosion. Regarding the annealing treatment, while inducing a significant degree of lattice recovery, we have avoided the formation of secondary phases, at least within the sensitivity of conventional XRD. However, the formation of nanoprecipitates and substitutional Cr clusters can not be excluded.

B. Magnetic properties

The magnetic characterization was performed using a superconducting quantum interference device (SQUID) magnetometer (*Quantum Design* MPMS XL-5) following strict procedures in order to avoid measurement artifacts and external magnetic contributions. These procedures were developed based on statistically relevant tests, which allowed us to determine the practical limits of SQUID magnetometry for the detection of ferromagnetism under various sample preparation, processing and handling conditions.[15] Unless otherwise specified, the measurements shown and discussed below were performed with the field perpendicular to the GaN *c*-axis, i.e., parallel to the film plane. The field-dependent measurements were performed with decreasing field.

1. Absence of ferromagnetic order

A small hysteresis, with a saturation moment always below 1×10^{-6} emu, was observed in some of the samples, up to room temperature. No correlation was found with respect to the fluence or annealing conditions. Since the same residual ferromagnetic-like behavior was observed in unimplanted control samples, we attribute it to small ferromagnetic contaminations.[15] As such, we can conclude that:

Finding I. None of the samples, regardless of substrate, fluence or annealing treatment, showed ferromagnetic behavior above the range dominated by ferromagnetic contaminations (i.e. with saturation moments $> 1 \times 10^{-6}$ emu), from 300 K down to 2 K.

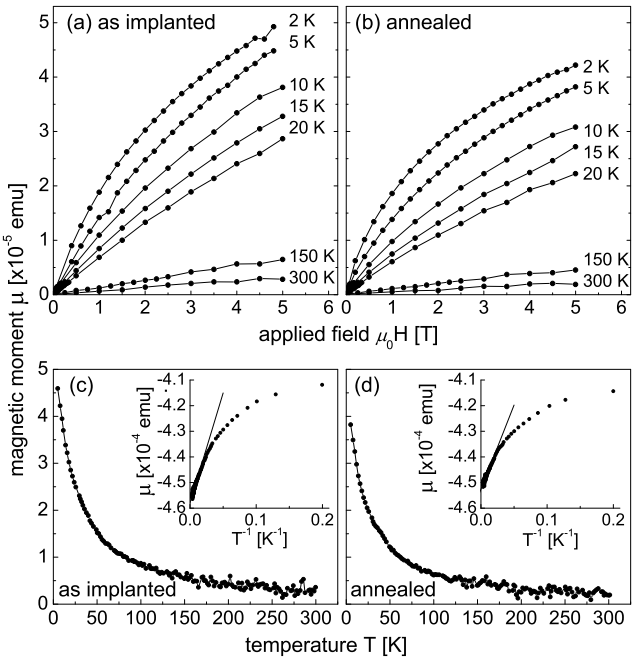

FIG. 2: Representative set of SQUID measurements, for sample A70 ($x_p = 0.35$) before [(a) and (c)] and after [(b) and (d)] annealing: *M-H* data [(a) and (b)] at 2, 5, 10, 15, 20, 150 and 300 K and *M-T* data [(c) and (d)] for an applied field of 5 T, all corrected for the diamagnetic background. Insets: Uncorrected *M-T* data of (c) and (d) plotted versus T^{-1} with a linear fit between 100 and 300 K.

Since intrinsic irreversibility was not observed in any of the samples, only one quarter of the *M-H* loops (magnetization as a function of applied field) is shown in the remainder of this article, i.e., only the data corresponding to positive and decreasing field.

As a representative example, a typical set of measurements is shown in Fig. 2 for sample A70 ($x_p = 0.35$) before [(a) and (c)] and after [(b) and (d)] annealing. The magnetic moment (μ) was measured as a function of applied field (*M-H*) up to 5 T at temperatures between 2 K and 300 K [(a) and (b)] and as a function of temperature (*M-T*) between 5 K and 300 K with an applied field of 5 T [(c) and (d)]. All the data in Fig. 2 are corrected for the diamagnetic component (dominated by the substrate) and exhibit typical paramagnetic (PM) behavior. This diamagnetic background was estimated from a linear fit to $\mu(T^{-1})$ above 100 K [insets of (c) and (d)], assuming a Curie behavior of the paramagnetic component and a

temperature independent diamagnetic term:

$$\chi = \frac{\mu}{H} = \chi_C + \chi_{DM} = \frac{C}{T} + \chi_{DM}, \tag{1}$$

where χ is the total magnetic susceptibility, χ_C the Curie term, χ_{DM} the diamagnetic term, C the Curie constant and T the temperature. The diamagnetic susceptibility was further corrected by subtracting the very small contribution of ferromagnetic contaminations (when present), estimated from the *M-H* data at 300 K between 2 T and 5 T (in saturation). The result was checked for consistency by comparing it with the diamagnetic susceptibility obtained from the linear fit to the *M-H* data at 150 K and 300 K, taking into account the paramagnetic component (linear at $T > 100$ K to a good approximation). The Si substrates, both before and after deposition of the GaN thin films, showed a small temperature dependence of χ_{DM}, most likely due to Van Vleck paramagnetism, which has also been observed in other semiconductor substrates, e.g. GaAs.[49] The χ_{DM} value used to correct the *M-H* data of the samples grown on Si was itself corrected for this small temperature dependence, based on measurements of unimplanted samples (as both the diamagnetic and the Van Vleck paramagnetic susceptibilities are extensive properties, i.e. scale with the substrate's mass). We note that, in general, the paramagnetic contribution does not necessarily follow the Curie term in Eq. (1), but rather a Curie-Weiss law:

$$\chi_{CW} = \frac{C}{T - \Theta}, \tag{2}$$

where Θ is the Weiss constant which accounts for magnetic interactions. Nonetheless, Eq. (1) holds for $|\Theta/T| \ll 1$, which we show below to be the case in our data. From this point on, all the data that are shown or referred to were corrected for the diamagnetic substrate background using this method. This was found to be more accurate than, for example, subtracting *M-H* data measured prior to implantation. Small differences in sample mounting can result in a change of a few percent of the total measured moment. Since the diamagnetic signal largely dominates, the curves resulting from this subtraction would be affected by an erroneous linear component. At least qualitatively, all the samples show a behavior similar to that of sample S70 (Fig. 2). We can thus conclude that:

Finding II. All samples exhibit paramagnetic behavior.

Before discussing the details of this paramagnetism in terms of field and temperature dependence, we will describe how the effective moment per Cr atom evolves with increasing Cr concentration.

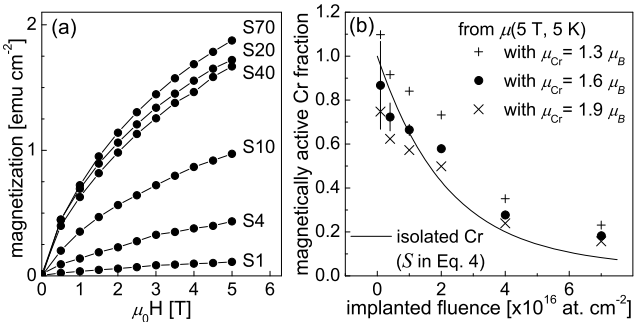

FIG. 3: (a) *M-H* at 5 K, in units of emu per unit of the film surface area, after annealing, for the films grown on Si. Note that full saturation is not reached. (b) Fraction of magnetically active Cr atoms, assuming different values of moment per atom ($\mu_{\rm Cr}$) at 5 K and 5 T and fraction of isolated Cr atoms estimated using Eq. (4) (line), as a function of implanted fluence. The best fit is obtained for $\mu_{\rm Cr} = 1.6$ μ_B (•); the data is also shown for $\mu_{\rm Cr} = 1.3$ μ_B (+) and $\mu_{\rm Cr} = 1.6$ μ_B (×) for comparison. Note that $\mu_{\rm Cr} = 1.6$ μ_B is the *non-saturated* moment per Cr atom (at 5 K and 5 T).

2. Cr-moment quenching with increasing Cr concentration

Figure 3 (a) shows the magnetization at 5 K, for the implanted and annealed GaN samples grown on Si (the results are equivalent for the Al_2O_3 series). The magnetization does not increase linearly with Cr concentration; there is a clear saturation for fluences above 2×10^{16} cm^{-2}, which, based on the RBS/C data, can not be ascribed to a saturation of the Cr content due to film erosion. We attribute this effect to the antiparallel alignment of the magnetic moments of Cr atoms sitting in nearest cation neighbor sites, due to strong antiferromagnetic (AFM) interactions. A similar moment-quenching effect has been observed in other DMS systems, e.g. Co-doped ZnO.[23,24] To model this behavior, we assume that all Cr impurities randomly occupy Ga sites[31,50,51] and that only isolated Cr atoms, i.e., without Cr nearest cation neighbors in the Ga sublattice, effectively contribute to the magnetization. The fraction of isolated Cr atoms in the GaN hexagonal lattice (S') can be estimated using Behringer's equation

$$S' = (1 - x)^{12}, \tag{3}$$

where x is the fractional concentration of Cr atoms.[52] Since in implanted samples x is a function of depth l, one must integrate S' over the film

thickness as

$$S = \int_0^\infty p(l)S'(l)\,dl, \tag{4}$$

with

$$p(l) = \frac{x(l)}{\int_0^\infty x(l)\,dl}, \tag{5}$$

where $x(l)$ is the concentration profile which we have simulated using TRIM. Assuming that each of the magnetically active Cr atoms contributes with a moment μ_{Cr} for a given field and temperature, one can extract the corresponding fraction from the experimental data and compare it to that of isolated Cr estimated using Eq. (4). Figure 3 (b) shows the fraction of magnetically active Cr atoms, using $\mu_{Cr} = 1.6\ \mu_B$ (at 5 K and 5 T) which yields the best fit to Eq. (4). The agreement is fairly good, particularly considering that μ_{Cr} is the only free parameter. Note that 1.6 μ_B is the *non-saturated* moment per Cr atom, which can explain why it is smaller than the expected 3 μ_B for the high-spin Cr^{3+} ($3d^3$) state, predicted by Hunds rules and by *ab initio* calculations.[53] At high concentration, the model somewhat underestimates the active Cr fraction. This is likely to result from considering the simplest case for which only the isolated Cr atoms contribute to the magnetization. For low concentrations, the majority of the non-isolated Cr atoms are in the form of pairs (dimers). Such a dimer configuration may indeed produce an almost perfect antiparallel alignment of the two magnetic moments. However, for higher concentrations, larger complexes of three and more atoms are formed. For these larger substitutional clusters, particularly those containing an odd number of Co atoms, the quenching of the Cr moment may be less efficient due to frustration effects and the presence of uncompensated moments, which may thus contribute to the measured magnetization. This discussion can be concluded as:

Finding III. Strong antiferromagnetic interactions between the Cr atoms in nearest cation neighbor complexes impose the antiparallel alignment of the corresponding magnetic moments. This results in a Cr-moment quenching effect, i.e. a decrease of the effective moment per Cr atom with increasing Cr concentration.

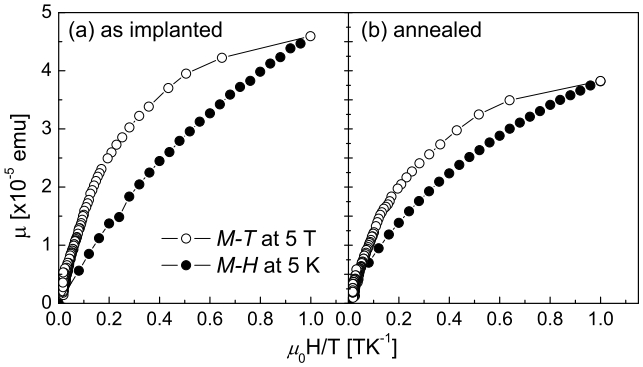

FIG. 4: Magnetic moment plotted versus H/T for sample A70 ($x_p = 0.35$) before (a) and after (b) annealing, using M-T data between 5 K and 300 K with an applied field of 5 T (○) and M-H data at 5 K up to 5 T (●). As expected, the data do not overlap, i.e. the magnetization does not follow a Brillouin behavior.

3. Paramagnetism

While I, II and III constitute the major findings of this work, it is worth discussing in more detail the paramagnetism of the uncompensated (or not fully compensated) Cr moments in GaN and compare it to the intensively studied and thus better understood wide-gap DMS materials Mn-doped GaN and Co-doped ZnO.

The magnetization of ideal non-interacting magnetic moments with constant total angular momentum quantum number J in a magnetic field H follows the Brillouin function $B_J(H,T)$. This is obviously not the case for Cr moments in GaN, which are subject to (1) the anisotropic GaN crystal field of the host and, as we have shown above, (2) magnetic interactions. The non-Brillouin behavior of our samples is easily confirmed by plotting the M-H and M-T data together as a function of H/T (Fig. 4). As expected, contrary to what would happen for an ideal Brillouin paramagnet [$\mu(H,T,J) \propto B_J(H/T)$], the curves do not overlap. In the following, we discuss to what extent we find evidence of both effects, (1) anisotropic crystal field and (2) magnetic interactions, in Cr-implanted GaN.

The most easily observable effect of an anisotropic crystal field [effect (1)] on a paramagnetic $3d$ moment is the resulting anisotropic magnetization. The trigonal crystal field in the wurtzite structure induces a magnetic anisotropy via the spin-orbit interaction, which can be described by an effective spin-Hamiltonian with a zero-field splitting constant D and an

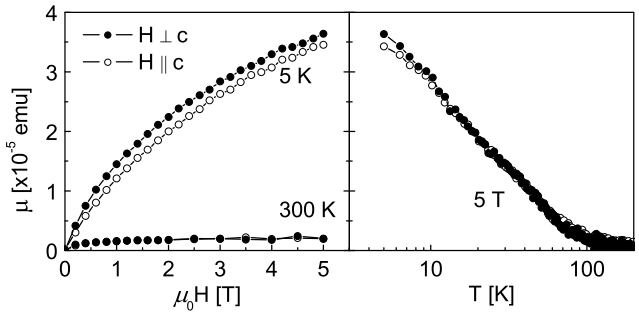

FIG. 5: Comparison of the measured magnetization of sample S70 ($x_p = 0.35$), after annealing, for magnetic field applied perpendicular (•) and parallel (◦) to the GaN c-axis: (a) M-H data at 5 K; (b) M-T data with an applied field of 5 T

anisotropic effective g-factor ($g_\parallel$ for parallel and $g_\perp$ for perpendicular magnetic field with respect to the c-axis). A strongly anisotropic magnetization was observed, for example, for Mn^{3+} ions in GaN[20] and Co^{2+} ions in ZnO,[21] and successfully described by well-established values of the phenomenological parameters D, $g_\parallel$ and $g_\perp$ (Ref. 21) or more detailed Hamiltonians (Ref. 20). Figure 5 shows M-H and M-T data of sample A70 ($x_p = 0.35$) for field applied parallel and perpendicular to the sample plane, i.e. perpendicular and parallel to the GaN c-axis, respectively. Although some degree of anisotropy can be resolved, the effect is much weaker than that observed in Mn-doped GaN[20] and Co-doped ZnO.[21] Because the parameters D, $g_\parallel$ and $g_\perp$ have never been determined for Cr impurities in GaN or similar materials, one can not predict the magnetic anisotropy for Cr-doped GaN under these experimental conditions. Nonetheless, the fact that the effect is so small in our samples can be explained, at least partially, by the significant disorder induced by implantation (section II A), which disturbs the crystal periodicity and consequently the crystal field anisotropy.

In general, the presence of magnetic interactions [effect (2)] can be inferred from magnetization data as a perturbation to the paramagnetic behavior above the associated ordering temperature. In principle, this can be modeled using an effective temperature $(T - \Theta)$ where Θ accounts for the magnetic interactions,[54] which has been done, for example, for Mn-doped GaN[22] and Co-doped ZnO.[24–26] Applying a similar approach to our data, Fig. 6 shows the $\mu^{-1}(T)$ data of sample A70 ($x_p = 0.35$) before and after annealing and a fit to the Curie-Weiss law Eq. (2), which corresponds to the Curie law with an effective temperature $T - \Theta$. The data were fitted

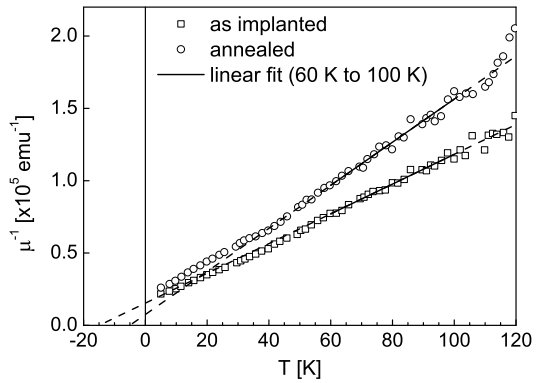

FIG. 6: $\mu^{-1}(T)$ data of sample A70 ($x_p = 0.35$) before and after annealing and a Curie-Weiss fit after Eq. (2) between 60 K and 100 K (line). The results of the fit are discussed in the text in terms of antiferromagnetic interactions and crystal field effects.

only between 60 K and 100 K to avoid a possible contribution from frozen O_2 between 30 K and 60 K and the large data dispersion above 100 K. The fit yields a negative Θ, $-15(3)$ K and $-5(3)$ K before and after annealing, respectively, which can in principle be interpreted as a signature of antiferromagnetic interactions. We note, however, that this type of analysis should be applied very carefully. In Ref. 21 it is shown that, while the paramagnetism of Co-doped ZnO is correctly modeled using an adequate effective spin Hamiltonian *without* considering magnetic interactions, attempting to fit the same data using inadequate models such as the Brillouin function or the Curie law would require the use of an effective temperature $T - \Theta$ ($T + T_0$ in Ref. 21), which could be misinterpreted as an effect of antiferromagnetic interactions. Nevertheless, in our case, because part of the Cr atoms in nearest-cation-neighbor complexes are not fully compensated, i.e. have a finite contribution to the magnetization (section II B 2), it is reasonable to conclude that Θ contains at least a contribution from the nearest-cation-neighbor AFM interactions.

Finally we will briefly discuss the effect of thermal annealing on the magnetic behavior. We have shown in Fig. 6 that $|\Theta|$ decreases from $-15(3)$ K to $-5(3)$ K upon thermal annealing, indicating a change in crystal field (1) or a weakening of the AFM interactions (2) or a combination of both. The changes in magnetic behavior induced by thermal annealing are even more evident in the *M-H* data. This is ilustrated in Fig. 7 where we show the 5 K, 20 K and 300 K *M-H* data for samples S20 ($x_p = 0.10$) and A70 (x_p

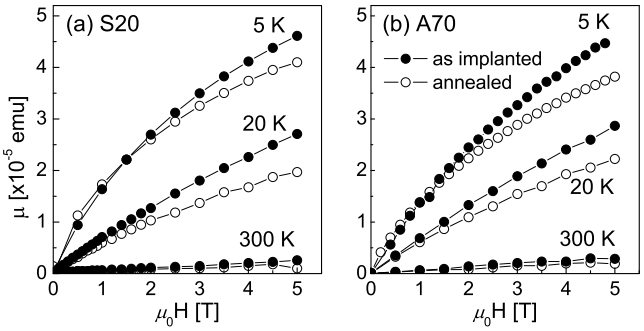

FIG. 7: *M-H* data at 5 K, 20 K and 300 K for samples S20 ($x_p = 0.10$) (a) and A70 ($x_p = 0.35$) (b), before (•) and after (○) annealing.

= 0.35): consistently throughout the entire concentration range, thermal annealing reduces the magnetization, except for very low temperatures and fields where it does the opposite. Structurally, the annealing can have two effects which may explain these changes in magnetic behavior:

(i) Annealing of lattice defects as demonstrated by RBS/C, above. Lattice defects in the vicinity of Cr atoms modify the crystal field (1) and may even mediate magnetic interactions between distant Cr moments (2). Some point defects may even contribute to the magnetization directly. For example, it has been predicted that Ga vacancies induce non-vanishing magnetic moments in the neighboring N atoms[55] and that N vacancies enhance the magnetic moment of isolated Cr impurities.[53,56]

(ii) Aggregation of Cr atoms in substitutional clusters or in small precipitates of Cr or CrN which may be undetectable by XRD. By modifying the dopant spatial distribution, i.e. the relative distance between Cr atoms and the local arrangement of their neighbors, Cr aggregation would also affect the crystal fields (1) and the magnetic interactions (2).

In short, thermal annealing can induce two distinct structural modifications [(i) and (ii)] each of which can modify each of the two parameters which control the magnetic behavior [(1) and (2)]. Such an intricate interplay complicates a more quantitative approach to this discussion, which we thus simply conclude as:

Finding IV. Uncompensated Cr atoms behave as paramagnetic moments perturbed by antiferromagnetic interactions in an anisotropic crystal field. Although minimally, thermal annealing affects this paramagnetism, possibly due to an interplay between defect annealing and Cr aggregation.

III. DISCUSSION

The main finding of this study is that the magnetic interactions between Cr moments in GaN are not ferromagnetic but antiferromagnetic. This has been inferred from the decrease in effective moment per Cr atom with increasing Cr concentration, as well as a Curie-Weiss behavior consistent with antiferromagnetic interactions. This observation of predominantly antiferromagnetic interactions in Cr-doped GaN is in contrast with previous experimental reports of ferromagnetic order, e.g. Refs. 27–31 for Cr incorporated during growth and Refs. 32 and 33 for implanted Cr. This is not unexpected, however. The literature of the last ten years on more extensively studied DMS materials, e.g. Mn-doped GaN, experienced a similar evolution. Despite the many theoretical predictions and experimental reports of high-temperature ferromagnetism, recent studies did not show any indication of high-temperature ferromagnetic order in single-phase Mn-doped GaN.[11,20,22] In fact, it is worthwhile discussing in more detail these two cases, Cr- and Mn-doped GaN, together. Two types of magnetic behavior have been comprehensively demonstrated in single-phase Mn-doped GaN: short-ranged antiferromagnetic interactions between Mn^{2+} ($3d^5$) moments[22] and ferromagnetic order of Mn^{3+} ($3d^4$) moments with a Curie temperature below 10 K.[11] The latter only occurs under stringent growth conditions to ensure epitaxial growth and, most importantly, to minimize the formation of compensating defects such as N vacancy donors.[11] However, because the Mn 3+/2+ acceptor level is deep in the GaN bandgap, the associated holes are strongly localized. Since the coupling between distant moments via *p-d* Zener exchange[57] requires itinerant holes, the observed Curie temperatures are very low (< 10 K). More commonly, such stringent growth conditions are not satisfied and compensating donor defects are formed. The Mn impurities are thus incorporated as compensated Mn^{2+} and the *p-d* Zener model does not apply. Consequently, only nearest cation neighbor AFM interactions are observed,[22] which are likely to result from indirect superexchange between the Mn $3d$ moments mediated by the N $2p$ band. Indeed, significant hybridization of the Mn

$3d$ and N $2p$ states has been observed.[58] This understanding of the magnetic interactions between Mn impurities in GaN in different charge states provides a good framework to interpret our results in the Cr-doping case. Chromium is incorporated in GaN as Cr^{3+} ($3d^3$),[50,51] with only a donor level (3+/4+) in the bandgap.[59] In the absence of p-holes to mediate p-d Zener exchange, our results show that the magnetic behavior of Cr^{3+} ($3d^3$) is very similar to that of Mn^{2+} ($3d^5$): short-ranged antiferromagnetic interactions, which as for Mn^{2+}, are likely to result from indirect superexchange mediated by the N $2p$ band. Indeed, the necessary hybridization of the Cr $3d$ and N $2p$ states has also been observed.[50,51] We must note, however, that we can not exclude other possible origins of antiferromagnetic behavior, such as the formation of Cr or CrN secondary phases, which although not detected by XRD, can not be fully excluded. Both Cr and CrN are antiferromagnetic, with Néel (ordering) temperatures of 308 K[60] and 270 K,[61] respectivelly (in bulk).

As an alternative to the p-d Zener models discussed in the previous paragraph, high-temperature ferromagnetism in wide-gap DMS materials has also been predicted on the basis of bound magnetic polaron (BMP) models.[35] Here, the magnetic moments interact via electrons associated with a defect impurity band. Since these defect electrons occupy large orbits, each defect can interact with several dopant moments and form a magnetic polaron. Ferromagnetism results from the percolation of such polarons. However, the exchange energy density necessary to produce high-temperature ferromagnetism at a few % doping corresponds to a magnetic exchange much stronger than that observed in the strongest of the known ferromagnetic materials.[36] One can thus expect that the critical temperatures associated with this type of magnetic order are well below room temperature.

Our results support the view that the source of high-temperature ferromagnetism often observed in transition-metal doped GaN may be non-intrinsic, i.e., associated with ferromagnetic precipitates or contaminations. This is in line with a very recent overview of the last ten years of DMS research, which concluded that little proof has been found of high temperature ferromagnetism in wide-gap DMS materials.[1]

IV. CONCLUSIONS

In summary, we have experimentally demonstrated the absence of ferromagnetic order in Cr-implanted GaN, from 300 K down to 2 K, for Cr

fractional concentrations between 0.005 and 0.35. We have shown that the magnetic interactions between Cr moments in GaN are, in fact, antiferromagnetic. Strong antiferromagnetic interactions between the Cr atoms in nearest cation neighbor complexes result in Cr-moment quenching (compensation), i.e. a decrease of the effective moment per Cr atom, with increasing concentration. Uncompensated Cr atoms behave as paramagnetic moments perturbed by antiferromagnetic interactions in an anisotropic crystal field. Although minimally, thermal annealing affects the magnetic behavior, possibly due to an interplay between defect annealing and Cr aggregation.

These results suggest that neither types of models of ferromagnetism proposed for dilute magnetic semiconductors, i.e. *p-d* Zener exchange or bound magnetic polarons (BMP), operate in Cr-implanted GaN. Together with recent reports on well-characterized Mn-doped GaN, our study supports the view that the high-temperature ferromagnetism observed in transition-metal doped GaN may be non-intrinsic.

Acknowledgments

This work was supported by the Research Foundation - Flanders (FWO), the SPIRIT (Support of Public and Industrial Research using Ion Beam Technology) project (contract no. 227012), KULeuven projects GOA/2009/006 and INPAC EF/05/005 and the IUAP P6/42 program. L. M. C. Pereira acknowledges the scholarship SFRH/BD/35761/2007 granted by the Portuguese Foundation for Science and Technology (FCT). T. Som acknowledges the FWO for a fellowship.

[1] T. Dietl, Nat. Mater. **9**, 965 (2010).
[2] Y. Matsumoto, M. Murakami, T. Shono, T. Hasegawa, T. Fukumura, M. Kawasaki, P. Ahmet, T. Chikyow, S. Koshihara, and H. Koinuma, Science **291**, 854 (2001).
[3] S. J. Pearton, C. R. Abernathy, D. P. Norton, A. F. Hebard, Y. D. Park, L. A. Boatner, and J. D. Budai, Mater. Sci. Eng. R-Rep. **40**, 137 (2003).
[4] W. Prellier, A. Fouchet, and B. Mercey, J. Phys.-Condens. Matter **15**, R1583 (2003).
[5] S. J. Pearton, W. H. Heo, M. Ivill, D. P. Norton, and T. Steiner, Semicond. Sci. Technol. **19**, R59 (2004).
[6] C. Liu, F. Yun, and H. Morkoc, J. Mater. Sci.-Mater. Electron. **16**, 555 (2005).

[7] S. Dhar, O. Brandt, M. Ramsteiner, V. F. Sapega, and K. H. Ploog, Phys. Rev. Lett. **94**, 037205 (2005).
[8] H. Pan, J. B. Yi, L. Shen, R. Q. Wu, J. H. Yang, J. Y. Lin, Y. P. Feng, J. Ding, L. H. Van, and J. H. Yin, Phys. Rev. Lett. **99**, 127201 (2007).
[9] M. Venkatesan, C. B. Fitzgerald, and J. M. D. Coey, Nature **430**, 630 (2004).
[10] K. R. Kittilstved, W. K. Liu, and D. R. Gamelin, Nat. Mater. **5**, 291 (2006).
[11] E. Sarigiannidou, F. Wilhelm, E. Monroy, R. M. Galera, E. Bellet-Amalric, A. Rogalev, J. Goulon, J. Cibert, and H. Mariette, Phys. Rev. B **74**, 041306 (2006).
[12] D. W. Abraham, M. M. Frank, and S. Guha, Appl. Phys. Lett. **87**, 252502 (2005).
[13] A. Ney, T. Kammermeier, V. Ney, K. Ollefs, and S. Ye, J. Magn. Magn. Mater. **320**, 3341 (2008).
[14] M. A. Garcia, E. Fernandez Pinel, J. de la Venta, A. Quesada, V. Bouzas, J. F. Fernandez, J. J. Romero, M. S. Martin Gonzalez, and J. L. Costa-Kramer, J. Appl. Phys. **105**, 013925 (2009).
[15] L. M. C. Pereira, J. P. Araujo, M. J. Van Bael, K. Temst, and A. Vantomme, J. Phys. D: Appl. Phys. **44**, 215001 (2011).
[16] Z. Sun, W. Yan, G. Zhang, H. Oyanagi, Z. Wu, Q. Liu, W. Wu, T. Shi, Z. Pan, P. Xu, et al., Phys. Rev. B **77**, 245208 (2008).
[17] S. Zhou, K. Potzger, G. Talut, H. Reuther, J. von Borany, R. Groetzschel, W. Skorupa, M. Helm, J. Fassbender, N. Volbers, et al., J. Appl. Phys. **103**, 023902 (2008).
[18] S. Zhou, K. Potzger, J. von Borany, R. Grotzschel, W. Skorupa, M. Helm, and J. Fassbender, Phys. Rev. B **77**, 035209 (2008).
[19] S. Zhou, K. Potzger, K. Kuepper, J. Grenzer, M. Helm, J. Fassbender, E. Arenholz, and J. D. Denlinger, J. Appl. Phys. **103**, 043901 (2008).
[20] W. Stefanowicz, D. Sztenkiel, B. Faina, A. Grois, M. Rovezzi, T. Devillers, F. d'Acapito, A. Navarro-Quezada, T. Li, R. Jakiela, et al., Phys. Rev. B **81**, 235210 (2010).
[21] A. Ney, T. Kammermeier, K. Ollefs, S. Ye, V. Ney, T. C. Kaspar, S. A. Chambers, F. Wilhelm, and A. Rogalev, Phys. Rev. B **81**, 054420 (2010).
[22] S. Granville, B. J. Ruck, F. Budde, H. J. Trodahl, and G. V. M. Williams, Phys. Rev. B **81**, 184425 (2010).
[23] A. Ney, K. Ollefs, S. Ye, T. Kammermeier, V. Ney, T. C. Kaspar, S. A. Chambers, F. Wilhelm, and A. Rogalev, Phys. Rev. Lett. **100**, 157201 (2008).
[24] P. Sati, C. Deparis, C. Morhain, S. Schafer, and A. Stepanov, Phys. Rev. Lett. **98**, 137204 (2007).
[25] Q. Xu, S. Zhou, D. Marko, K. Potzger, J. Fassbender, M. Vinnichenko, M. Helm, H. Hochmuth, M. Lorenz, M. Grundmann, et al., J. Phys. D-Appl. Phys. **42**, 085001 (2009).
[26] H. B. de Carvalho, M. P. F. de Godoy, R. W. D. Paes, M. Mir, A. Ortiz de Zevallos, F. Iikawa, M. J. S. P. Brasil, V. A. Chitta, W. B. Ferraz, M. A. Boselli, et al., J. Appl. Phys. **108**, 079906 (2010).

[27] M. Hashimoto, Y. K. Zhou, M. Kanamura, and H. Asahi, Solid State Commun. **122**, 37 (2002).
[28] S. E. Park, H. J. Lee, Y. C. Cho, S. Y. Jeong, C. R. Cho, and S. Cho, Appl. Phys. Lett. **80**, 4187 (2002).
[29] Y. K. Zhou, M. Hashimoto, M. Kanamura, and H. Asahi, J. Supercond. **16**, 37 (2003).
[30] J. J. Kim, H. Makino, M. Sakurai, D. C. Oh, T. Hanada, M. W. Cho, T. Yao, S. Emura, and K. Kobayashi, J. Vac. Sci. Technol. B **23**, 1308 (2005).
[31] R. K. Singh, S. Y. Wu, H. X. Liu, L. Gu, D. J. Smith, and N. Newman, Appl. Phys. Lett. **86**, 012504 (2005).
[32] J. S. Lee, J. D. Lim, Z. G. Khim, Y. D. Park, S. J. Pearton, and S. N. G. Chu, J. Appl. Phys. **93**, 4512 (2003).
[33] J. Q. Wang, P. P. Chen, X. G. Guo, Z. F. Li, and W. Lu, J. Cryst. Growth **275**, 393 (2005).
[34] B. Pipeleers, S. M. Hogg, and A. Vantomme, J. Appl. Phys. **98**, 123504 (2005).
[35] J. M. D. Coey, M. Venkatesan, and C. B. Fitzgerald, Nat. Mater. **4**, 173 (2005).
[36] J. M. D. Coey, P. Stamenov, R. D. Gunning, M. Venkatesan, and K. Paul, New J. Phys. **12**, 053025 (2010).
[37] M. J. Wang, L. Yuan, C. C. Cheng, C. D. Beling, and K. J. Chen, Appl. Phys. Lett. **94**, 061910 (2009).
[38] S. O. Kucheyev, J. S. Williams, C. Jagadish, J. Zou, and G. Li, Phys. Rev. B **62**, 7510 (2000).
[39] A. Vantomme, S. M. Hogg, M. F. Wu, B. Pipeleers, M. Swart, S. Goodman, D. Auret, K. Iakoubovskii, G. J. Adriaenssens, K. Jacobs, et al., Nucl. Instrum. Methods Phys. Res. Sect. B **175**, 148 (2001).
[40] W. Jiang and W. J. Weber, Nucl. Instrum. Methods Phys. Res. Sect. B **242**, 431 (2006).
[41] S. O. Kucheyev, J. S. Williams, J. Zou, C. Jagadish, and G. Li, Appl. Phys. Lett. **78**, 1373 (2001).
[42] J. A. Vanvecht, Phys. Rev. B **7**, 1479 (1973).
[43] J. S. Williams, Mater. Sci. Eng. A **253**, 8 (1998).
[44] L. Gu, S. Wu, H. X. Liu, R. K. Singh, N. Newman, and D. J. Smith, J. Magn. Magn. Mater. **290**, 1395 (2005).
[45] J. Nord, K. Nordlund, B. Pipeleers, and A. Vantomme, Mater. Sci. Eng. B **105**, 111 (2003).
[46] J. P. Biersack and L. Haggmark, Nucl. Instr. and Meth. **174**, 257 (1980).
[47] S. O. Kucheyev, J. S. Williams, J. Zou, C. Jagadish, and G. Li, Nucl. Instrum. Methods Phys. Res. Sect. B **175**, 214 (2001).
[48] A. Bonanni, A. Navarro-Quezada, T. Li, M. Wegscheider, Z. Matej, V. Holy, R. T. Lechner, G. Bauer, M. Rovezzi, F. D'Acapito, et al., Phys. Rev. Lett. **101**, 135502 (2008).
[49] A. Ney, J. S. Harris, Jr., and S. S. P. Parkin, J. Phys.-Condens. Matter **18**, 4397 (2006).
[50] T. Takeuchi, Y. Harada, T. Tokushima, M. Taguchi, Y. Takata, A. Chainani,

J. J. Kim, H. Makino, T. Yao, T. Yamamoto, et al., Phys. Rev. B **70**, 245323 (2004).
[51] M. Hashimoto, S. Emura, H. Tanaka, T. Honma, N. Umesaki, S. Hasegawa, and H. Asahi, J. Appl. Phys. **100**, 103907 (2006).
[52] R. E. Behringer, J. Chem. Phys **29**, 537 (1958).
[53] X. Y. Cui, J. E. Medvedeva, B. Delley, A. J. Freeman, and C. Stampfl, Phys. Rev. B **75**, 155205 (2007).
[54] K. H. J. Buschow and F. R. De Boer, *Physics of Magnetism and Magnetic Materials* (Kluwer Academic Publishers, 2004), p. 24.
[55] J. Hong, J. Appl. Phys. **103**, 063907 (2008).
[56] B. Xu and B. C. Pan, J. Appl. Phys. **105**, 103710 (2009).
[57] T. Dietl, H. Ohno, F. Matsukura, J. Cibert, and D. Ferrand, Science **287**, 1019 (2000).
[58] D. Wang, X. Zhang, J. Wang, and T. Koide, Solid State Commun. **149**, 192 (2009).
[59] U. Gerstmann, A. T. Blumenau, and H. Overhof, Phys. Rev. B **63**, 075204 (2001).
[60] C. Kittel, *Introduction to solid state physics* (Wiley, 2004).
[61] K. Inumaru, K. Koyama, N. Imo-oka, and S. Yamanaka, Phys. Rev. B **75**, 054416 (2007).

Article IX

Paramagnetism and antiferromagnetic interactions in phase-pure Fe-implanted ZnO

L. M. C. Pereira,[1,2,3] U. Wahl,[3,4] J. G. Correia,[3,4] M. J. Van Bael,[5] S. Decoster,[2] K. Temst,[2] A. Vantomme,[2] A. M. Pereira,[1] and J. P. Araújo[1]

[1]*IFIMUP and IN-Institute of Nanoscience and Nanotechnology, Department of Physics and Astronomy, Faculdade de Ciências da Universidade do Porto, 4169-007 Porto, Portugal*

[2]*Instituut voor Kern- en Stralingsfysica and INPAC, K.U.Leuven, 3001 Leuven, Belgium*

[3]*Instituto Tecnológico e Nuclear, UFA, 2686-953 Sacavém, Portugal*

[4]*Centro de Física Nuclear da Universidade de Lisboa, 1649-003 Lisboa, Portugal*

[5]*Laboratory of Solid-State Physics and Magnetism and INPAC, K.U.Leuven, 3001 Leuven, Belgium*

Abstract

As the origin of the high temperature ferromagnetism often observed in wide-gap dilute magnetic semiconductors (DMS) becomes increasingly debated, there is a growing need for comprehensive studies on the major wide-gap DMS systems focusing on the phase-pure region of the materials' phase diagram. Here we report on the magnetic and structural properties of Fe-doped ZnO prepared by ion implantation of ZnO single crystals. A detailed structural characterization shows that the Fe impurities substitute for Zn in ZnO in a wurtzite $Fe_xZn_{1-x}O$ phase which is coherent with the ZnO host. In addition, the density of beam-induced defects is progressively decreased by thermal annealing up to 900°C, from highly disordered as implanted to highly crystalline upon annealing. Based on a detailed analysis of the magnetometry data, we demonstrate that isolated Fe impurities occupying Zn substitutional sites behave as localized paramagnetic moments down to 2 K, irrespective of Fe concentration and the density of beam-induced defects. With increasing local concentration of Zn-substitutional Fe, strong nearest-cation-neighbor antiferromagnetic interactions favor the antiparallel alignment of the Fe moments.

In preparation for *Physical Review B*

I. INTRODUCTION

The current view on wide-gap dilute magnetic semiconductors (DMS) is moving towards the belief that the often observed high-temperature ferromagnetism is not intrinsic, i.e. that it does not result from long-range magnetic order of randomly distributed magnetic dopants.[1] While limited experimental evidence exists that DMS materials are intrinsically ferromagnetic at room temperature, a number of non-intrinsic sources of ferromagnetic-like behavior in DMS materials have been identified and are becoming increasingly well documented: magnetic contamination,[2–5] instrumental artifacts[4,5] and chemical and/or structural segregation of the transition metal dopants into non-DMS phases.[6–14]

Following the first report of high temperature ferromagnetism in Co-doped TiO_2[15] and the prediction by Dietl *et al.*[16] that highly *p*-type Mn-doped ZnO and GaN could attain a Curie temperature (T_C) above room temperature, ferromagnetism at and above room temperature was reported in a rapidly growing number of wide-gap DMS materials (cf. e.g. the reviews 17–20). However, with the growing understanding of the most studied of these materials, issues of irreproducibility and instability became increasingly evident. As the origin of the observed ferromagnetism became increasingly debated during the last few years, reports began to emerge which comprehensively described the magnetic behavior of some of these materials (e.g. Refs. 21–27). Doing so requires sweeping growth, doping and post-processing conditions within relevant ranges, and performing both (1) magnetic characterization which carefully takes into account potential magnetic contamination and technique-specific artifacts, and (2) structural characterization which undeniably establishes either the phase pureness of the DMS material or identifies the segregated secondary phase(s). Such combined magneto-structural characterization then allows to position a given sample (in a given processing step) in the system's phase diagram, of the form sketched in Fig. 1.

In the true DMS region of the phase diagram, the transition metal impurities are randomly and substitutionally distributed in the host. *Intrinsic ferromagnetism* can be defined as ferromagnetic order of the localized moments of these randomly distributed transition-metal impurities via a long-range order mechanism, as is the case in narrow-gap DMSs such as $Ga_{1-x}Mn_xAs$ and $In_{1-x}Mn_xAs$.[1] However, comprehensive studies on this region of the phase diagram of wide-gap DMS systems, on carefully characterized materials with respect to phase pureness, revealed only paramag-

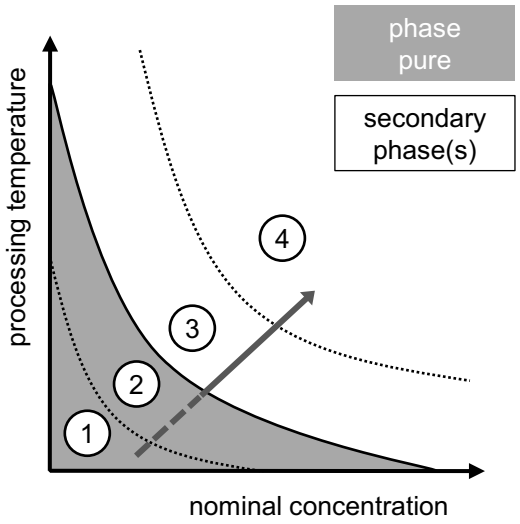

FIG. 1: Representation of the phase diagram of a semiconductor (A_yB_z) doped with a transition-metal (X), depending on processing temperature (of growth, implantation or annealing) and the nominal concentration (x) of the transition metal dopant. The gray area represents the phase-pure region, where the transition metal impurities substitute one of the host's constituents (e.g. element A), maintaining the host's crystal structure, i.e. forming a $X_xA_{y-x}B_z$ alloy. The impurities may be randomly distributed [region (1)] or, for sufficiently high concentrations or temperatures, aggregate in impurity-rich regions, i.e. x may vary across the $X_xA_{y-x}B_z$ alloy without a well defined interface [region (2)]. For sufficiently high processing temperatures or concentration (white region), the transition metal impurities may segregate into small precipitates of a $X_{x'}A_{y'}B_{z'}$ secondary phase with a different structure compared to that of the host. Depending on various factors, including not only processing temperature and impurity concentration but also others such as the preparation method, different secondary phases may form [regions (3) and (4)]. The arrow indicates the regions which are currently understood for Fe-implanted ZnO (discussed in the text).

netism (e.g. in Co-doped ZnO[22] and Mn-doped GaN[21]), antiferromagnetic interactions (e.g. in Co-doped ZnO,[24,25,28,29] Mn-doped GaN,[23] and Cr in GaN[30]), or at best, ferromagnetic order with very low T_C (e.g. $T_C < 10$ K in Mn-doped GaN[31]).

With increasing processing temperature (either during growth, implantation or annealing), the impurities tend to aggregate and segregate. This

segregation may be only chemical, i.e. the crystal structure is maintained and only the local impurity concentration varies across the material alternating between impurity-rich and impurity-poor regions (e.g. in Co-doped ZnO[6] and Mn-doped GaN[7]). In DMS literature, this type of chemical segregation is usually referred to as *spinodal decomposition*, regardless of the aggregation mechanism. For sufficiently high concentration and temperature, phase segregation may occur, i.e. the impurities precipitate in nanocomposites with a well defined interface with the host structure (e.g. in ZnO doped with Fe, Co and Ni[8–14]). Although unwanted in the DMS context, this self-assembly of magnetic and/or metallic nanocomposites in a semiconductor host constitutes a topic of its own, with various potential applications.[1] Fe-implanted ZnO is a remarkably rich DMS system in which to study the magnetism of both the phase pure and the phase segregated regions of the phase diagram. One of the advantages of ion implantation is that ion bombardment results in lattice disorder, which is believed to be crucial in establishing the ferromagnetic order, either in the form of point defects in bound magnetic polaron (BMP) models,[32] or in the form of extended defects in charge transfer ferromagnetism (CTF) models.[33] In addition, Fe impurities may be incorporated in ZnO both as Fe^{2+} and Fe^{3+}, making it a potentially suitable mixed-valency impurity in CTF systems. However, despite the various reports of intrinsic ferromagnetism in Fe-implanted ZnO (e.g. 34–37), the extensive work by Zhou *et al.*, with carefully characterized samples in terms of phase pureness, has shown that the ferromagnetic-like behavior originates from superparamagnetic precipitates formed at sufficiently high processing temperatures and Fe concentrations: α-Fe clusters which are oxidized and then converted to the spinel ferrite $ZnFe_2O_4$ with increasing annealing temperature and duration.[8–11] Although this segregated region of the phase diagram of Fe-implanted ZnO is rather well established (continuous part of the arrow in Fig. 1), both in terms of structure and magnetism, the magnetic behavior of the Fe impurities in phase pure $Fe_xZn_{1-x}O$ is still poorly understood (dashed part of the arrow in Fig. 1).

In this paper, we investigate the magnetism of phase pure $Fe_xZn_{1-x}O$ prepared by Fe^+ ion-implantation in ZnO single crystals. By varying the nominal Fe concentration and the degree of structural disorder, we aim at identifying the type of magnetic interactions between the Fe moments and how it is affected by lattice defects.

II. EXPERIMENT

Commercial ZnO wurtzite [0001] single-crystals (CrysTec GmbH), hydrothermally grown and Zn-face polished, were implanted with $^{56}Fe^{+}$ ions at room temperature to three different fluences: 1×10^{15} at. cm^{-2}, 5×10^{15} at. cm^{-2} and 1×10^{16} at. cm^{-2}, referred to below as S1, S5 and S10 respectively. An implantation energy of 60 keV and a beam angle of 10° with respect to the sample surface (to minimize ion channeling) results in a peak atomic concentration x_p of 0.0068 (0.68%), 0.034 (3.4%) and 0.068 (6.8%), at a projected ion range R_p of 297 Å with a straggling of 134 Å, estimated using MARLOWE.[38] In order to avoid sample contamination with ferromagnetic impurities,[2] the implantations were carried out using a Mo sample-holder and the samples were placed in a ceramic boat during annealing. Three samples were prepared for each of the fluences: one for magnetic characterization using SQUID magnetometry, one for damage characterization using RBS/C and one for impurity lattice location using β^{-} emission channeling. Structural and magnetic characterization was performed in the as implanted sampes and after thermal annealing in vacuum ($< 10^{-5}$ mbar) in 100°C steps (10 min each step) up to 900°C.

A. Rutherford backscattering and channeling spectrometry (RBS/C)

Defect accumulation and recovery were characterized using Rutherford backscattering and channeling spectrometry (RBS/C), with a 1.57 MeV He^{+} beam and two detectors at backscattering angles of 168° and 105°. The 168° backscattering geometry was used to characterize the channeling minimum yield $\chi_{\min}$ along the [0001] axis. $\chi_{\min}$ is the ratio of the backscattering yield with the incident beam aligned with the crystal axis to the yield for a random beam incidence, and is a measure of the lattice disorder induced by ion implantation.[39] The 15° glancing angle geometry (with respect to the sample surface) of the second detector was used for enhanced depth resolution of the damage profile.

B. SQUID magnetometry

The magnetic characterization was performed using a superconducting quantum interference device (SQUID) magnetometer (*Quantum De-*

sign MPMS XL-5) following strict procedures in order to avoid measurement artifacts and external magnetic contributions. These procedures were developed based on statistically relevant tests, which allowed us to determine the practical limits of SQUID magnetometry for the detection of ferromagnetism under various sample preparation, processing and handling conditions.[2] All measurements were performed with the field perpendicular to the *c*-axis, i.e., parallel to the sample plane. The field-dependent measurements were performed with decreasing field.

C. β^- emission channeling

The emission channeling (EC) technique allows to determine the lattice location of impurities in single crystals, making use of the charged particles emitted by a radioactive isotope of the impurity element under study.[40] The screened Coulomb potential of atomic rows and planes determines the anisotropic scattering of the particles emitted isotropically during decay. Along low-index crystal directions of single crystals, this anisotropic scattering results in well defined channeling or blocking effects. Because these effects strongly depend on the initial position of the emitted particles, they result in emission patterns which are characteristic of the lattice site(s) occupied by the probe atoms. Several reviews on emission channeling can be found in the literature,[40–43] and the technique has previously been used to investigate the lattice location of Fe,[44] Co,[45] Mn,[45] and Cu[46] in ZnO, in the low fluence ($\sim 10^{13}$ cm^{-2}) regime.

Each of the three samples implanted with stable ^{56}Fe for emission channeling experiments, were subsequently co-implanted with radioactive ^{59}Fe (with a half life $t_{1/2} = 46$ d) up to a fluence of 2×10^{13} cm^{-2}, by implanting the precursor isotope ^{59}Mn($t_{1/2} = 4.6$ s) which decays to ^{59}Fe. The radioactive implantations were carried out at the on-line isotope separator facility ISOLDE at CERN, which provides mass-separated beams of radioactive Mn isotopes produced by means of 1.4-GeV proton-induced nuclear fission from a uranium carbide UC_2 targets and chemically selective laser ion sources.[47] The β^- decay of ^{59}Mn transfers a recoil energy of about 200 eV to its ^{59}Fe daughter. This ensures that the ^{59}Fe atoms are re-implanted, i.e. that they do not inherit the ^{59}Mn lattice site. The implantations were performed at room temperature, under a tilt angle of 7° with respect to the surface normal, with an energy of 60 keV, resulting in a projected range R_P of 299 Å and a 136 Å straggling, estimated using the MARLOWE code.[38] Because the concentration of radioactive ^{59}Fe probes is at least two orders

of magnitude below that of stable ^{56}Fe, the increase in total Fe concentration compared to the samples used for RBS/C and SQUID measurements can be neglected. In addition, because the depth profiles of ^{56}Fe and ^{59}Fe overlap almost perfectly, with a difference in R_p and straggling of the order of about 3%, one can assume that the ^{59}Fe probes accurately represent the site location behavior of all Fe impurities.

Angular-dependent emission yields of the β^- particles emitted during decay were measured at room temperature, along four crystallographic directions ([0001], [$\bar{1}$102], [$\bar{1}$101] and [$\bar{2}$113]), in the as-implanted state and after *in situ* capless annealing in vacuum ($< 10^{-5}$ mbar) up to 900°C. These patterns were recorded using a position- and energy-sensitive detection system similar to that described in Ref. 48. Using the *many-beam* formalism for electron channeling in single crystals,[40] theoretical emission patterns were calculated for probes occupying substitutional Zn (S_{Zn}) and O (S_O) sites with varying root-mean-square (rms) displacements, the main interstitial sites and interstitial sites resulting from displacements along the [0001] or the basal directions. Quantitative lattice location is provided by fitting the experimental patterns with theoretical ones using the two-dimensional fit procedure outlined in Ref. 48. Corrections for secondary electrons that reach the detector were implemented by subtracting an isotropic background from every pattern. This secondary electron contribution was estimated based on Geant4[49,50] simulations of electron scattering, taking into account the elemental composition and geometry of the sample, sample holder and vacuum chamber.

III. RESULTS AND ANALYSIS

A. Structural disorder characterized using RBS/C

Figure 2 (a) shows representative RBS/C spectra measured in backscattering geometry (168°) for an unimplanted sample and sample S5 after different annealing steps. As typical for ZnO (e.g. Ref. 51), lattice disorder in the Zn sublattice accumulates in two regions: (1) in the bulk of the crystal (bulk peak), where the energy loss is maximum as the implanted ions are slowed down to the point that nuclear stopping dominates over electronic stopping and the host atoms are thus more efficiently displaced; (2) near the sample surface (surface peak), which acts as a sink for mobile defects created during the ion bombardment. The channeling minimum yield $\chi_{\min}$ is thus determined separately for these two regions. Bulk $\chi_{\min}$ are plotted

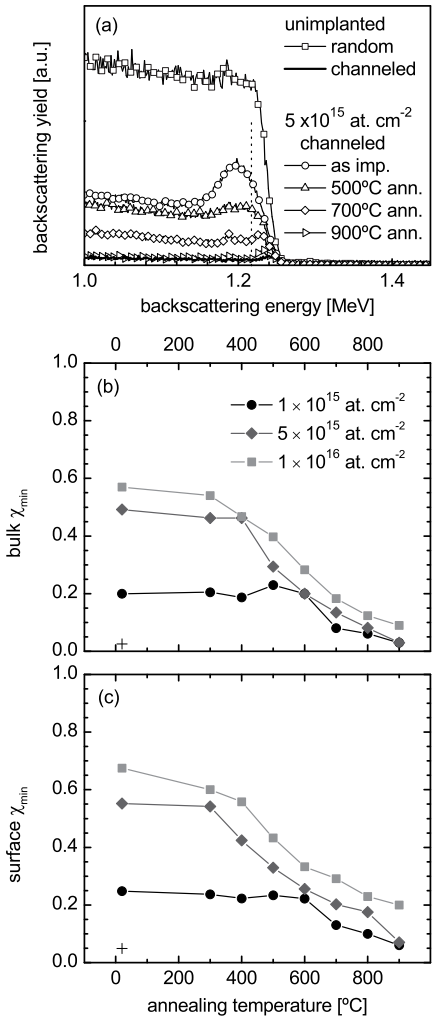

FIG. 2: (a) RBS/C spectra measured in backscattering geometry (168°) aligned with the [0001] axis (channeling) for an unimplanted sample and sample S5 (5×10^{15} cm^{-2}) after different annealing steps, compared to the spectrum measured in a random beam orientation, for the unimplanted sample (the dashed line separates the surface and bulk energy windows used to calculate the corresponding $\chi_{\min}$). (b) Bulk and (c) surface $\chi_{\min}$ of the three samples, as a function of annealing temperature. Bulk and surface $\chi_{\min}$ of the unimplanted samples are also indicated (+).

in Fig. 2 (b) and surface $\chi_{\min}$ in Fig. 2 (c), for the three fluences and annealing steps up to 900°C. High fluences (of the order of 1×10^{16} cm^{-2}) are required to induce significant lattice disorder ($\chi_{\min} > 50$ %), which reflects the efficient *dynamic annealing* which characterizes ZnO and is responsible for its known high radiation resistance.

The beam-induced damage is removed quite efficiently by thermal annealing. Both bulk and surface $\chi_{\min}$ decrease with increasing annealing temperature, particularly between 400°C and 900°C. After annealing at 900°C, the bulk $\chi_{\min}$ for fluences of 1×10^{15} cm^{-2} and 5×10^{15} cm^{-2} (3% in both cases) is nearly the same as prior to implantation (2.5%). The recovery at the surface is also very efficient for these fluences, with $\chi_{\min}$ of 6% and 7% for 1×10^{15} cm^{-2} and 5×10^{15} cm^{-2}, respectively, compared to 5% prior to implantation. For a fluence of 1×10^{16} cm^{-2} the recovery is somewhat less efficient, indicating that higher fluence implantation creates defect complexes which are more stable with respect to thermal annealing. This is in agreement with the general rule of thumb that annealing of extended defects in semiconductors requires a temperature of about two thirds of the material's melting point (in units of K), which for ZnO corresponds to about 1200°C. Nevertheless, a variation of the $\chi_{\min}$ in the bulk region (i.e. in the region where the majority of the Fe impurities are located) from 67% in the as implanted state down to 9% after 900°C annealing is quite satisfactory for the purpose of this work. This brings up the question of how exactly the lattice recovery evolves with annealing within the bulk region. Figure 3 shows the RBS/C spectra measured in glancing geometry (which provides an increased depth resolution) of sample S10 after each annealing step. It shows that below 600°C the decrease in the bulk peak inensity is more pronounced in the region between the Fe end of range (EOR) and the surface. The damage in the EOR region appears to be stabilized in complexes involving the Fe impurities and is annealed only above 600°C. This is discussed in more detail below, together with the emission channeling results on the lattice location of the Fe impurities.

As a final remark on Fig. 3, it is interesting to note that the low temperature annealing (between 300°C and 500°C), reveals an additional defect peak in the region between the surface and bulk defect peaks (dashed rectangle), which was also observed in Au implanted ZnO[51] and coined as *middle defect peak* (MDP). In Ref. 51, the MDP was attributed to a localized band of lattice defects, which nucleates in the near surface region due to incomplete dynamic annealing during ion bombardment. The spatial separation between vacancies and interstitials in the collision cascades

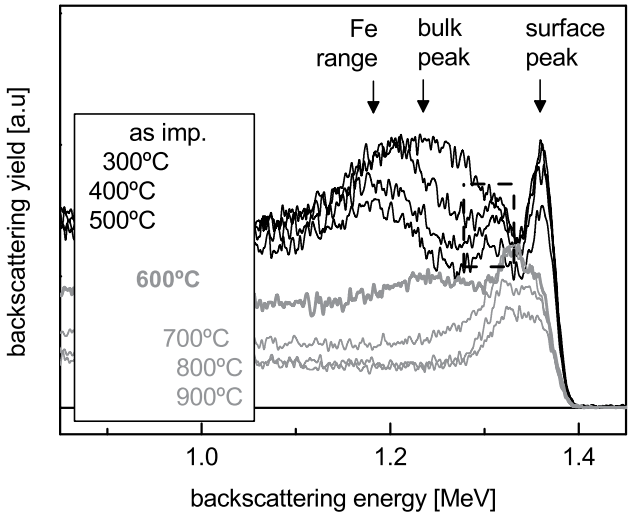

FIG. 3: RBS/C spectra measured in glancing geometry (15° with respect to the sample surface) in channeling orientation of sample S10 (1×10^{16} cm^{-2}) for the different annealing stages. The correspondence between each spectrum and the annealing step after which it was measured can be inferred from the yield intensity: the higher the annealing temperature the lower the backscattering yield. The different damage regions are indicated: surface peak, bulk peak and the region corresponding to the Fe end of range (arrows), as well as a middle defect peak (MDP) region (dashed rectangle).

may contribute to such incomplete dynamic annealing, by creating an excess of vacancies near the surface and an excess of interstitials in the EOR region.[51] An MDP is also present in sample S5 (with a fluence of 5×10^{15} cm^{-2}), but not in S1 (1×10^{15} cm^{-2}) (not shown). The main difference between the MDPs in samples S5 and S10 is that the MDP almost completely disappears in S5 after 900°C annealing whereas in S10 it persists. This is likely related to the more extended character of the MDP defect band in S10 (due to the larger fluence). The still relatively large surface $\chi_{\min}$ of sample S10 (20%) compared to samples S5 and S1 (6-7%) after 900°C is most likely due to the MDP. In addition, the angular straggling induced by MDP-related disorder on the probing He^+ beam is at least partly responsible for the higher bulk $\chi_{\min}$ of sample S10 compared to samples S5 and S1 at the end of the annealing sequence.

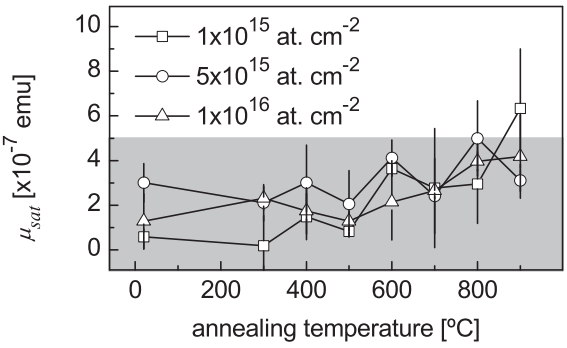

FIG. 4: Saturation moment $\mu_{\rm sat}$ as a function of annealing temperature, obtained from the linear fit to the 300 K *M-H* data at high fields (1–2 T). All three samples have an area of approximately 0.25 cm^2, so that the data can be compared directly. The shaded area below 5×10^{-7} emu corresponds to the regime at which ferromagnetic-like contamination and measurement artifacts dominate, i.e. the reliability limit for detection of ferromagnetism.[2]

sample	fluence [at. cm^{-2}]	max. FM $\mu_{\rm Fe}$ [μ_B]	max. α-Fe fraction
S1	1×10^{15}	0.18	8.1%
S5	5×10^{15}	0.05	2.4%
S10	1×10^{16}	0.02	0.8%

TABLE I: Maximum ferromagnetic moment per Fe atom ($\mu_{\rm Fe}$), and maximum fraction of Fe impurities in α-Fe precipitates (assuming a moment per Fe atom of 2.2 μ_B), compatible with the maximum saturation moment determined at 300 K for each sample/fluence.

B. SQUID magnetometry at room temperature

For all samples, a small hysteresis could be resolved at room temperature, for some of the annealing stages. Figure 4 compiles the saturation moment $\mu_{\rm sat}$ for the three fluences, as a function of annealing temperature, obtained from the linear fit to the 300 K magnetization data at high fields (1–2 T). The saturation moment remains consistently below 5×10^{-7} emu and appears to increase with annealing temperature. Because there is no correlation with implanted fluence and since the same type of residual hystereses are observed in unimplanted control samples[2], we attribute this

effect to small ferromagnetic contamination. The apparent increase in saturation moment with annealing temperature (Fig. 4) is simply a consequence of the increase in number of processing steps, i.e. increasing number of potentially contaminating events. In any case, we can not exclude that some residual ferromagnetic moment arises from intrinsic ferromagnetism associated with the Fe doping or other beam induced defects. Based on the maximum saturation value for each fluence, Table I lists the maximum ferromagnetic moment per Fe atom for each implanted fluence. Ferromagnetic-like behavior can also be observed if a fraction of the implanted Fe precipitates in superparamagnetic α-Fe clusters, as demonstrated by Zhou *et al.*.[8–11] Table I also lists the maximum fraction of precipitated Fe, assuming that all the ferromagnetic-like moment originates from α-Fe clusters with a moment per Fe atom of 2.2 μ_B (of bulk α-Fe). Note that the higher fraction for the lower fluence sample is merely a consequence of dividing a similar saturation moment by a much smaller number of atoms. Since the fraction of Fe atoms in clusters increases with Fe concentration,[10] one can conclude that the maximum fraction of clustered Fe in our samples is given by the value obtained for the highest fluence, i.e. less than 1%.

C. Impurity lattice site location using β^- emission channeling

Figure 5 (a)-(d) shows the experimental emission patterns along the [0001], [$\bar{1}$102], [$\bar{1}$101] and [$\bar{2}$113] directions of sample S1 following 300°C annealing. Figure 5 (e)-(h) shows the best fits of the corresponding theoretical yields, obtained by varying the fraction of Fe on substitutional S_{Zn} sites (best fit for a fraction of 77(5)%) and varying its rms displacement u_1 from the ideal S_{Zn} site (best fit for $u_1 = 0.08(1)$ Å). The remaining Fe fraction contributes with an isotropic emission yield, and is discussed next. Figure 6 compiles the fit results for the different fluences and annealing stages: the fractions of Fe impurities in S_{Zn} are plotted in Fig. 6 (a) and the corresponding rms displacements u_1 in Fig. 6 (b).

1. Random fraction.

The random fractions are virtually independent of annealing temperature and increase with implanted fluence. They correspond to Fe atoms which are located either in (1) crystalline secondary phases which are not coherent with the host structure, or in (2) highly disordered regions. Based

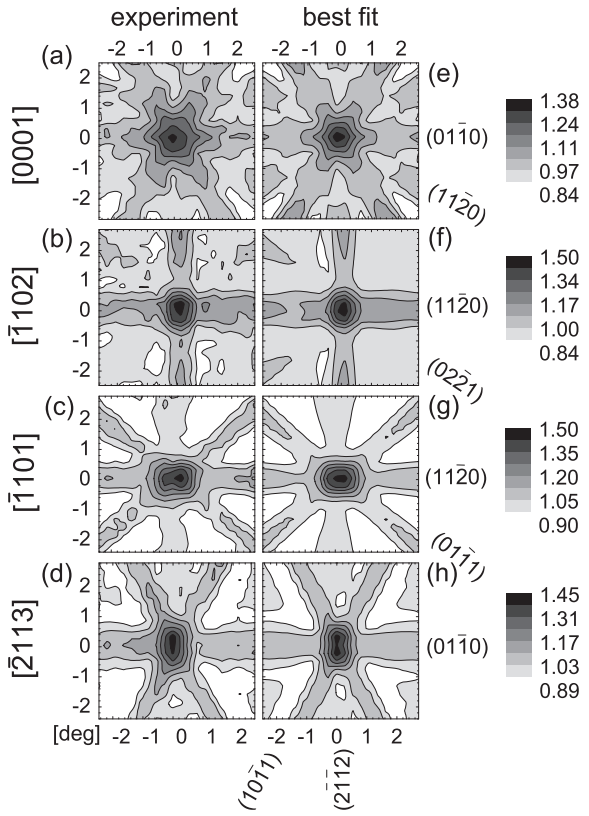

FIG. 5: (a)-(d) Normalized experimental emission patterns along the [0001], [$\bar{1}$102], [$\bar{1}$101] and [$\bar{2}$113] directions of sample S1 (1×10^{15} cm^{-2}) following 300°C annealing. (e)-(h) Corresponding best fits of theoretical yields, obtained by varying the fraction of Fe on substitutional S_{Zn} sites (best fit for a fraction of 77(5)%) and varying its rms displacement u_1 from the ideal S_{Zn} site (best fit for $u_1 = 0.08(1)$ Å).

on the work of Zhou *et al.*, case (1) would correspond to metallic α-Fe nanoclusters. However, these can be excluded based on the SQUID measurements at room temperature (maximum Fe fractions in α-Fe nanoclusters is below 1%). We interpret the observed random fraction as case (2), i.e. Fe impurities located in highly disordered (or even amorphous) regions. Because the random Fe fractions are very small and do not induce measurable ferromagnetism, their (potentially) magnetic behavior is assumed in the remainder of this article to be negligeble compared to the net magnetic moment of the substitional Fe fraction. Note that the random fractions may even be somewhat overestimated, as a result of enhanced electron

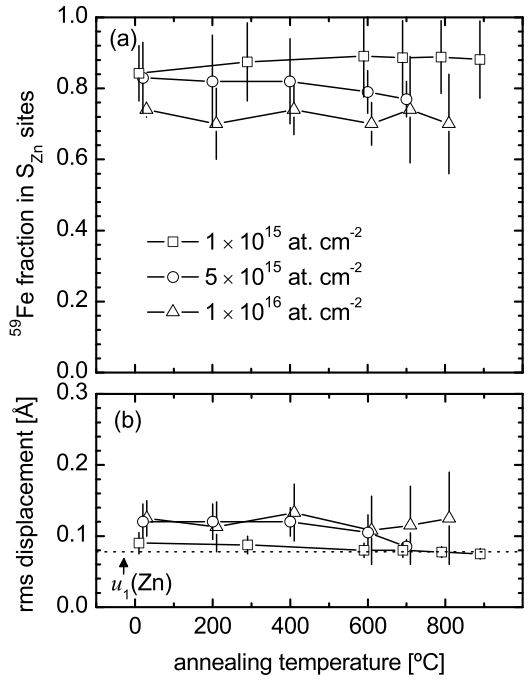

FIG. 6: (a) Fractions of ^{59}Fe impurities in Zn substitutional (S_{Zn}) sites and (b) the corresponding rms displacements u_1 obtained from fitting the experimental patterns with theoretical ones, as described in the text (the dashed line indicates the thermal vibration amplitude of the Zn atoms in the lattice).

dechanneling due to beam-induced lattice disorder.[40–43]

2. Substitutional Fe.

The substitutional fraction consists of Fe atoms occupying sites which are aligned with the Zn sublattice along the four measured directions. These sites can either be (1) true Zn sites in the ZnO wurtzite structure or (2) Fe sites in a secondary phase crystallite which are aligned with the Zn sublattice of the host ZnO structure. Even though the crystallites of the spinel ferrite $ZnFe_2O_4$ identified by Zhou *et al.*[9,10] can be crystallographically aligned with the ZnO wurtzite structure, the Fe sublattice in such structures is not coherent with the Zn sublattice in the host ZnO matrix. Hence, we are left with case (1). However, occupying nearly ideal Zn sites in the

ZnO wurtzite structure does not necessarily mean that the Fe is randomly distributed. From the EC results, one can only conclude that the majority of the Fe impurities are located in the cation sites of a wurtzite alloy of formula $Fe_xZn_{1-x}O$; x may vary locally along the lateral dimensions of the implanted layer, creating Fe-rich and Fe-poor regions. Such aggregation effects are limited by the mobility of the Fe impurities; although randomly incorporated in the crystal during implantation, they may become mobile and aggregate at sufficiently high annealing temperatures. Because aggregation implies a decrease of the average minimum distance between neighboring Fe impurities, it enhances the magnetic interactions between the Fe localized moments. Emission channeling is however unable to probe the uniformity of the Fe distribution. Aggregation is discussed in detail next, based on the magnetometry measurements. However, before analyzing the magnetism in more detail, it is worth discussing the fluence and temperature dependence of u_1. The rms displacement u_1, obtained from fitting the EC patterns, can in principle be divided in two components: the thermal vibration amplitude of Fe impurities in Zn sites, which is expected to be similar to that of the Zn atoms ($u_1(\mathrm{Zn}) = 0.08$ Å)[52], and static displacements from the ideal Zn sites. Such static displacements can result from (1) local relaxation due to the size and electronegativity mismatch between Fe and Zn, (2) strain-related or direct Coulomb interactions with neighboring point defects (i.e. impurity-defect complexes such as Zn or O vacancies), or (3) disorder induced by extended defects, which locally "bend" the atomic rows and planes. *If the impurity-defect structure (2) is well defined and has few equivalent geometries*, it may be resolved by EC as a static displacement from the substitutional site along a well defined crystallographic direction. Otherwise, the ensemble of substitutional impurities describes a distribution of displacement direction and amplitude, which can be satisfactorily described by an isotropic rms displacement, which adds to the thermal vibration amplitude. We consider this to be the case in our data, as we were unable to identify a preferential direction of displacement, even though several possibilities were tested, including for example static displacements towards the O or Zn nearest neighbors. The fitted u_1 values, plotted in Fig. 6, show that the degree of displacement from ideal Zn sites, and thus the disorder in the vicinity of the Fe impurities, increases with fluence, as expected and as observed in the RBS/C data. More importantly, it shows that the disorder in the close vicinity of the Fe impurities anneals only between 600°C and 800°C, as u_1 decreases to the thermal vibration amplitude, which is consistent with our previous emission channeling ex-

periments on low fluence Fe-implanted ZnO.[44] Combining with the RBS/C results above, this provides a quite detailed insight in the overall damage accumulation and annealing in the EOR region. Thermal annealing up to 600°C efficiently anneals the damage in the region between the Fe EOR and the surface, as shown by the RBS/C data in Fig. 3. However, most of the damage in the EOR region persists, most likely because it is stabilized by the impurity-defect complexes involving the Fe impurities and native point defects created during implantation, displacing the Fe atoms from the ideal Zn sites and thus explaining the u_1 values significantly above the thermal vibration amplitude of Zn in ZnO. According to the extensive work of Weyer *et al.* using Mössbauer spectroscopy,[53–55] these impurity-defect complexes are most likely Zn-vacancy related, which is supported by EPR measurements.[56] This damage is only annealed between 600°C and 800°C, as the complexes dissociate allowing the lattice defects to diffuse away from the Fe impurities. This is consistent with Fig. 3, where the disorder associated with the Zn sublattice (which can be attributed to local relaxation of the lattice in the vicinity of the Zn vacancies) appears to diffuse to the surface between 600°C and 800°C. For sample S10 (1×10^{16} cm^{-2}), the large error bars make it unclear if the rms displacements decreased or not between 600°C and 800°C [Fig. 6 (b)]. In any case, it appears that more extended defects (with higher thermal stability) are created in sample S10. This would explain the lower quality of its EC spectra (which results in larger error bars in both the S_{Zn} fractions and u_1) and the higher bulk χ_{min} even after 900°C. It is also consistent with previous studies on damage accumulation in Au-implanted ZnO,[51] where it is observed that implantation fluences of the order of 1×10^{15} cm^{-2} lead to the formation of point defect clusters and extended planar defects parallel to the basal plane of the ZnO wurtzite structure (in our case, such defect structures form at higher fluences, $> 5 \times 10^{15}$ cm^{-2}, because of the lower mass of Fe).

D. Low temperature magnetization and correlation with the structural characterization

Let us start by summarizing the main findings so far:

1. The analysis of the emission channeling data shows that the large majority of Fe impurities occupy Zn sites in the ZnO wurtzite structure, i.e. the implanted layer consists of a singlecrystalline wurtzite alloy of formula $Fe_xZn_{1-x}O$ where x may or may not vary across the

samples's lateral dimensions.

2. The absence of measurable room temperature ferromagnetism (or superparamagnetism) shows that the remaining Fe impurities, the random fraction in the EC data, can not be attributed to known secondary phases in Fe-implanted ZnO, i.e. metallic α-Fe or the spinel ferrite $ZnFe_2O_4$.

3. The analysis of the RBS/C data shows that thermal annealing allows to tune the degree of disorder in the $Fe_xZn_{1-x}O$ layers from dense damage profiles down to a nearly fully recovered structure. Combining the RBS/C and the EC results, we conclude that point-like native defects created by implantation form impurity-defect complexes with the Fe impurities. Thermal annealing at 700°C and above induced the dissociation of these complexes allowing for the native defects to diffuse towards the surface.

4. The single-crystalline wurtzite alloy $Fe_xZn_{1-x}O$ does not display high temperature ferromagnetism in a wide range of beam-induced defect density.

Two major questions remain unanswered:

1. If not high temperature ferromagnetism, what *is* the magnetic behavior of wurtzite $Fe_xZn_{1-x}O$ and how does it depend on the density of lattice defects?

2. How does thermal annealing affect the uniformity of x in $Fe_xZn_{1-x}O$?

Addressing question (2) experimentally and directly is extremely challenging. Fortunately, as we show next, addressing question (1) indirectly addresses (2). In order to answer (1) we will focus on sample S5 (5×10^{15} cm^{-2}) for the following reasons. As we show below, the large number of paramagnetic impurities in the ZnO substrates (relative to the number of implanted Fe ions) dominates the magnetic signal of sample S1 (1×10^{15} cm^{-2}), thus precluding a detailed analysis. On the other hand, from the EC data of sample S10 (1×10^{16} cm^{-2}), it can not be determined beyond doubt if the damage is completely annealed in the vicinity of the Fe impurities, making sample S10 less suitable for investigating possible changes in magnetic behavior upon dissociation of the impurity-defect complexes. In addition, if the Fe impurities do aggregate, this should occur at lower

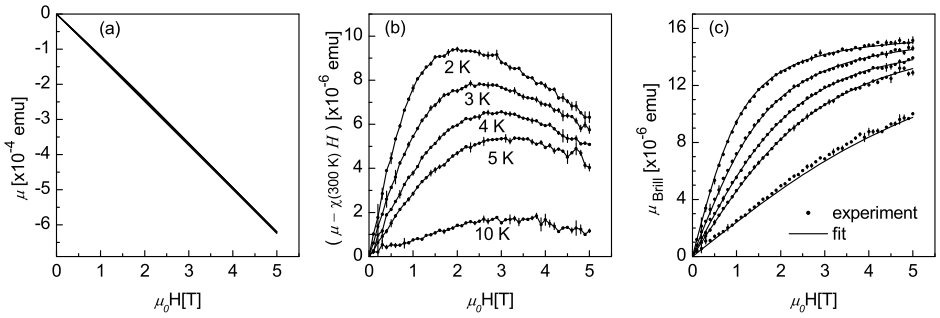

FIG. 7: (a) Isothermal *M-H* (magnetic moment μ as a function of applied field H) data of sample S5 prior to implantation at 2 K, 3 K, 4 K, 5 K, 10 K and 300 K. (b) Data subtracted of the diamagnetic component determined from the 300 K data. (c) Brillouin-like component and corresponding fit, according to the model described in the text.

annealing temperatures in S10 due to the higher Fe concentration, which makes it more difficult to separate the effects of defect annealing and Fe aggregation on the magnetic behavior.

In the following, we analyze the magnetometry data of sample S5 at low temperatures, focusing on the relevant processing stages: prior to implantation, in order to characterize the magnetic background of the ZnO substrate; as-implanted, when the uniformity of the Fe distribution should be maximum; after 500°C annealing, when most of the damage which does not overlap with the Fe profile has been removed; and after 700°C annealing, when most of the defects which more directly interact with the Fe impurities have been removed.

1. Unimplanted sample

Figure 7 (a) shows the isothermal *M-H* (magnetic moment μ as a function of applied field H) data of sample S5 prior to implantation at several temperatures from 2 K to 300 K. The non-linear component of the *M-H* curves at low temperatures is revealed [Fig. 7 (b)] after subtracting the (negative) linear component at 300 K estimated from the linear fit of the high field range (2-5 T). The shape of these curves suggests a Brillouin-like paramagnetic behavior superimposed on a small negative slope. The Brillouin-like component can be attributed to paramagnetic impurities, most likely transition metal impurities incorporated in the ppm range dur-

ing hydrothermal growth.[57] The negative slope at low temperature can be explained by a decreasing van Vleck susceptibility (paramagnetic) of the ZnO substrate with decreasing temperature (from 300 K to $\leq 10K$), due to the temperature dependence of the ZnO bandgap E_g. This has been observed in a number of semiconductor materials and is discussed in some detail in Ref. 58 for GaAs substrates. The low temperature data can then be fitted using the *Ansatz*

$$\mu(H,T) = \mu_{\mathrm{Brill}}(H,T) + \Delta\mu_{\mathrm{vV}}(H,T)\,, \tag{1}$$

where μ_{Brill} is the Brillouin-like magnetic moment of the paramagnetic impurities and $\Delta\mu_{\mathrm{vV}}$ accounts for the variation of the van Vleck paramagnetic susceptibility of the ZnO substrate. The Brillouin-like component can be expressed as

$$\mu_{\mathrm{Brill}}(H,T) = NgJ\mu_B B_J(x)\,, \quad (x \equiv \frac{gJ\mu_B H}{k_B T})\,, \tag{2}$$

where N is the number of paramagnetic impurities, g is the Landé g factor, J is the total angular momentum quantum number and $B_J(x)$ is the Brillouin function

$$B_J(x) = \frac{2J+1}{2J}\coth\left(\frac{2J+1}{2J}x\right) - \frac{1}{2J}\coth\left(\frac{1}{2J}x\right)\,. \tag{3}$$

Assuming that the orbital momentum L is fully quenched ($L = 0$), which we show below to be a good approximation in this case, J is given by the spin quantum number S ($J = S$) and $g = 2.00$. To a first approximation, we can assume that the van Vleck paramagnetic susceptibility varies very little from 10 K to 2 K, so that $\Delta\mu_{\mathrm{vV}}$ can be taken as

$$\Delta\mu_{\mathrm{vV}}(H,T) = \Delta\chi_{\mathrm{vV}}\,H\,, \tag{4}$$

where $\Delta\chi_{\mathrm{vV}}$ is temperature and field independent. Figure 7 (c) shows the data in (b) and the fit using the described *Ansatz*, with S, N and $\Delta\chi_{\mathrm{vV}}$ as free parameters. Using the parameters determined from the fit, the data in (c) have also been compensated for the Brillouin component at 300 K (almost linear), which had been subtracted in (b) together with the diamagnetic component. The best fit reproduces the data remarkably well, with $S = 2.6(2)$, $N = 3.11(3)$ (i.e. a concentration of 4×10^{16} cm^{-3}) and $\Delta\chi_{\mathrm{vV}}$ corresponding to about 1% of the diamagnetic susceptibility at 300 K. The Brillouin component is consistent with Fe^{3+} (d^5 $S = 5/2$), a

well known impurity in hydrothermally grown ZnO,[59] including the crystals grown by CrysTec GmbH.[57] The small $\Delta\chi_{\mathrm{vV}}$ is consistent with the expected small temperature dependence of the van Vleck paramagnetic susceptibility. Note that all the data are fitted simultaneously, i.e. the same N, S and $\Delta\chi_{\mathrm{vV}}$ values are optimized simultaneously for the different temperatures.

The derivation of the Brillouin function does not take into account anisotropic crystal fields. In wurtzite materials like ZnO, substitutional impurities are subject to a trigonal crystal field. Via the spin-orbit interaction, this anisotropic crystal field induces a strong magnetic anisotropy, which can be described by a zero-field splitting of the fundamental state and by an anisotropic effective g-factor in an effective spin Hamiltonian H_s of the form

$$H_s = \mu_B g_{\parallel} H_z S_z + \mu_B g_{\perp}(H_x S_x + H_y S_y) + D S_z^2 \,, \tag{5}$$

where S is the spin quantum number and D describes the zero-field splitting and $g_{\parallel}$ and $g_{\perp}$ are the effective g-factors for directions of magnetic field parallel and perpendicular to the wurtzite c-axis, respectively. Therefore, in general, the $\mu(H,T)$ behavior of paramagnetic impurities in the crystal field of the ZnO wurtzite lattice can not be correctly reproduced by the Brillouin function. The fact that it does in our case shows that the zero-field splitting constant for this particular impurity in ZnO is very small. This is typically the case for $S = 5/2$ moments (e.g. $D = -0.0074$ meV for Fe^{3+} d^5 in ZnO,[60] $D = -0.0027$ meV for Mn^{2+} d^5 in ZnO[61] and $D = -0.0093$ meV for Mn^{2+} d^5 in GaN[62]), which is consistent with the fitted S.

Because the implantation affects only a very thin layer of less than 1/1000 of the whole substrate thickness, this background can be taken as unchanged after implantation, allowing us to isolate the magnetization associated with the implanted Fe impurities and beam induced defects.

2. As-implanted sample

Figure 8 (a) shows the low temperature *M-H* curves of sample S5 in the as-implanted state, subtracted of the diamagnetic susceptibility at 300 K. Fitting the data with the same *Ansatz* (1) gives a reasonable agreement [Fig. 8 (b)]. To be more precise, the data are fitted to a sum of two terms of the form of (1). For one of them, the parameters N, S and $\Delta\chi_{\mathrm{vV}}$ are set (i.e. fixed) to those obtained for the unimplanted sample, so that the free N, S and $\Delta\chi_{\mathrm{vV}}$ parameters of the second term describe the implanted

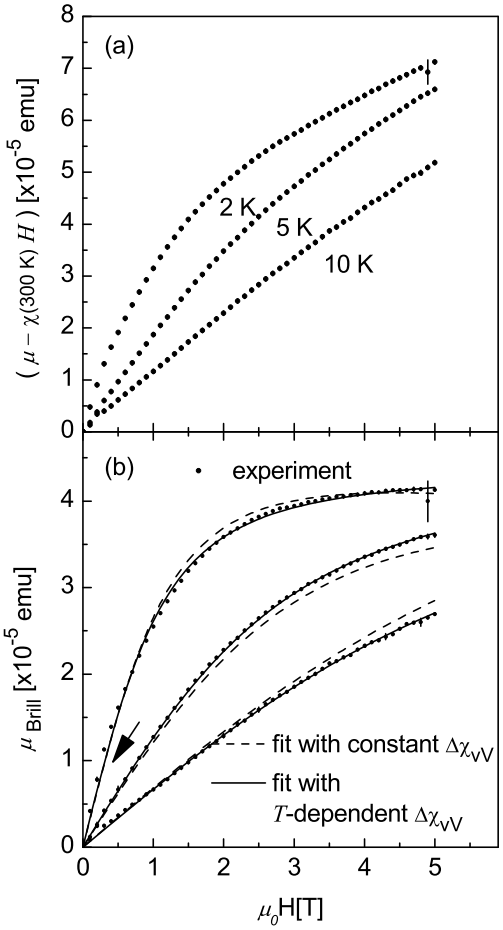

FIG. 8: (a) Isothermal *M-H* data of sample S5, in the as-implanted state, at 2 K, 5 K and 10 K corrected for the dimagnetic susceptibility at 300 K. (b) Brillouin-like component of the experimental data and corresponding theoretical fits according to the model described in the text. The best fit is obtained for $S = 5/2$, with $\Delta\chi_{\mathrm{vV}}$ (eq. (4)) taken as temperature independent (dashed line) or temperature dependent (solid line). The arrow indicates the region of poor fit *even* when $\Delta\chi_{\mathrm{vV}}$ is allowed to vary.

layer. The agreement is improved by allowing $\Delta\chi_{\mathrm{vV}}$ to be temperature dependent, which is implemented in the fitting as follows. First, the 2 K *M-H* curve, which carries more "information" as it provides a wider range of H/T (and thus of x in eq. (2)), is fitted with the *Ansatz* (1) with N,

S and $\Delta\chi_{\mathrm{vV}}$ as free parameters. The *M-H* curves for 5 K and 10 K are then fitted separately, fixing the N and S values determined from the 2 K *M-H*, and varying only $\Delta\chi_{\mathrm{vV}}$. Figure 8 (b) compares the experimental data to the best fit, both of which have been compensated for the Brillouin component (linear) at 300 K, which had been subtracted in (a) together with the diamagnetic component. The agreement is again remarkably good, supporting the existence of two types of paramagnetism: Brillouin-like and van Vleck-like.

Brillouin-like component. The best fit is obtained for $S = 2.5(1)$, i.e. $S = 5/2$ within the error, which is the expected behavior for the implanted Fe if it is incorporated as Fe^{3+} d^5. The zero-field splitting D for Fe^{3+} d^5 is sufficiently small (-0.0074 meV)[60] for the Brillouin function to be a good approximation. Although 2+ is the "neutral" charge state of Fe impurities substituting group-II Zn in ZnO, a 3+ charge state is favored in the following conditions: (1) if the Fermi level is close enough to the valence band so that the 3+/2+ transition level at $E_C - 1.4$ eV[63] is ionized; (2) by direct charge transfer from neighboring acceptor defects. It has been suggested, based on Mössbauer experiments, that Fe impurities in impurity-defect complexes with Zn vacancies created during Fe implantation are indeed in the 3+ charge state.[53–55] This is also supported by EPR measurements,[56] and is consistent with our RBS/C and EC results discussed above, which also indicate the formation of such complexes.

The small deviations from the Brillouin fit [arrow in Fig. 8 (b)] can be attributed to a small fraction of the implanted Fe impurities in the 2+ charge state. In principle one could attempt to incorporate such a fraction in the fit. However, D, $g_{\parallel}$ and $g_{\perp}$ [eq. (5)] are unknown for Fe^{2+} in ZnO, thus introducing too many free parameters in the fit. For Fe^{2+} in GaN, in principle a very similar case, $D = 0.27$ meV eV,[64] i.e. sufficiently high to induce the observed deviations from Brillouin behavior in [Fig. 8 (b)].

Another important observation concerns the fitted number of paramagnetic centers $N = 5.6(4) \times 10^{14}$, i.e. only about 45% of the number of implanted Fe impurities. The decreased N can in part be attributed to fitting the data with a high spin Fe^{3+} d^5 ($S = 5/2$), when a fraction may in fact be Fe^{2+} d^6 ($S = 2$). In addition, it is possible that the magnetic moment of Fe impurities in highly damaged regions (the random fraction in EC, i.e. 16% of the implanted

Fe) may be quenched. However, even these two effects combined are insufficient to explain the "missing" 55% of the Fe impurities. There must exist another source of Fe moment quenching: mutual compensation of the magnetic moment of neighboring Fe impurities due to the antiparallel alignement of their spins, imposed by strong nearest-cation-neighbor antiferromagnetic interactions. Even if the Fe impurities are randomly incorporated in Zn sites in ZnO upon implantation, there is a finite fraction that occupies nearest-cation-neighbor sites: 34% according to the Behringer equation[65] with $x = x_p$. If the mgnetic interaction between neighboring Fe moments is antiferromagnetic, the resulting antiparallel alignment of their spins renders this fraction "invisible" in the magnetization data. A similar moment-quenching effect has been observed in other DMS systems, e.g. Co-doped ZnO[24,25] and Cr-doped GaN.[30]

van Vleck-like component. There is an important observation, independent of any fitting, which we did not mention so far: the total magnetic moment at 2 K and 5 T [Fig. 8 (a)] of 7.1×10^{-5} emu, is larger than that expected from the Fe impurities even if all would contribute with the maximum spin-only value of 5 μ_B (5.8×10^{-5} emu in total). It is even more so, as the curve seems to be far from saturation. There is then an additional contribution from paramagnetic defects in the implanted layer other than the Fe impurities. The fitting presented above indicates that it can be described by a van Vleck-like paramagnetic susceptibility, of the form

$$\chi_{\mathrm{vV}}(T) = \frac{\mu_{\mathrm{vV}}(H,T)}{H} = \chi_{\mathrm{vV}}(300\,\mathrm{K}) + \Delta\chi_{\mathrm{vV}}(T)\,. \qquad (6)$$

We attribute this Vleck-like paramagnetic component to native defects created during implantation, which is further supported as we analyze the changes induced by annealing, below. The temperature dependence of $\Delta\chi_{\mathrm{vV}}$ is shown in Fig. 10. $\Delta\mu_{\mathrm{vV}}$ decreases with temperature, i.e. this van Vleck susceptibility component decreases with increasing temperature, which is the opposite to what was observed above for van Vleck susceptibility of the substrate (due to the temperature dependence of the bandgap), and supports their distinct origins (one, the perfect crystal, and the other, the beam-induced damage). Note that it is very difficult to estimate the absolute magnitude of either van Vleck susceptibilities, since it is virtually impossible to separate it from the purely (Langevin-like) diamagnetic

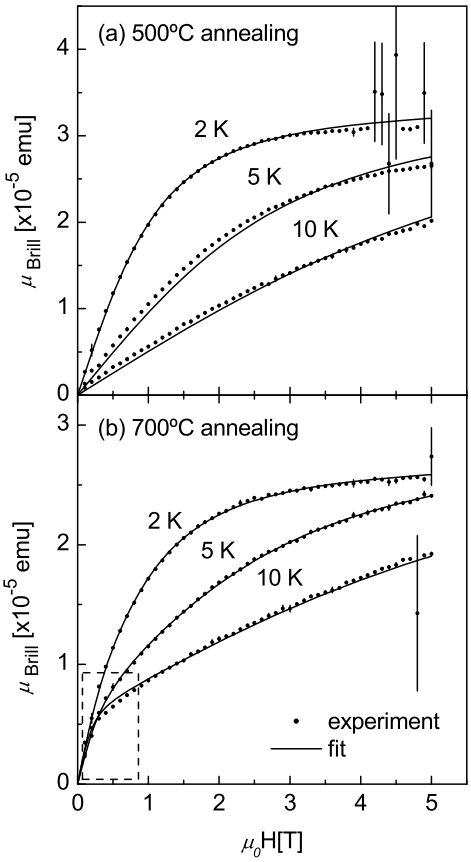

FIG. 9: Brillouin-like component of the isothermal *M-H* data at 2 K, 5 K and 10 K of sample S5 and corresponding theoretical fits (models described in the text): (a) following 500°C; (b) following 700°C.

susceptibility solely based on our data. The theoretical description of such defect-related van Vleck paramagnetism and its temperature dependence is however beyond the scope of this work.

3. Following 500° C annealing

Following 500°C annealing, the *M-H* data are still relatively well reproduced by the model above [Fig. 9 (a)], though clearly not as well as for the as-implanted state. Compared to the as-implanted state, the fit-

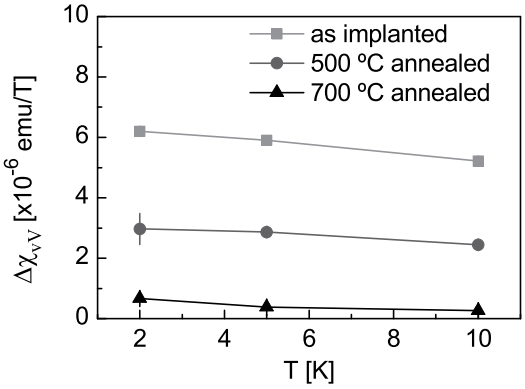

FIG. 10: Measurement temperature and annealing temperature dependence of $\Delta\chi_{vV}$ (eq. (4)), obtained from fitting the low temperature *M-H* data of sample S5.

ted $S = 2.4(6)$ remains unchanged within the error, and N decreases to $3.6(6) \times 10^{14}$. This indicates that one or both of the following modifications occurred upon annealing: (1) part of the Fe^{3+} fraction was converted to Fe^{2+} due to partial annealing of defects; (2) part of the isolated (magnetically active) Fe impurities suffered short range diffusion and formed pairs or larger complexes with other Fe impurities (thus contributing with a vanishingly small moment). As we show below, the analysis of the data corresponding to the next annealing step, indicates that, in fact, both (1) and (2) occurred. Note that also the van Vleck component decreased with annealing (Fig. 10), which is consistent with the decrease in defect density as probed by RBS/C.

4. Following 700 °C annealing

Something fundamentally different (at least apparently) occurs with 700°C annealing. Fitting the data with the same model as for the previous annealing step, i.e. with only one S value for the implanted Fe component, gives $S = 5.8(4)$, i.e. more than double than the maximum spin only value of 5/2 for a $3d$ moment. This indicates the formation of sufficiently large complexes, where although antiferromagnetic interactions dominate, frustration effects or uncompensated spins in the boundaries of these small complexes result in a nonvanishing net moment. Although it can hardly

be expected that the Brillouin function would correctly describe the behavior of such a complex system, it is worthwhile attempting to extract more information from the data, by allowing *two* Brillouin-like fractions with the corresponding N, N_2, S and S_2 free parameters, in addition to $\Delta\chi_{\mathrm{vV}}$. Figure 9 (b) compares the experimental data to the best fit obtained using a similar approach to the previous annealing stages but introducing the second Brillouin component with the corresponding N_2 and S_2 parameters free at all temperatures. The best fit of the 2 K data is obtained for $S = 1.8(7)$ and $S_2 = 9(3)$. For the 5 K and 10 K data, the best fit S_2 values vary considerably, up to $S = 70(15)$, showing that the large-S fraction is in fact very poorly described by the Brillouin function. Nevertheless, the fit supports that part of the Fe impurities did aggregate in larger complexes. In fact, this can be inferred independently of any fit from the increase in low-field susceptibility (dashed rectangle in Fig. 9) without an increase in saturation moment of the Brillouin-like component. In addition, the decrease of the small-S component from $S \approx 5/2$ (in the previous annealing steps) to $S \approx 2$, suggests that the isolated Fe^{3+} d^5 ($S = 5/2$) fraction was largely converted to Fe^{2+} d^6 ($S = 2$). Note that although the Brillouin function is likely not the best approximation for the magnetization of Fe^{2+} d^6 ($S = 2$) moments (with non-negligible zero-field splitting constant D), it is sufficient to indicate that the moment per *isolated* Fe impurity decreases upon annealing, using very few free parameters in the fit, which can be interpreted as Fe^{3+} being converted to Fe^{2+}.

Regarding the van Vleck component, it nearly vanishes after 700°C annealing (Fig. 10), consistent with further damage recovery. This is also discussed in more detail below.

IV. DISCUSSION

A. Paramagnetic Fe fraction

Table II compiles the best fit parameters of the Brillouin component of the low temperature *M-H* data. Combined with the structural characterization and based on the discussion above, the following interpretation can be extracted regarding the Brillouin component.

	S	N [$\times 10^{14}$]	S_2	N_2 [$\times 10^{14}$]
as implanted	2.5(1)	5.6(4)	-	-
500°C annealed	2.4(6)	3.6(6)	-	-
700°C annealed	1.8(7)	1.8(7)	9(3)	0.2(1)

TABLE II: Best fit parameters of the Brillouin component of the low temperature *M-H* data of sample S5, obtained using the models described in the text.

1. As implanted at room temperature

Upon implantation, the vast majority of the Fe impurities are more or less randomly incorporated in Zn substitutional sites. A small fraction of these may be isolated from other defects, assuming the 2+ charge state and a d^6 ($S = 2$) paramagnetic moment. The majority, on the other hand, forms impurity-defect complexes with neighboring native point defects, most likely Zn vacancies (acceptors), assuming a 3+ charge state and a d^5 ($S = 5/2$) paramagnetic moment. The zero-field splitting constant of Fe^{3+} d^5 ($S = 5/2$) is sufficiently small ($D = -0.007$ meV)[60] for the Brillouin function to be a good approximation of the magnetization data. The formation of such complexes upon high fluence implantation, and the resulting 3+ charge state of the Fe impurities has been established by the Mössbauer experiments of Weyer *et al.*. The perturbation induced by the neighboring native defects on the crystal field is extremely small (of the order of 10^{-6} meV[56]), so that its effect on the magnetization can be neglected.

2. Following annealing at moderate temperatures

Thermal annealing at moderate temperatures (~ 500°C) has two parallel effects on the paramagnetic Fe impurities: (i) thermally activated dissociation of part of the impurity-defect complexes, converting the Fe^{3+} d^5 ($S = 3/2$) impurities in such complexes to isolated and uncompensated Fe^{2+} d^6 ($S = 2$); (ii) the increased mobility of the Fe impurities at moderated temperatures allows for part of the Fe impurities to diffuse across short distances and form cation-substitutional Fe-Fe dimers. Based on the decrease in N from $5.6(4) \times 10^{14}$ to $3.6(6) \times 10^{14}$, we can estimate that about one third of the isolated Fe impurities are converted to small com-

plexes, where strong nearest-cation-neighbor antiferromagnetic interactions impose the antiparallel alignment of the Fe spins, resulting in a vanishingly small net magnetic moment per complex. As mentioned above, a similar moment-quenching effect has been observed in other DMS systems, e.g. Co-doped ZnO[24,25] and Cr-doped GaN.[30] The dissociation effect (1) is difficult to quantify based on our magnetization data, but has been observed at similar temperatures in ion implanted Fe in ZnO.[53] Note that it is conceivable that effect (1) and (2) are correlated, i.e. that the Fe^{3+} impurities are immobilized in impurity-defect complexes at low temperatures, and that it is the dissociation of these complexes at higher temperatures which allows for the Fe impurities to diffuse and form the Fe-Fe dimers.

3. Following high temperature annealing

Thermal annealing at higher temperatures ($\sim 700°$C) accelerates both (thermally activated) processes (i) and (ii). The isolated Fe fraction is mostly converted to Fe^{2+} (by impurity-defect complex dissociation) and decreases in number (N) (by Fe aggregation and resulting magnetic compensation), corresponding to about a third of that in the as-implanted state. However, unlike after 500°C annealing, the decrease in the isolated fraction can not be attributed to dimer formation only. A high-spin fraction also appears (with S_2 and N_2), corresponding to about 40% of the Fe-related magnetization, which we attribute to Fe aggregates larger than dimers (i.e. with more than two Fe atoms per complex). These aggregates can be regarded as regions of the $Fe_xZn_{1-x}O$ layer where x is significantly larger than x_p and approches 1. In such regions, strong nearest-cation-neighbor antiferromagnetic interactions favor the antiparallel alignement of the Fe spins. However, frustration effects and uncompensated spins, due to the lack of translation symmetry (random Zn/Fe cation-site occupation) of such structures as well as their finite size, result in a nonvanishing net moment per complex, probably describing very broad distributions in size and moment per aggregate.

B. Fe aggregation and segregation mechanisms

Based on the combination of the RBS/C, EC and magnetization results, we have excluded the formation of significant fractions (above a few %) of any magnetic secondary phase, from the as-implanted state up to

900°C annealing. This appears to contradict the work of Zhou *et al.*,[10] where, for similar Fe concentrations, significant fractions of the implanted Fe impurities segregate in (1) metallic α-Fe nanoprecipitates at processing temperature of about 500–800°C, and in (2) spinel ferrite $ZnFe_2O_4$ nanoprecipitates at processing temperatures above $\sim$ 800°C. Instead, in our samples, thermal annealing simply promotes aggregation in Fe-rich regions, i.e. the host's wurtzite structure is maintained and x varies locally across the $Fe_xZn_{1-x}O$ implanted layer.

We attribute the difference in Fe aggregation and segregation processes to different defect accumulation mechanisms, which in addition may also explain the discrepancy in the observed dependency of charge state upon implantation and annealing. In Ref. 10, for implantation near-room-temperature (as in the present work) the majority of the impurities tend to be incorporated as Fe^{2+} and be converted to Fe^{3+} upon annealing, which is the opposite of what Weyer *et al.* have observed for lower fluences,[53–55] and of what we infer from our magnetization data. In our case (and in the work of Weyer *et al.*,[53–55] although at lower fluences), defect accumulation is dominated by point-like defects. The formation of extended defects and highly disordered regions in our sample, at least in the Fe range region, was minimal, as evidenced by the nearly full recovery of crystallinity at relatively low annealing temperatures (compared to the temperatures required to anneal extended defects). However, if the implantation conditions are such that the damage accumulation is dominated by the formation of extended defects, as we suggest to be the case in Ref. 10, significant volumes of the implanted layer may be rendered nearly amorphous. In such regions, it is possible that Fe takes a 2+ charge state thus explaining the charge state discrepancy. At moderate temperatures (500–800°C), the mobility of Fe impurities in such regions allows for their aggregation. However, because the crystallinity is strongly decreased in those regions, it may be energetically favorable for the Fe impurities to precipitate into α-Fe, instead of forming wurtzite $Fe_xZn_{1-x}O$. This can be pictured as resulting from the lack of an epitaxial ZnO "template" for the formation of wurtzite $Fe_xZn_{1-x}O$ in those regions. From this stage on, the phase evolution must certainly differ. In our case, the Fe impurities are "blocked" in a (highly crystalline and energetically favorable) wurtzite $Fe_xZn_{1-x}O$ phase, coherent with the ZnO host and thermally stable at least up to 900°C. In the case of Refs. 9 and 10, where α-Fe has formed, increasing the annealing temperatures leads to the oxidation of those metallic clusters and, at even higher temperatures and sufficiently long annealing treatments, these oxide

clusters are converted into spinel $ZnFe_2O_4$.

This picture of disorder-limited or disorder-driven Fe aggregation and phase segregation is strongly supported by the work of Zhou *et al.*. They have shown that annealing the ZnO substrates prior to implantation may suppress the formation of α-Fe clusters, which occurs in non-preannealed samples. Based on our discussion of the previous paragraph, this can be explained as follows. Preannealing of the substrates removes some types of extended defects in the near surface region ($< 1\ \mu$m) which would otherwise act as nucleation centers for the highly disordered regions, under the implantation conditions in Refs. 8–11. In our case, although the implantations were carried out without preannealing of the substrates, many factors may still determine a different damage accumulation mechanism in our samples, including a possibly different defect microstructure of the purchased substrates and different implantation conditions (implantation temperature, energy, angle, fluence rate, etc.).

C. Van Vleck-like paramagnetism associated with beam-induced damage

The constant $\Delta\chi_{\mathrm{vV}}$ [eq. (4)], at 2 K, is plotted in Fig. 11 as a function of annealing temperature, normalized to its maximum value in the as implanted state. In an attempt to identify from which type (or region) of defects the van Vleck paramagnetic component originates, Fig. 11 compares $\Delta\chi_{\mathrm{vV}}$ to the bulk and surface χ_{min} as well as number of Fe^{3+} (N in the Brillouin-like fits above), which is in principle a measure of the number of lattice defects involved in the Fe^{3+}-defect complexes. All data sets overlap within experimental error, which is quite remarkable considering that very different quantities are compared. However, though strongly supporting the defect-related origin of this van Vleck-like paramagnetism, this comparison is unable to discern which of the defect component(s) is involved.

D. Magnetic interactions in the phase-pure region of the phase diagram

The main finding of this study is that, while isolated Fe moments in wurtzite $Fe_xZn_{1-x}O$ (i.e. for locally small x) are paramagnetic, strong antiferromagnetic interactions between nearest-cation-neighbors Fe impurities

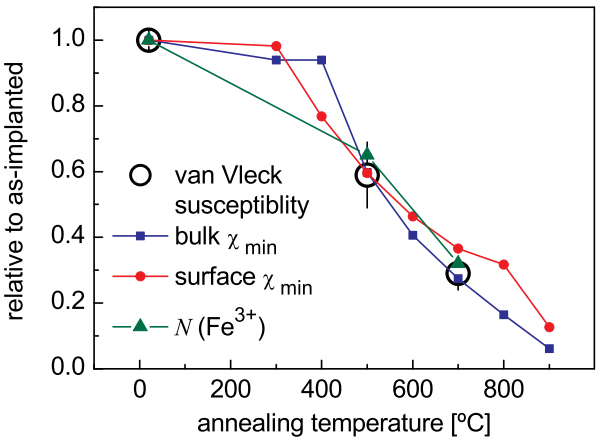

FIG. 11: Annealing temperature dependence of the constant associated with the van Vleck paramagnetic susceptibility [$\Delta\chi_{\mathrm{vV}}$ in eq. (4)] determined at 2 K, compared to the quantities that most directly measure the densities of the varies types (or regions) of defects which may originate it: bulk and surface χ_{min} as well as the number N of Fe^{3+} impurities (N in the Brillouin-like fits, i.e. a measure of the amount of defects involved in the Fe^{3+}-defect complexes). All values are normalized to the respective maximum value, in the as-implanted state.

(i.e. for $x \to 1$ locally) favor the antiparallel alignment of their moments. This is essentially the same behavior as for Co impurities,[24,25,28,29] which is consistent with the antiferromagnetic nature of the corresponding oxides FeO and CoO, with Néel temperatures of 198 K and 291 K,[66] respectively. This indicates that the magnetic interactions between the localized 3*d* moments of the Fe impurities result from indirect superexchange via the O 2*p* band, not from ferromagnetic *p*-*d* Zener exchange.[16] However, this is not surprising since, unlike Mn in GaAs and InAs, Fe does not introduce the *p*-holes required to mediate *p*-*d* Zener exchange.

As an alternative to *p*-*d* Zener exchange, high-temperature ferromagnetism in wide-gap DMS materials has also been predicted on the basis of bound magnetic polaron (BMP) models.[32] Here, the magnetic moments interact via electrons of an impurity band associated with lattice defects, as those created during implantation. Since these defect electrons occupy large orbits, each defect can interact with several dopant moments and form a magnetic polaron; the percolation of such polarons may establish ferromagnetic order between the localized moments. However, even though we have considerably varied the density of *beam-induced* defects in the $Fe_xZn_{1-x}O$

layers, we did not observe ferromagnetic order down to 2 K. This inability to induce ferromagnetic order can probably be extended to any type of lattice defects, since the exchange energy density necessary to produce high-temperature ferromagnetism with a few % of transition-metal doping corresponds to a magnetic exchange much stronger than that observed in the strongest known ferromagnetic materials.[33]

It thus appears that for high-temperature ferromagnetism to be achieved in these materials, a different mechanism should be explored that does not rely on ordered 3*d* local moments and Heisenberg-type exchange as in *p*-*d* Zener exchange and BMP models. Very recently a different type of model has been proposed that seems to offer exactly that. The charge-transfer ferromagnetism (CTF) model[33] relies on Stoner-type ferromagnetism. It requires two distinct types of defects, one that creates a narrow impurity band and another to play the role of charge reservoir. If both types of defects are present, electrons can be transfered to or from the reservoir until the filling level of the impurity band satisfies the spontaneous spin-split criterion. In dilute magnetic semiconductors, the impurity band can originate, for example, from grain boundaries or beam-induced defects, while mixed-valency impurities may behave as charge reservoirs. However, although Fe and other 3*d* transition metals have more than one charge state within the ZnO band-gap, the types of defects produced during implantation appear not to satisfy the stringent requirements for the role of impurity-band.

V. CONCLUSIONS

In summary, based on a combined magnetic and structural characterization, we have studied the magnetic behavior of phase pure $Fe_xZn_{1-x}O$ prepared by ion implantation. We have shown that isolated Fe impurities, occupying Zn substitutional sites, behave as localized paramagnetic moments down to 2 K, irrespective of Fe concentration and the density of beam-induced defects. With increasing local concentration of Zn-substitutional Fe, strong nearest-cation-neighbor antiferromagnetic interactions favor the antiparallel alignment of the localized Fe moments, resulting in an efficient moment-quenching.

Together with recent comprehensive studies on transition-metal doped ZnO and other wide-gap semiconductors such as GaN, our results indicate that Heisenberg-type exchange mechanisms, such as *p*-*d* Zener and bound magnetic polaron (BMP) models, do not produce high temperature ferromagnetism in wide-gap semiconductors. This is turn supports the view

that the high temperature ferromagnetism often oberved in wide-gap DMS materials is not intrinsic.

Acknowledgments

This work was supported by the Portuguese Foundation for Science and Technology (PTDC/FIS/66262/2006, CERN/FP/116320/2010, SFRH/BD/35761/2007), the Research Foundation - Flanders (FWO), the EURONS project (RII3-CT-2004-506065), the SPIRIT project (contract no. 227012), KULeuven projects GOA/2009/006 and INPAC EF/05/005 and the IUAP P6/42 program.

[1] T. Dietl, Nat. Mater. **9**, 965 (2010).
[2] L. M. C. Pereira, J. P. Araujo, M. J. Van Bael, K. Temst, and A. Vantomme, J. Phys. D: Appl. Phys. **44**, 215001 (2011).
[3] D. W. Abraham, M. M. Frank, and S. Guha, Appl. Phys. Lett. **87**, 252502 (2005).
[4] A. Ney, T. Kammermeier, V. Ney, K. Ollefs, and S. Ye, J. Magn. Magn. Mater. **320**, 3341 (2008).
[5] M. A. Garcia, E. Fernandez Pinel, J. de la Venta, A. Quesada, V. Bouzas, J. F. Fernandez, J. J. Romero, M. S. Martin Gonzalez, and J. L. Costa-Kramer, J. Appl. Phys. **105**, 013925 (2009).
[6] Z. Sun, W. Yan, G. Zhang, H. Oyanagi, Z. Wu, Q. Liu, W. Wu, T. Shi, Z. Pan, P. Xu, et al., Phys. Rev. B **77**, 245208 (2008).
[7] G. Martinez-Criado, A. Somogyi, S. Ramos, J. Campo, R. Tucoulou, M. Salome, J. Susini, M. Hermann, M. Eickhoff, and M. Stutzmann, Appl. Phys. Lett. **86**, 131927 (2005).
[8] K. Potzger, S. Zhou, H. Reuther, K. Kuepper, G. Talut, M. Helm, J. Fassbender, and J. D. Denlinger, Appl. Phys. Lett. **91**, 062107 (2007).
[9] S. Zhou, K. Potzger, H. Reuther, G. Talut, F. Eichhorn, J. von Borany, W. Skorupa, M. Helm, and J. Fassbender, J. Phys. D-Appl. Phys. **40**, 964 (2007).
[10] S. Zhou, K. Potzger, G. Talut, H. Reuther, J. von Borany, R. Groetzschel, W. Skorupa, M. Helm, J. Fassbender, N. Volbers, et al., J. Appl. Phys. **103**, 023902 (2008).
[11] S. Zhou, K. Potzger, G. Talut, H. Reuther, K. Kuepper, J. Grenzer, Q. Xu, A. Muecklich, M. Helm, J. Fassbender, et al., J. Phys. D-Appl. Phys. **41** (2008).
[12] S. Zhou, K. Potzger, J. von Borany, R. Grotzschel, W. Skorupa, M. Helm, and J. Fassbender, Phys. Rev. B **77**, 035209 (2008).
[13] S. Zhou, K. Potzger, K. Kuepper, J. Grenzer, M. Helm, J. Fassbender, E. Arenholz, and J. D. Denlinger, J. Appl. Phys. **103**, 043901 (2008).

[14] R. P. Borges, B. Ribeiro, A. R. G. Costa, C. Silva, R. C. da Silva, G. Evans, A. P. Goncalves, M. M. Cruz, and M. Godinho, Eur. Phys. J. B **79**, 185 (2011).
[15] Y. Matsumoto, M. Murakami, T. Shono, T. Hasegawa, T. Fukumura, M. Kawasaki, P. Ahmet, T. Chikyow, S. Koshihara, and H. Koinuma, Science **291**, 854 (2001).
[16] T. Dietl, H. Ohno, F. Matsukura, J. Cibert, and D. Ferrand, Science **287**, 1019 (2000).
[17] S. J. Pearton, C. R. Abernathy, D. P. Norton, A. F. Hebard, Y. D. Park, L. A. Boatner, and J. D. Budai, Mater. Sci. Eng. R-Rep. **40**, 137 (2003).
[18] W. Prellier, A. Fouchet, and B. Mercey, J. Phys.-Condes. Matter **15**, R1583 (2003).
[19] S. J. Pearton, W. H. Heo, M. Ivill, D. P. Norton, and T. Steiner, Semicond. Sci. Technol. **19**, R59 (2004).
[20] C. Liu, F. Yun, and H. Morkoc, J. Mater. Sci.-Mater. Electron. **16**, 555 (2005).
[21] W. Stefanowicz, D. Sztenkiel, B. Faina, A. Grois, M. Rovezzi, T. Devillers, F. d'Acapito, A. Navarro-Quezada, T. Li, R. Jakiela, et al., Phys. Rev. B **81**, 235210 (2010).
[22] A. Ney, T. Kammermeier, K. Ollefs, S. Ye, V. Ney, T. C. Kaspar, S. A. Chambers, F. Wilhelm, and A. Rogalev, Phys. Rev. B **81**, 054420 (2010).
[23] S. Granville, B. J. Ruck, F. Budde, H. J. Trodahl, and G. V. M. Williams, Phys. Rev. B **81**, 184425 (2010).
[24] A. Ney, K. Ollefs, S. Ye, T. Kammermeier, V. Ney, T. C. Kaspar, S. A. Chambers, F. Wilhelm, and A. Rogalev, Phys. Rev. Lett. **100**, 157201 (2008).
[25] P. Sati, C. Deparis, C. Morhain, S. Schafer, and A. Stepanov, Phys. Rev. Lett. **98**, 137204 (2007).
[26] A. Bonanni, A. Navarro-Quezada, T. Li, M. Wegscheider, Z. Matej, V. Holy, R. T. Lechner, G. Bauer, M. Rovezzi, F. D'Acapito, et al., Phys. Rev. Lett. **101**, 135502 (2008).
[27] A. Bonanni, M. Kiecana, C. Simbrunner, T. Li, M. Sawicki, M. Wegscheider, M. Quast, H. Przybylinska, A. Navarro-Quezada, R. Jakiela, et al., Phys. Rev. B **75**, 125210 (2007).
[28] Q. Xu, S. Zhou, D. Marko, K. Potzger, J. Fassbender, M. Vinnichenko, M. Helm, H. Hochmuth, M. Lorenz, M. Grundmann, et al., J. Phys. D-Appl. Phys. **42**, 085001 (2009).
[29] H. B. de Carvalho, M. P. F. de Godoy, R. W. D. Paes, M. Mir, A. Ortiz de Zevallos, F. Iikawa, M. J. S. P. Brasil, V. A. Chitta, W. B. Ferraz, M. A. Boselli, et al., J. Appl. Phys. **108**, 079906 (2010).
[30] L. M. C. Pereira, T. Som, J. Demeulemeester, M. J. Van Bael, K. Temst, and A. Vantomme, J. Phys.: Condens. Matter **23**, 346004 (2011).
[31] E. Sarigiannidou, F. Wilhelm, E. Monroy, R. M. Galera, E. Bellet-Amalric, A. Rogalev, J. Goulon, J. Cibert, and H. Mariette, Phys. Rev. B **74**, 041306 (2006).
[32] J. M. D. Coey, M. Venkatesan, and C. B. Fitzgerald, Nat. Mater. **4**, 173 (2005).
[33] J. M. D. Coey, P. Stamenov, R. D. Gunning, M. Venkatesan, and K. Paul, New

J. Phys. **12**, 053025 (2010).
[34] K. Potzger, S. Q. Zhou, H. Reuther, A. Mucklich, F. Eichhorn, N. Schell, W. Skorupa, M. Helm, J. Fassbender, T. Herrmannsdorfer, et al., Appl. Phys. Lett. **88**, 052508 (2006).
[35] P. Wu, G. Saraf, Y. Lu, D. H. Hill, R. Gateau, L. Wielunski, R. A. Bartynski, D. A. Arena, J. Dvorak, A. Moodenbaugh, et al., Appl. Phys. Lett. **89**, 012508 (2006).
[36] Y. Y. Song, K. S. Park, D. V. Son, S. C. Yu, H. J. Kang, S. W. Shin, C. N. Whang, J. H. Lee, J. H. Song, and K. W. Lee, J. Korean Phys. Soc. **50**, 1706 (2007).
[37] R. Kumar, A. P. Singh, P. Thakur, K. H. Chae, W. K. Choi, B. Angadi, S. D. Kaushik, and S. Patnaik, J. Phys. D-Appl. Phys. **41**, 155002 (2008).
[38] M. T. Robinson, Phys. Rev. B **40**, 10717 (1989).
[39] W. K. Chu, J. W. Mayer, and M. A. Nicolet, *Backscattering Spectrometry* (Academic, New York, 1978).
[40] H. Hofsass and G. Lindner, Phys. Rep. **201**, 121 (1991).
[41] H. Hofsass, U. Wahl, and S. G. Jahn, Hyperfine Interact. **84**, 27 (1994).
[42] H. Hofsass, Hyperfine Interact. **97**, 247 (1996).
[43] U. Wahl, Hyperfine Interact. **129**, 349 (2000).
[44] E. Rita, U. Wahl, J. G. Correia, E. Alves, and J. C. Soares, Appl. Phys. Lett. **85**, 4899 (2004).
[45] L. M. C. Pereira, U. Wahl, S. Decoster, J. G. Correia, L. M. Amorim, M. R. da Silva, J. P. Araujo, and A. Vantomme, Phys. Rev. B **84**, 125204 (2011).
[46] U. Wahl, E. Rita, J. G. Correia, E. Alves, and J. G. Soares, Phys. Rev. B **69**, 012102 (2004).
[47] V. N. Fedoseyev, K. Batzner, R. Catherall, A. H. M. Evensen, D. ForkelWirth, O. C. Jonsson, E. Kugler, J. Lettry, V. I. Mishin, H. L. Ravn, et al., Nucl. Instrum. Methods Phys. Res. Sect. B-Beam Interact. Mater. Atoms **126**, 88 (1997).
[48] U. Wahl, J. G. Correia, S. Cardoso, J. G. Marques, A. Vantomme, G. Langouche, and ISOLDE Collaboration, Nucl. Instrum. Methods Phys. Res. B **136**, 744 (1998).
[49] S. Agostinelli, J. Allison, K. Amako, J. Apostolakis, H. Araujo, P. Arce, M. Asai, D. Axen, S. Banerjee, G. Barrand, et al., Nucl. Instrum. Methods Phys. Res. Sect. A-Accel. Spectrom. Dect. Assoc. Equip. **506**, 250 (2003).
[50] J. Allison, K. Amako, J. Apostolakis, H. Araujo, P. A. Dubois, M. Asai, G. Barrand, R. Capra, S. Chauvie, R. Chytracek, et al., IEEE Trans. Nucl. Sci. **53**, 270 (2006).
[51] S. O. Kucheyev, J. S. Williams, C. Jagadish, J. Zou, C. Evans, A. J. Nelson, and A. V. Hamza, Phys. Rev. B **67** (2003).
[52] U. Wahl, E. Rita, J. G. Correia, E. Alves, J. P. Araujo, and ISOLDE Collaboration, Appl. Phys. Lett. **82**, 1173 (2003).
[53] G. Weyer, H. P. Gunnlaugsson, R. Mantovan, M. Fanciulli, D. Naidoo, K. Bharuth-Ram, and T. Agne, J. Appl. Phys. **102**, 113915 (2007).

[54] H. P. Gunnlaugsson, T. E. Molholt, R. Mantovan, H. Masenda, D. Naidoo, W. B. Dlamini, R. Sielemann, K. Bharuth-Ram, G. Weyer, K. Johnston, et al., Appl. Phys. Lett. **97**, 142501 (2010).
[55] T. E. Molholt, R. Mantovan, H. P. Gunnlaugsson, K. Bharuth-Ram, M. Fanciulli, H. P. Gislason, K. Johnston, Y. Kobayashi, G. Langouche, H. Masenda, et al., Physica B **404**, 4820 (2009).
[56] D. V. Azamat and M. Fanciulli, Physica B **401**, 382 (2007).
[57] M. Khalid, A. Setzer, M. Ziese, P. Esquinazi, D. Spemann, A. Poeppl, and E. Goering, Phys. Rev. B **81**, 214414 (2010).
[58] A. Ney, J. S. Harris, Jr., and S. S. P. Parkin, J. Phys.-Condens. Matter **18**, 4397 (2006).
[59] K. Maeda, M. Sato, I. Niikura, and T. Fukuda, Semicond. Sci. Technol. **20**, S49 (2005).
[60] R. Heitz, A. Hoffmann, and I. Broser, Phys. Rev. B **45**, 8977 (1992).
[61] E. Chikoidze, H. von Bardeleben, Y. Dumont, P. Galtier, and J. Cantin, J. Appl. Phys. **97**, 10D316 (2005).
[62] R. Heitz, P. Thurian, I. Loa, L. Eckey, A. Hoffmann, I. Broser, K. Pressel, B. K. Meyer, and E. N. Mokhov, Appl. Phys. Lett. **67**, 2822 (1995).
[63] S. J. Pearton, D. P. Norton, K. Ip, Y. W. Heo, and T. Steiner, J. Vac. Sci. Technol. B **22**, 932 (2004).
[64] S. Marcet, D. Ferrand, D. Halley, S. Kuroda, H. Mariette, E. Gheeraert, F. J. Teran, M. L. Sadowski, R. M. Galera, and J. Cibert, Phys. Rev. B **74**, 125201 (2006).
[65] R. E. Behringer, J. Chem. Phys **29**, 537 (1958).
[66] C. Kittel, *Introduction to solid state physics* (Wiley, 2004), eighth ed.

4.5 Discussion

This section is devoted to a more global discussion of the results. The aim is not to repeat what has been discussed and concluded in the various articles of the previous sections, but to give an overview of what can be learned by bringing together results from the research aiming at those (other) independent questions. The section starts with a comparison between the lattice location of transition-metals in narrow-gap GaAs (section 4.1) and wide-gap GaN and ZnO (section 4.2). An overview is then given of the different magnetic components which are superimposed in typical magnetometry data of dilute magnetic materials (Article I and sections 4.3 and 4.4). This is followed by a discussion of possible implications of anion substitution (section 4.2) on the magnetism of transition-metal doped ZnO and GaN (sections 4.3 and 4.4). The section ends with a discussion of limitations of the emission channeling technique which are relevant for the findings presented in this thesis.

4.5.1 Lattice location of transition-metal impurities: comparison between narrow-gap GaAs and wide-gap GaN and ZnO

Figure 4.1 summarizes the results on the lattice location of Mn in GaAs of different doping types and of Mn and Co in ZnO and GaN. In sections 4.1 and 4.2, these two sets of data were discussed within the specific contexts of narrow-gap and wide-gap DMS materials independently. Even though these studies focus on a limited number of transition-metal elements, in only three host materials, it is worthwhile discussing the results within the broader context of lattice location of impurities in semiconductors, i.e. narrow-gap *versus* wide-gap.

For all three materials, the majority fraction corresponds to cation substitutional sites (Ga in GaAs and GaN, Zn in ZnO). Chemically, 3*d* transition metals are more similar to the post-transition metals Ga and Zn. In particular, the ionic radii and electronegativity of Mn and Co are significantly closer to those of Ga and Zn compared to As, N and O, all of which makes it energetically favorable for Mn and Co to substitute the cations. The majority cation substitution observed in both the narrow-gap GaAs and the wide-gap GaN and ZnO is therefore consistent with this expectation. Next we discuss two aspects for which marked differences between the two classes of materials are observed: the thermal stability of the cation-substitutional fractions and the occupied minority sites.

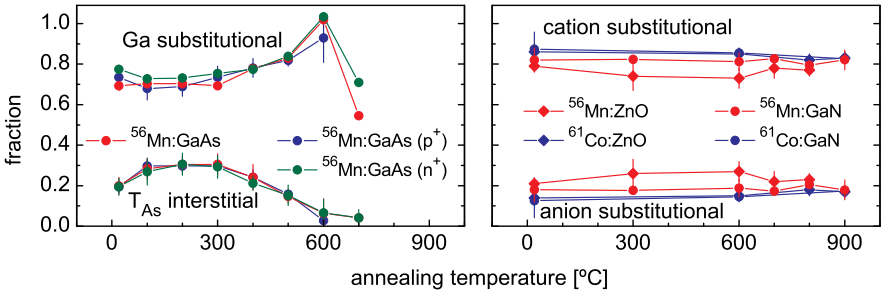

Figure 4.1: Overview of the emission channeling results. (Left) Ga-substitutional and As-tetrahedral interstitial fractions of ^{56}Mn in GaAs of different doping types (section 4.1). (Right) Cation and anion substitutional fractions of ^{56}Mn and ^{61}Co in ZnO and GaN (section 4.2).

4.5.1.1 Thermal stability of the cation-substitutional impurities

The cation-substitutional fractions of Mn and Co in ZnO and GaN remain virtually unchanged up to 900°C. On the other hand, Ga-substitutional Mn in GaAs starts to diffuse already at 700°C (discussed in more detail in Article III). This higher thermal stability of Mn and Co impurities in GaN and ZnO compared to Mn in GaAs reflects the higher binding energy associated with the higher "rigidity" of GaN and ZnO compared to GaAs. A good measure of bond strength is the material's Debye temperature, which indeed is considerably higher for GaN (600 K) and ZnO (920 K) than for GaAs (360 K).

It is also interesting to note that the thermal stability of the cation-substitutional impurities is much higher than in typical DMS, with Co and Mn concentrations of the order of %. While we observe that Ga-substitutional Mn in GaAs become mobile at about $\sim$ 700°C for a concentration below 0.05% (c.f. section 4.1 for more details), Mn segregation occurs already at $\sim$ 300°C in $Ga_{1-x}Mn_xAs$ materials with a Mn concentration of the order of a few percent [1]. Similarly, while we observe that cation-substitutional Mn and Co are immobile up to 900°C for concentrations below 0.05% (c.f. section 4.2 for more details), phase segregation is typically observed for temperatures between 700°C and 900°C in materials implanted with impurity concentrations of the order of a few percent [2–6]. This shows how disorder, alloying and strain effects can significantly decrease the thermal stability of substitutional impurities, favoring impurity

aggregation and consequent phase segregation.

4.5.1.2 Stable minority sites

In addition to the majority cation-substitutional fractions, minority-site fractions were observed in all five impurity-host combinations. Whereas for narrow-gap GaAs the minority fraction consists of *interstitial* Mn (in tetrahedral interstitial sites with As nearest neighbors), in wide-gap GaN and ZnO it consists of impurities in anion *substitutional* sites. For Mn in particular, which was studied in all three materials, one can ask the following questions.

1. Why is interstitial Mn observed in narrow-gap GaAs and not in wide-gap GaN and ZnO?

2. Conversely, why is anion-substitutional Mn observed in GaN and ZnO and not in GaAs?

In principle one can assume that due to the high energy scales inherent to a far-from-equilibrium process such as ion implantation, there is a finite probability of incorporation of the impurities in different types of lattice sites, even those with a high formation energy. What determines which lattice sites remain occupied after the system "cools down" (when the atoms come to rest) is the stability of the impurities in each of those lattice sites, for the temperature at which the implantation and measurements are carried out (normally the same). In this context, stability refers to the tendency of a certain defect configuration to be converted to another. For example, interstitials may be created momentarily upon implantation; if their migration barriers for diffusion are comparable to k_BT, they may diffuse and combine with the vacancies also created upon implantation.[1] Answering question (1) above, one can then assume that interstitial Mn is momentarily formed upon implantation in all three materials GaAs, GaN and ZnO. Because the activation energy for diffusion of interstitial Mn in GaAs is relatively high (1.7–2.3 eV) Mn is stable (and is thus observed) in interstitial sites from room temperature up to 500°C (c.f. section 4.1). However, because the migration barriers of interstitial Mn and Co are probably sufficiently low to allow for the impurities to diffuse and combine with vacancies at room temperature, only substitutional fractions are observed.

[1] These effects of spontaneous annihilation of defects during or shortly after implantation are generally referred to as *dynamic annealing*.

In fact, it is probably during this process of interstitials filling available vacancies that Mn and Co impurities are incorporated in anion sites in GaN and ZnO. Following this reasoning, question (2) can be reformulated as follows. Why can Mn impurities "fill" N/O vacancies in GaN/ZnO and not As vacancies in GaAs? From the point of view of chemical similarities, one would actually expect the opposite. One is tempted to conjecture that since interstitial Mn has a high migration energy in GaAs, a Mn impurity is retained in the interstitial site, i.e. is simply not allowed to diffuse and fill the nearest As vacancy. Such hand-waving arguments are, however, far too speculative. It is difficult to derive general trends from such limited studies, especially for transition-metals, which have a very rich and often puzzling behavior. Systematic studies along the following lines could help to clarify these open questions (which are nevertheless outside the scope of this thesis):

- Studying the lattice location of transition-metals in compound semiconductors with properties related to or in between those of GaAs on the one hand and GaN and ZnO on the other, would allow us to better understand the effect of the bandgap. Among others, GaP (similar to GaAs but wider bandgap), InN (similar to GaN but very narrow gap), AlN (extremely wide-gap), would be interesting materials to explore.

- Studying the lattice location of other transition-metal elements, in particular in GaAs, would in principle show whether other transition-metals also form interstitials. Experiments are under way for ^{59}Fe and ^{65}Ni. Both ^{59}Fe and ^{65}Ni show interstitial fractions. In fact, for ^{65}Ni, the majority fraction is interstitial following annealing at 450°C.

- Studying the temperature dependence, e.g. by implanting and measuring below room temperature, could show whether it is possible to "freeze out" the interstitial transition-metals in GaN and ZnO before they become substitutional by filling the available vacancies.

4.5.2 Magnetometry data of dilute magnetic semiconductors: overview of the different magnetic components

Figure 4.2 summarizes the different magnetic components which have been identified in the magnetization data of the various systems studied in this work (Article I and sections 4.3 and 4.4). Each component can be linked to its source as follows.

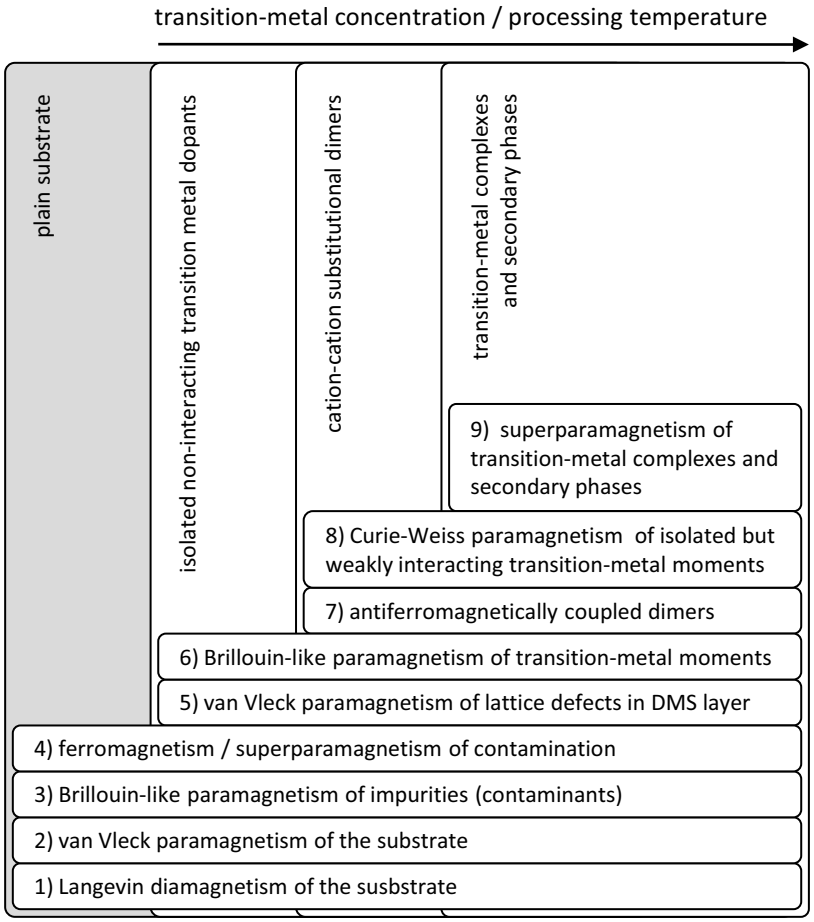

Figure 4.2: Overview of the various components which can be superimposed in the magnetometry data of dilute magnetic semiconductors (based on the results of Article I and sections 4.3 and 4.4).

4.5.2.1 Substrate

Based on their dependences on applied field and temperature, at least four components can be distinguished in the magnetization data of typical diamagnetic substrates such as the ones used in this study (Al_2O_3, Si, ZnO, MgO and $SrTiO_3$).

1) Langevin diamagnetism. Langevin diamagnetism is associated with the tendency of electrons to partially shield the interior of a body from an applied magnetic field. The classical Langevin derivation of the diamagnetic susceptibility χ_{DM} gives

$$\chi_{\mathrm{DM}} = -\frac{NZe^2}{6mc^2}\left\langle \rho^2 \right\rangle \tag{4.1}$$

where N is the number of atoms, Z their atomic number, e is the electron charge, m the electron mass and $\left\langle \rho^2 \right\rangle$ is the mean square distance of the electrons from the nucleus [7]. Although largely simplified, this derivation is quite illustrative of the origin of diamagnetism in solids and of its general dependencies in temperature and field: the susceptibility is field-independent (i.e. the magnetic moment is linear in H) and negative, which is in fact what defines diamagnetism. This expression also implies that the magnetic susceptibility of diamagnetic materials is temperature independent ($\left\langle \rho^2 \right\rangle$ is virtually independent of temperature), which is in many cases true but not in general, as discussed next in terms of van Vleck paramagnetism.

At moderate applied fields (~ 1 T) the magnetic moment of diamagnetic materials is typically orders of magnitude smaller than that of paramagnetic or ferromagnetic materials of equivalent mass or volume. However, since the substrate is also typically several orders of magnitude larger than the magnetic material which is deposited on it (or, in our case, the implanted layer in its near surface region), the diamagnetic component can be relevant. In fact, for all the samples studied here (c.f. Articles I and VII-IX), the diamagnetic component is the dominant one.

2) Van Vleck paramagnetism. The quantum mechanical treatment of the magnetic susceptibility of a real semiconductor crystal is a very complex problem. An insightful and relatively good approximation is given within the bond-orbital model (BOM) [8], in which the magnetic susceptibility is decomposed in three terms:

$$\chi = \chi_c + \chi_{\mathrm{L}} + \chi_{\mathrm{p}}\,. \tag{4.2}$$

The first two are diamagnetic contributions which originate from the core (χ_c) and valence (χ_{L}) electrons, and the third is a van Vleck paramagnetic component (χ_{p}) due to the valence electrons [8]. The core diamagnetic term (χ_c) is equivalent to the classical Langevin term (4.1). The valence

diamagnetic term (χ_{L}) is essentially equivalent to the core term χ_c but the charge distribution is evaluated for the bonding electrons. Due to its dependence in $(r - r_i)^2$, which is related to the bond length, and N, χ_{L} has a linear dependence on α, the linear thermal expansion coefficient.[2] However, because α is of the order of 10^{-6} K^{-1}, χ_{L} is essentially temperature independent. The van Vleck-type paramagnetic term (χ_{p}) is determined by the energy separation $(E_a - E_b)$ of bonding (b_i) and anti-bonding (a_j) states

$$\chi_{\mathrm{p}} = \frac{Ne^2}{2m^2c^2(E_a - E_b)} \sum_{i,j} \langle a_j \left| l_{zi} \right| b_i \rangle \ , \tag{4.3}$$

where l_z is the z component of the orbital angular momentum operator. The temperature dependence of χ_{p} (4.3) is dominated by the temperature dependence of $(E_a - E_b)$ which in turn is proportional to the bandgap E_g and of the order of 10^{-4} K^{-1}. A simplified version of (4.3) has been suggested in [9] which shows this dependence

$$\chi_{\mathrm{p}} = \frac{B}{\beta E_g} \, , \tag{4.4}$$

where β is a proportionality factor of the order of unity and B is proportional to an average of the matrix elements in (4.3), which has been shown in [8] to be a decreasing function of increasing polarity (or ionicity) α_{P} of the material. In short, χ_{p} decreases with increasing bandgap E_g and polarity (or ionicity) α_{P}, and its temperature dependence scales with the temperature dependence of the bandgap. For GaAs, for example, this temperature dependence of χ (dominated by the temperature dependence of χ_p) is very small ($-\chi$ increases by about 1% from 300 K to 5 K), and for materials with wider bandgaps and more ionic, such as ZnO and Al_2O_3, it is even smaller. However, because the magnetic signal of a DMS film can be dominated by that of the substrate, even such small temperature dependencies must be taken into account (c.f. section 4.4, articles VIII and IX).

Note that conduction electrons may also contribute to the susceptibility. These effects are known as Landau diamagnetism and Pauli paramagnetism and can be very important in non-ferromagnetic metals and doped semiconductors. However, because the substrates that were used in this work are highly insulating, such effects can be neglected.

[2] Because $(r - r_i)^2 \propto \alpha^2$ and $N \propto \alpha^{-3}$.

3) Brillouin-like behavior of paramagnetic (contaminant) impurities. Macroscopic amounts of a compound are bound to contain impurities which were non-intentionally incorporated. Some of these impurities can display Brillouin-like paramagnetic behavior. The 3*d* transition metals Fe, Co and Ni are common examples of such paramagnetic impurities. The concentration of impurities in substrates which are produced for applications in IC technology (e.g. Si and GaAs substrates) tend to be orders of magnitude lower compared to substrates of ZnO and $SrTiO_3$. For example, the Si substrates on which the GaN thin films were grown (c.f. Article VIII) showed no detectable paramagnetic contamination within SQUID sensitivity. On the other hand, the ZnO substrates used as host material for Fe implantation (c.f. Article IX) were heavily contaminated. Brillouin-like paramagnetism is described in some detail in section 4.5.2.2 below, in the context of the transition-metal impurities incorporated intentionally (component 6 in Fig. 4.2).

Unlike for the diamagnetic background of the substrates, correcting for the Brillouin-like contribution of paramagnetic impurities is far from trivial, due to the non-trivial dependence on applied field and temperature. For high temperature measurements ($\sim$ 100 K), the paramagnetic susceptibility is approximately linear and can in principle be corrected for along with the linear diamagnetic background of the substrate. This was the case of the work described in Article VII, in which only room-temperature measurements were performed. However, for low temperature measurements, as is often required, this is no longer the case. Hence, measurements should ideally be carried out in samples for which the intrinsic signal of the magnetic thin film or nanostructures is well above that of the paramagnetic impurities. This was the case for our measurements of Cr-implanted GaN (GaN films grown on Si and Al_2O_2) (Article VIII). When this is not possible, the substrates must be carefully characterized prior to implantation (or deposition). This was the case for the work described in Article IX. ZnO substrates were characterized prior to Fe implantation. The Brillouin behavior of the paramagnetic impurities was then thoroughly analyzed in detail and taken into account in the analysis of the data following Fe implantation. Note, however, that the intrinsic magnetic signal must be at least comparable to that of the impurities, or any apparent changes in magnetic behavior upon implantation or deposition may simply be due to some degree of setup-related irreproducibility.

4) Ferromagnetic-like behavior of contaminant material. The ferromagnetic-like contributions of magnetic contamination were thoroughly described and discussed in Article I. The main conclusions can be summarized as follows. Under common experimental conditions (in terms of sample preparation, processing and handling), magnetic contamination is likely to occur. The saturation moment of the ferromagnetic-like component of the contaminant material can be as high as 10^{-4} emu, which is comparable to the typical values for magnetic thin films and nanostructures deposited on diamagnetic substrates. Adequate experimental procedures, such as those described in Article I, minimize such ferromagnetic-like background very efficiently. When such procedures are followed, extrinsic ferromagnetic-like signals can be reproducibly kept below 5×10^{-7} emu.

4.5.2.2 Dilute limit

In the dilute limit, possible magnetic interactions between the transition metal impurities can be neglected. In this case, two paramagnetic components can be distinguished in the magnetometry data: van Vleck paramagnetism of lattice defects and Brillouin-like paramagnetism of transition-metal impurities.

5) Van Vleck paramagnetism of lattice defects. An unexpected paramagnetic component was observed in Fe-implanted ZnO (Article IX). Based on its linear dependence in applied field, we classified this component as van Vleck paramagnetism. Based on the fact that the correspondent susceptibility scaled with the defect density estimated from the RBS/C data, we tentatively identified the source as implantation induced defects. Further theoretical and experimental investigations may clarify the origin and nature of this component.

6) Brillouin-like paramagnetism of transition-metal impurities. The diamagnetism and paramagnetism introduced above describe crystals composed of atoms or ions with $J = 0$, where $\hbar\mathbf{J}$ is the total angular momentum, i.e. the sum of the orbital $\hbar\mathbf{L}$ and spin $\hbar\mathbf{S}$ angular momenta. $J = 0$ for atoms or ions with orbits which are filled (closed orbitals),[3] which is the case of the materials (substrates and thin films) which were used in this work, assuming that they are pure and defect free. It may no longer be

[3] If the ground state obeys the Hund's rules, $J = 0$ also in orbitals with one atom short from being half-filled. This is however a special case of what is described here.

the case if the materials are doped with impurities (or contaminated with impurities during growth). For $3d$ transition metal impurities, which are the typical magnetic dopants in DMS materials and are also very common contaminants even in high quality substrates, this is necessarily not the case. $3d$ transition metals have incomplete $3d$ shells, which in most cases implies that $J \neq 0$.

The magnetic-field dependent term in the Hamiltonian of an atom or ion with $J \neq 0$ in the free space is given by the Larmor interaction energy

$$H_L = -\mu_{\mathbf{at}} \cdot \mathbf{H} = m_J g \mu_B \,, \tag{4.5}$$

where μ_B is the Bohr magnetron, m_J is the azimuthal quantum number and has the values J, $J-1$, ..., $-J$. The g factor (or spectroscopic splitting factor) for an electron spin is $g = 2.0023$, usually taken as 2.00. For a free atom or ion, the g factor is given by the Landé equation, which is a function of only J, L and S. Taking into account Maxwell–Boltzmann statistics,[4] the magnetic moment of N atoms or ions can then be shown [7] to be

$$\mu = NgJ\mu_B B_J(x) \,, \quad (x \equiv \frac{gJ\mu_B H}{k_B T}) \,, \tag{4.6}$$

where the Brillouin function $B_J(x)$ is

$$B_J(x) = \frac{2J+1}{2J}\coth\left(\frac{2J+1}{2J}x\right) - \frac{1}{2J}\coth\left(\frac{1}{2J}x\right) . \tag{4.7}$$

$B_J(x)$ is plotted in Fig. 4.3 (d) for $L = 0$ and $J = S = 3/2$ at $T = 2$ K. Note that as $T \to 0$ for finite fixed H, $M \to Ng\mu_B J$, i.e. each ion is completely aligned by the field, $|J_z|$ has its maximum value J and μ is "saturated". Increasing J or decreasing T decreases the field at which μ saturates.

When $g\mu_B JH \ll k_B T$, the small-x expansion gives

$$\chi_C = \frac{N(g\mu_B)^2}{3}\frac{J(J+1)}{k_B T} \,, \quad (k_B T \gg g\mu_B JH) \,, \tag{4.8}$$

or

$$\chi_C = \frac{C}{T} \,, \tag{4.9}$$

[4] The zero-field ground state is degenerate and for for low fields the splitting of the $(2J+1)$ lowest-lying states is comparable to $k_b T$.

which is known as Curie's law (with C the Curie constant). Note that the paramagnetic susceptibility (4.8) is larger than the temperature-independent Larmor diamagnetic susceptibility (4.1) by a factor of the order of 5×10^2 at room temperature and 3×10^5 at 5 K.

The Brillouin function description is valid for ions or atoms in a spherically symmetric free space. However, ions or atoms in a lattice are subject to its anisotropic crystal field. Crystal field effects have a major influence on the paramagnetism of transition metals, particularly for the $3d$ series (partially filled $3d$ orbitals) where it *quenches* the orbital moment $\mathbf{L}$ (i.e. $\mathbf{L} = 0$ and $\mathbf{J} = \mathbf{S}$). The influence of the crystal field goes beyond the orbital moment quenching and are particularly important in the description of the paramagnetism of transition-metal doped ZnO and GaN (c.f. section 1.4.2.3). Since ZnO and GaN are wurtzite materials, the transition-metal impurities are subject to a trigonal crystal field. Combined with spin-orbit interaction, this anisotropic crystal field induces a strong magnetic anisotropy, which can be described by a zero-field splitting of the fundamental state and by an anisotropic effective g-factor in an effective spin Hamiltonian H_s of the form

$$H_s = \mu_B g_{\parallel} H_z S_z + \mu_B g_{\perp} (H_x S_x + H_y S_y) + D S_z^2 \,, \tag{4.10}$$

where S is the spin quantum number and D describes the zero-field splitting and $g_{\parallel}$ and $g_{\perp}$ are the effective g-factors for directions of magnetic field parallel and perpendicular to the wurtzite c-axis, respectively. H_s (4.10) can be used to calculate the energy levels of the S manifold $|M_S\rangle = |-S\rangle$, $|-S+1\rangle$, ..., $|-S\rangle$ by diagonalizing the matrix $\langle M_S| H_s |M_S\rangle$ for $H \parallel c$ ($H = H_z$) and $H \perp c$ ($H = H_x$).

Simply by comparing the Hamiltonians (4.10) and (4.5), one can expect that the deviation from Brillouin behavior due to crystal field effects increases with increasing zero-field splitting D. As discussed in section 1.4.2.3, magnetic ions with $S = 5/2$ (Mn^{2+} and Fe^{3+}) have two orders of magnitude smaller zero-field splitting than other spin configurations with $S = 3/2$ and $S = 2$. The g-factors for $S = 5/2$ spin configuration are also nearly independent of the direction of magnetic field, and the values of $g_{\parallel}$ and $g_{\perp}$ are close to 2. Hence, the magnetization of these $S = 5/2$ ions can be described to a good approximation by the Brillouin function. This was the case in our analysis of the magnetometry data of Fe-implanted ZnO (Article IX), in which we used the Brillouin function to model the magnetization of the Fe^{3+} fraction. For ions with $S = 2$ (Mn^{3+}, Fe^{2+} and Co^{3+}) and

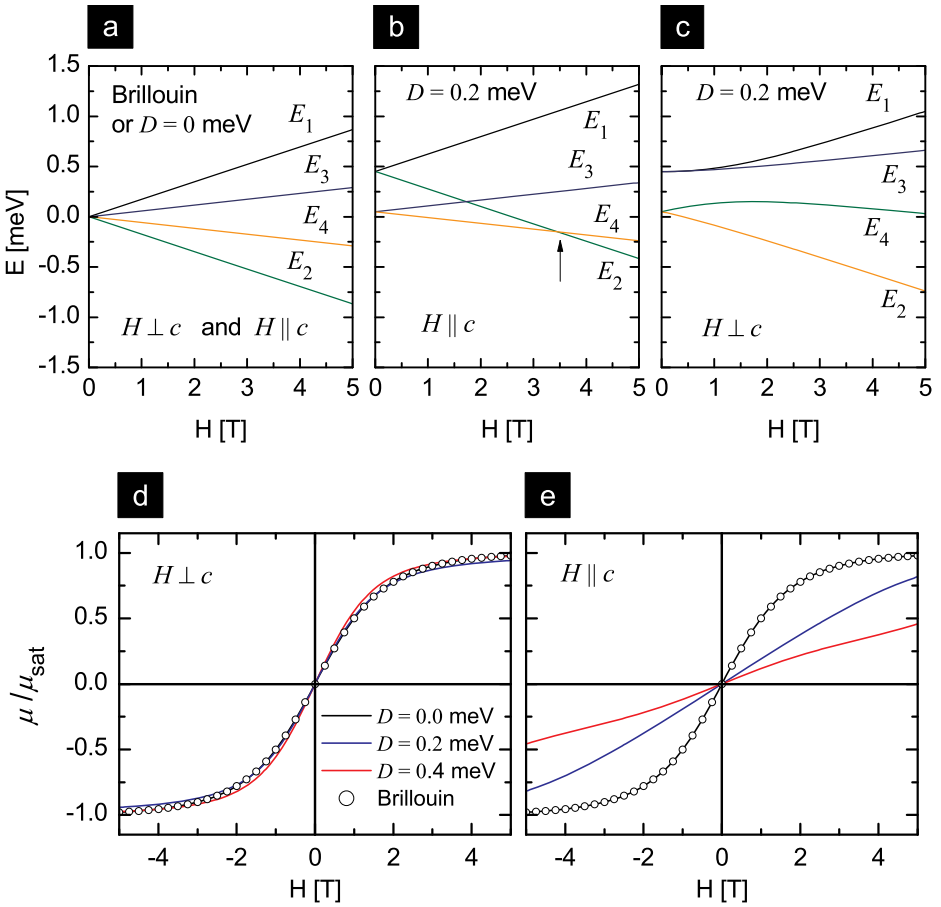

Figure 4.3: Calculated energy levels for a spin $S = 3/2$ with isotropic g-factor $g_\perp = g_\parallel = g$ according to the free atom Hamiltonian (4.5) (a) and the effective spin model (4.10) with $D = 0.2$ meV for $H \parallel c$ (b) and $H \perp c$ (c). The arrow indicates the level crossing. Calculated $\mu(H)$ at 2 K for $H \parallel c$ (d) and $H \perp c$ (e) for Brillouin (free atom) behavior (circles) and for different values of D (lines).

$S = 3/2$ (Co^{2+}), the zero field splitting is of the order of 0.3 meV (c.f. section 1.4.2.3) which, as shown below, induces a strong magnetic anisotropy which requires a somewhat more complex description. We were unable to explicitly take into account such crystal field effects in the analysis of the paramagnetic behavior of Cr^{3+} ($S = 3/2$) in Cr-doped GaN (Article VIII) and of Fe^{2+} ($S = 2$) in Fe-doped ZnO, since there are no reported values of the anisotropic g-factors and zero-field splitting parameters of Cr^{3+} in GaN and Fe^{2+} in ZnO. However, due to its generality and relevance in the analysis of magnetization data of DMS materials, it is instructive to give here an example of how such crystal field effects induce deviations from the Brillouin behavior. Consider a transition metal impurity with $S = 3/2$ (e.g. Co^{2+} or Cr^{3+}), and for simplicity, an isotropic $g_{\parallel} = g_{\perp} = g = 2.00$. For $H \parallel c$, the matrix obtained from H_s (4.10) and the basis $|-3/2\rangle$, $|-1/2\rangle$, $|1/2\rangle$ and $|3/2\rangle$ is diagonal and energy levels are given by

$$E_1 = \frac{9D}{4} + \frac{3}{2}\mu_B g_{\parallel} H_z\,, \quad E_2 = \frac{9D}{4} - \frac{3}{2}\mu_B g_{\parallel} H_z\,,$$
$$E_3 = \frac{D}{4} + \frac{1}{2}\mu_B g_{\parallel} H_z\,, \quad E_4 = \frac{D}{4} - \frac{1}{2}\mu_B g_{\parallel} H_z\,.$$

The four energy levels are plotted in Fig. 4.3 (c) as a function of field H, for $D = 0.2$ meV. At moderate magnetic fields the lowest energy level E_4 is $S = 1/2$-like. At high fields the $S = 3/2$-like E_2 level becomes the lowest lying in energy (arrow in Fig. 4.3). For $H \perp c$, the diagonalization gives

$$E_1 = \frac{5D}{4} + \frac{1}{2}\mu_B g_{\perp} H_x + \sqrt{\mu_B^2 g_{\perp}^2 H_x^2 - D g_{\perp}\mu_B H_x + D^2}\,,$$
$$E_2 = \frac{5D}{4} + \frac{1}{2}\mu_B g_{\perp} H_x - \sqrt{\mu_B^2 g_{\perp}^2 H_x^2 - D g_{\perp}\mu_B H_x + D^2}\,,$$
$$E_3 = \frac{5D}{4} - \frac{1}{2}\mu_B g_{\perp} H_x + \sqrt{\mu_B^2 g_{\perp}^2 H_x^2 - D g_{\perp}\mu_B H_x + D^2}\,,$$
$$E_4 = \frac{5D}{4} - \frac{1}{2}\mu_B g_{\perp} H_x - \sqrt{\mu_B^2 g_{\perp}^2 H_x^2 - D g_{\perp}\mu_B H_x + D^2}\,.$$

These levels are plotted in Fig. 4.3 (c). In this case the lowest lying level E_4 is $S = 3/2$-like and no crossing of the energy levels occurs.

Calculating $\mu(H)$ of such system is similar to the derivation of the Brillouin behavior, but the partition function is now built using the energy levels E_i (E_1 to E_4). In Fig. 4.3, $\mu(H, T = 2\,\mathrm{K})$ is plotted for $H \perp c$ (d) and $H \parallel c$ (e) with an isotropic g-factor $g_{\perp} = g_{\parallel} = 2$ and different values of zero-field splitting D. For $D = 0$ (and isotropic g), the effective spin Hamiltonian

(4.10) is equivalent to the free atom case (4.5), i.e. μ is isotropic and given by the Brillouin function. With increasing D, the deviation from Brillouin behavior becomes increasingly noticeable, particularly for $H \parallel c$, which results in a pronounced magnetic anisotropy.

4.5.2.3 Intermediate magnetic impurity concentration

With increasing concentration, the isolated-impurity approximation, used above to describe the dilute limit, no longer holds. Magnetic interactions must be taken into account. In section 4.4 (Articles VIII and IX), we identified two distinct magnetization components from which the effect of magnetic interactions can be inferred: impurity dimers antiferromagnetically coupled via strong nearest-cation-neighbor interactions, and Curie-Weiss paramagnetism of isolated but weakly interacting transition-metal moments.

7) Antiferromagnetically coupled dimers. For a few % of randomly distributed cation-substitutional impurities, the fraction of cation-cation dimers (two impurity ions in nearest-cation-neighbor sites) is significant. In wurtzite ZnO or GaN, for example, the concentration of isolated ions and dimers in is given by $x_{\text{isolated}} = x(1-x)^{12}$ and $x_{\text{dimers}} = 12x^2(1-x)^{18}$, respectively [10]. For $x = 0.02$ (2%), $x_{\text{isolated}} = 0.016$ and $x_{\text{dimers}} = 0.0033$, i.e., about 78% of the impurities are isolated, 17% form pairs, and the remaining 5% form complexes of more than two impurities. We analyzed the magnetization data of Cr-implanted GaN taking dimer formation into account (Article VIII). We concluded that strong nearest-cation-neighbor antiferromagnetic interactions between Cr ions in a dimer configuration impose the antiparallel alignement of the Cr moments. These magnetically self-compensated dimers contribute to the net magnetization with a vanishingly small moment, i.e. they are magnetically *quenched*.

8) Curie-Weiss paramagnetism of isolated but weakly interacting transition-metal moments. Taking the example of the previous paragraph, the 78% of the transition metal impurities which do not form pairs may still magnetically interact. Since the distance between interacting particles is larger than that between nearest-cation neighbors, the interaction is, in principle, weaker than that described in the previous paragraph. These interactions may be so weak that the associated ordering temperature may not be reached experimentally. Typically, the effect of magnetic

interactions above the associated ordering can be modeled by replacing the temperature T in the Curie law (4.9) by an effective temperature $T - \theta$. This is known as the Curie-Weiss law

$$\chi = \frac{C}{T - \theta}\,, \tag{4.11}$$

where θ is the Weiss temperature. If $\theta > 0$, the interaction is ferromagnetic. Typically $\theta \gtrsim T_C$, with T_C being the ferromagnetic ordering temperature, or Curie temperature. If $\theta < 0$, the interaction is antiferromagnet. In general $-\theta > T_N$, with T_N being the antiferromagnetic ordering temperature, or Néel temperature. Based on this approach, we suggested that isolated Cr impurities in GaN weakly and antiferromagnetically interact with Cr neighbors outside the nearest-cation-neighbor shell (Article VIII). We note, however, that this type of analysis should be applied very carefully. In [11] it is shown that, while the paramagnetism of Co-doped ZnO is correctly modeled using an adequate effective spin Hamiltonian *without* considering magnetic interactions, attempting to fit the same data using the Brillouin function or the Curie law would require the use of an effective temperature $T - \theta$ ($T + T_0$ in [11]), which could be misinterpreted as an effect of antiferromagnetic interactions.

4.5.2.4 Percolation and segregation threshold

With increasing concentration or processing temperature, the magnetic impurities tend to aggregate in large complexes (e.g. substitutional Fe clusters in Article IX) or to segregate into secondary phases (c.f. section 1.4.1). Depending on the size and type of magnetic order within these magnetic "nanoparticles", different behaviors can be observed. The magnetic impurities within very small complexes (few atoms) may order ferromagnetically and thus contribute to a paramagnetic-like component with and average moment per complex which is larger than that of isolated moments. The complexes may be relatively large but dominated by antiferromagnetic interactions, in which case only a fraction of uncompensated spins may contribute to the net moment per complex. This was suggested to be the case for the Fe "substitutional clusters" in ZnO (Article IX). On the other hand, if ferromagnetic order dominates and the complexes or precipitates are sufficiently large (but still in the single-domain regime), the system can be considered superparamagnetic. In fact, in Fig. 4.2, all these effects are included in the **superparamagnetic component (9)**. If the

average moment per particle in less than about 100 μ_B, the component is more paramagnetic-like: at low temperatures the magnetization loops show a Brillouin-like behavior; at higher temperatures (of the order of 100 K), the component is Curie-like, i.e. linear in applied magnetic field and inversely dependent in temperature (c.f. Articles VIII and IX). If, on the other hand, the complex or particle is large enough, i.e. with an average moment per particle of several thousand μ_B, the behavior of the system is more superparamagnetic-like: field and temperature dependence approximately described by the Langevin function, possibly displaying field-cooled (FC) versus zero-field-cooled (ZFC) irreversibility (c.f. e.g. [3, 12]).

4.5.2.5 Beyond the scope of DMS

Although the "chart" in Fig. 4.2 was compiled in the specific context of diamagnetic semiconductors implanted with transition-metal impurities, its usefulness spans a much wider range of fields. For example, the substrates which have been used (Al_2O_3, Si, ZnO, MgO and $SrTiO_3$) are common to various other applications and research fields which also largely rely on magnetometry. Extra components (i.e. what would be"layers" 10 and higher in Fig. 4.2) can then be added depending on the intrinsic magnetic nature of the material under study. Depending on the specific sample which is measured, some of these "background" components (1-9) can be relevant, others negligible. In one extreme, one or more of these "background" components dominate over the signal of the component of interest (layer 10). In that case, unless that background can be correctly accounted/corrected for, the measurement is useless. On the other extreme, the component of interest dominates over all the others, and corrections are not necessary.

The summary in Fig. 4.2 illustrates the extreme complexity inherent to the characterization of magnetic materials with very small magnetic signals. During the last 20 years, major technological developments in magnetometry techniques, namely in SQUID magnetometry, have allowed condensed-matter physicists and materials scientists to measure smaller and smaller magnetic structures. However, as we thrive on applying Feynman's insight "there's plenty of room at the bottom" to the field of nanomagnetism, we must not forget that there is also plenty of magnetism everywhere; literally everywhere. Even dust, that omnipresent but almost invisible entity which we struggle to eliminate in sophisticated cleanrooms, is potentially magnetic. Common dust contains a few % of Fe in its composition [13], which can be in metallic or oxide forms, i.e. spanning a whole range of magnetic

order structures. One would expect this figure to be even higher in laboratories where magnetic materials are synthesized and characterized on a daily basis. The growing number of reports of ferromagnetism in materials which are later shown not to be ferromagnetic makes us wonder: is the magnetometry community evolving as fast as the magnetometers it uses?

4.5.3 Implications of anion substitution on the magnetism of transition-metal doped ZnO and GaN

A "global" discussion of the results in this thesis would be incomplete without an analysis of the potential effects of anion substitution (presented in section 4.2) on the magnetic behavior of transition-metal doped ZnO and GaN (presented in sections 4.3 and 4.4). In section 4.2, the potential implications of anion substitution on the magnetism of wide-gap DMS are discussed in terms of self-compensation mechanisms and their effects on the magnetic interactions between the $3d$ magnetic moments. However, those potential "links" between section 4.2 and sections 4.3 and 4.4 are not discussed explicitly in any of those sections since the studied materials differ significantly. Even though all materials have been implanted under similar conditions, the transition-metal concentrations differ by at least one order of magnitude ($< 0.05\%$ for lattice location experiments and 0.3–35% for magnetic characterization), making the transferability of the results a matter of speculation. Only one selected system, Fe-implanted ZnO, was studied simultaneously in terms of impurity lattice location and magnetism (Article IX). There, Fe impurities were shown not to occupy anion (O) sites for any of the implantation and annealing conditions. Although this establishes the generality of the results in this particular system, it also means that nothing can be learned regarding the role of anion substitution in magnetic order mechanisms. In principle, there is no reason to consider anion substitution as a potential means of inducing high-temperature ferromagnetism in wide-gap DMS. This discussion then comes down to one main question. Can the absence of ferromagnetism in Mn- and Co-implanted ZnO and GaN be explained on the basis of anion substitution (and thus specific to ion-implanted materials) instead of a general lack of mechanisms of high-temperature ferromagnetic order in wide-gap DMS? Based on our results alone, one would answer "perhaps". A more categorical answer can only be given based on a critical review of the literature on materials prepared using methods different from ion implantation. Such litereture analyses are given in the introductory section 1.4.2 and the results sections

4.3 and 4.4 of this thesis. Based on them, the author's opinion is that the answer is "no".

4.5.4 Limitations of the emission channeling technique

In sections 4.1 and 4.2 on the lattice location of transition-metal impurities using the emission channeling technique, we compared our results to those of previous studies using different techniques and discussed potential sources of error. In this section we will review and extend that discussion specifically in terms of limitations of the emission channeling technique. In the context of this thesis, the general aim of determining the *lattice location of the impurities* can be divided in three specific aims:

1. To identify the occupied lattice sites, in particular minority (but significant) sites;

2. To study the thermal stability of impurities in those sites;

3. To assess the phase pureness of a doped layer.

Regarding minority sites (1) and thermal stability (2), the limitations of the emission channeling technique can be expressed mostly in terms of generality. In the current implementations of the technique, the impurity probes can only be incorporated using ion implantation. Possible extrapolation or generalization of the results of such experiments to materials doped during growth is highly non-trivial, since the impinging atom energy varies by several orders of magnitude depending on the doping/growth method: for example, of the order of 0.1 eV for molecular beam epitaxy (MBE), 1 eV for sputtering deposition, 10 eV for pulsed laser deposition (PLD), 1 keV for ion implantation. Lattice sites associated with high formation energies can thus be populated in significantly higher amounts by impurities incorporated by ion implantation compared to other processes closer to equilibrium. In addition, the high-energy particle bombardment inherent to ion implantation creates lattice defects (beam-induced damage) which may exist in much lower or even negligible concentrations in materials prepared by other methods. Such defects may play a role in determining the lattice location of the impurities, for example, by changing the material's Fermi-level or due to strain effects. In addition, the formation of impurity-defect complexes may affect the thermal stability of the impurities in the occupied lattice sites. Beam-induced damage also poses a limit on the concentration/fluence regimes which can be studied with emission channeling.

With increasing implanted fluence, the reduced crystallinity deteriorates the channeling effects, and in the amorphization limit precludes emission channeling measurements.

The phase pureness (3) can in some cases be assessed by comparing the fraction of impurities in substitutional sites (in a phase which is structurally coherent with the host) versus a *random* fraction in a non-coherent phase. We used this approach in the case of Fe-implanted ZnO (section 4.4, Article IX). However, such approaches are only valid when one can rule out the formation of secondary phases with a crystallographic structure which is perfectly coherent with the host. This, in turn, can be inferred from studies using techniques which are complementary to emission channeling, such as x-ray absorption fine structure XAFS, small-angle X-ray scattering (SAXS) and Mössbauer spectroscopy.

Bibliography

[1] K. M. Yu, W. Walukiewicz, T. Wojtowicz, I. Kuryliszyn, X. Liu, Y. Sasaki, and J. K. Furdyna, "Effect of the location of Mn sites in ferromagnetic $Ga_{1-x}Mn_xAs$ on its Curie temperature," *Phys. Rev. B*, vol. 65, p. 201303, 2002.

[2] S. Zhou, K. Potzger, J. von Borany, R. Grotzschel, W. Skorupa, M. Helm, and J. Fassbender, "Crystallographically oriented Co and Ni nanocrystals inside ZnO formed by ion implantation and postannealing," *Phys. Rev. B*, vol. 77, p. 035209, 2008.

[3] S. Zhou, K. Potzger, G. Talut, H. Reuther, J. von Borany, R. Groetzschel, W. Skorupa, M. Helm, J. Fassbender, N. Volbers, M. Lorenz, and T. Herrmannsdoerfer, "Fe-implanted ZnO: Magnetic precipitates versus dilution," *J. Appl. Phys.*, vol. 103, p. 023902, 2008.

[4] R. P. Borges, B. Ribeiro, A. R. G. Costa, C. Silva, R. C. da Silva, G. Evans, A. P. Goncalves, M. M. Cruz, and M. Godinho, "Magnetic and transport properties of transition-metal implanted ZnO single crystals," *Eur. Phys. J. B*, vol. 79, p. 185, 2011.

[5] Y. Wang, J. Zou, Y. J. Li, B. Zhang, and W. Lu, "Mn behaviors in Mn-implanted ZnO," *Acta Mater.*, vol. 57, p. 2291, 2009.

[6] W. Kim, H. J. Kang, S. K. Noh, J. Song, and C. S. Kim, "Magnetic clusters in Co ion-implanted GaN," *J. Magn. Magn. Mater.*, vol. 310, p. E729, 2007.

[7] C. Kittel, *Introduction to solid state physics.* Wiley, 2004.

[8] D. J. Chadi, R. M. White, and W. A. Harrison, "Theory of magnetic-susceptibility of tetrahedral semiconductors," *Phys. Rev. Lett.*, vol. 35, p. 1372, 1975.

[9] S. Hudgens, M. Kastner, and H. Fritzsch, "Diamagnetic susceptibility of tetrahedral semiconductors," *Phys. Rev. Lett.*, vol. 33, p. 1552, 1974.

[10] R. E. Behringer, "Number of Single, Double, and Triple Clusters in a System Containing Two Types of Atoms," *J. Chem. Phys*, vol. 29, p. 537, 1958.

[11] A. Ney, T. Kammermeier, K. Ollefs, S. Ye, V. Ney, T. C. Kaspar, S. A. Chambers, F. Wilhelm, and A. Rogalev, "Anisotropic paramagnetism of Co-doped ZnO epitaxial films," *Phys. Rev. B*, vol. 81, p. 054420, 2010.

[12] H. G. Silva, H. L. Gomes, Y. G. Pogorelov, L. M. C. Pereira, G. N. Kakazei, J. B. Sousa, J. P. Araujo, J. F. L. Mariano, S. Cardoso, and P. P. Freitas, "Magnetic and transport properties of diluted granular multilayers," *J. Appl. Phys.*, vol. 106, p. 113910, 2009.

[13] M. M. Mills, C. Ridame, M. Davey, J. La Roche, and R. J. Geider, "Iron and phosphorus co-limit nitrogen fixation in the eastern tropical North Atlantic," *Nature*, vol. 435, 2005.

Chapter 5

Conclusions

In this PhD thesis, we addressed two major aspects of DMS materials: (1) **structure**, in terms of lattice location of the transition-metal impurities as well as their interaction with lattice defects; (2) **magnetism**, investigating the possibility of inducing room temperature ferromagnetism in the most promising wide-gap DMS systems, and among those, comprehensively describing the magnetic behavior in the phase-pure region of the phase diagram of representative impurity-host combinations. Aiming at the specific challenges currently being faced by each of the two main classes of DMS materials, i.e narrow- and wide-gap, we studied Mn-doped GaAs, which is the "canonical" narrow-gap DMS (with the highest Curie temperature reported so far) and transition-metal doped ZnO and GaN, which are the most intensively studied wide-gap DMS systems.

In **Mn-doped GaAs**, we investigated the **lattice location of Mn impurities** in the low concentration regime ($< 0.05\%$) in undoped and heavily *p*- and *n*-type doped GaAs, as a function of annealing temperature up to $\sim$700°C. In addition to the majority substituting for Ga, a significant fraction of Mn occupies tetrahedral interstitial sites with As nearest neighbors. The interstitial fraction is stable up to 400°C, with an activation energy for diffusion of 1.7–2.3 eV. Substitutional Mn becomes mobile at higher temperatures, $\sim$700°C, with an activation energy of $\sim$3 eV. Since varying the GaAs doping character, and thus the concentration of potentially trapping defects, has no measurable effect on the migration energy of the interstitial fraction, we conclude that the observed high thermal stability is characteristic of isolated interstitial Mn. Being difficult to reconcile with the general belief that interstitial Mn is the donor defect that out-diffuses at $\sim$200°C, our findings motivate a careful reassessment of the structural

effects of low temperature annealing of $Ga_{1-x}Mn_xAs$. First, placing the diffusion of interstitial Mn well above 200 °C reopens the problem of identifying the donor defect that diffuses at low temperatures. Second, and more importantly, it suggests new strategies and prospects for achieving pure substitutional doping and higher Curie temperatures in $Ga_{1-x}Mn_xAs$. First of all, one may question if attempting to induce the out-diffusion of Mn_I by thermal annealing is an adequate route, since interstitial Mn is immobile up to temperatures where phase segregation is known to occur. On the other hand, since the interstitial Mn remains in the matrix after low temperature annealing, it may still be possible to increase the Curie temperature of Mn-doped GaAs above the current record value of 185 K. If a post-processing method can be developed which either removes the interstitial Mn fraction or converts it to substitutional, higher hole and effective Mn concentrations, and consequently higher Curie temperatures, can in priciple be achieved. For example, it may be possible to incorporate the interstitial Mn atoms in substitutional sites by, intentionally creating Ga vacancies (*e.g.* by electron irradiation) and *locally* exciting the Mn_I atoms (*e.g.* by flash-lamp or pulsed laser annealing), promoting the short ranged $Mn_I + V_{Ga} \rightarrow Mn_{Ga}$ reaction while avoiding long range diffusion and subsequent phase segregation. Since it is believed that a Curie temperature of 300 K can be achieved with $x \approx 0.10$ of purely substitutional Mn, and given that it is currently possible to grow high quality films with $x > 0.10$ (where a fraction is however incorporated interstitially), such post-growth processing may allow for the realization of room temperature ferromagnetism in $Ga_{1-x}Mn_xAs$.

Regarding the **lattice location of Mn and Co in ZnO and GaN** in the low concentration regime ($< 0.05\%$), we have determined that, in addition to the majority substituting for the host cations (Zn in ZnO and Ga in GaN), significant fractions of the Mn and Co impurities occupy substitutional anion sites (O in ZnO and N in GaN). These anion substitutional fractions are virtually unaffected by thermal annealing up to 900°C. Combined with previous emission channeling studies on the lattice location of Fe (located in between Mn and Co in $3d$ series of the periodic system) in ZnO and GaN, the following conclusions can be drawn: (1) Unlike Fe, minority fractions ($\sim 20 - 30\%$) of implanted Mn and Co impurities occupy anion sites in GaN and ZnO; (2) These anion site fractions are larger for Mn than for Co in both GaN and ZnO; (3) Mn and Co impurities have a high thermal stability in both cation and anion sites. Although anion site fractions have never been identified before for Mn nor Co in ZnO and only

for Mn in GaN, a number of arguments can be put forward which suggest that anion-site Co and Mn defects may indeed have low formation energies, particularly under a high concentration of anion vacancies (or equivalently under O- or N-deficient conditions). In fact, anion substitution may explain previous experimental observations of high charge states of Mn and Co impurities in GaN and ZnO, up to 4+, which are hardly compatible with cation substitutional impurities. A generalization of these effects will require the assessment of the formation energies of these defects, as well as an experimental reassessment of the lattice location of Mn and Co in GaN and ZnO for different preparation methods and growth conditions. The implications of anion substitution by Mn and Co in GaN and ZnO are of fundamental importance for the magnetism of these materials. Not only does the magnetic behavior of magnetic impurities depend directly on the lattice site they occupy, self-compensation effects by minority anion substitution may change the charge state of the majority cation substitutional fraction and thus indirectly control their magnetic interactions and order mechanisms.

In line with the emerging picture of defect-related ferromagnetism, the **search for room temperature ferromagnetism in transition-metal doped ZnO and GaN** focused on ion-implanted materials, where the potentially beneficial defects are created upon ion bombardment and can to a large extent be removed by thermal annealing. In order to use SQUID magnetometry as a reliable tool for detection of the typically very small ferromagnetic hysteresis, methods and procedures were developed which ensure that the magnetic signal originating from magnetic contamination can be reproducibly kept below a well defined value, of the same order as the signal due to setup-related artifacts. Following these procedures, none of the wide-gap DMS systems prepared by ion implantation of Mn, Fe and Co in ZnO and GaN showed measurable room temperature ferromagnetism. Given the wide range of material, implantation and post-processing parameters covered in this work, these results strongly suggest that ion-implanted wide-gap DMS materials are not ferromagnetic at room temperature.

Aiming at a **comprehensive description of the magnetism of wide-gap DMS materials**, we investigated the structure and magnetism of Cr-implanted GaN and Fe-implanted ZnO, two important impurity-host combinations which are not as well understood as more intensively studied systems such as Co- and Mn-doped ZnO and Mn-doped GaN. In Cr-implanted GaN, we aimed at studying the magnetic interactions between Cr moments, by varying the Cr atomic concentrations from the very di-

lute regime to well above the percolation threshold. In Fe-implanted ZnO, we aimed at a comprehensive description of the material's structure in terms of phase pureness and lattice location of the Fe impurities, as well as a detailed modeling of the paramagnetism observed under a varying density of beam-induced disorder. For both systems, we showed that the magnetic interactions between the transition-metal moments are, in fact, strong nearest-cation-neighbor antiferromagnetic interactions, which favor the antiparallel alignment of the localized moments. Such nearest-cation-neighbor antiferromagnetic interactions are consistent with those found in the corresponding nitride (CrN) and oxide (FeO), both antiferromagnetic materials with high Néel (ordering) temperatures. In agreement with several other comprehensive reports of absence of ferromagnetism in materials prepared using various other methods, our findings support the view of a growing fraction of the DMS community that *the transition-metal impurities in wide-gap semiconductors do not order ferromagnetically at high temperatures* [1]. The often observed high-temperature ferromagnetism can, alternatively, be attributed to non-intrinsic sources, such as a non-uniform distribution of the magnetic impurities, magnetic contamination or setup-related artifacts.

The absence of Heisenberg-type ferromagnetic exchange in wide-gap materials can hardly be considered surprising. Mechanisms of the type of *p-d* Zener exchange, which successfully describe the ferromagnetism of Mn-doped narrow-gap semiconductors such as GaAs and InAs, miss a basic requirement in wide-gap semiconductors. Because transition metals are deep centers in these materials, they do not introduce the itinerant holes required to mediate the magnetic interactions. On the other hand, in defect-related mechanisms, as in bound magnetic polaron (BMP) and similar models, the exchange energy density necessary to produce high-temperature ferromagnetism with a few % of transition-metal doping corresponds to a magnetic exchange much stronger than that observed in the strongest of the known ferromagnetic materials. Recently, a different type of model has been proposed which does not rely on ordered $3d$ local moments and Heisenberg-type exchange. This charge-transfer ferromagnetism (CTF) [2, 3] requires two distinct types of defects: one that creates a narrow impurity band and another to play the role of charge reservoir. If both types of defects are present, electrons can in principle be transferred to or from the reservoir until the filling level of the impurity band satisfies the spontaneous spin-split (Stoner) criterion. In dilute magnetic semiconductors, the impurity band can originate, for example, at grain boundaries or beam-induced

defects, while mixed-valency impurities may behave as charge reservoirs. Such CTF mechanisms could in principle explain the two main features of the high-temperature ferromagnetism observed in wide-gap DMS materials. First, CTF models predict nearly temperature-independent and anhysteretic magnetization loops (up to room temperature), which are typically observed in ferromagnetic wide-gap DMS materials. Second, the difficulty to produce and reproduce a ferromagnetic wide-gap DMS could be explained by the difficulty in monitoring and controlling the concentrations of the two types of defects involved in the CTF mechanism. However, as we have shown in Article I, the magnetic behavior of samples contaminated by Fe-containing tools or setup parts displays the same nearly temperature-independent and anhysteretic magnetization loops. Unambiguous evidence of charge-transfer ferromagnetism in wide-gap DMS materials has not been reported so far.

Outlook

From a broader and more fundamental point of view, the main implications of the results presented in this thesis concern the understanding of (1) the lattice location of transition-metal impurities in semiconductors and (2) the magnetic interactions between localized moments in dilute magnetic systems.

Challenging the current paradigms of low thermal stability of interstitial Mn in GaAs and pure cation substitution by Co and Mn in ZnO and GaN (1), our results raise several fundamental questions which go beyond their direct implications on the DMS field. Why does interstitial Mn in GaAs have such a high activation energy for diffusion? What physical mechanism allows for Mn and Co to substitute O and N, which are chemically so different? Why had both of these phenomena so far passed undetected? Although we provide some answers throughout this thesis, a reformulation of these paradigms will require further theoretical and experimental investigation. Very concretely, our results motivate a theoretical reassessment of the lattice location and thermal stability of transition-metals in GaAs, GaN and ZnO using density functional theory (DFT) calculations. For wide-gap semiconductors in particular, the use of DFT to study the magnetic and electrical behavior of impurities has been extensively developed during the last decade [1]. The challenges that highly-charged defects (which we propose to be the case for anion-substitutional Mn and Co) pose to DFT theory are an interesting test to its prediction power. On the experimental side,

the results of our emission channeling experiments question the suitability of more widely used techniques (e.g. XAFS) to detect and identify minority sites. Establishing (and possibly improving) the sensitivity of XAFS and related techniques to multi-site occupancy is also of major importance in the context of electrical and optical doping.

If, on the one hand, our lattice location results (1) defy established paradigms and (educated) intuition, then on the other, our main conclusions regarding the magnetism of wide-gap DMS (2) are a "return" to more conventional and well-established theories of magnetism. Long-range magnetic order in dilute magnetic systems requires mediators, i.e. itinerant carriers. This is the case, for example, in narrow-gap semiconductors such as GaAs and InAs doped with Mn, where ferromagnetic exchange is mediated by the valence-band holes introduced by the Mn impurities. However, being deep centers in wide-gap semiconductors, $3d$ transition metal impurities do not introduce such carriers. In addition, their "magnetic" $3d$ states are too distant in energy from the host bands to allow for efficient hybridization with free carrier states introduced by donor or acceptor co-doping. Spontaneously spin-split impurity bands and other defect-related mechanisms are, in principle, an alternative route for high-temperature ferromagnetism in semiconductors [4]. Indeed, some evidence exists of defect-related ferromagnetism in other materials which do not contain magnetic moments localized in magnetic impurities nor itinerant carriers to mediate magnetic interactions. Some examples are graphite [5, 6], hexaborides [7] and topological insulators [8,9]. Two questions remain, however. Are these effects intrinsic or can they be attributed to magnetic contamination and other experimental artifacts? Assuming that they are intrinsic, can dilute magnetic semiconductors incorporate similar phenomena? Answering these questions will require developments both on the theoretical and experimental sides. One of the major barriers towards establishing this new class of magnetic materials is, indeed, the lack of detailed models which make clear predictions of their behavior. This problem can, of course, be put the other way around. On the experimental side, the major challenge is achieving reproducibility, i.e. to find the archetype material which is easy to prepare and reproduce [4]. If this magnetic "fruitfly" is discovered, such signatures may then be found by serendipity, and the development of the appropriate models may follow by design.

From a more applied perspective, the results presented in this thesis have profound implications in the context of technological development

and implementation of DMS: the search for a semiconductor material with carrier-mediated ferromagnetic order above room temperature.

On the narrow-gap DMS side, our results open new prospects for increasing T_C in $Ga_{1-x}Mn_xAs$ through post-processing methods alternative to thermal annealing. This would allow to circumvent the technical difficulties in further film-growth development, which led to the stagnation of the record T_C value around 185 K during the last few years [1, 10]. However, even if such complex post-processing methods can be developed, it is unclear if they can deliver Curie temperatures which are compatible with practical applications. In addition, an increased processing complexity implies an increased difficulty for industrial implementation.

On the wide-gap side, the prospects for the discovery of a DMS system with high-temperature, carrier-mediated ferromagnetism are even more limited. Our results support the viewpoint that the high-temperature ferromagnetism often observed in wide-gap DMS materials is not intrinsic [1]. As discussed in the previous paragraphs, one can not exclude that a class of wide-gap DMS exists where high-temperature ferromagnetic order is not carrier mediated. The coming years will tell if such materials do indeed exist. However, even more than the existence of such materials, their usefulness in practical applications is still very unclear.

As a final comment, while there is still much to learn in terms of structure and magnetism of DMS materials, the future of semiconductor spintronics may rely on slightly different approaches. Proximity effects at ferromagnet-semiconductor interfaces, for example in $Fe/Ga_{1-x}Mn_xAs$ junctions, locally enhance the T_C of the $Ga_{1-x}Mn_xAs$ layer [11]. Such heterostructures may in principle circumvent the efficiency problems in metal-semiconductor spin-injection, since spin-polarized conduction can occur via the interfacial layer of the ferromagnetic semiconductor. Other promising alternatives to DMS are *antiferromagnetic* semiconductors. Exploiting the strong antiferromagnetic interactions characteristic of magnetic insulators may allow for the development of functional heterostructures [12, 13].

Bibliography

[1] T. Dietl, "A ten-year perspective on dilute magnetic semiconductors and oxides," *Nat. Mater.*, vol. 9, p. 965, 2010.

[2] J. M. D. Coey, K. Wongsaprom, J. Alaria, and M. Venkatesan, "Charge-transfer ferromagnetism in oxide nanoparticles," *J. Phys. D-Appl. Phys.*, vol. 41, p. 134012, 2008.

[3] J. M. D. Coey, P. Stamenov, R. D. Gunning, M. Venkatesan, and K. Paul, "Ferromagnetism in defect-ridden oxides and related materials," *New J. Phys.*, vol. 12, p. 053025, 2010.

[4] J. M. D. Coey in *Handbook of Spin Transport and Magnetism* (E. I. Tsymbal and I. Zutic, eds.), ch. Magnetism of Dilute Oxides, Chapman and Hall/CRC, 2011.

[5] P. Esquinazi, D. Spemann, R. Hohne, A. Setzer, K. H. Han, and T. Butz, "Induced magnetic ordering by proton irradiation in graphite," *Phys. Rev. Lett.*, vol. 91, p. 227201, 2003.

[6] J. Cervenka, M. I. Katsnelson, and C. F. J. Flipse, "Room-temperature ferromagnetism in graphite driven by two-dimensional networks of point defects," *Nat. Phys.*, vol. 5, p. 840, 2009.

[7] L. S. Dorneles, M. Venkatesan, M. Moliner, J. G. Lunney, and J. M. D. Coey, "Magnetism in thin films of CaB6 and SrB6," *Appl. Phys. Lett.*, vol. 85, p. 6377, 2004.

[8] Rui Yu, Wei Zhang, Hai-Jun Zhang, Shou-Cheng Zhang, Xi Dai, and Zhong Fang, "Quantized Anomalous Hall Effect in Magnetic Topological Insulators," *Science*, vol. 329, p. 61, 2010.

[9] M. Z. Hasan and C. L. Kane, "Colloquium: Topological insulators," *Rev. Mod. Phys.*, vol. 82, p. 3045, 2010.

[10] T. Jungwirth, K. Y. Wang, J. Masek, K. W. Edmonds, J. Konig, J. Sinova, M. Polini, N. A. Goncharuk, A. H. MacDonald, M. Sawicki, A. W. Rushforth, R. P. Campion, L. X. Zhao, C. T. Foxon, and B. L. Gallagher, "Prospects for high temperature ferromagnetism in (Ga,Mn)As semiconductors," *Phys. Rev. B*, vol. 72, p. 165204, 2005.

[11] M. Sperl, F. Maccherozzi, F. Borgatti, A. Verna, G. Rossi, M. Soda, D. Schuh, G. Bayreuther, W. Wegscheider, J. C. Cezar, F. Yakhou, N. B. Brookes, C. H. Back, and G. Panaccione, "Identifying the character of ferromagnetic Mn in epitaxial Fe/(Ga,Mn)As heterostructures," *Phys. Rev. B*, vol. 81, p. 035211, 2010.

[12] A. B. Shick, S. Khmelevskyi, O. N. Mryasov, J. Wunderlich, and T. Jungwirth, "Spin-orbit coupling induced anisotropy effects in bimetallic antiferromagnets: A route towards antiferromagnetic spintronics," *Phys. Rev. B*, vol. 81, p. 212409, 2010.

[13] T. Jungwirth, V. Novak, X. Marti, M. Cukr, F. Maca, A. B. Shick, J. Masek, P. Horodyska, P. Nemec, V. Holy, J. Zemek, P. Kuzel, I. Nemec, B. L. Gallagher, R. P. Campion, C. T. Foxon, and J. Wunderlich, "Demonstration of molecular beam epitaxy and a semiconducting band structure for I-Mn-V compounds," *Phys. Rev. B*, vol. 83, p. 035321, 2011.

Curriculum Vitae

Publications

- **Direct identification of interstitial Mn in heavily p-type doped GaAs and evidence of its high thermal stability**

  L. M. C. Pereira, U. Wahl, S. Decoster, J. G. Correia, M. R. da Silva, A. Vantomme and J. P. Araújo

  Applied Physics Letters **98**, 201905 (2011)

- **Mixed Zn and O substitution of Co and Mn in ZnO**

  L. M. C. Pereira, U. Wahl, S. Decoster, J. G. Correia, L. M. Amorim, M. R. da Silva, J. P. Araújo and A. Vantomme

  Physical Review B **84**, 125204 (2011)

- **Practical limits for detection of ferromagnetism using highly sensitive magnetometry techniques**

  L. M. C. Pereira, J. P. Araújo, M. J. Van Bael, K. Temst and A. Vantomme

  Journal of Physics D: Applied Physics **44**, 215001 (2011)

  (featured as a highlight in *Europhysics News* July-August 2011)

- **Paramagnetism and antiferromagnetic interactions in Cr-doped GaN**

  L. M. C. Pereira, T. Som, J. Demeulemeester, M. J. Van Bael, K. Temst and A. Vantomme

  Journal of Physics - Condensed Matter **23**, 346004 (2011)

  (featured as a *LabTalk* item in September 2011)

- **Diluted manganese on the bond-centered site in germanium**

  S. Decoster, S. Cottenier, U. Wahl, J. G. Correia, L. M. C. Pereira, C. Lacasta, M. R. da Silva and A. Vantomme

  Applied Physics Letters **97**, 151914 (2010)

- **Magnetic and transport properties of diluted granular multilayers**

  H. G. Silva, H. L. Gomes, Y. G. Pogorelov, L. M. C. Pereira, G. N. Kakazei, J. B. Sousa, J. P. Araújo, J. F. L. Mariano, S. Cardoso and P. P. Freitas

  Journal of Applied Physics **106**, 113910 (2009)

In preparation

- **Evidence of N substitution by Mn in wurtzite GaN**

  L. M. C. Pereira, U. Wahl, S. Decoster, J. G. Correia, L. M. Amorim, M. R. da Silva, A. Vantomme and J. P. Araújo

  In preparation for *Physical Review Letters*

- **Paramagnetism and antiferromagnetic interactions in phase-pure Fe-implanted ZnO**

  L. M. C. Pereira, U. Wahl, J. G. Correia, M. Van Bael, S. Decoster, A. Vantomme and J. P. Araujo

  In preparation for *Physical Review B*

- **Cation versus anion substitution of transition metals in GaN and ZnO**

  L. M. C. Pereira, U. Wahl, S. Decoster, J. G. Correia, L. M. Amorim, M. R. da Silva, A. Vantomme and J. P. Araújo

  In preparation for *Physical Review B*

- **Stability and diffusion of interstitital and substitutional Mn in GaAs of different doping types**

  L. M. C. Pereira, U. Wahl, S. Decoster, J. G. Correia, L. M. Amorim, M. R. da Silva, J. P. Araújo, A. Vantomme

  In preparation for *Physical Review B*

- **Searching for room temperature ferromagnetism in transition metal implanted ZnO and GaN**

  L. M. C. Pereira, J. P. Araújo, U. Wahl, M. J. Van Bael, K. Temst, A. Vantomme

  In preparation for *Journal of Applied Physics*

Selected communications in international conferences

Oral presentations

- **Lattice location of transition metals in dilute magnetic semiconductors**

  L. M. C. Pereira, U. Wahl, A. Vantomme, J. P. Araújo

  56th Annual Conference on Magnetism and Magnetic Materials (MMM), Scottsdale, USA, 2011

- **Evidence of high thermal stability of interstitial Mn in heavily p-doped GaAs**

  L. M. C. Pereira, U. Wahl, S. Decoster, J. G. Correia, L. M. Amorim, M. R. da Silva, A. Vantomme, J. P. Araújo

  55th Annual Conference on Magnetism and Magnetic Materials (MMM), Atlanta, USA, 2010

- **Anomalous Ferromagnetism in Fe-implanted ZnO**

  L. M. C. Pereira, U. Wahl, J. G. Correia, J. P. Araújo

  53rd Annual Conference on Magnetism and Magnetic Materials (MMM), Austin, USA, 2008

Poster presentations

- **Practical limits for detection of ferromagnetism using high sensitivity magnetometry**
  L. M. C. Pereira, J. P. Araújo, M. J. Van Bael, K. Temst and A. Vantomme
  56th Annual Conference on Magnetism and Magnetic Materials (MMM), Scottsdale, USA, 2011

- **Lattice location of Mn implanted into GaAs: Identification of interstitial Mn and evidence of its high thermal stability**
  L. M. C. Pereira, U. Wahl, S. Decoster, J. G. Correia, J. P. Araújo, A. Vantomme
  17th International Conference on Ion Beam Modification of Materials (IBMM), Montréal, Canada, 2010

- **Room Temperature Ferromagnetism with Giant Magnetic Moment in Fe:ZnO**
  L. M. C. Pereira, U. Wahl, J. G. Correia, J. P. Araújo
  9th International Workshop on Non-Crystalline Solids (IWNCS), Porto, Portugal, 2008

Distinctions and awards

2007 **Prof. Moreira de Araújo Award**
Attributed to the best student(s) completing the degree in Physics in the Faculty of Sciences of the University of Porto

2007 **Eng. António de Almeida Award**
Attributed to the best best student(s) completing the degree in Physics in the Faculty of Sciences of the University of Porto (awarded by the Foundation Eng. António de Almeida)

2008 **Best Poster Prize**
9th International Workshop on Non-Crystalline Solids (IWNCS)
Porto, Portugal, 2008

2011 **Best Student Presentation Award**
56th Annual Conference on Magnetism and Magnetic Materials
Scottsdale, USA, 2011